**Distribution Agreement**

In presenting this thesis or dissertation as a partial fulfillment of the requirements for an advanced degree from Emory University, I hereby grant to Emory University and its agents the non-exclusive license to archive, make accessible, and display my thesis or dissertation in whole or in part in all forms of media, now or hereafter known, including display on the world wide web. I understand that I may select some access restrictions as part of the online submission of this thesis or dissertation. I retain all ownership rights to the copyright of the thesis or dissertation. I also retain the right to use in future works (such as articles or books) all or part of this thesis or dissertation

Signature:

_____ _____

Haiming Zhu Date

**Quantum Confined Semiconductor Nanocrystals for Efficient Charge Separation and Solar-to-fuel Conversion**

By

Haiming Zhu

Doctor of Philosophy

Chemistry

_____

Dr. Tianquan Lian

Advisor

_____

Dr. Michael C. Heaven

Committee Member

_____

Dr. R. Brian Dyer

Committee Member

Accepted:

_____

Lisa A. Tedesco. Ph.D.

Dean of the James T. Laney School of Graduate Studies

_____

Date

# Quantum Confined Semiconductor Nanocrystals for Efficient Charge Separation and Solar-to-fuel Conversion

By

Haiming Zhu
B.S., University of Science and Technology of China, P.R. China, 2008

Advisor: Tianquan Lian, Ph.D.

An abstract of
A dissertation submitted to the Faculty of the
James T. Laney School of Graduate Studies of Emory University
in partial fulfillment of the requirements for the degree of
Doctor of Philosophy
in Chemistry
2014

# Abstract


## Quantum Confined Semiconductor Nanocrystals for Efficient Charge Separation and Solar-to-fuel Conversion

**By Haiming Zhu**

The advancement of solar-to-fuel conversion requires not only efficient catalysts but also efficient light harvesting and charge transfer centers. Because of their tunable electronic, optical and chemical properties, quantum confined semiconductor nanocrystals represent an interesting system for fundamental and practical charge transfer studies. In this dissertation, we investigated the single and multiple charge transfer from various quantum confined semiconductor nanocrystals as well as implemented them in solar-to-fuel conversion.

We first studied single exciton charge separation and recombination from CdX (X=S, Se, Te) quantum dots (QDs), CdSe/ZnS type I and CdTe/CdSe type II core/shell QDs. We observed the rate of electron transfer from CdX QDs increases at decreasing size (and increasing driving force), showing a lack of Marcus inverted regime. We proposed an Auger-assisted electron transfer model, in which the electron transfer can be coupled to the hole excitation. In CdSe/ZnS type I QDs, with increasing shell thickness, both the charge separation and recombination rates decrease exponentially, which agrees well with the exponential decreases of the electron and hole densities at QD surface. In CdTe/CdSe type II QDs, the shell localized electron and core localized hole enable ultrafast electron transfer while simultaneously retards the charge recombination process, which leads to the idea of "*wavefunction engineering*" for QD charge transfer.

We then studied multiexciton annihilation and dissociation from CdSe/CdS type II QDs and CdSe nanorods (NRs). We show that the multiexciton dissociation efficiency (MED) can be significantly enhanced by controlling the band alignment and shapes of semiconductor NCs. The enhanced MED efficiencies are due to the electron and hole distributions in these nanomaterials, which simultaneously retard Auger recombination and facilitate interfacial electron transfer.

Finally, we demonstrated efficient redox mediator generation and $H_2$ evolution using asymmetric CdSe/CdS seeded NRs. Time resolved spectroscopy study shows that the higher efficiency of CdSe/CdS NRs is due to ultrafast electron transfer, hole filling and slow charge recombination. Using ZnSe/CdS seeded NRs, we show wavelength dependent photocatalytic behavior and we found that under rod excitation, ultrafast electron transfer from CdS rod and fast localization of hole to ZnSe seed suppressing charge recombination loss thus enhancing photocatalytic performance.

# Quantum Confined Semiconductor Nanocrystals for Efficient Charge Separation and Solar-to-fuel Conversion

By

Haiming Zhu
B.S., University of Science and Technology of China, P.R. China, 2008

Advisor: Tianquan Lian, Ph.D.

A dissertation submitted to the Faculty of the
James T. Laney School of Graduate Studies of Emory University
in partial fulfillment of the requirements for the degree of
Doctor of Philosophy
in Chemistry
2014

# ACKNOWLEDGEMENT

First, I would like to express my deepest thank to my advisor, Dr. Tianquan Lian, for his guidance and support throughout my graduate career. His wide knowledge and critical thinking have been of great value to my scientific research. The balance between free environment and high standard he has set in the Lian lab has stimulated our enthusiasm and motivation. He has set a good example for my future career of how to performe independent researches but also conduct fruitful collaborations. Aside from the scientific work, his genuine understanding and sincere support to me have helped me overcome those difficult times, including my PhD/Postdoc application and the birth of my baby. Without him, I couldn't have such an uneventful and enjoyable graduate journey. I also wish to extend my sincere thanks to my graduate committee members, Dr. Michael C. Heaven and Dr. Brian Dyer, for their insightful questions, helpful comments and interesting suggestions.

I would like to thank my lab colleagues and my friends for their support and friendship. Dr. Jier Huang and Dr. Chantelle Anfuso introduced me laser and optics knowledge and skills in my first year in graduate school. Dr. William Rodríguez has been keeping the laser running, which greatly facilitates this work. Dr. Shengye Jin always likes sharing and discussing his ideas and thoughts with me even after his departure from Emory. Dr. Zhuangqun Huang introduced me quantum dot synthesis and was always ready to help me with books/equipments that I need. Dr. Ye Yang and Mr. Kaifeng Wu, who have been working with me closely, are invaluable sources for discussing projects, ideas and literatures. Hongjin Lv from our collaboration group has worked with me together on the photochemistry work. I am also grateful to other friends and colleagues: Dr. Zheng Liu, Dr. Xu Xiang, Dr. Allen Ricks, Dr. Weiming Liu, Dr. Burai Tarak, Dr. Zheyuan Chen, Dr. Jinquan Chen, Dr. Chris Keating, Lewen Yang, Nannan Han, Qiuyang Li, David Wu, Hugh H. Green, Tony Xu, and Elisabeth McClure. They have contributed to my development more generally as a scientist, friend and human being.

Last but not least, I would like to thank my entire family for their support over the years. My father Jian Zhu, mother Yun Ma and my mother-in-law Qiuping Ma have given me enormous encouragement and support especially in taking care of my son. My wife, Nianhui Song, has given me infinite understanding and support by encouraging me throughout the graduate career. My lovely son, Bruce, has provided me with endless motivation and happiness.

# Table of Content

# List of Figures

conventional (i=I, upper panles) and Auger-assisted (i=II, lower panels) ET models. ET rate constants to different acceptors have been scaled to have similar values for the smallest size of QDs and the scaling factors are indicated in the figure. (D) Measured (symbols) and predicted (lines) ET rates as a function of driving force according to the conventional (DI) and Auger-assisted (DII) ET models. The predicted values are calculated according to Eq. 3.5 and Eq. 3.14 with λ values of 0.3 (black solid line), 0.4 (red dashed line), 0.5 (green dashed line) eV. The measured ET rate constants of from CdX QDs (CdS: blue, CdSe: red, CdTe: dark green) to molecular acceptors ($MB^+$: circles, $MV^{2+}$: triangles, AQ: diamonds) have been scaled by the R dependent prefactors in Eq. 3.15 ($CH\Psi 1\mathrm{Se(R)}02$) and Eq. 3.16 ($C\Psi 1\mathrm{Se(R)}02\mathrm{R}2$), respectively, to account for the size and materials dependent variation of coupling strength. The C and $C_H$ values for each series of QD-acceptor complexes are chosen such that QD-acceptors with the same driving force have the same scaled ET rates regardless of their chemical nature. ..... 49

**Figure 3.5.** Conventional (i=I, upper panel) and Auger-assisted (i=II, lower panel) models for ET from QDs. (Ai) Single particle picture, showing the electron and hole levels before and after the ET process. In conventional ET(AI), the 1S electron is transferred from QD* ($1S_e$) to the electron acceptor (A) without changing the hole level ($1S_h$). In Auger-assisted ET(AII), ET can be coupled with a change in the hole energy level, giving rise to a continuum of product states, each corresponding to the hole in a different excited level. (Bi) State representation showing the energy of the ground (QD-A), excited (QD*-A) and charge-separated states ($QD^+$-$A^-$) as well as the ET (with rate $k_{ET}$ or $k_{AET}$) and back ET ($k_R$) processes. (Ci) Marcus representation showing the energy of the reactant and product states as a function of the nuclear displacement along the ET

# List of Tables

# Chapter 1. Introduction

Reproduced in part with permission from Energy Environ. Sci. 2012, 5 (11), 9406-9418. and Acc. Chem. Res. 2013, 46 (6), 1270-1279.

## 1.1. Introduction of Semiconductor Nanocrystals for Solar Energy Conversion

Worldwide energy demand currently exceeds 13 TW and is expected to be more than doubled (30 TW) by 2050 and tripled (46 TW) by the end of the century.[1,2] Fossil fuels alone will not be sufficient to meet the demand in a long run and in an environmentally sustainable way. The incident solar energy on earth per hour is more than the current world energy consumption in an entire year. Therefore, efficient solar energy conversion is a promising approach for meeting the world energy demand, making it one of the most important scientific challenges today. [2-4]

There are two general approaches for solar energy conversion.[4] In the first approach (as shown in Figure 1.1), solar energy is converted into chemical fuels (solar-to-fuel conversion). Since chemical fuels are a high density, storable, and transportable energy source, direct solar-to-fuel conversion also addresses the energy storage problem.[3,5] In the second approach, solar energy is directly converted into electricity

through photovoltaic devices or solar cells.[6,7] The complete solar-to-fuel conversion systems often consist of two parts: a photoanode for the oxidation of water to form $O_2$ and $H^+$, and a (photo)cathode for the reduction of water or $CO_2$ to generate fuels. The overall reactions in the photocathode and photoanode involve many processes. For example, The reaction on a triadic photocathode (Figure 1.1B) involves i) light harvesting by the sensitizer with an efficiency $\phi_{LH,}$ ii) charge collection from the excited sensitizer to catalysis through either direct transfer or electron mediator with an efficiency $\phi_{col}$, iii) the catalytic reaction to generate fuels with an efficiency $\phi_{cat}$. The overall solar-to-fuel conversion quantum efficiency is determined by the efficiencies of all three processes, $\Phi = \phi_{LH} \times \phi_{col} \times \phi_{cat}$. Clearly, efficient solar-to-fuel conversion requires the development of not only efficient catalysts (to increase $\phi_{cat}$) but also efficient sensitizers and novel approaches for light harvesting and charge separation (to increase both $\phi_{LH}$ and $\phi_{col}$).

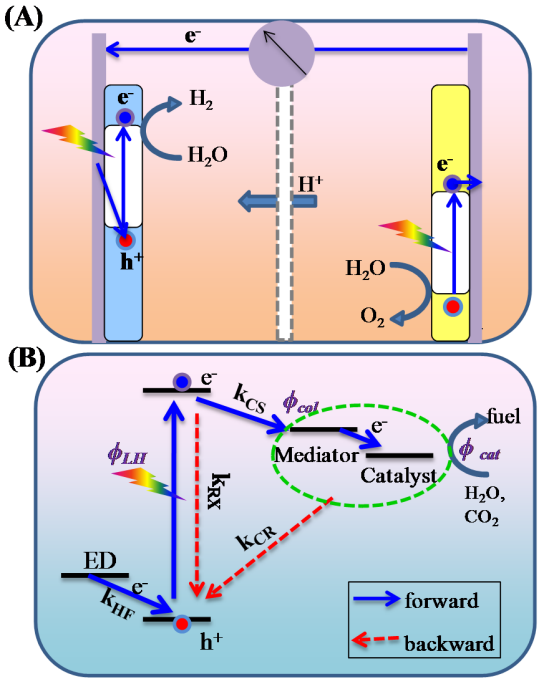

**Figure 1.1.** (A) Schematic illustration of a water splitting photoelectrochemical cell, consisting of a photoanode and photocathode compartments separated by a $H^+$ permeable membrane. Water is oxidized in the photoanode to form O2 and $H^+$ and reduced in the photocathode to form H2. (B) Schematic depiction of major processes in the fuel forming reaction in the photocathode side, involving the electron donor (ED), sensitizer, mediator and catalyst. The competitions between the forward (electron transfer and hole filling, with rate constants $k_{CS}$ and $k_{HF}$, respectively) and backward (electron – hole and charge recombination, with rate constants $k_{RX}$ and $k_{CR}$, respectively) reactions determine the charge collection efficiency ($\phi$col).

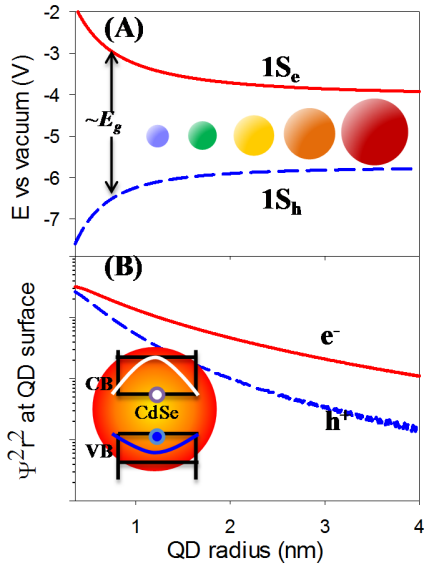


**Figure 1.2.** 1S electron (red solid line) and 1S hole (blue dashed line) energy levels (A) and their radial distribution functions ($\Psi^2r^2$ ) at the QD surface (B) as a function of CdSe

QD radius calculated according to an effective mass model, in which the electron and hole are treated as particles confined in finite spherical potential wells.[8-11]

Compared with molecular chromophores, inorganic semiconductor nanocrystals (NCs) typically exhibit much larger extinction coefficients over a broader spectral range, which should lead to improved light harvesting performance.[12-14] Unlike bulk semiconductors in which the carriers can undergo trap mediated recombination before diffusing to the surface to be extracted,[15] the large surface-to-volume ratio and the quantum confinement in NCs significantly enhance the surface amplitude of carrier wavefunctions, which facilitates interfacial carrier extraction to the surrounding charge collection network.[16-22] Shown in Figure 1.2 are 1S electron and hole energy levels and their surface densities as a function of CdSe quantum dot (QD) radius calculated with an effective mass model.[8-11] Because of the quantum confinement effect, the light harvesting properties, redox potentials as well as charge transfer dynamics of NCs can be tuned by changing their size, providing additional control of material properties.[17,23-26] In addition, the surface of colloidal NCs can be readily modified to bind specific functional targets (including catalysts) and to be soluble in a preferred reaction environment.[27-29] Although the efficiency is still a subject of intense debate and appears to be modest,[30-39] recently reported multiexciton generation (MEG) phenomenon in semiconductor NCs, a process by which multiple excitons are generated by one absorbed high energy photon, has further intensified the interests of using these materials for charge separation applications.[11,19,40-42] Indeed, semiconductors NCs have been successfully incorporated

into a variety of photovoltaic devices, e.g. solar cells and photodetectors[40,41,43] and photocatalytic reactions, e.g. cofactor generation, water splitting and $CO_2$ fixation.[44-46]

## 1.2. Interfacial Electron Transfer from Semiconductor Nanocrytals

The overall charge separation efficiency $\phi_{col}$ from NC sensitizers, as illustrated in Figure 1.1, depends on the competitions of i) electron-hole recombination (with rate $k_{RX}$) *vs* charge separation ($k_{CS}$) and ii) charge recombination ($k_{CR}$) *vs* hole filling (or regeneration) by sacrificial electron donors or external bias ($k_{HF}$). Because of these competing processes, efficient overall charge separation requires fast interfacial electron transfer ($k_{RX} << k_{CS}$) and fast hole removal ($k_{CR} << k_{HF}$) from NCs.

Despite extensive interfacial electron transfer studies from quantum confined semiconductor nanocrystals (e.g. QDs, nanorods), the factors that control the interfacial charge transfer properties from NCs remain unclear. Due to the strong electron-nuclear interaction in molecules, inter- and intra- molecular electron transfer (ET) is accompanied by large rearrangement of the nuclear configuration, which are described by the Marcus ET theory,[47-50] exhibiting the well-known dependences of ET rates on the driving force in the Marcus normal, barrier-less, and inverted regimes.[48,51,52] In many bulk semiconductor materials (such as CdX, X=S, Se, and Te), the week electron-nuclear and electron-electron interaction justify the treatment of electrons and holes as quasi-free and independent particles, in which photoinduced electron transfer requires negligible change

in nuclear configurations or the motion of the accompanying holes.[53] In excitonic nanomaterials, such as QDs, both the electron-hole interaction and electron-phonon interactions fall between those of the bulk semiconductor materials and molecular chromophores and the appropriate model for describing and controlling photoinduced charge transfer (or exciton dissociation) still lacks. The tunable optical and electronic properties of semiconductor QDs provides an ideal platform for testing and exploring the electron transfer model from excitonic nanomaterials.

Herein, we first studied the size/driving dependent electron transfer rates from CdS, CdSe and CdTe QDs to different electron acceptors (anthraquinone, methylviologen and methylene blue) by transient absorption spectroscopy. We show that the rate of photoinduced electron transfer from QDs increases at decreasing QD size (and increasing driving force), showing a lack of Marcus inverted regime behavior over an apparent driving force range of ~ 0-1.3 V. We account for this unusual driving force dependence by proposing an Auger-assisted electron transfer model, in which the transfer of the electron can be coupled to the excitation of the hole, circumventing the unfavorable Frank-Condon overlap in the Marcus inverted regime. These results will be discussed in Chapter 3.

We also studied the charge separation and recombination rates from CdSe/ZnS type I core/shell QDs of different shell thicknesses to anthroquinone molecules (as electron acceptor). With the increasing shell thickness $d$, both the charge separation and recombination rates decrease exponentially, $k(d) = k_0 e^{-\beta d}$, with exponential factors of 0.35±0.03 per Å and 0.91±0.14 per Å, respectively. Model calculations of these

core/shell QDs show that the trends in charge separation and recombination rates agree well with the exponential decreases of the electron and hole densities at the QD surface with the shell thickness. This finding suggests the relative electron (hole) density on QDs surface could be used to ascertain the relative electronic coupling thus electron (hole) transfer rate from QDs. These results will be discussed in Chapter 4.

## 1.3. Multiexciton Annihilation and Dissociation in Semiconductor Nanocrytals

A unique property of semiconductor NCs is the generation and accommodation of multiple excitons (electron and hole, e-h, pairs bound by Coulomb interaction) per particle by either optical excitation or electric pumping. These multiple excitons can be converted to multiple emitted photons or separated external charges, with potential applications in advanced nanoscale optoelectronic devices ranging from high power light emitting diodes,[54,55] low-threshold lasing media,[56-58] and multi-photon sources[59] to highly sensitive photodetectors and efficient photovoltaic/catalytic cells.[40,41,60] Recent reports of multiexciton generation (MEG) by one absorbed photon have intensified the interest of using semiconductor NCs as light harvesting and charge separating components for delivering multiple carriers in photocatalytic and photovoltaic devices, despite its modest efficiency.[61-65] However, Auger recombination, wherein an electron-hole pair recombines by transferring its energy to another particle (carrier or exciton), significantly shortens the

multiexciton lifetime.[66,67] Therefore, the development and improvement of advanced NC based optoelectronic devices requires the understanding of multiexciton annihilation (MEA) dynamics in NCs and schemes for their efficient conversion to emitted photons (for emission applications) or separated external charges (for photovoltaic/catalytic applications) in competition with their fast Auger recombination (as shown in Figure 1.3). One possible scheme for the utilization of short-lived multiexcitons in solar energy conversion is the ultrafast exciton dissociation by interfacial charge transfer from NCs to acceptors.[11,19,22,42,64]

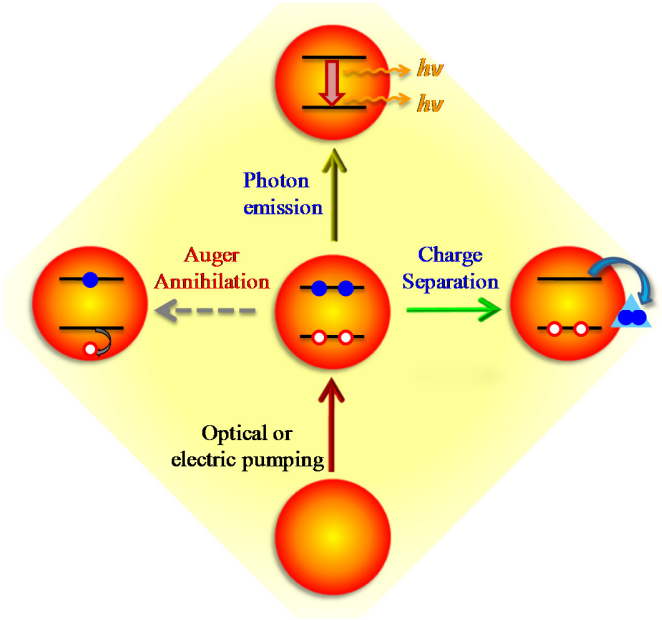


**Figure 1.3.** Schematic depiction of multiexciton generation, annihilation and conversion to emitted photons or separated charges. The competition between Auger annihilation and photoemission or charge separation determines the multiexciton conversion efficiencies.

The extraction of multiple electrons from one QD has been demonstrated previously in both QD-based photovoltaic devices[40,41,60] and QD-molecular acceptor complexes[19,42]. In this work, compared to core-only CdSe QDs, we show the efficiency of multiexciton dissociation can be significantly boosted by engineering the bandalignment (in CdSe/CdS quasi-type II QDs study) and shape (in CdSe quantum rods study) of semiconductor NCs. The enhanced MED efficiencies are due to the electron and hole distributions in these nanomaterials, which simultaneously retard Auger recombination and facilitate interfacial electron transfer. These results will be discussed in Chapter 6 and Chapter 7, respectively.

## 1.4. Semiconductor Nanoheterostructures for Charge Transfer and Solar-to-fuel Conversion

### 1.4.1. Classification of Semiconductor Nanoheterostructures

The advancement in the synthesis of colloidal semiconductor NCs has led to the preparation of more sophisticated semiconductor nanoheterostructures (SNHs) with multiple component materials and nonspherical shapes that can be tuned for desired functions.[68-73] For example, CdX, ZnX, and PbX (X=S, Se, Te) based semiconductor materials have been extensively tailored and combined into spherical core/shell QDs, linear dot-in-rod, rod/rod, branched tetrapods, octapods and even curved nanostructures.

By tailoring the potential energy profile through material choice and degree of quantum confinement *via* size and shape of the components, the electron and hole wavefunctions in SNHs can be independently engineered to control a variety of photophysical properties, including energy levels, emission quantum yield, single and multiple exciton state lifetimes.

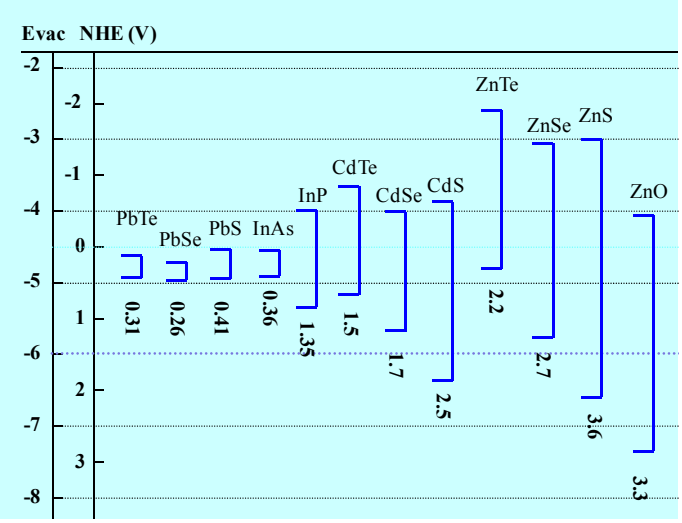


**Figure 1.4.** Bulk conduction and valance band edge positions (*vs* vacuum and NHE) and bandgaps of common semiconductor materials at ~300 K.[74-80]

Figure 1.4 gives an overview of the bulk band edge positions of semiconductor materials that are commonly used in NC synthesis. It should be noted that there are considerable uncertainties in these reported values.[74-80] Based on the relative energy offsets of conduction band (CB) and valance band (VB) edges ($\Delta U_C$ and $\Delta U_V$) of the component materials, the band alignment of semiconductor heterostructures is typically

classified as type I, quasi-type II and type II. Examples of these band alignments are shown in Figure 1.5 for core/shell heterostructures. In type I materials, such as CdX (X=S, Se, Te)/ZnS, both the CB and VB edges of CdX locate within the band gap of ZnS to form a "nested" configuration. Therefore, both the lowest energy photoexcited electron and hole are primarily confined in the material with a narrower band gap (CdX). Type II heterostructures, such as CdX (X=S, Se, Te)/ZnTe, CdTe/CdSe, CdTe/CdS, or ZnSe/CdS, are characterized by a staggered band alignment with the lowest energy levels for the electron and the hole in different materials. Consequently, the photoexcited CB electron and VB hole are localized in different materials across the heterostructure, forming a "spatially indirect" exciton with a band gap determined by the CB edge of one material and VB edge of another. In the quasi-type II regime, one carrier is confined in one domain while the other is delocalized over the whole heterostructure.

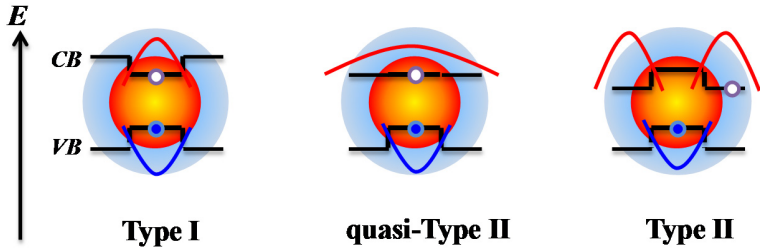


**Figure 1.5.** Schematic representation of Type I, quasi-Type II and Type II band alignment and carrier localization in core/shell heterostructures. The black lines indicate the band edge positions in the core and shell materials. The red and blue (inverted) lines depict the electron and hole envelope functions, respectively.

For colloidal semiconductor nanoheterostructrures, the lowest energy levels for excited electron ($1S_e$) and hole ($1S_h$) are shifted up by confinement energies ($\Delta E_e$ and $\Delta E_h$) from the CB and VB edges, respectively, of the bulk materials because of the quantum confinement effect. Therefore, besides the bulk band offsets between the material compositions, their size and shape also affect the carrier distribution and band alignment in SNHs. An "energy criterion" has been proposed to serve as a rough guide of carrier localization regimes in SNHs.[81,82] That is, an electron (hole) can be assumed to be primarily localized in one material if $\Delta E_e < \Delta U_C$ ($\Delta E_h < \Delta U_V$) or delocalized in both materials if $\Delta E_e > \Delta U_C$ ($\Delta E_h > \Delta U_V$). For example, because of strong quantum confinement, PbS/PbSe core/shell QDs of small core size, which has a type II band alignment in bulk materials, behave as a type I nanoheterostructure because both 1S electron and hole confinement energies are larger than the conduction and valance band offsets ($\Delta E_e >> \Delta U_C$ and $\Delta E_h >> \Delta U_V$) and the wavefunctions of both the electron and hole extend throughout both materials.[76,83] On the other hand, PbSe/CdSe core/ shell QDs of small core size, which has a type I bulk band alignment, show quasi-type II features because of the large electron confinement energy in the PbSe core ($\Delta E_e > \Delta U_C$).[77,84]

The size dependent confinement energy can be used to tune the band alignment in SNHs, which significantly alter their photophysical properties, including carrier energy relaxation, carrier spin relaxation, single and multiple exciton lifetime, electron-hole exchange interaction, and charge transfer rates.[9,78,85-88] It has been shown that CdTe/CdSe[87,89], CdSe/CdS[78,90], CdS/ZnSe[81], ZnSe/CdSe[91,92] core/shell QDs can be tuned

from type I to type II regimes by changing either the core size or shell thickness. For example, a transition from the quasi-type II to type I band alignment can be realized in CdSe/CdS core/shell QDs ($\Delta U_C \approx 0.3$ eV, $\Delta U_V \approx 0.5$ eV) by increasing the core size.[78,79] The confinement energy and spatial distribution (envelop function) for the lowest energy electron/hole in SNHs can be well described by the effective mass model,[8-11,78,81,82,87,88,93] which in principle allows the computational design of SNHs with desired carrier spatial distributions. However, special care must be taken when dealing with SNHs with small band offsets due to interfacial strain and distortion in nanostructures.[88,94-97]

### 1.4.2. Semiconductor Nanoheterostructures for Charge Transfer and Solar-to-fuel Conversion

In the simplest NCs, i.e. single component spherical quantum dots (QDs), the electron-hole recombination lifetime is typically 10 - 20 ns for colloidal CdX (X = S, Se, Te) QDs at room temperature and is size-independent because of negligible variation of electron-hole overlap with QD dimensions.[98] With decreasing particle size, quantum confinement effect increases both the electron and hole energy and surface densities (as shown in Figure 1.2B), which increases the rate for both the charge separation ($k_{CS}$, electron transfer) and charge recombination ($k_{CR}$, hole transfer) processes in QD-electron acceptor complexes.[8,9,11,20,99] Therefore, it remains difficult to optimize the overall charge

separation efficiency by selectively and rationally controlling the competing processes in single component QDs.

Semiconductor nanoheterostructures offer additional opportunities to effectively control their charge transfer properties by engineering the electron/hole wavefunctions. In Chapter 5, we show with type II core/shell QDs, such as CdTe/CdSe, in which the lowest energy conduction band electron is largely localized in the shell while the lowest energy valence band hole is localized in the core, the intrinsic excited electron lifetime can be significantly prolonged. Using CdTe/CdSe-anthraquinone (AQ) complexes, we show this spatial distribution enables ultrafast electron transfer to the surface adsorbed electron acceptors due to enhanced electron density on the shell materials, while simultaneously retards the charge recombination process because the shell acts as a tunneling barrier for the core localized hole. This finding also suggests the "*wavefunction engineering*" idea for QD charge transfer.

In solar-to-fuel conversion applications, to sustain a photoreduction reaction, in addition to electron transfer to the redox mediator or catalyst, efficient filling of the hole by an electron from an external circuit (or a sacrificial electron donor in a model system) is also required for the accumulation of reducing equivalents in the catalysts (Figure 1.1B). Therefore, instead of core/shell QDs, an asymmetric nanoheterostructure where both electron and hole are exposed to carrier extract network is highly desirable. Herein, we reported a redox mediator based approach for solar-to-fuel conversion using semiconductor NCs. We compared the quantum yields of methyl viologen radical generation and hydrogen evolution using NCs of different compositions and dimensions

as the light harvesting and charge separation component. Compared to $Ru(bipy)_3^{2+}$, CdSe seed and CdSe/CdS core/shell quantum dots and CdS nanorods, the quantum yields are significantly higher in the CdSe/CdS dot-in-rod nanorods. Time resolved spectroscopy study shows the higher efficiency of CdSe/CdS quasi-type II DIR is due to ultrafast electron transfer to $MV^{2+}$, fast hole filling by MPA, and slow charge recombination. These results will be discussed in Chapter 8.

To further reveal the carrier dynamics in seeded nanorods and its effect on their charge transfer properties (such as the origna for the slow charge recombination in $MV^{2+}$ photoreduction) and photocatalytic performance, we studied the redox mediator (methyl viologen, $MV^{2+}$) photoreduction process with ZnSe/CdS type II dot-in-rod nanorod by combining steady state photochemistry and time resolved spectroscopy under different excitation wavelengths. These results will be discussed in Chapter 9.

## 1.4. Conclusion

In conclusion, we have conducted a series of studies of photo-induced excited state dynamics and interfacial charge transfer properties in zero-dimensional and one-dimensional quantum confined semiconductor nanocrystals and nanoheterostructures by transient absorption spectroscopy. In QD single exciton charge separation and recombination studies, the effect of driving force (through QD size) and electronic coupling (through shell composition/thickness) have been systematically investigated to

fundemantally understand the factors controlling the electron transfer from QDs. In NC multiexciton dissociation studies, the effect of band alignment and shape of nanocrystal have been investigated to explore the approaches to enhance the multiexciton dissociation efficiencies. For seeded nanorod heterostructures, we implemented them in solar-to-fuel conversion reactions and characterized each reaction step with time resolved spectroscopy techniques to identify the mechanisms behind the steady state performance.

The rest of this work is organized as follows: Chapter 2 summarizes the experimental procedures, including the preparation of samples and experimental techniques. Chapter 3 studies the size (driving force) dependent electron transfer from CdX (X=S, Se, Te) QDs and proposes the "Auger-assisted electron transfer" idea for exciton dissociation in excitonic nanomaterials. Chapter 4 and 5 present the effect of shell thicknesses and core/shell compositions on core/shell QD charge separation and recombination rates and introduces the "wavefunction engineering" idea for rationally controlling charge transfer processes from QDs. Chapter 6 and 7 examine the effect of nanocrystals band alignment and shape on their multiexciton annihilation and dissociation processes. Chapter 8 and 9 demonstrate the using of asymmetric seeded nanorod for solar-to-fuel conversion and reveal the fundemantal carrier dynamics and charge transfer processes for photocatalytic performances.

## References

(1) Hoffert, M. I.; Caldeira, K.; Benford, G.; Criswell, D. R.; Green, C.; Herzog, H.; Jain, A. K.; Kheshgi, H. S.; Lackner, K. S.; Lewis, J. S.; Lightfoot, H. D.; Manheimer, W.; Mankins, J. C.; Mauel, M. E.; Perkins, L. J.; Schlesinger, M. E.; Volk, T.; Wigley, T. M. L. *Science* **2002**, *298*, 981.

(2) Lewis, N. S.; Crabtree, G. *Basic Research Needs for Solar Energy Utilization*, U.S. Department of Energy, 2005.

(3) Lewis, N. S.; Nocera, D. G. *Proc. Natl. Acad. Sci.* **2006**, *103*, 15729.

(4) Blankenship, R. E.; Tiede, D. M.; Barber, J.; Brudvig, G. W.; Fleming, G.; Ghirardi, M.; Gunner, M. R.; Junge, W.; Kramer, D. M.; Melis, A.; Moore, T. A.; Moser, C. C.; Nocera, D. G.; Nozik, A. J.; Ort, D. R.; Parson, W. W.; Prince, R. C.; Sayre, R. T. *Science* **2011**, *332*, 805.

(5) Gray, H. B. *Nat Chem* **2009**, *1*, 7.

(6) O'Regan, B.; Gratzel, M. *Nature* **1991**, *353*, 737.

(7) Bach, U.; Lupo, D.; Comte, P.; Moser, J. E.; Weissortel, F.; Salbeck, J.; Spreitzer, H.; Gratzel, M. *Nature* **1998**, *395*, 583.

(8) Zhu, H.; Song, N.; Lian, T. *J. Am. Chem. Soc.* **2010**, *132*, 15038.

(9) Zhu, H.; Song, N.; Lian, T. *J. Am. Chem. Soc.* **2011**, *133*, 8762.

(10) Zhu, H.; Yang, Y.; Song, N.; Rodríguez-Cordoba, W.; Lian, T. *Proc. SPIE* **2011**, *8098*, 809802.

(11) Zhu, H.; Song, N.; Rodríguez-Córdoba, W.; Lian, T. *J. Am. Chem. Soc.* **2012**, *134*, 4250.

(12) Yu, W. W.; Qu, L. H.; Guo, W. Z.; Peng, X. G. *Chem. Mater.* **2003**, *15*, 2854.

(13) Jasieniak, J.; Smith, L.; Embden, J. v.; Mulvaney, P.; Califano, M. *J. Phys. Chem. C* **2009**, *113*, 19468.

(14) Moreels, I.; Lambert, K.; Smeets, D.; De Muynck, D.; Nollet, T.; Martins, J. C.; Vanhaecke, F.; Vantomme, A.; Delerue, C.; Allan, G.; Hens, Z. *ACS Nano* **2009**, *3*, 3023.

(15) Landsberg, P. T. *Recombination in semiconductors*; Cambridge University Press: Cambridge, 2003.

(16) Boulesbaa, A.; Issac, A.; Stockwell, D.; Huang, Z.; Huang, J.; Guo, J.; Lian, T. *J. Am. Chem. Soc.* **2007**, *129*, 15132.

(17) Huang, J.; Stockwell, D.; Huang, Z.; Mohler, D. L.; Lian, T. *J. Am. Chem. Soc.* **2008**, *130*, 5632.

(18) Jin, S.; Lian, T. *Nano Lett.* **2009**, *9*, 2448.

(19) Huang, J.; Huang, Z.; Yang, Y.; Zhu, H.; Lian, T. *J. Am. Chem. Soc.* **2010**, *132*, 4858.

(20) Yang, Y.; Rodríguez-Córdoba, W.; Lian, T. *J. Am. Chem. Soc.* **2011**, *133*, 9246.

(21) Song, N.; Zhu, H.; Jin, S.; Lian, T. *ACS Nano* **2011**, *5*, 8750.

(22) Zhu, H.; Lian, T. *J. Am. Chem. Soc.* **2012**, *134*, 11289.

(23) Robel, I.; Kuno, M.; Kamat, P. V. *J. Am. Chem. Soc.* **2007**, *129*, 4136.

(24) Tvrdy, K.; Frantsuzov, P. A.; Kamat, P. V. *Proc. Natl. Acad. Sci.* **2011**, *108*, 29.

(25) Brus, L. E. *J. Chem. Phys.* **1983**, *79*, 5566.

(26) Brus, L. E. *J. Chem. Phys.* **1984**, *80*, 4403.

(27) Larson, D. R.; Zipfel, W. R.; Williams, R. M.; Clark, S. W.; Bruchez, M. P.; Wise, F. W.; Webb, W. W. *Science* **2003**, *300*, 1434.

(28) Alivisatos, P. *Nat Biotech* **2004**, *22*, 47.

(29) Aldana, J.; Wang, Y. A.; Peng, X. G. *J. Am. Chem. Soc.* **2001**, *123*, 8844.

(30) Ben-Lulu, M.; Mocatta, D.; Bonn, M.; Banin, U.; Ruhman, S. *Nano Lett.* **2008**, *8*, 1207.

(31) Pijpers, J. J. H.; Ulbricht, R.; Tielrooij, K. J.; Osherov, A.; Golan, Y.; Delerue, C.; Allan, G.; Bonn, M. *Nat. Phys.* **2009**, *5*, 811.

(32) Midgett, A. G.; Hillhouse, H. W.; Hughes, B. K.; Nozik, A. J.; Beard, M. C. *J. Phys. Chem. C* **2010**, *114*, 17486.

(33) Nair, G.; Chang, L.-Y.; Geyer, S. M.; Bawendi, M. G. *Nano Lett.* **2011**, *11*, 2145.

(34) Schaller, R. D.; Sykora, M.; Jeong, S.; Klimov, V. I. *J. Phys. Chem. B* **2006**, *110*, 25332.

(35) McGuire, J. A.; Joo, J.; Pietryga, J. M.; Schaller, R. D.; Klimov, V. I. *Acc. Chem. Res.* **2008**, *41*, 1810.

(36) Trinh, M. T.; Houtepen, A. J.; Schins, J. M.; Hanrath, T.; Piris, J.; Knulst, W.; Goossens, A. P. L. M.; Siebbeles, L. D. A. *Nano Lett.* **2008**, *8*, 1713.

(37) Beard, M. C.; Midgett, A. G.; Hanna, M. C.; Luther, J. M.; Hughes, B. K.; Nozik, A. J. *Nano Lett.* **2010**, *10*, 3019.

(38) Allan, G.; Delerue, C. *ACS Nano* **2011**, *5*, 7318.

(39) Cunningham, P. D.; Boercker, J. E.; Foos, E. E.; Lumb, M. P.; Smith, A. R.; Tischler, J. G.; Melinger, J. S. *Nano Lett.* **2011**, *11*, 3476.

(40) Sambur, J. B.; Novet, T.; Parkinson, B. A. *Science* **2010**, *330*, 63.

(41) Semonin, O. E.; Luther, J. M.; Choi, S.; Chen, H.-Y.; Gao, J.; Nozik, A. J.; Beard, M. C. *Science* **2011**, *334*, 1530.

(42) Matylitsky, V. V.; Dworak, L.; Breus, V. V.; Basche, T.; Wachtveitl, J. *J. Am. Chem. Soc.* **2009**, *131*, 2424.

(43) Keuleyan, S.; Lhuillier, E.; Brajuskovic, V.; Guyot-Sionnest, P. *Nat Photon* **2011**, *5*, 489.

(44) Burai, T. N.; Panay, A. J.; Zhu, H.; Lian, T.; Lutz, S. *ACS Catalysis* **2012**, *2*, 667.

(45) Brown, K. A.; Dayal, S.; Ai, X.; Rumbles, G.; King, P. W. *J. Am. Chem. Soc.* **2010**, *132*, 9672.

(46) Sato, S.; Arai, T.; Morikawa, T.; Uemura, K.; Suzuki, T. M.; Tanaka, H.; Kajino, T. *J. Am. Chem. Soc.* **2011**, *133*, 15240.

(47) Marcus, R. A. *J. Chem. Phys.* **1956**, *24*, 966.

(48) Marcus, R.; Sutin, N. *Biochim. Biophys. Acta* **1985**, *811*, 265.

(49) Closs, G. L.; Miller, J. R. *Science* **1988**, *240*, 440.

(50) Barbara, P. F.; Meyer, T. J.; Ratner, M. A. *J. Phys. Chem.* **1996**, *100*, 13148.

(51) Miller, J. R.; Calcaterra, L. T.; Closs, G. L. *J. Am. Chem. Soc.* **1984**, *106*, 3047.

(52) Akesson, E.; Walker, G. C.; Barbara, P. F. *J. Chem. Phys.* **1991**, *95*, 4188.

(53) Marcus, R. A. *J. Chem. Phys.* **1965**, *43*, 679.

(54) Colvin, V. L.; Schlamp, M. C.; Alivisatos, A. P. *Nature* **1994**, *370*, 354.

(55) Shen, Y. C.; Mueller, G. O.; Watanabe, S.; Gardner, N. F.; Munkholm, A.; Krames, M. R. *Appl. Phys. Lett.* **2007**, *91*, 141101.

(56) Klimov, V. I.; Ivanov, S. A.; Nanda, J.; Achermann, M.; Bezel, I.; McGuire, J. A.; Piryatinski, A. *Nature* **2007**, *447*, 441.

(57) Kambhampati, P. *Acc. Chem. Res.* **2010**, *44*, 1.

(58) Kambhampati, P. *J. Phys. Chem. Lett.* **2012**, 1182.

(59) Fisher, B.; Caruge, J. M.; Zehnder, D.; Bawendi, M. *Phys. Rev. Lett.* **2005**, *94*, 087403.

(60) Sukhovatkin, V.; Hinds, S.; Brzozowski, L.; Sargent, E. H. *Science* **2009**, *324*, 1542.

(61) Nair, G.; Geyer, S. M.; Chang, L.-Y.; Bawendi, M. G. *Phys. Rev. B* **2008**, *78*, 125325.

(62) Stewart, J. T.; Padilha, L. A.; Qazilbash, M. M.; Pietryga, J. M.; Midgett, A. G.; Luther, J. M.; Beard, M. C.; Nozik, A. J.; Klimov, V. I. *Nano Lett.* **2011**, *12*, 622.

(63) Miaja-Avila, L.; Tritsch, J. R.; Wolcott, A.; Chan, W. L.; Nelson, C. A.; Zhu, X. Y. *Nano Lett.* **2012**, *12*, 1588.

(64) Chan, W.-L.; Ligges, M.; Jailaubekov, A.; Kaake, L.; Miaja-Avila, L.; Zhu, X.-Y. *Science* **2011**, *334*, 1541.

(65) Tyagi, P.; Kambhampati, P. *J. Chem. Phys.* **2011**, *134*, 094706.

(66) Klimov, V. I.; Mikhailovsky, A. A.; McBranch, D. W.; Leatherdale, C. A.; Bawendi, M. G. *Science* **2000**, *287*, 1011.

(67) Klimov, V. I. *Annu. Rev. Phys. Chem.* **2007**, *58*, 635.

(68) Cozzoli, P. D.; Pellegrino, T.; Manna, L. *Chem. Soc. Rev.* **2006**, *35*, 1195.

(69) Peter Reiss, M. P., Liang Li, *Small* **2009**, *5*, 154.

(70) Carbone, L.; Cozzoli, P. D. *Nano Today* **2010**, *5*, 449.

(71) Donega, C. d. M. *Chem. Soc. Rev.* **2011**, *40*, 1512.

(72) Ghosh Chaudhuri, R.; Paria, S. *Chem. Rev.* **2012**, *112*, 2373.

(73) Lo, S. S.; Mirkovic, T.; Chuang, C.-H.; Burda, C.; Scholes, G. D. *Adv. Mater.* **2011**, *23*, 180.

(74) Wei, S.-H.; Zunger, A. *Appl. Phys. Lett.* **1998**, *72*, 2011.

(75) Berger, L. I. *Semiconductor materials*; CRC Press, 1997.

(76) Bartnik, A. C.; Wise, F. W.; Kigel, A.; Lifshitz, E. *Phys. Rev. B* **2007**, *75*, 245424.

(77) De Geyter, B.; Justo, Y.; Moreels, I.; Lambert, K.; Smet, P. F.; Van Thourhout, D.; Houtepen, A. J.; Grodzinska, D.; de Mello Donega, C.; Meijerink, A.; Vanmaekelbergh, D.; Hens, Z. *ACS Nano* **2011**, *5*, 58.

(78) García-Santamaría, F.; Chen, Y.; Vela, J.; Schaller, R. D.; Hollingsworth, J. A.; Klimov, V. I. *Nano Lett.* **2009**, *9*, 3482.

(79) Steiner, D.; Dorfs, D.; Banin, U.; Della Sala, F.; Manna, L.; Millo, O. *Nano Lett.* **2008**, *8*, 2954.

(80) Grätzel, M. *Heterogeneous photochemical electron transfer*; CRC Press Boca Raton, FL, 1989; Vol. 91.

(81) Ivanov, S. A.; Piryatinski, A.; Nanda, J.; Tretiak, S.; Zavadil, K. R.; Wallace, W. O.; Werder, D.; Klimov, V. I. *J. Am. Chem. Soc.* **2007**, *129*, 11708.

(82) Piryatinski, A.; Ivanov, S. A.; Tretiak, S.; Klimov, V. I. *Nano Lett.* **2007**, *7*, 108.

(83) Trinh, M. T.; Polak, L.; Schins, J. M.; Houtepen, A. J.; Vaxenburg, R.; Maikov, G. I.; Grinbom, G.; Midgett, A. G.; Luther, J. M.; Beard, M. C.; Nozik, A. J.; Bonn, M.; Lifshitz, E.; Siebbeles, L. D. A. *Nano Lett.* **2011**, *11*, 1623.

(84) Lee, D. C.; Robel, I.; Pietryga, J. M.; Klimov, V. I. *J. Am. Chem. Soc.* **2010**, *132*, 9960.

(85) Pandey, A.; Guyot-Sionnest, P. *Science* **2008**, *322*, 929.

(86) He, J.; Zhong, H.; Scholes, G. D. *Phys. Rev. Lett.* **2010**, *105*, 046601.

(87) Oron, D.; Kazes, M.; Banin, U. *Phys. Rev. B* **2007**, *75*, 035330.

(88) Brovelli, S.; Schaller, R. D.; Crooker, S. A.; García-Santamaría, F.; Chen, Y.; Viswanatha, R.; Hollingsworth, J. A.; Htoon, H.; Klimov, V. I. *Nat. Commun.* **2011**, *2*, 280.

(89) Chuang, C.-H.; Lo, S. S.; Scholes, G. D.; Burda, C. *J. Phys. Chem. Lett.* **2010**, 2530.

(90) Sitt, A.; Sala, F. D.; Menagen, G.; Banin, U. *Nano Lett.* **2009**, *9*, 3470.

(91) Balet, L. P.; Ivanov, S. A.; Piryatinski, A.; Achermann, M.; Klimov, V. I. *Nano Lett.* **2004**, *4*, 1485.

(92) Nanda, J.; Ivanov, S. A.; Htoon, H.; Bezel, I.; Piryatinski, A.; Tretiak, S.; Klimov, V. I. *J. Appl. Phys.* **2006**, *99*, 034309.

(93) Pellegrini, G.; Mattei, G.; Mazzoldi, P. *J. Appl. Phys.* **2005**, *97*, 073706.

(94) Lupo, M. G.; Della Sala, F.; Carbone, L.; Zavelani-Rossi, M.; Fiore, A.; Lüer, L.; Polli, D.; Cingolani, R.; Manna, L.; Lanzani, G. *Nano Lett.* **2008**, *8*, 4582.

(95) Müller, J.; Lupton, J. M.; Lagoudakis, P. G.; Schindler, F.; Koeppe, R.; Rogach, A. L.; Feldmann, J.; Talapin, D. V.; Weller, H. *Nano Lett.* **2005**, *5*, 2044.

(96) Luo, Y.; Wang, L.-W. *ACS Nano* **2009**, *4*, 91.

(97) Smith, A. M.; Mohs, A. M.; Nie, S. *Nat Nano* **2009**, *4*, 56.

(98) Crooker, S. A.; Barrick, T.; Hollingsworth, J. A.; Klimov, V. I. *Appl. Phys. Lett.* **2003**, *82*, 2793.

(99) Tisdale, W. A.; Williams, K. J.; Timp, B. A.; Norris, D. J.; Aydil, E. S.; Zhu, X.-Y. *Science* **2010**, *328*, 1543.

# Chapter 2. Experimental Methods

## 2.1. Sample Preparation

### 2.1.1. Synthesis of CdS, CdSe, CdTe and ZnSe Quantum Dots

**CdS quantum dots.** The oleic acid (OA) capped capped wurtzite CdS QDs were synthesized following a literature procedure[1]. Typically, a mixture (4 g in total) of CdO (0.0128 g, 0.10 mmol), oleic acid (0.30 ± 21.2 mmol), and ODE was heated to 300 °C. A solution of sulfur (0.0016 g, 0.05 mmol) in ODE was swiftly injected into this hot solution, and the reaction mixture was allowed to cool to 250 °C for the growth of CdS nanocrystals. CdS QDs of different sizes can be obtained by varying the amount of oleic acid and reaction time. The size and concentration of CdS QDs were determined using reported 1S exciton absorption band position and extinction coefficients of CdS QDs.[2]

**CdSe quantum dots.** Octydecylamine (ODA) capped CdSe QDs were synthesized according to a previously published procedure.[3] Briefly, a mixture of 0.8 mmol of CdO, 3.2 mmol of stearic acid and 12 ml of 1-octadecene (ODE) was heated to about 280 °C under $N_2$ protection. After CdO was dissolved, the solution was cooled to 80 °C and 3g of ODA was added into the flask. The solution was reheated to 270 °C, to which a selenium stock solution (2 mmol of Se dissolved in 2 ml of ODE and 0.5 g of

triobutylphosphine) was swiftly injected. The growth of CdSe QDs was carried out at 250 °C for 20 seconds. After precipitation with methanol and redissolving in hexane, the size and concentration of CdSe QDs were determined using reported 1S exciton absorption band position and extinction coefficients of CdSe QDs.[2,4]

High quality wurtzite CdSe seeds for dot-in-rod nanorod synthesis were synthesized following a literature procedure.[5] Briefly, 0.06 g Cadmium Oxide (CdO), 0.28 g Octadecylphosphonic acid (ODPA) and 3g Trioctylphosphine oxide (TOPO) were mixed in a 25 mL flask and heated to 300 °C under Argon flow. After CdO powder were dissolved and the solution became clear, 1.5 g Trioctylphosphine (TOP) was injected. When the temperature reached 350 °C, selenium (Se) precursor (0.058g Se+0.36g TOP) was swiftly injected and after 5 s, the reaction was stopped by removing the heating mantle. The CdSe seed was precipitated by ethanol and re-dissolved in chloroform for further use. The size and concentration of CdSe QDs were determined using reported 1S exciton absorption band position and extinction coefficients of CdSe QDs.[2,4]

**CdTe quantum dots.** CdTe seed QDs were synthesized according to a previously published procedure with slight modification.[6] Briefly, 0.10 g CdO was dissolved in a mixture of 0.45 g 1-tetradecylphosphonic acid (TDPA) and 20 ml 1-octadecene (ODE) by heating to about 290 °C under Ar protection. After the mixture became clear and colorless, a tellurium stock solution (0.13 g tellurium powder dissolved in 3 ml trioctylphosohine (TOP)) was swiftly injected. The growth of CdTe QDs was carried out at 280 °C for 10 seconds. After precipitation with methanol and redissolving in heptane,

the size and concentration of CdTe QDs were determined for further shell coating using reported 1S exciton absorption band position and extinction coefficients of CdTe QDs.[2]

**ZnSe quantum dots.** ZnSe QDs were synthesized according to the procedure reported.[7] Briefly, ODA (7 g) is dried under vacuum at 130 °C for at least 90 minutes and afterwards heated to 300 °C under Ar atmosphere. Se (63 mg, 0.8 mmol) is dissolved in TOP (2.0 g) and diethylzinc in hexane solution (0.8 mL, 1 M) is added. This solution is now rapidly injected into the ODA and the temperature is quickly set to 265 °C for nanocrystals growth. The QD size can be controlled by reaction time and zinc precursor injected.

### 2.1.2. Synthesis of CdSe/ZnS, CdSe/CdS and CdTe/CdSe Core/Shell Quantum Dots

The core for core/shell QD growth can be obtained from above procedure. All of shell precursor solutions are freshly prepared under Ar-atmosphere. For each shell growth, a calculated amount of a given precursor solution was injected with a syringe using standard air-free procedures. The zinc precursor solution (0.08 M) was prepared by dissolving ZnO (0.128 g, 0.0016 mol) in oleic acid (5 mL, 0.0158 mol) and ODE (15 mL) at 300 °C and the colorless solution kept above 100 °C. The cadmium injection solution (0.08 M) was prepared by dissolving CdO (0.2053 g, 0.0016 mol) in oleic acid (3 mL, 0.0095 mol) and ODE (17 mL) at 250 °C. The sulfur precursor solution (0.08 M) was prepared by dissolving sulfur (51.28 mg) in ODE (20 mL) at room temperature. The Se

precursor solution (0.08 M) was prepared by dissolving Se (126 mg) in mixture solution of 1 mL tributylphosphine (TBP) and 19 mL ODE at room temperature.

The shell growth can be performed with successive ion layer adsorption and reaction (SILAR) method.[8,9] Take ZnS shell for example, 5 mL of ODE and 1 g of ODA were loaded into a 25 mL reaction vessel, and CdSe-NCs in hexane ( $1*10^{-4}$ mmol) were added, and the system was pumped down at room temperature for 10 min to remove the hexanes and at 100 °C under vacuum for another 20 min to remove other undesired materials of low vapor pressure. Subsequently, the solution was heated to 190 °C under Ar-flow and the calculated amount of Zn precursor was injected dropwisely. A period of 10 min after Zn precursor injection, the calculated amount of S precursor was injected dropwisely. Then the solution was heated to 220 °C where the shell growth was performed. The layer was allowed to react for 20 min before another layer was added. Then let the solution cool to 190°C and repeat the injections. After all the injections, the solution was kept for another 30min at 240 °C.

### 2.1.3. Synthesis of CdSe Nanorods

Phosphonic acid capped CdSe nanorods were synthesized using previously reported method with small modification.[10] Briefly, 0.128 g CdO, 0.668 g octadecylphosphonic acid (ODPA) and 2 g tri-n-octylphosphine oxide (TOPO) were mixed in a 25 mL reaction flask and heated to 260 °C under argon atmosphere until CdO

was completely dissolved. To prepare the Se precursor, 2 mL tri-n-octylphosphine (TOP) solution containing 80 mg Se was sonicated until Se power was completely dissolved to yield a transparent solution. At 260 °C, 1 mL Se precursor was swiftly injected and the resulting solution was allowed to react at 240 °C. After 10 min, additional 10 mL Se precursor was added drop-wise in 30 min. The CdSe nanorods were purified by precipitation and redispersed in chloroform. The representative TEM image of as prepared CdSe nanorods are shown in Figure 2A.

### 2.1.4. Synthesis of CdS Nanorod and CdSe/CdS and ZnSe/CdS Dot-in-rod Nanorods

The CdS nanorods, CdSe/CdS and ZnSe/CdS dot-in-rod nanorods were synthesized following a seeded growth method.[5,11] The synthesis of CdS, CdSe and ZnSe seeds was described above. To grow the CdS rod, 0.29 g ODPA, 0.08 g hexylphosphonic acid (HPA), 0.06 g CdO and 3 g TOPO were mixed in a 25mL flask and heated to 300°C under Argon flow. After CdO powder were fully dissolved and the solution became clear, 1.5 g Trioctylphosphine (TOP) was injected and the temperature was raised to 350 °C. CdS (or CdSe or ZnSe) seeds (0.8 μmol) and S precursor (0.12 g S in 1.5 g TOP) were swiftly injected. After 8 minutes, the heating mantle was removed and CdS (or CdSe/CdS or ZnSe/CdS) nanorods were precipitated with ethanol and redispersed in chloroform for future use. The representative TEM images of CdS, CdSe/CdS and ZnSe/CdS nanorods are shown in Figure 2.1 B, C and D, respectively.

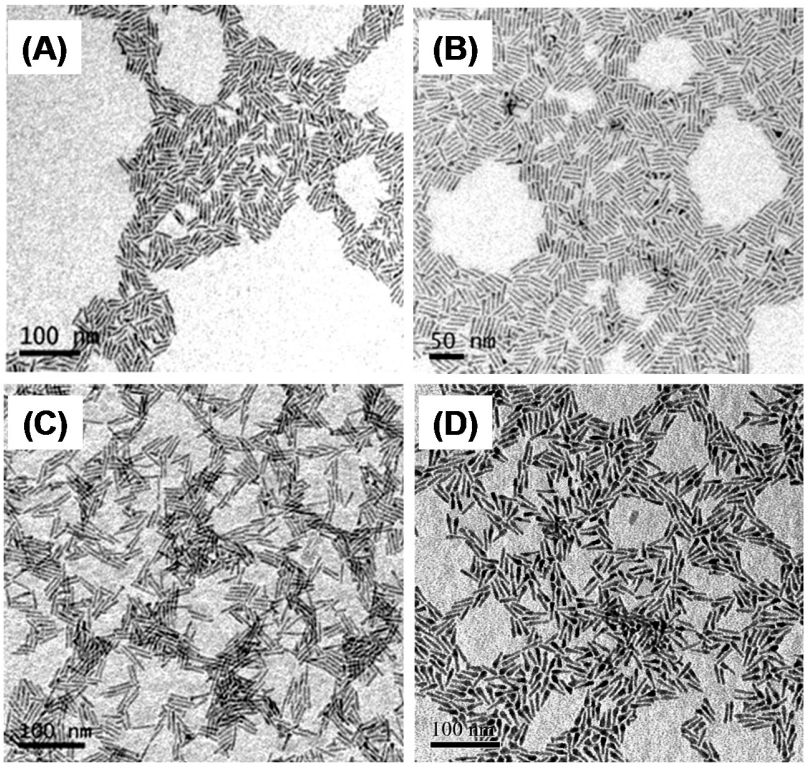


**Figure 2.1.** TEM images of CdSe (A), CdS (B), CdSe/CdS (C) and ZnSe/CdS (D) nanorods.

### 2.1.5. Preparation of Nanocrystal-molecule Adsorbate Complexes for Spectroscopy Measurement

Different molecular adsorbates are used as electron/hole acceptors, as shown in Figure 2.2. Methylene Blue ($MB^+$), Methy Viologen ($MV^{2+}$), Anthraquinone-2,3-dicarboxylic acid (AQ), 1,4-Benzoquinone (BQ) are used as electron acceptors and

Phenothiazine (PTZ) as hole acceptor. Nanocrystal-adsorbate complex for spectroscopy study were prepared by adding molecules into nanocrystal heptane solution or adding highly concentrated molecule-methanol solution into nanocrystals chloroform solution, followed by sonication and filtration to remove undissolved acceptor molecules. Since $MB^+$, $MV^{2+}$ and AQ molecules are not soluble in heptane, all dissolved acceptor molecules are believed to be bound to the QD. The ratio of adsorbed $MB^+$ ($MV^{2+}$, AQ) to QD was controlled by the amount of acceptor molecules added and was determined by UV-Vis absorption spectra based on the published QD extinction coefficients. BQ and PTZ molecules can be dissolved in nanocrystals solvent and their ratio are not calculated.

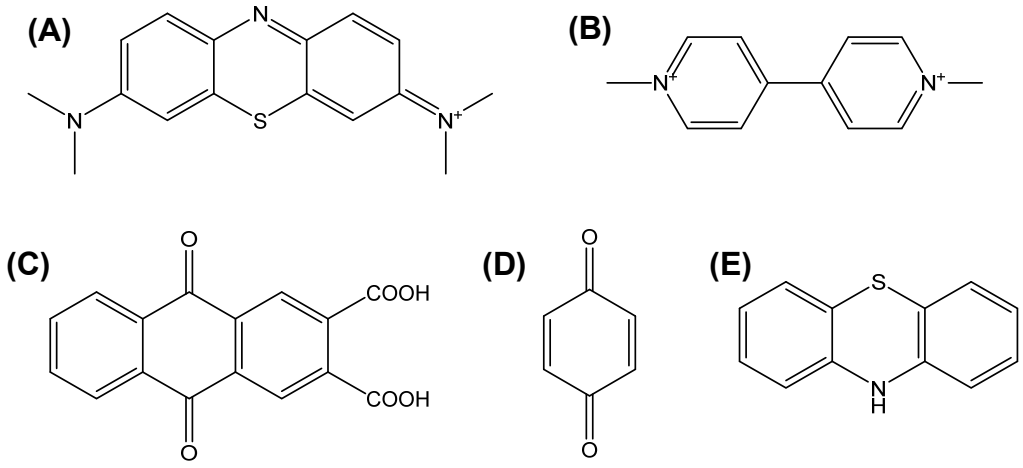


**Figure 2.2.** Molecular structures of Methylene Blue (A), Methy Viologen (B), Anthraquinone-2,3-dicarboxylic acid (C), 1,4-Benzoquinone (D), Phenothiazine (E)

### 2.1.6. Preparation of Water Soluble Nanocrystals

The NCs prepared above were transformed into water by ligand exchange with 3-mercaptopropionic acid (MPA).[12] Excess amount of MPA (20μL) was dissolved in 10 mL methanol and the pH of the solution was adjusted to above 10 with tetramethylammonium hydroxide. A few mg NCs were added and the solution was refluxed at 70°C overnight with $N_2$ in dark. The MPA capped NCs were precipitated with ethyl acetate and isolated by centrifugation and decantation. After drying, the precipitate was redissolved in water for further use.

### 2.1.7. Preparation of Pt Nanoparticle Catalyst

Pt particles used as the catalyst for hydrogen evolution were synthesized by thermal reduction of $H_2PtCl_6$ with citrate[13]. After refluxing the solution for 4h, excess citrate was removed by Amberlite-MB-1 exchange in an ice bath. After filtration, Polyvinyl alcohol (PVA, mass ratio PVA/Pt = 1/1) was added as protective agent and the solution was stirred overnight. The concentration of Pt in reaction solution for $H_2$ evolution was estimated to be ~ 0.8 mM based on reported extinction coefficient.[14]

## 2.2. Time Resolved Spectroscopy Setup

### 2.2.1. Femitosecond Transient Absorption Setup

Our tunable femtosecond transient absorption setup is based on a regenerative amplified Ti:sapphire laser system from Coherent (800 nm, 130 fs, 3 mJ/pulse, and 1 kHz repetition rate), nonlinear frequency mixing techniques and the Helios spectrometer (Ultrafast Systems LLC). Briefly, the 800 nm output pulse from the regenerative amplifier was split in two parts with a 10% beamsplitter. One part, with 0.3 μJ/pulse was used to pump a Coherent Opera Optical Parametric Amplifier (OPA) which generates two tunable near-IR pulses from 1.1 to 2.5 μm. This signal and idler beams were separated with a dichroic mirror, and used separately to generate the 495 and 565 nm excitation beam by sum frequency mixing with the 800 nm fundamental beam in a type I β-BBO crystal. The transmitted 800 nm beam, with pulse energy of about 2.7 μJ, was split again into two parts. One part, with ~ 2.4 μJ/pulse, was frequency doubled in a β-BBO crystal to generate the 400 nm excitation pulses at 400 nm. The remaining 800 nm beam was used to generate a white light continuum (WLC) in a sapphire window, which were split into a probe and a reference beams. The probe beam was focused with an Al parabolic reflector onto the sample (with a beam diameter of ~150 μm at the sample). The reference and probe beams were focused into a fiber optics coupled multichannel spectrometer with CMOS sensors and detected at a frequency of 1 KHz. The intensity of the pump pulse used in the experiment was controlled by a variable neutral-density filter wheel. The pump beam diameter at the sample was ~360 μm. The delay between the pump and probe pulses was controlled by a motorized delay stage. The pump pulses were

chopped by a synchronized chopper to 500 Hz and the change in optical density at the sample resulted from the pump pulse was calculated. For all spectroscopy measurements, the samples were kept in a 1 mm cuvette and constantly stirred by a magnetic stirrer to avoid photodegradation.

### 2.2.2. Nanosecond Transient Absorption Setup

Nanosecond (0.5 ns to 1 μs) transient absorption was performed with the EOS spectrometer (Ultrafast Systems LLC). The pump pulses at 400 nm were generated in the regenerative amplified Ti:sapphire laser system as described above. The white light continuum pulse (380 -1700 nm, 0.5 ns pulse width, 20 KHz repetition rate) was generated by focusing a Nd:YAG laser into a photonic crystal fiber. The delay time between the pump and probe pulses was controlled by a digital delay generator (CNT-90, Pendulum Instruments). The probe and reference beams were detected by the same multichannel spectrometers used in the femtosecond setup. To correct for slight difference of excitation intensity of the data acquired by fs and ns instruments under the single exciton conditions, the signal size of the ns kinetics was slightly scaled such that these transient kinetics overlap at the 0.6-1.4 ns.

### 2.2.3. Time Resolved Fluorescence Setup

Time–resolved fluorescence measurements were performed in the time-correlated single photon counting (TCSPC) mode under right-angle sample geometry.11 A modelocked Ti:Sapphire laser (Tsunami oscillator pumped by a 10 W Millennia Pro, Spectra- Physics) was used to generate femtosecond laser pulses (~100 fs) with a repetition rate of 80 MHz. Pump pulses at 400 nm were produced by doubling the output centered at 800 nm in a BBO crystal. The emission was detected by a micro-channel-platephotomultiplier tube (Hamamatsu R3809U-51), the output of which was amplified and analyzed by a TCSPC board (Becker & Hickel SPC 600).

## 2.3. Steady State $MV^{2+}$ Photoreduction

Light-driven $MV^{2+}$ reduction was performed in a standard threaded-top fluorescence cuvette (Spectrocell, RF-3010-T) with a total volume of ~3 ml and a path-length of 1 cm. The cuvette was filled with 2.0 ml reaction solutions of sensitizers, $MV^{2+}$, sacrificial electron donor (MPA for NCs and Triethanolamine (TEOA) for $Ru(bipy)_3^{2+}$; both neutralized to 7 with HCl or NaOH before mixing) and buffer (50 mM phosphate). The reaction cell was sealed with a rubber septum, degassed and filled with Argon. The removal of oxygen was confirmed with HP5890A model gas chromatograph equipped with a thermal conductivity detector and a HP-MOLESIEVE capillary GC column (30m × 0.535 mm × 25.00 μm) packed with 5Å molecular sieves. The integrity of the seal was tested by monitoring the absorption spectra reduced $MV^{+\cdot}$ in dark, which shows slightly

(~5%) decrease after 1 h. All procedures were performed with a minimum exposure to ambient light. Before illumination, the UV-Vis absorption spectrum of the solution was taken as zero time. The reaction was initiated by unblocking the stabilized light source of a certain wavelength with constant stirring of the solution (by a magnetic stirrer). The UV-Vis absorption spectra of the solution were taken after a certain time of illumination (seconds), interrupting the illumination by less than 20 s for each spectrum recording. Error bars on $MV^{+\cdot}$ concentrations were calculated from at least two independent experiments.

The $MV^{+\cdot}$ generation quantum yield for these sensitizers is defined as $\Phi_{MV} = \Delta(MV^{+\cdot})/ \Delta(\hbar v)$ where $\Delta(MV^{+\cdot})$ is the $MV^{+\cdot}$ generation rates and $\Delta(\hbar v)$ is the photon absorption rates by the reaction solution, respectively. $MV^{+\cdot}$ generation rates $\Delta(MV^{+\cdot})$ were obtained from the slope of the initial three pointes. The photon absorption rate $\Delta(\hbar v)$ was calculated from the illumination power and the absorbance of the reaction solution. The illumination power was measured at the front of the reaction cell using a digital laser power meter (OPHIR, model NOVA II). The amount of absorbed light can be determined from sample absorbance and the measured power after correcting the loss by the cuvette front window. The loss of an empty cell was determined to be 14% by UV/Vis spectrometer, from which we assume a 7% loss for each window.

## 2.4. Light Driven $H_2$ Evolution

The $H_2$ generation reaction was performed in a cylindrical cuvette (NSG, 32UV10) with a total volume of ~2.5 ml following the same operation procedures as the $MV^{2+}$ reduction experiment described above. The reaction volume (2.0 ml) and the concentrations of $MV^{2+}$, NCs and MPA remain unchanged. A different buffer (50 mM phosphate, pH 6.2) and a higher light intensity (8.0 mW) were used and PVA-Pt (0.8 mM) were added as the $H_2$ evolution catalysts

Analysis of $H_2$ in the reaction headspace was performed using a HP5890A model gas chromatograph equipped with a thermal conductivity detector and a HP-MOLESIEVE capillary GC column (30m x 0.535 mm x 25.00 μm) packed with 5Å molecular sieves. Argon was used as a carrier gas. Typically, the $H_2$ amount was quantified by withdrawing a gas sample from the headspace without stopping the reaction. Error bars on $H_2$ were calculated from at least two independent experiments.

Quantum yield for $H_2$ generation is defined as $\Phi_{MV} = 2\Delta(H_2)/ \Delta(\hbar\nu)$ where $\Delta(H_2)$ is the $H_2$ generation rates. For external quantum yield, $\Delta(\hbar\nu)$ is the incident light intensity (8.0 mW) which was measured at the front of the reaction cell using a digital laser power meter (OPHIR, model NOVA II). To estimate the internal quantum yield, the photon loss has to be corrected. The photon loss in this system comes from three processes: 1) scattering and reflection of cuvette front window (~9% loss), 2) scattering of suspended NCs in water, and 3) absorption by PVA-Pt catalyst. Because the scattering loss of the suspension is not taken into account, the estimated internal quantum yield should be taken as the lower limit.

## References

(1) Yu, W. W.; Peng, X. G. *Angew. Chem. Int. Ed.* **2002**, *41*, 2368.

(2) Yu, W. W.; Qu, L. H.; Guo, W. Z.; Peng, X. G. *Chem. Mater.* **2003**, *15*, 2854.

(3) Li, J. J.; Wang, Y. A.; Guo, W.; Keay, J. C.; Mishima, T. D.; Johnson, M. B.; Peng, X. *J. Am. Chem. Soc.* **2003**, *125*, 12567.

(4) Jasieniak, J.; Smith, L.; Embden, J. v.; Mulvaney, P.; Califano, M. *J. Phys. Chem. C* **2009**, *113*, 19468.

(5) Carbone, L.; Nobile, C.; De Giorgi, M.; Sala, F. D.; Morello, G.; Pompa, P.; Hytch, M.; Snoeck, E.; Fiore, A.; Franchini, I. R.; Nadasan, M.; Silvestre, A. F.; Chiodo, L.; Kudera, S.; Cingolani, R.; Krahne, R.; Manna, L. *Nano Lett.* **2007**, *7*, 2942.

(6) Peng, Z. A.; Peng, X. G. *J. Am. Chem. Soc.* **2001**, *123*, 183.

(7) Dorfs, D.; Salant, A.; Popov, I.; Banin, U. *Small* **2008**, *4*, 1319.

(8) Li, J. J.; Wang, Y. A.; Guo, W. Z.; Keay, J. C.; Mishima, T. D.; Johnson, M. B.; Peng, X. G. *J. Am. Chem. Soc.* **2003**, *125*, 12567.

(9) Xie, R. G.; Kolb, U.; Li, J. X.; Basche, T.; Mews, A. *J. Am. Chem. Soc.* **2005**, *127*, 7480.

(10) Peng, Z. A.; Peng, X. *J. Am. Chem. Soc.* **2002**, *124*, 3343.

(11) Talapin, D. V.; Nelson, J. H.; Shevchenko, E. V.; Aloni, S.; Sadtler, B.; Alivisatos, A. P. *Nano Lett.* **2007**, *7*, 2951.

(12) Aldana, J.; Wang, Y. A.; Peng, X. G. *J. Am. Chem. Soc.* **2001**, *123*, 8844.

(13) Brugger, P. A.; Cuendet, P.; Graetzel, M. *J. Am. Chem. Soc.* **1981**, *103*, 2923.

(14) Henglein, A.; Ershov, B. G.; Malow, M. *J. Phys. Chem.* **1995**, *99*, 14129.

# Chapter 3. Electron Transfer from CdX Quantum Dots of Different Sizes: the Study of Driving Force



## 3.1. Introduction

In recent years, quantum confined semiconductor nanomaterials, such as quantum dots (QDs), nanorods and carbon nanotubes have emerged as a new class of light harvesting and charge separation materials for solar energy conversion.[1-8] For these applications, one of the most fundamental and crucial steps is the dissociation of excitons (bound electron-hole pairs) in these materials through interfacial charge (electron or hole) transfer to acceptor materials. Due to the strong electron-nuclear interaction in molecules, inter- and intra- molecular electron transfer (ET) is accompanied by large rearrangement of the nuclear configuration, which are described by the Marcus ET theory,[9-12] exhibiting the well-known dependences of ET rates on the driving force in the Marcus normal, barrier-less, and inverted regimes.[10,13,14] In many bulk semiconductor materials (such as CdX, X=S, Se, and Te), the week electron-nuclear and electron-electron interaction justify the treatment of electrons and holes as quasi-free and independent particles, in

which photoinduced electron transfer requires negligible change in nuclear configurations or the motion of the accompanying holes.[15] In excitonic nanomaterials, such as QDs, both the electron-hole interaction and electron-phonon interactions fall between those of the bulk semiconductor materials and molecular chromophores and the appropriate model for describing photoinduced charge transfer (or exciton dissociation) remains unclear.

In an effort to test theoretical models for describing ET from excitonic nanomateirals, in this paper, we investigate electron transfer in QD-molecular complexes. Because of the quantum confinement effect, semiconductor QDs exhibit atomic-like discrete electronic levels and corresponding excitonic transitions that can be widely tuned by their size.[16,17] Such size dependent energetics provides an ideal platform for testing ET models. In a recent study of ET from QDs to metal oxide films, it was shown that ET rates increase at larger driving force even when it far exceeds the reorganization energy.[18-20] This trend was attributed to the existence of a continuum of conduction band states and their increasing density at higher energy in metal oxides, similar to previous reports for ET from molecules to oxides.[21,22] Previous studies of ET in QD-acceptor complexes have also reported faster ET rates at smaller QD size.[23] Unfortunately, the range of driving force was limited and a critical test of ET models has not been possible.

In this chapter, we investigate the size dependence of ET processes from CdS, CdSe and CdTe QDs to three molecular acceptors, methylene blue ($MB^+$), methyl viologen ($MV^{2+}$) and anthraquinone (AQ), as shown in Figure 3.1. The combination of band edges of bulk materials, size tunable confinement energies, and acceptor redox potentials ($\emptyset_{A/A^-}$ : 4.7 V (*vs* vacuum),[24,25] $MV^{2+}$ ~ -4.26 V[26] and AQ ~ -4 V[27]) enables an

examination of ET rates over an apparent driving force range of ~ 0 - 1.3 eV (energy gap between the lS electron and the adsorbate LUMO). The observed ET rates increase with decreasing QD size, regardless of QD compositions and acceptor redox potentials, in marked contrast with the conventional ET model currently used in the literature. We propose an Auger-assisted model for ET from QDs, in which the excess energy of the electron can be conserved by hole excitation, overcoming the unfavorable Franck-Condon overlap in the Marcus inverted regime and enhancing the ET rate. This model can satisfactorily explain the observed size dependent ET rates and is supported by theoretical/computational modeling.

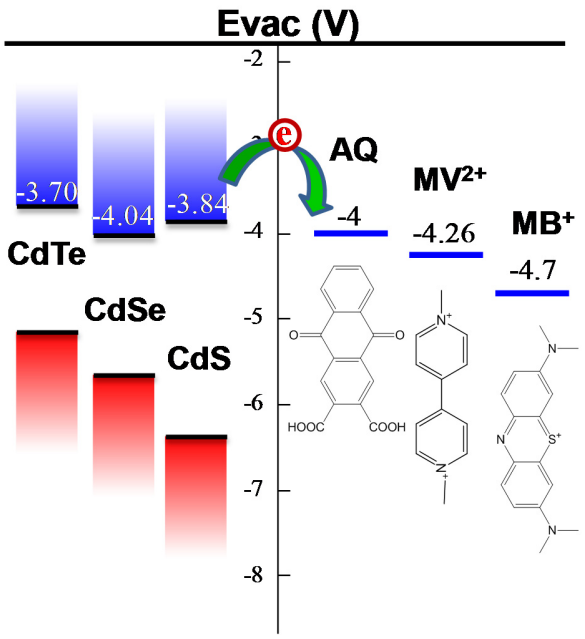

**Figure 3.1.** Schematic diagram of bulk conduction band edge positions of CdX (X=S, Se, Te) and reduction potentials of acceptor molecules (*vs* vacuum). The schematic structures of acceptor molecules are also shown.

## 3.2. Results and Discussion

### 3.2.1. Steady State and Transient Absorption Spectra of CdX QD and QD-acceptor complexes

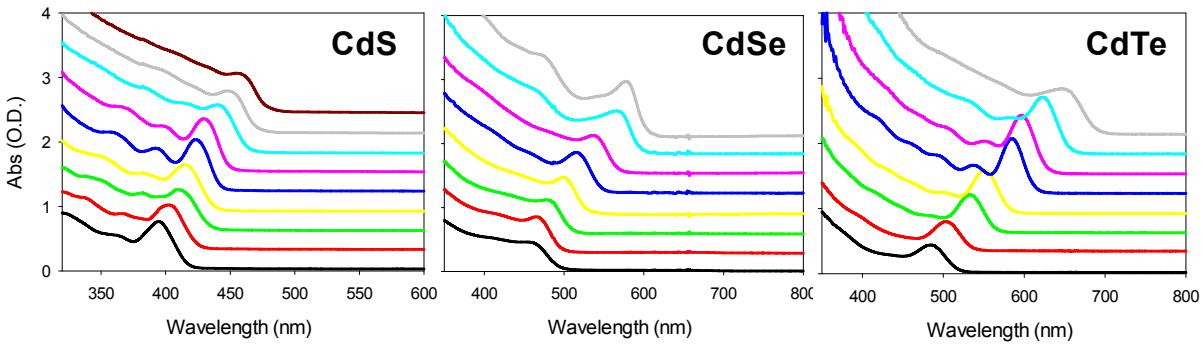


**Figure 3.2.** UV-Vis absorption spectra of synthesized CdS, CdSe and CdTe QDs of different sizes (in heptane) for this study.

The UV-Vis absorption spectra Oleic acid (OA) capped CdS, CdSe and CdTe QDs of different sizes are shown in Figure 3.2. From the effective mass modeling (Appendix 1) as well as an empirical sizing curve[28], the radius of these synthesized QDs

can be determined to be in the range of 1 ~ 2.2 nm. Representative TA spectra of CdS (radius R = 1.53 nm) QDs and their complexes with $MB^+$, $MV^{2+}$ and AQ are shown in Figure 3.3 (Similar spectra for CdSe (R = 1.53 nm) and CdTe (R = 1.59 nm) QDs are shown in Figure A.3.2). All samples are measured at low excitation fluence to ensure negligible contributions of multi-exciton states. As shown in Figure 3.3 A, the TA spectra of free CdS QDs consist of a long-lived bleach of 1S exciton band due to the state filling of the 1S electron level and derivative like features caused by the presence of the exciton.[29] The spectra of CdS-$MB^+$ complexes show a much faster 1S exciton bleach recovery (compared with free QDs without molecular acceptors) that is accompanied by the formation of the bleach of $MB^+$ ground state (GS) absorption at ~650 nm with same kinetics (Figure 3.3 B inset).[25,30] For the CdS-$MV^{2+}$ and CdS-AQ complexes, the recovery of 1S bleach is accompanied by the formation of reduced adsorbates ($MV^{+\cdot}$ and $AQ^-$ radicals) signals at ~600 nm and ~630 nm, respectively (Figure 3.3 C and D).[29,31-33] Therefore, the photoinduced ET processes from the excited QDs to adsorbates can be monitored by the kinetics of either the QD (1S exciton bleach recovery) or adsorbate (ground state bleach or radical formation) TA features, as shown in Figure A.3.3.

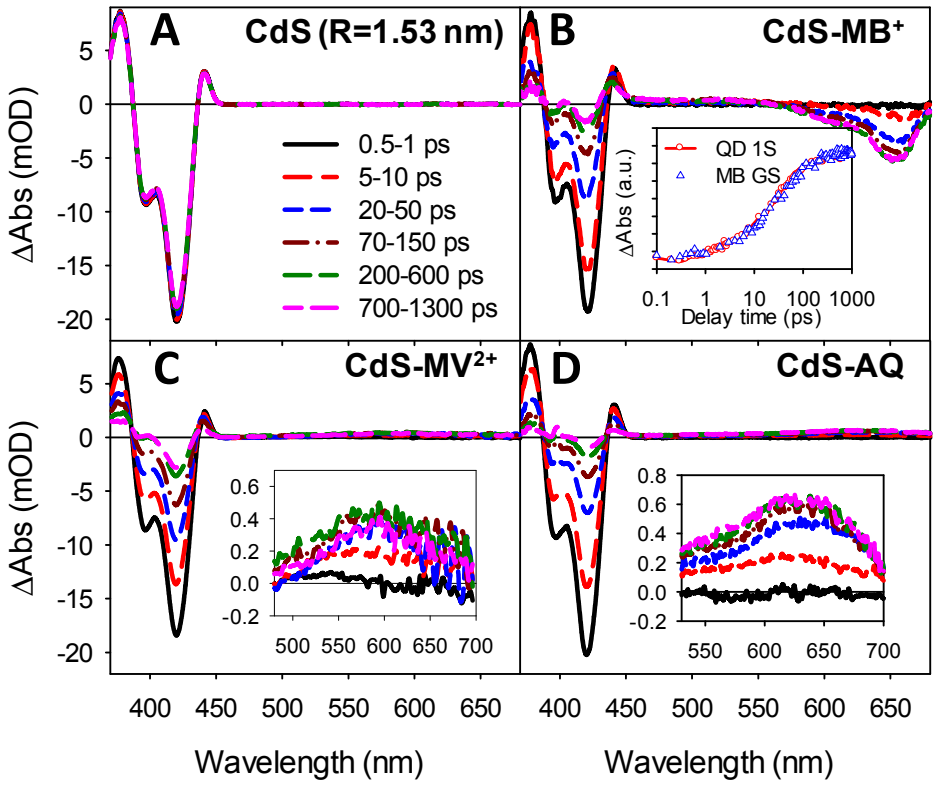


**Figure 3.3.** Representative TA spectra of (A) free CdS QDs (R=1.53 nm), (B) CdS-$MB^+$ complexes, (C) CdS-$MV^{2+}$ complexes, and (D) CdS-AQ complexes at indicated delay time windows after 400 nm excitation. (Inset in B) Comparison of QD 1S bleach recovery kinetics (red circles) and the $MB^+$ GS bleach formation kinetics (blue triangles) in CdS-$MB^+$ complexes. The $MB^+$ GS bleach signal has been normalized and inverted for better comparison. (Inset in C and D) expanded views of the spectra at 500−700 nm showing the formation of radicals.

QD-acceptor ET rates depend on the number of acceptors per QD, whose distribution is governed by Poisson statistics.[29,34,35] To compare ET rates among different

QD-acceptor complexes with different ratios, we determine an "intrinsic" ET rate ($k_1$) in 1:1 complexes from the measured ET kinetics using the following model.[36]

The exciton decay kinetics of free QD is given by:

$$N^*(t) = N^*(0) \cdot g(t) = N^*(0) \cdot \sum_i A_i e^{-k_{i0}t} \qquad (3.1)$$

where N*(t) is the excited QD population at time t after the excitation and $A_i$ and $k_{i0}$ are the amplitude and time constant of the i$^{th}$ component of the multi-exponential decay function, g(t). g(t) can be measured directly by studying the free QDs under the same conditions.

For QD-acceptor complexes, the fraction of QDs with *n* acceptors is assumed to obey the Poisson distribution [29,34]:

$$f(n) = \frac{m^n e^{-m}}{n!} \qquad (3.2)$$

Here $m$ is the average number of adsorbates per QD in the sample, which can be determined from UV-Vis spectra. We further assume that ET rates from QDs to acceptors increase linearly with the number of acceptors per QD. In a QD-acceptor complex with n acceptors, the ET rate is $k_n = n \cdot k_1$, where $k_1$ is the ("intrinsic") ET rate in a QD-acceptor complex with only one acceptor (i.e the 1:1 complex). It is also reasonable to assume that the ET rate is independent of the heterogeneous distribution of intrinsic decay rates in free QDs. With these assumptions, the exciton decay kinetics in an ensemble of QD-acceptor complexes is give by:

$$N^*(t) = N^*(0) \cdot \sum_i A_i \sum_{n=0}^{\infty} f(n) e^{-(k_{i0}+k_n)t}$$

$$= N^*(0) \cdot \sum_i A_i \, e^{-k_{i0}t} \sum_{n=0}^{\infty} \frac{m^n e^{-m}}{n!} e^{-n \cdot k_1 t}$$

$$= N^*(0) \cdot g(t) e^{-m} \sum_{n=0}^{\infty} \frac{m^n}{n!} e^{-n \cdot k_1 t}$$

$$= N^*(0) \cdot g(t) e^{-m} EXP(m e^{-k_1 t}) \qquad (3.3)$$

At $t_{1/2}$, when the excited QD population $N^*(t)$ in QD-acceptor complex decays to half of the initial amplitude $N^*_{t=0}$, we have

$$1/2 = N^*(t)/N^*(0) = g(t_{1/2}) e^{-m} EXP(m e^{-k_1 t_{1/2}})$$

and

$$k_1 = -\frac{1}{t_{1/2}} ln[1 - \frac{ln(2g(t_{1/2}))}{m}] \qquad (3.4)$$

$t_{1/2}$ and g($t_{1/2}$) can be determined from the transient decay kinetics of 1S exciton in QD-acceptor complexes and free QDs, respectively. Together with m determined from UV-vis spectra, the intrinsic ET rate constant in the 1:1 QD-acceptor can be calculated according to eq. 3.4 for all samples. The intrinsic ET rates for all QD-acceptor complexes are listed in Table A.3.2 and plotted as a function of radius in Figure A.3.3. For reason

yet to be understood, the ET times from CdSe QDs to $MV^{2+}$ are <100 fs and cannot be reliably extracted to examine its size dependence and are not included in this study.

### 3.2.2. Size/Driving Force Dependent Electron Transfer Rates of CdX QDs

We first examine how ET rates depend on the size of QDs within each series of QD-acceptor complexes. The intrinsic ET rates are plotted as a function of QD size for CdS, CdSe and CdTe in Figure 3.4 A, B and C, respectively. Because of the large variation of ET rates to different acceptors, to facilitate comparison, the rate constants have been scaled to have similar values for the smallest QDs in each QD-acceptor series. The scaling factors for each QD-acceptor series are listed in the figures. For all QD-acceptor complexes, ET rate increases with decreasing QD size, regardless of the QD compositions and molecular acceptors. The size dependence is more pronounced for AQ compared to $MB^+$. For example, decreasing the CdS radius from 2.2 to 1.2 nm, the ET rate constant increases by ~ 350 folds for AQ, ~ 25 folds for $MV^{2+}$ and ~10 folds for $MB^+$.

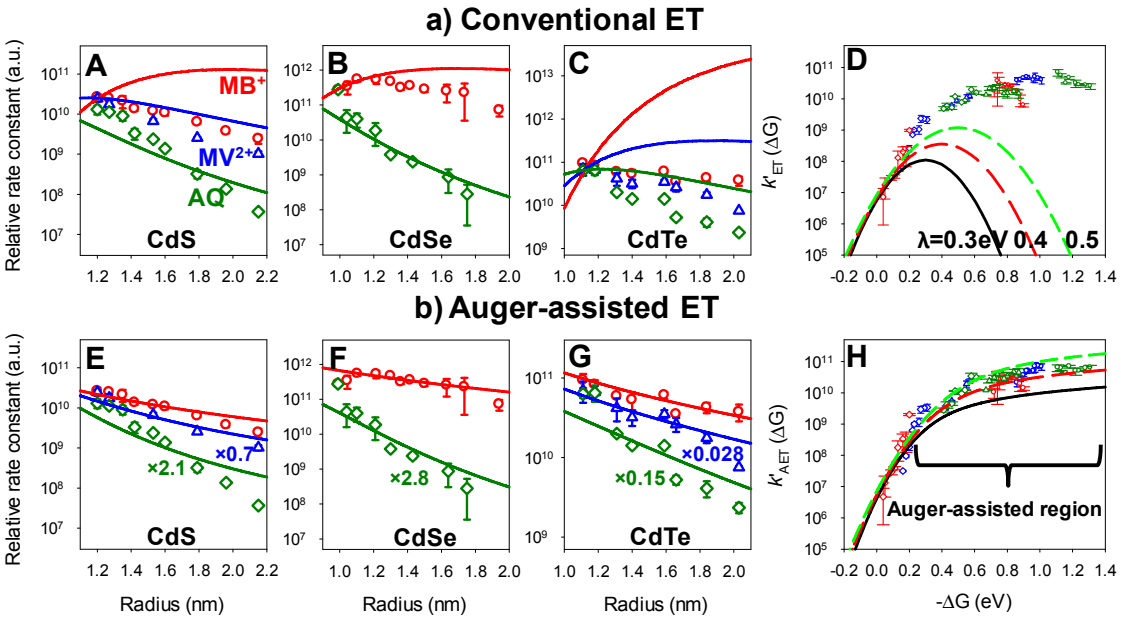


**Figure 3.4.** (A-C) Measured size-dependent ET rates (symbols) of CdS (Ai) CdSe (Bi) and CdTe (Ci) QDs to $MB^+$ (red circles), $MV^{2+}$ (blue triangle), and AQ (green diamond), and theoretical fits (solid line) calculated assuming λ = 0.4 V according to the conventional (i=I, upper panles) and Auger-assisted (i=II, lower panels) ET models. ET rate constants to different acceptors have been scaled to have similar values for the smallest size of QDs and the scaling factors are indicated in the figure. (D) Measured (symbols) and predicted (lines) ET rates as a function of driving force according to the conventional (DI) and Auger-assisted (DII) ET models. The predicted values are calculated according to Eq. 3.5 and Eq. 3.14 with λ values of 0.3 (black solid line), 0.4 (red dashed line), 0.5 (green dashed line) eV. The measured ET rate constants of from CdX QDs (CdS: blue, CdSe: red, CdTe: dark green) to molecular acceptors ($MB^+$: circles, $MV^{2+}$: triangles, AQ: diamonds) have been scaled by the R dependent prefactors in Eq. 3.15 ($C_H|\Psi_{1Se}(R)_0|^2$) and Eq. 3.16 ($C|\Psi_{1Se}(R)_0|^2R^2$), respectively, to account for the

size and materials dependent variation of coupling strength. The C and $C_H$ values for each series of QD-acceptor complexes are chosen such that QD-acceptors with the same driving force have the same scaled ET rates regardless of their chemical nature.

In the conventional ET model that is widely used in QD electron transfer study,[18,19,31] it is assumed that as the 1S electron is transferred from the excited QD (QD*) to the acceptor (A), the hole remains at the $1S_h$ level, as shown in Figure 3.5 AI. Therefore the electronic coupling strength *H(R),* depends on the wavefunction overlap between the QD 1S electron level and molecular LUMO, and can be assumed to be proportional to the amplitude of the 1S electron density at the QD surface, i.e. $|H(R)|^2 = C_H|\Psi_{1Se}(R)_0|^2$ , where $C_H$ is a size independent factor that depends on the QD material and molecule.[31] With these approximations, the nonadiabatic ET rate from the QD to adsorbate can be described by Marcus ET theory:[10]

$$k_{ET}(R) = C_H \frac{2\pi}{\hbar} \frac{|\Psi_{1Se}(R)_0|^2}{\sqrt{4\pi\lambda k_B T}} \exp[-\frac{(\lambda+\Delta G(R))^2}{4\lambda k_B T}] \quad (3.5)$$

where ΔG is the free energy change and λ the total reorganization energy for ET between the reactant and product state.

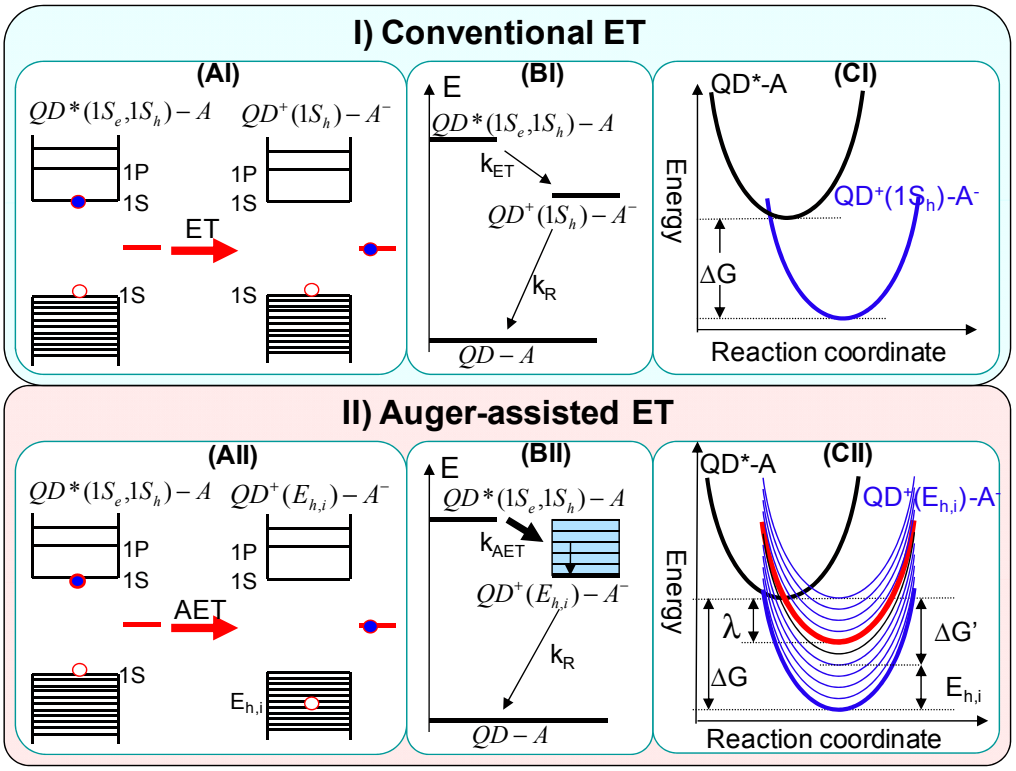


**Figure 3.5.** Conventional (i=I, upper panel) and Auger-assisted (i=II, lower panel) models for ET from QDs. (Ai) Single particle picture, showing the electron and hole levels before and after the ET process. In conventional ET(AI), the 1S electron is transferred from QD* ($1S_e$) to the electron acceptor (A) without changing the hole level ($1S_h$). In Auger-assisted ET(AII), ET can be coupled with a change in the hole energy level, giving rise to a continuum of product states, each corresponding to the hole in a different excited level. (Bi) State representation showing the energy of the ground (QD-A), excited (QD*-A) and charge-separated states ($QD^+$-$A^-$) as well as the ET (with rate $k_{ET}$ or $k_{AET}$) and back ET ($k_R$) processes. (Ci) Marcus representation showing the energy of the reactant and product states as a function of the nuclear displacement along the ET

coordinate. (Di) Calculated ET rates as a function of driving force at indicated reorganization energies for conventional (i=I) and Auger assisted (i=II) models.

The 1S electron density at the QD surface, $\Psi_{1Se}(R)_0$, can be calculated using the effective mass model. Also obtained are 1S electron/hole energy levels and their Columbic binding energies. The values of ΔG for each QD-acceptor complex can be calculated using the following method.

For QD-molecular acceptor (QD-A) complexes, before electron transfer, the initial state of the whole system is $QD^*(1S_e, 1S_h)$-A, the corresponding free energy can be written as:

$$E_i = E_{1Se} + E_{1Sh} + E_{e-h} + E_A \qquad (3.6)$$

where $E_{1Se}$ and $E_{1Sh}$ are the 1S electron and hole energies, respectively, $E_{e\text{-}h}$ the electron-hole binding energy in excited QDs, and $E_A$ the energy of electron acceptor molecule A.

After electron transfer, the final state of the whole system is QD $(1S_h)$-$A^-$ and the system free energy is

$$E_f = E_{1Sh} + E_{CS} + E_{c(h)} + E_{A^-} + E_{c(e)} \qquad (3.7)$$

where $E_{CS}$ is the electron-hole binding energy in charge separated state (with a 1S hole in the QD and an electron in the acceptor molecule), $E_{c(h)}$ the charging energy of putting a hole in the QD, $E_{c(e)}$ the charging energy of putting an electron in acceptor molecule, $E_{A^-}$ is the energy of reduced acceptor molecule $A^-$.

Therefore, the total free energy change of electron transfer is

$$\begin{aligned}\Delta G &= E_f - E_i \\ &= (E_{1Sh} + E_{CS} + E_{c(h)} + E_{A^-} + E_{c(e)}) - (E_{1Se} + E_{1Sh} + E_{e-h} + E_A) \\ &= -E_{1Se} - E_{e-h} + E_{CS} + E_{c(h)} + (E_{A^-} + E_{c(e)} - E_A) \\ &= -E_{1Se} - E_{e-h} + E_{CS} + E_{c(h)} + E_{A/A^-}\end{aligned} \tag{3.8}$$

where $E_{A^-} + E_{c(e)} - E_A$ is the free energy change for reducing the acceptor molecule A, which is denoted as $E_{A-/A}$ and related to the molecule reduction potential ($\phi_{A/A^-}$) by $E_{A/A^-} = e\phi_{A/A^-}$. $E_{1Se}$ and $E_{1Sh}$ are calculated from the effective mass modeling.

The QD charging energy ($E_{c(h)}$) has been previously calculated for ET at CdSe QD-metal oxide interface.[19] Similarly, the charging energy $E_{c(h)}$ for QD-molecular acceptor complexes here can be derived as

$$E_{c(h)}(R) = \frac{0.786e^2}{8\pi R\varepsilon_{QD}} + \frac{e^2}{8\pi R\varepsilon_{sol}} \tag{3.9}$$

where R is the radius of QDs and $\varepsilon_{QD}$ and $\varepsilon_{sol}$ are the dielectric constant of QDs and solvent (1.92 for heptane), respectively.

Because the QD is much bigger than the adsorbed electron acceptor molecule, the electron-hole binding energy in charge separated state $E_{CS}$ can be calculated by approximating the molecule as a point charge on the QD surface, as shown in Figure 3.6 A. For simplification, assuming infinite potential from capping ligand, the 1S hole envelop wavefunction of QDs is

$$\psi(r) = \frac{\sin(\pi r / R)}{r\sqrt{2\pi R}} \qquad (3.10)$$

Then the distribution of 1S hole is

$$\rho(r) = e\left|\psi(r)\right|^2 = e\frac{\sin^2(\pi r / R)}{2\pi R r^2} \qquad (3.11)$$

The coulomb attraction between the electron and hole in charge separated state is

$$E_{cs}(R) = \int_0^R dr \int_0^\pi d\theta \int_0^{2\pi} d\varphi \frac{r^2 \sin\theta e^2 \rho(r)}{4\pi\varepsilon_{QD}\sqrt{r^2\sin^2\theta + (R - r\cos\theta)^2}} \qquad (3.12)$$

The calculated $E_{c(h)}$, $E_{CS}$, $E_{e\text{-}h}$ for CdSe QDs of different sizes are shown in Figure 3.6 B. Together with $E_{1Se}$ (calculated from effective mass modeling) and molecule acceptor reduction potential energy $E_{A\text{-}/A}$, the free energy change (ΔG) for different size QDs can be obtained and are listed in Table A.3.2. Because of the difference in the molecules' redox potentials, the driving force (-ΔG) for ET from the QDs to these acceptors follows the order of $MB^+$ (1.31 ~ 0.72 eV) > $MV^{2+}$ (0.84 ~ 0.42 eV) >AQ (0.61 ~ 0.04 eV).

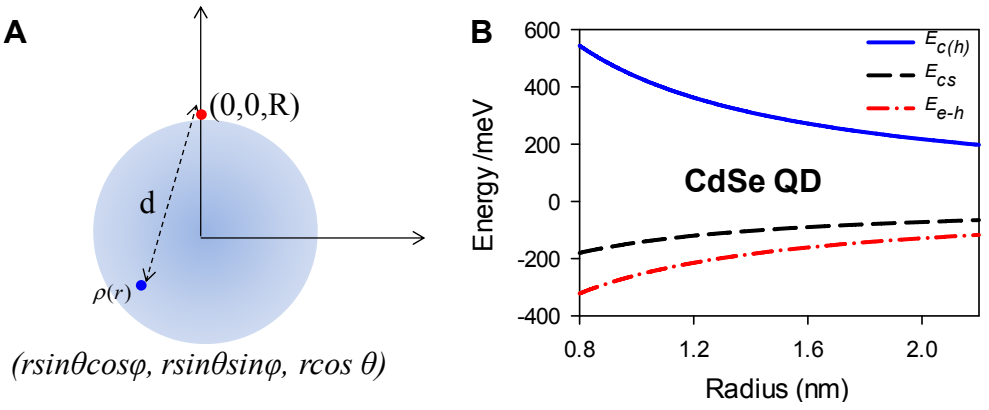


**Figure 3.6.** (A) The electron in acceptor molecule is treated as a point charge on QD surface for $E_{CS}$ calculation. (B) Calculated charging energy ($E_{c(h)}$), electron-hole binding energy in charge separated state ($E_{CS}$), electron-hole binding energy in excited QDs ($E_{e\text{-}h}$) as a function of QD radius in CdSe.

The reorganization energy λ for ET processes contains the inner-sphere contribution from the nuclear displacement of the reactants and products ($\lambda_i$) and the outer-sphere contribution ($\lambda_o$) from the solvent dielectric response. For QD-molecular acceptor complex, $\lambda_i$ mostly comes from the electron acceptor molecule and the QD contribution is negligible because of the weak electron-lattice coupling.[15] Previous size dependent ET studies of QDs on semiconductor oxides suggest a QD reorganization energy of about 10 meV.[18,19] Previous quantum mechanical calculations on similar aromatic organic molecules yield $\lambda_i$ values of 100-300 meV.[37-39] The dielectric continuum model predicts a negligible value of solvent reorganization energy $\lambda_o$ in nonpolar solvents,[10] which has been shown to be inconsistent with some experimental results.[40,41] A molecular solvation model that includes the quadruple contribution yields $\lambda_o$ in the

range 100-200 meV for nonpolar solvents.[42] Therefore, the total reorganization energy (λ) for the QD-molecule acceptor complexes in heptane is estimated to be 200 ~ 500 meV. With these values of $\Psi_{1Se}(R)_0$, $\Delta G(R)$ and λ, the ET rate constants as a function of QD size can be calculated according to Eq. 3.5. The calculated rates with λ = 400 meV are shown in Figure 3.4 upper panel (A, B, C), where the amplitudes have been rescaled for comparison with experimental results (qualitatively similar results are obtained for λ in the 200 ~ 500 meV range).

As shown in Figure 3.4 upper panel, for all QD-acceptor complexes the observed ET rates increase at decreasing QD sizes (or increasing driving force). For ET from CdS and CdSe QDs to AQ molecules, the estimated -ΔG values (0.04 ~ 0.31 eV) are smaller than λ, falling in the Marcus normal regime, and the observed size dependence of the ET rates can be qualitatively described by the conventional ET model.[10] ET from CdS or CdSe QDs to $MB^+$ and from CdTe QDs to $MB^+$ and $MV^{2+}$ molecules, for which the -ΔG values (0.67 ~ 1.31 eV) significantly exceed λ, is in the Marcus inverted regime (Figure 3.4 DI and Figure 3.5 upper panel), where the conventional ET model predicts a slower ET rate with decreasing size (increasing driving force), in strong disagreement with the experiment.

In the conventional ET model, we have assumed that the electron transfer is independent from the hole dynamics. This assumption has been shown to be often inadequate in QDs, in which the enhanced Coulomb interaction has led to correlated electron and hole dynamics, such as Auger-assisted hot carrier thermalization and multicarrier Auger recombination.[8,43-46] We propose an Auger-assisted ET model, as

depicted in Figure 3.5 AII, in which the excess electron energy (the energy difference between the 1S level and the acceptor LUMO) can also be conserved by the excitation of 1S holes to a deeper level with energy $E_{h,i}$ below the 1S hole, in addition to the vibrations of the lattice and acceptor molecules. The excited hole can then relax efficiently within the densely spaced valance band levels.[47] Because of the quasi-continuum nature of the hole states in these QDs, instead of one product state ($QD^+[1S_h]$-$A^-$) involved in the conventional ET model, there is a manifold of product states ($QD^+[E_{h,i}]$-$A^-$), corresponding to the excitation of the hole to different levels ($E_{h,i}$) (Figure 3.5 BII and CII). In the non-adiabatic limit, the total ET rate is the sum of Auger-assisted ET rates to these product states, which is given by:

$$k_{AET}(R) = \sum_i k_{AET}(R, E_{h,i}) = \sum_i \frac{2\pi}{\hbar} \frac{\left|H_{AET}(R,E_{h,i})\right|^2}{\sqrt{4\pi\lambda k_B T}} \exp[-\frac{(\lambda+\Delta G'(R,E_{h,i}))^2}{4\lambda k_B T}] \quad (3.13)$$

The driving force for Auger-assisted ET $\Delta G'(R, E_{h,i}) = \Delta G(R) + E_{h,i}$ is smaller than that for the conventional ET, ΔG (referred to as the apparent driving force), by the amount of hole excitation energy ( $E_{h,i}$). The electronic coupling strength, $H_{AET}(R,E_{h,i})$, depends not only on the overlap of the 1S electron and acceptor orbitals (as in conventional ET), but also on the electron - hole Coulomb interaction, which is inversely proportional to the QD radius $R$.[17,48] We further assume that the dense hole levels in CdX QDs can be described by a quasi-continuum with a density of states (DOS) $\rho_h(E_h, R)$ and the electronic coupling matrix element is independent of the hole energy level. As shown in Figure A.3.4, for CdSe QDs of different radius (between 0.8-2 nm), the calculated DOS of the quasi-continuous valence band states within 1 eV from the band edge increases

linearly with hole energy and QD volume and can be well represented by $\rho_h(E_h, R)dE_h \propto E_h R^3 dE_h$. Thus, the total ET rate to all product states can be simplified to:

$$k_{AET}(R) = C|\Psi_{1Se}(R)_0|^2 R^2 \int_{E_h=0}^{\infty} dE_h E_h \frac{2\pi}{\hbar} \frac{1}{\sqrt{4\pi\lambda k_B T}} \exp[-\frac{(\lambda+\Delta G(R)+E_h)^2}{4\lambda k_B T}] \quad (3.14)$$

The ET rates calculated according to the Auger-assisted model (Eq. 3.14) with λ = 400 meV are shown in Figure 3.4 AII, BII and CII. The calculated rates for each QD-acceptor series have been scaled by a common scaling factor for better comparison with our experimental values. The predicted size dependence of Auger-assisted ET rates agrees well with the measured trends for all QDs and acceptors.

The key difference between the conventional and Auger-assisted ET models is dramatically different dependences on the driving force in the Marcus inverted regime, as shown in Figure 3.4 DI and DII. To more clearly illustrate this dependence, we define scaled ET rates, in which the size and material dependent coupling strength can be removed and only the driving force dependence remains. The scaled rates for the conventional, $k'_{ET}(\Delta G)$, and Auger-assisted, $k'_{AET}(\Delta G)$, ET processes are:

$$k'_{ET}(\Delta G) = \frac{k_{ET}(R)}{C_H|\Psi_{1Se}(R)_0|^2} = \frac{2\pi}{\hbar} \frac{1}{\sqrt{4\pi\lambda k_B T}} \exp[-\frac{(\lambda+\Delta G(R))^2}{4\lambda k_B T}] \quad (3.15)$$

$$k'_{AET}(\Delta G) = \frac{k_{AET}(R)}{C|\Psi_{1Se}(R)_0|^2 R^2} = \int_{E_h=0}^{\infty} dE_h E_h \frac{2\pi}{\hbar} \frac{1}{\sqrt{4\pi\lambda k_B T}} \exp[-\frac{(\lambda+\Delta G(R)+E_h)^2}{4\lambda k_B T}] \quad (3.16)$$

Shown in Figure 3.4 DI and DII are the measured scaled ET rate constants as a function of driving force. To obtain these rates, the measured rate constants were divided by the size and material dependent scaling factor, $C_H|\Psi_{1Se}(R)_0|^2$ and $C|\Psi_{1Se}(R)_0|^2 R^2$

for the conventional (Figure 3.4 DI) and Auger-assisted (Figure 3.4 DII) ET models, respectively. One common $C_H$ and $C$ factors are chosen for each series of QD-acceptor complexes (of different QD sizes) to account for the material dependent coupling strength. These factors are chosen such that QD-acceptor complexes with the same driving force have the same ET rates, as defined in Eq. 3.15 and 3.16, regardless of their sizes and materials. It can be seen from Figure 3.4 DI and DII, when -ΔG is small ( < 0.4 eV), the logarithm of the scaled ET rates show a steep rise with increasing driving force; and when -ΔG exceeds ~ 0.4 eV, it increases more slowly with the driving force.

To compare with the experimental values, the scaled ET rates for the conventional and Auger-assisted ET models are calculated according to Eq. 3.15 and 3.16, respectively, using λ values of 0.3, 0.4 and 0.5 eV. For conventional ET model, as predicted by the Marcus theory, with increasing driving force, the ET rate increases in the normal regime (-ΔG < λ), reaches a maximum (at -ΔG = λ), and decreases in the inverted regime (-ΔG > λ), contrary to the experimental results (Figure 3.4 DI). For Auger-assisted ET model, the predicted rates increase with the driving force at -ΔG < λ, similar to the conventional ET model. However, the Auger-assisted ET rate continues to increase with driving force in the inverted regime (-ΔG > λ), in qualitative agreement with the experimental results.

The origin for the lack of Marcus inverted regime behavior in Auger-assisted ET model can be attributed to the presence of the continuum of product states, to which ET can occur with effective driving forces (-ΔG') ranging from 0 (hole excitation takes all the free energy change) to -ΔG (hole is not excited) and corresponding activation barriers of $(\lambda+\Delta G')^2/4\lambda$. When the apparent driving force (-ΔG) is larger than λ, the rate for the

pathway with no hole excitation (the conventional pathway) decreases due to increasing activation barrier. However, there exist Auger-assisted activationless reaction channels where the effective driving force $-\Delta G' = (-\Delta G) - E_h$ is close to λ, and ET process is barrier-less. We denote the regime where -ΔG > λ as Auger assisted regime (Figure 3.5 DII), because ET occurs most effectively with the excitation of holes, overcoming the unfavorable Frank-Condon overlap in the Marcus inverted regime in the conventional ET pathway.

For intramolecular ET processes, the unfavorable Frank-Condon overlap in the Marcus inverted regime can also be reduced by ET to excited states of the reduced molecular acceptors,[49] or by the excitation of high frequency vibration modes.[12,50] In QD-acceptor complexes, the electron-hole Coulomb interaction within the QDs are in the 130-260 meV range (R= 1~2 nm, depending on size), which is much larger than the QD-adsorbate interaction (estimated to be less 10 meV from the shift of QD 1S exciton band upon adsorbate binding), suggesting that the Auger-assisted pathway is the most-likely mechanism. This is supported by previous studies of hot-electron relaxation in QDs, which have shown that Auger cooling is much faster than relaxation via excitation of surface ligand vibrations and lattice phonons.[43,44,51-53] A direct experimental proof of the Auger-assisted ET pathway would require the observation of hole excitation. Unfortunately, hot holes in CdX (X=S, Se and Te) QDs relax back to the band edge on the subpicosecond time scales,[47,51] which is faster than the ET time observed in this experiment. Therefore, direct observation of hole excitation is not possible. Another experimental proof would be measuring the driving force dependence of electron transfer

rates from QDs in the absence of holes. However, this is also difficult to realize experimentally. Using the hole accepting molecules we know, including thiols and phenothiazine, the hole removal time (typically on the order of hundreds of picosecond to nanosecond[7,54-56]) is too slow to compete with the interfacial electron transfer process, especially for those in the Auger-assisted regime. Furthermore, previous experimental and theoretical evidence also suggests that trapped carriers on QD surface can also be involved in Auger recombination process.[46,57] To provide further evidence to support the proposed mechanism, we have turned to computational modeling of the ET processes in QD-acceptor complexes.

### 3.2.3. Computational Simulation of Auger-assisted Electron Transfer from CdX QDs

The first computational study is performed using time-domain density functional theory combined with nonadiabatic molecular dynamics, as explained in Appendix 6. The system comprises a $Cd_{33}Se_{33}$ QD in contact with the $MB^+$ molecule (Figure A.3.5 and A.3.6). Photo-excitation promotes an electron from the QD HOMO to the QD LUMO, leaving a hole in the HOMO orbital. The details of the Auger-assisted ET process are illustrated in Figure 3.7 (a), which shows the time evolution of the energies of various parts of the system along a representative trajectory. During ET, the electron energy decreases on a picosecond timescale, indicating the transfer of the electron from QD LUMO to $MB^+$ LUMO. At the initial stage, the energy lost by the electron is gained

exclusively by the hole, confirming the proposed Auger-assisted ET mechanism. The hole never gains the full $\Delta G$ of energy lost by the electron, because the hole energy is dissipated by phonons, which is evident in the anti-correlated decrease of hole energy and increase of phonon energy at longer time. Figure 3.7 (b) shows the calculated Auger-assisted ET rates as a function of $-\Delta G$ values from 0.75 to 1.35 eV. These results are averages over multiple nuclear trajectories at a given $\Delta G$ value. With increasing $-\Delta G$, the Auger ET rate increases slightly. In contrast, conventional ET processes (where the hole is fixed at the QD HOMO) exhibit an order of magnitude slower ET rates that *decrease* with increasing $-\Delta G$, showing the expected Marcus inverted regime behavior. Therefore, our *ab initio* results confirm that the Auger excitation of the hole eliminates the Marcus inverted region, in agreement with our experimental result.

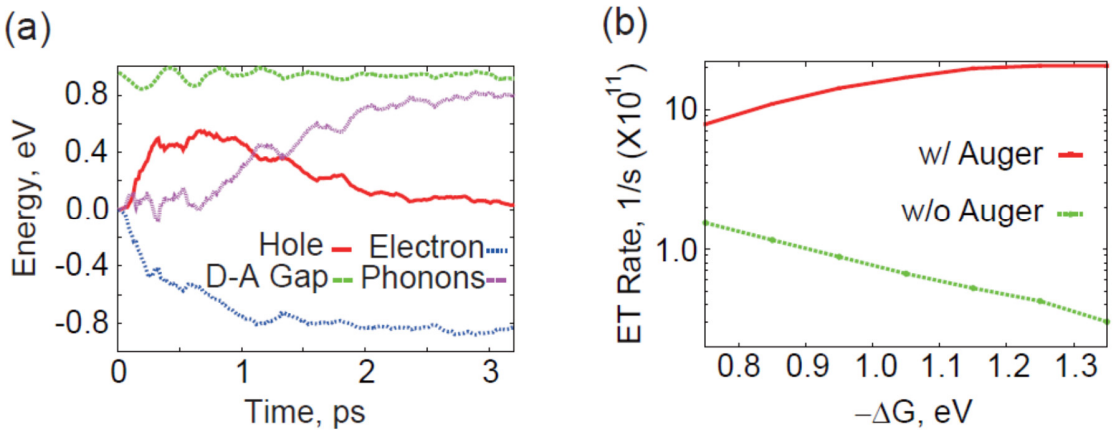


**Figure 3.7**. Time-domain *ab initio* modeling of Auger-assisted ET from CdSe QD to MB. (a) Time evolution of the electron, hole and phonon energies, and the donor-acceptor energy gap ($\Delta G$). The excess energy generated by the ET is accommodated by the excitation of hole, which is promoted from the QD HOMO to deeper VB orbitals. Later,

the hole relaxes by coupling to phonons. (b) Calculated ET rates as a function of driving force ( $-\Delta G$ ) for Auger-assisted and conventional ET processes.

The direct *ab initio* dynamics simulation described above is limited to small particles. Auger-assisted electron trapping times for QDs with sizes in our experimental range (R=1.02, 1.46 and 1.92 nm) have therefore been performed using the semiempirical pseudopotential method. Electron transfer from QD to adsorbates transforms a delocalized conduction band electron to a localized electron at the molecule. We mimic this process by considering the transfer of an electron from the QD LUMO to a surface trap whose energy coincides with that of the MB LUMO. The details of the calculation can be found in reference.[58] The calculated electron trapping times increase with increasing dot size, in agreement with the experimental findings. The transfer times for ET not accompanied by the excitation of the hole are about three orders of magnitude longer (i.e., a few nanoseconds or longer) than those with hole excitation, supporting the proposed Auger assisted ET pathway.

## 3.3. Conclusion

In conclusion, we show that the rate of photoinduced electron transfer from QDs (CdS, CdSe and CdTe) to molecular acceptors (anthraquinone, methylviologen and methylene blue) increases at decreasing QD size (and increasing driving force), showing

a lack of Marcus inverted regime behavior over an apparent driving force range of ~ 0-1.3 V. We account for this unusual driving force dependence by proposing an Auger-assisted electron transfer model, in which the transfer of the electron can be coupled to the excitation of the hole, circumventing the unfavorable Frank-Condon overlap in the Marcus inverted regime. This model is supported by computational studies of electron transfer and trapping processes in model QD-acceptor complexes.

Our study reveals a photoinduced electron transfer pathway from QDs that is fundamentally different from those in molecular chromophores and bulk semiconductor. Because Auger-type processes occur in most quantum confined nanomaterials (QDs, quantum rods, nanowires, carbon nanotudes, graphenes…), we believe that the Auger assisted ET model proposed for CdX QDs herein should be generally applicable for describing exciton dissociation in other excitonic nanomaterials.

## References

(1) Han, Z.; Qiu, F.; Eisenberg, R.; Holland, P. L.; Krauss, T. D. *Science* **2012**, *338*, 1321.

(2) Sambur, J. B.; Novet, T.; Parkinson, B. A. *Science* **2010**, *330*, 63.

(3) Tisdale, W. A.; Williams, K. J.; Timp, B. A.; Norris, D. J.; Aydil, E. S.; Zhu, X.-Y. *Science* **2010**, *328*, 1543.

(4) De Volder, M. F. L.; Tawfick, S. H.; Baughman, R. H.; Hart, A. J. *Science* **2013**, *339*, 535.

(5) Semonin, O. E.; Luther, J. M.; Choi, S.; Chen, H.-Y.; Gao, J.; Nozik, A. J.; Beard, M. C. *Science* **2011**, *334*, 1530.

(6) Zhu, H.; Lian, T. *Energy Environ. Sci.* **2012**, *5*, 9406.

(7) Zhu, H.; Song, N.; Lv, H.; Hill, C. L.; Lian, T. *J. Am. Chem. Soc.* **2012**, *134*, 11701.

(8) Zhu, H.; Yang, Y.; Lian, T. *Acc. Chem. Res.* **2013**, *46*, 1270.

(9) Marcus, R. A. *J. Chem. Phys.* **1956**, *24*, 966.

(10) Marcus, R.; Sutin, N. *Biochim. Biophys. Acta* **1985**, *811*, 265.

(11) Closs, G. L.; Miller, J. R. *Science* **1988**, *240*, 440.

(12) Barbara, P. F.; Meyer, T. J.; Ratner, M. A. *J. Phys. Chem.* **1996**, *100*, 13148.

(13) Miller, J. R.; Calcaterra, L. T.; Closs, G. L. *J. Am. Chem. Soc.* **1984**, *106*, 3047.

(14) Akesson, E.; Walker, G. C.; Barbara, P. F. *J. Chem. Phys.* **1991**, *95*, 4188.

(15) Marcus, R. A. *J. Chem. Phys.* **1965**, *43*, 679.

(16) Brus, L. E. *J. Chem. Phys.* **1983**, *79*, 5566.

(17) Brus, L. E. *J. Chem. Phys.* **1984**, *80*, 4403.

(18) Cánovas, E.; Moll, P.; Jensen, S. A.; Gao, Y.; Houtepen, A. J.; Siebbeles, L. D. A.; Kinge, S.; Bonn, M. *Nano Lett.* **2011**, *11*, 5234.

(19) Tvrdy, K.; Frantsuzov, P. A.; Kamat, P. V. *Proc. Natl. Acad. Sci.* **2011**, *108*, 29.

(20) Žídek, K.; Zheng, K.; Ponseca, C. S.; Messing, M. E.; Wallenberg, L. R.; Chábera, P.; Abdellah, M.; Sundström, V.; Pullerits, T. *J. Am. Chem. Soc.* **2012**, *134*, 12110.

(21) Asbury, J. B.; Hao, E.; Wang, Y. Q.; Ghosh, H. N.; Lian, T. Q. *J. Phys. Chem. B* **2001**, *105*, 4545.

(22) She, C. X.; Anderson, N. A.; Guo, J. C.; Liu, F.; Goh, W. H.; Chen, D. T.; Mohler, D. L.; Tian, Z. Q.; Hupp, J. T.; Lian, T. Q. *J. Phys. Chem. B* **2005**, *109*, 19345.

(23) Huang, J.; Stockwell, D.; Huang, Z.; Mohler, D. L.; Lian, T. *J. Am. Chem. Soc.* **2008**, *130*, 5632.

(24) Kamat, P. V.; Dimitrijevic, N. M.; Fessenden, R. W. *J. Phys. Chem.* **1987**, *91*, 396.

(25) Yang, Y.; Rodríguez-Córdoba, W.; Lian, T. *J. Am. Chem. Soc.* **2011**, *133*, 9246.

(26) Bird, C. L.; Kuhn, A. T. *Chem. Soc. Rev.* **1981**, *10*, 49.

(27) Cao, Y.; Rabinowitz, D. J.; Dixon, D. W.; Netzel, T. L. *Synthetic Commun.* **2009**, *39*, 4230

(28) Yu, W. W.; Qu, L. H.; Guo, W. Z.; Peng, X. G. *Chem. Mater.* **2003**, *15*, 2854.

(29) Morris-Cohen, A. J.; Frederick, M. T.; Cass, L. C.; Weiss, E. A. *J. Am. Chem. Soc.* **2011**, *133*, 10146.

(30) Huang, J.; Huang, Z.; Yang, Y.; Zhu, H.; Lian, T. *J. Am. Chem. Soc.* **2010**, *132*, 4858.

(31) Zhu, H.; Song, N.; Lian, T. *J. Am. Chem. Soc.* **2010**, *132*, 15038.

(32) Zhu, H.; Song, N.; Lian, T. *J. Am. Chem. Soc.* **2011**, *133*, 8762.

(33) Zhu, H.; Song, N.; Rodríguez-Córdoba, W.; Lian, T. *J. Am. Chem. Soc.* **2012**, *134*, 4250.

(34) Song, N.; Zhu, H.; Jin, S.; Zhan, W.; Lian, T. *ACS Nano* **2011**, *5*, 613.

(35) Song, N.; Zhu, H.; Jin, S.; Lian, T. *ACS Nano* **2011**, *5*, 8750.

(36) Rodgers, M. A. J.; Da Silva E Wheeler, M. F. *Chem. Phys. Lett.* **1978**, *53*, 165.

(37) Klimkāns, A.; Larsson, S. *Chem. Phys.* **1994**, *189*, 25.

(38) Amashukeli, X.; Winkler, J. R.; Gray, H. B.; Gruhn, N. E.; Lichtenberger, D. L. *J. Phys. Chem. A* **2002**, *106*, 7593.

(39) Gruhn, N. E.; Macías-Ruvalcaba, N. A.; Evans, D. H. *J. Phys. Chem. A* **2006**, *110*, 5650.

(40) Reynolds, L.; Gardecki, J. A.; Frankland, S. J. V.; Horng, M. L.; Maroncelli, M. *J. Phys. Chem.* **1996**, *100*, 10337.

(41) Cortes, J.; Heitele, H.; Jortner, J. *J. Phys. Chem.* **1994**, *98*, 2527.

(42) Zimmt, M. B.; Waldeck, D. H. *J. Phys. Chem. A* **2003**, *107*, 3580.

(43) Efros, A. L.; Kharchenko, V. A.; Rosen, M. *Solid State Commun.* **1995**, *93*, 281.

(44) Klimov, V. I.; Mikhailovsky, A. A.; McBranch, D. W.; Leatherdale, C. A.; Bawendi, M. G. *Phys. Rev. B* **2000**, *61*, R13349.

(45) Klimov, V. I.; Mikhailovsky, A. A.; McBranch, D. W.; Leatherdale, C. A.; Bawendi, M. G. *Science* **2000**, *287*, 1011.

(46) Cohn, A. W.; Schimpf, A. M.; Gunthardt, C. E.; Gamelin, D. R. *Nano Lett.* **2013**, *13*, 1810.

(47) Cooney, R. R.; Sewall, S. L.; Anderson, K. E. H.; Dias, E. A.; Kambhampati, P. *Phys. Rev. Lett.* **2007**, *98*, 177403.

(48) Klimov, V. I.; McBranch, D. W. *Phys. Rev. Lett.* **1998**, *80*, 4028.

(49) Petersson, J.; Eklund, M.; Davidsson, J.; Hammarström, L. *J. Phys. Chem. B* **2010**, *114*, 14329.

(50) Jortner, J. *J. Chem. Phys.* **1976**, *64*, 4860.

(51) Hendry, E.; Koeberg, M.; Wang, F.; Zhang, H.; de Mello, D.; aacute; C.; Vanmaekelbergh, D.; Bonn, M. *Phys. Rev. Lett.* **2006**, *96*, 057408.

(52) Cooney, R. R.; Sewall, S. L.; Dias, E. A.; Sagar, D. M.; Anderson, K. E. H.; Kambhampati, P. *Phys. Rev. B* **2007**, *75*, 245311.

(53) Pandey, A.; Guyot-Sionnest, P. *Science* **2008**, *322*, 929.

(54) Huang, J.; Huang, Z.; Jin, S.; Lian, T. *J. Phys. Chem. C* **2008**, *112*, 19734.

(55) Wuister, S. F.; Donega, C. D.; Meijerink, A. *J. Phys. Chem. B* **2004**, *108*, 17393.

(56) Liu, I. S.; Lo, H. H.; Chien, C. T.; Lin, Y. Y.; Chen, C. W.; Chen, Y. F.; Su, W. F.; Liou, S. C. *J. Mater. Chem.* **2008**, *18*, 675.

(57) Califano, M. *J. Phys. Chem. C* **2008**, *112*, 8570.

(58) Zhu, H.; Yang, Y.; Hyeon-Deuk, K.; Califano, M.; Song, N.; Wang, Y.; Zhang, W.; Prezhdo, O. V.; Lian, T. *Nano Lett.* **2013**.

(59) Berger, L. I. *Semiconductor materials*; CRC Press, 1997.

(60) Haus, J. W.; Zhou, H. S.; Honma, I.; Komiyama, H. *Phys. Rev. B* **1993**, *47*, 1359.

(61) Wei, S.-H.; Zunger, A. *Appl. Phys. Lett.* **1998**, *72*, 2011.

(62) Pellegrini, G.; Mattei, G.; Mazzoldi, P. *J. Appl. Phys.* **2005**, *97*, 073706.

(63) Finklea, H. O. *Semiconductor electrodes*; Elsevier Science Ltd, 1988; Vol. 55.

(64) Dabbousi, B. O.; RodriguezViejo, J.; Mikulec, F. V.; Heine, J. R.; Mattoussi, H.; Ober, R.; Jensen, K. F.; Bawendi, M. G. *J. Phys. Chem. B* **1997**, *101*, 9463.

(65) Hyeon-Deuk, K.; Prezhdo, O. V. *Nano Lett.* **2011**, *11*, 1845.

(66) Hyeon-Deuk, K.; Prezhdo, O. V. *ACS Nano* **2012**, *6*, 1239.

(67) Craig, C. F.; Duncan, W. R.; Prezhdo, O. V. *Physical Review Letters* **2005**, *95*, 163001.

# Appendix 1.

## Effective Mass Modeling

To quantify the size dependent driving force and electronic coupling strength, the 1S electron energy levels, wavefunctions and electron-hole Columbic binding energy were calculated by modeling it as a particle confined in spherical well of finite depth.[31,33] The parameters for effective mass calculations are shown in Table S1.[59-62] Some parameters, especially band edges, vary between literatures.[63] However, such uncertainty does not influence the trend of size dependent driving force and electronic coupling strength. The Schrodinger equation of the QD is solved numerically to obtain the envelope wavefunction, $\Psi_e(R)$ ($\Psi_h(R)$, and energy, $E_{1Se}$ ($E_{1Sh}$), of the 1S electron (hole). The Columbic binding ($E_{e\text{-}h}$) between the electron and hole is treated as a first-order perturbation,[16] from which the energy of the first exciton state can be calculated $E_{1S} = E_{1Se} - E_{1Sh} + E_{e\text{-}h}$. This model has successfully described the 1S exciton energies and wavefunctions in core only QDs and core shell QDs.[31-33,62,64]

**Table A.3.1.** Parameters of bulk CdS, CdSe and CdTe used in the effective mass calculation.

| | $m_e^*/m_0$ | $m_h^*/m_0$ | $\varepsilon/\varepsilon_0$ | CB/V (vs vacuum) | VB/V (vs vacuum) |
|---|---|---|---|---|---|

| | | | | | |
|---|---|---|---|---|---|
| CdS | 0.19 | 0.8 | 9 | -3.84 | -6.34 |
| CdSe | 0.13 | 0.45 | 10 | -4.04 | -5.74 |
| CdTe | 0.10 | 0.35 | 10 | -3.7 | -5.17 |
| ligand | 1 | 1 | 1 | -1 | -8.4 |

Shown in Figure A.3.1 are the calculated 1S exciton energies (black solid line) as a function of CdS (A), CdSe (B) and CdTe (C) QD radius and comparisons with experimentally determined sizing curves by Peng and coworkers (red circles)[28]. The good agreement between experimental results and our calculations validate this effective mass model. To be self-consistent, we'll rely on the calculated size dependent 1S exciton energy curve to determine our QD radii and associated 1S electron energy levels and 1S electron-hole binding energies in the driving force calculation to be discussed later. In addition, the 1S electron wavefunction $\Psi_{1Se}(R)$ is also obtained from effective mass modeling. The electron density at QDs surface $|\Psi_{1Se}(R)_0|^2$ for different QDs radius is shown in Figure A.3.1D, which reflects the size dependent electronic coupling strength with the adsorbate as discussed in the main text.[31]

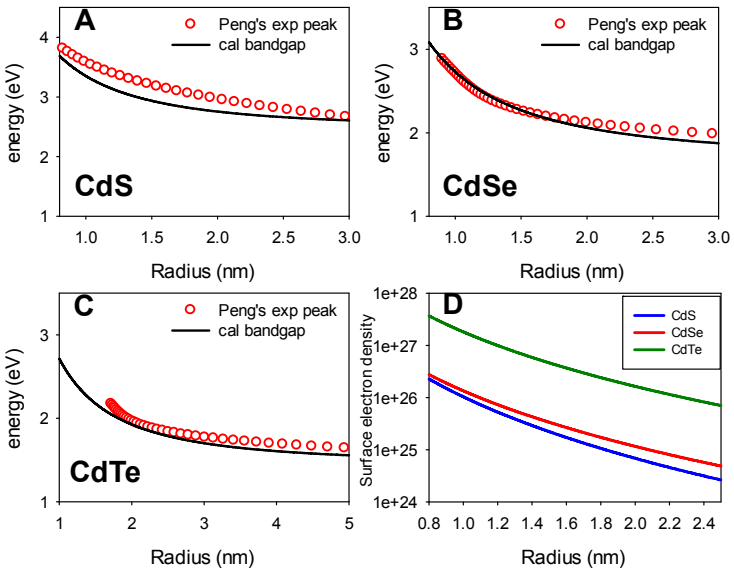


**Figure A.3.1.** Comparisons of calculated QD size dependent 1S exciton energy and Peng's experimental values[28] for CdS (A), CdSe (B) and CdTe (C). (D) Calculated surface electron density $|\Psi_{1Se}(R)_0|^2$ as a function of QD radius.

# Appendix 2.

## Representative TA Spectra of CdSe and CdTe with Different Acceptors

### (i) CdSe QDs

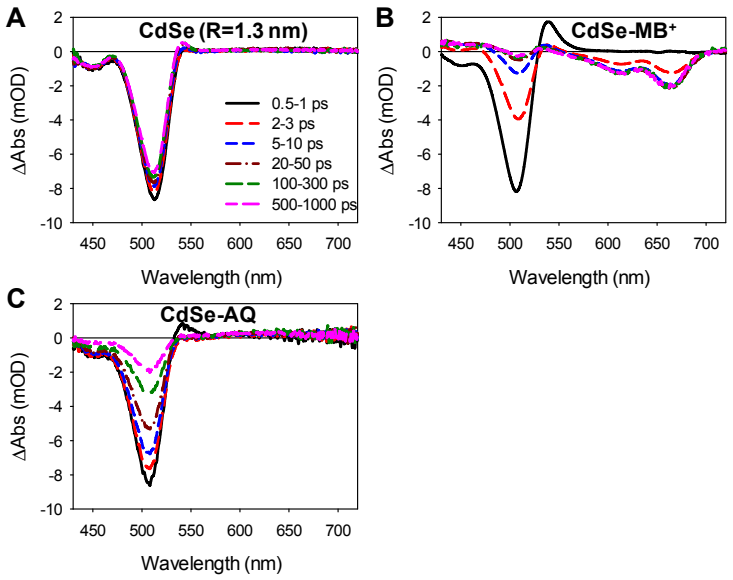


**(ii) CdTe QDs**

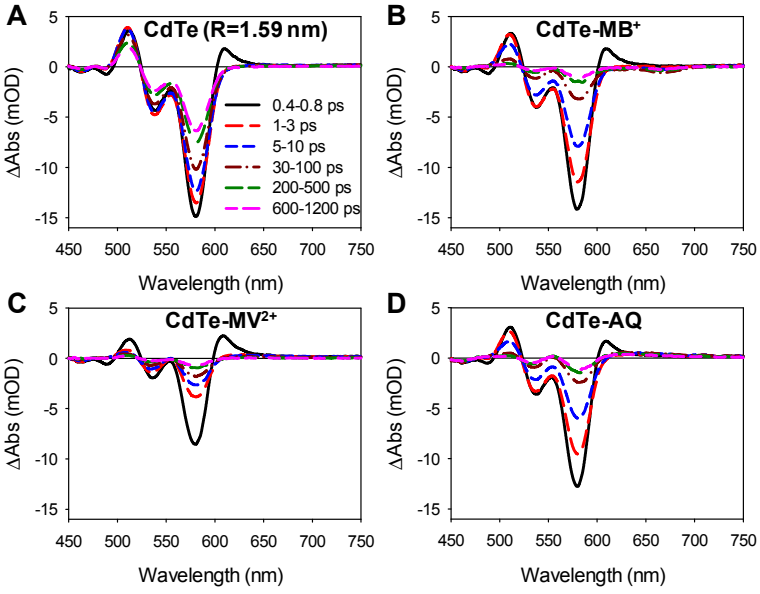


**Figure A.3.2.** Representative TA spectra of CdSe QDs R=1.3 nm (i) and CdTe QDs R=1.59 nm (ii) with different acceptors.

# Appendix 3.

## Size dependent ET kinetics from CdX QDs to different acceptors

### (i) CdS QDs

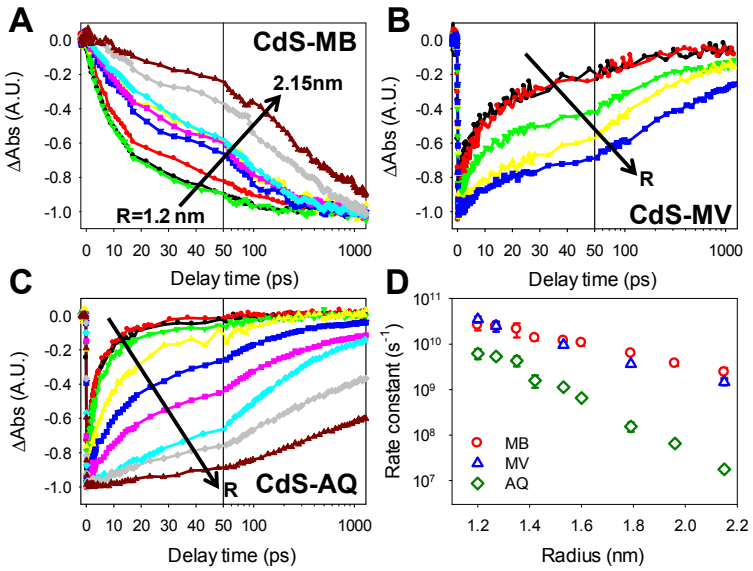


### (ii) CdSe QDs

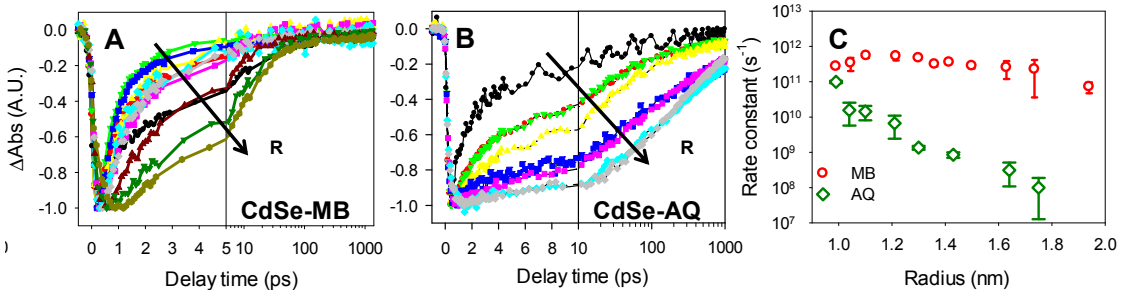

**(iii) CdTe QDs**

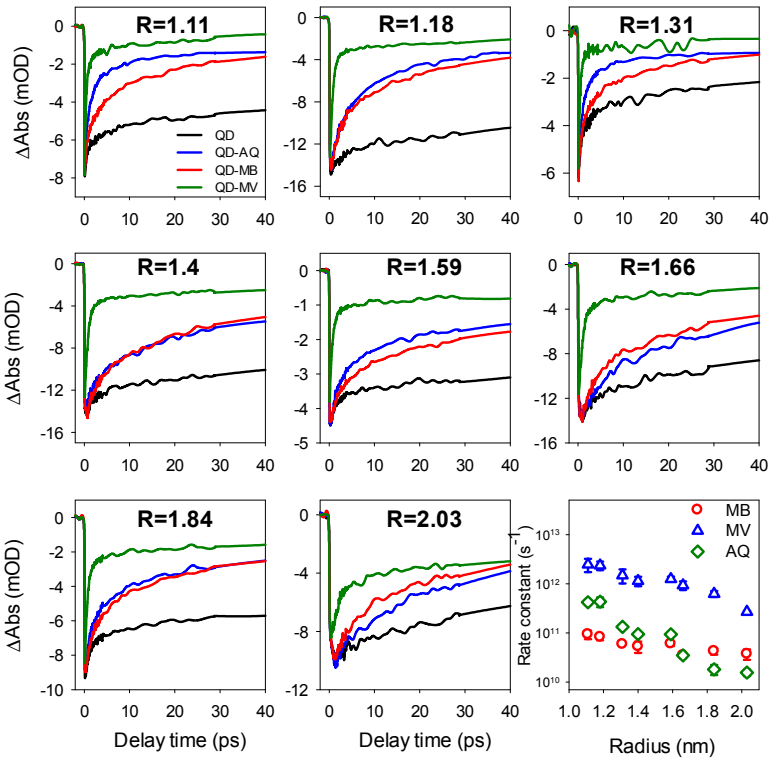


**Figure A.3.3.** Electron transfer kinetics for (i) CdS, (ii) CdSe and (iii) CdTe QDs of different sizes. $MB^+$ ground state bleach formation process was used for CdS-$MB^+$ complexes and 1S exciton bleach recovery kinetics for the rest. Also plotted is the extracted ET rate as a function of QD radius.

# Appendix 4.

**Size dependent ET rate and free energy change in QD/acceptor complexes**

**Table A.3.2.** Rate constant ($k_{ET}$) and driving force (-ΔG) for ET from CdX QDs to acceptors ($MB^+$, $MV^{2+}$ and AQ) as a function of QD radius

## (i) CdS QDs

| radius /nm | CdS-$MB^+$ | | CdS-$MV^{2+}$ | | CdS-AQ | |
|---|---|---|---|---|---|---|
| | -ΔG/eV | $k_{ET}/s^{-1}$ | -ΔG/eV | $k_{ET}/s^{-1}$ | -ΔG/eV | $k_{ET}/s^{-1}$ |
| 1.2 | 1.01 | $(2.60 \pm 0.60) \times 10^{10}$ | 0.57 | $(3.50 \pm 0.52) \times 10^{10}$ | 0.31 | $(6.19 \pm 1.55) \times 10^{9}$ |
| 1.27 | 0.99 | $(2.44 \pm 0.34) \times 10^{10}$ | 0.55 | $(2.50 \pm 0.60) \times 10^{10}$ | 0.29 | $(5.34 \pm 0.08) \times 10^{9}$ |
| 1.35 | 0.97 | $(2.11 \pm 0.72) \times 10^{10}$ | N/A | | 0.27 | $(4.30 \pm 1.01) \times 10^{9}$ |
| 1.42 | 0.96 | $(1.35 \pm 0.16) \times 10^{10}$ | N/A | | 0.26 | $(1.58 \pm 0.47) \times 10^{9}$ |
| 1.53 | 0.93 | $(1.19 \pm 0.07) \times 10^{10}$ | 0.49 | $(9.55 \pm 1.04) \times 10^{9}$ | 0.23 | $(1.13 \pm 0.13) \times 10^{9}$ |
| 1.6 | 0.92 | $(1.07 \pm 0.14) \times 10^{10}$ | N/A | | 0.22 | $(6.51 \pm 0.32) \times 10^{8}$ |
| 1.79 | 0.9 | $(6.26 \pm 0.50) \times 10^{9}$ | 0.46 | $(3.65 \pm 0.18) \times 10^{9}$ | 0.2 | $(1.53 \pm 0.34) \times 10^{8}$ |
| 1.96 | 0.88 | $(3.75 \pm 0.45) \times 10^{9}$ | N/A | | 0.18 | $(6.47 \pm 0.77) \times 10^{7}$ |
| 2.15 | 0.86 | $(2.41 \pm 0.60) \times 10^{9}$ | 0.42 | $(1.46 \pm 0.22) \times 10^{9}$ | 0.16 | $(1.76 \pm 0.12) \times 10^{7}$ |

## (ii) CdSe QDs

| radius /nm | CdSe-$MB^+$ | | CdSe-AQ | |
|---|---|---|---|---|
| | -ΔG/eV | $k_{ET}/s^{-1}$ | -ΔG/eV | $k_{ET}/s^{-1}$ |
| 0.99 | 0.9 | $(2.70 \pm 0.35) \times 10^{11}$ | 0.2 | $(9.87 \pm 0.77) \times 10^{10}$ |
| 1.05 | 0.88 | $(3.66 \pm 1.37) \times 10^{11}$ | 0.18 | $(1.56 \pm 0.99) \times 10^{10}$ |
| 1.10 | 0.86 | $(5.41 \pm 0.77) \times 10^{11}$ | 0.16 | $(1.43 \pm 0.06) \times 10^{10}$ |
| 1.22 | 0.83 | $(5.25 \pm 1.25) \times 10^{11}$ | 0.13 | $(6.65 \pm 4.23) \times 10^{9}$ |
| 1.3 | 0.81 | $(4.66 \pm 0.28) \times 10^{11}$ | 0.11 | $(1.35 \pm 0.17) \times 10^{9}$ |
| 1.36 | 0.8 | $(3.10 \pm 0.40) \times 10^{11}$ | N/A | |
| 1.42 | 0.79 | $(3.51 \pm 0.02) \times 10^{11}$ | 0.09 | $(8.50 \pm 1.50) \times 10^{8}$ |
| 1.5 | 0.77 | $(2.78 \pm 0.45) \times 10^{11}$ | N/A | |
| 1.63 | 0.75 | $(2.50 \pm 1.02) \times 10^{11}$ | 0.05 | $(3.10 \pm 2.02) \times 10^{8}$ |
| 1.74 | 0.74 | $(2.24 \pm 1.88) \times 10^{11}$ | 0.04 | $(1.00 \pm 0.87) \times 10^{8}$ |
| 1.94 | 0.72 | $(7.13 \pm 0.24) \times 10^{10}$ | N/A | |

### (iii) CdTe QDs

| radius /nm | CdTe-$MB^+$ | | CdTe- $MV^{2+}$ | | CdTe-AQ | |
|---|---|---|---|---|---|---|
| | -ΔG/eV | $k_{ET}/s^{-1}$ | -ΔG/eV | $k_{ET}/s^{-1}$ | -ΔG/eV | $k_{ET}/s^{-1}$ |
| 1.11 | 1.31 | $(9.32 \pm 1.80) \times 10^{10}$ | 0.87 | $(2.48 \pm 0.72) \times 10^{12}$ | 0.61 | $(4.22 \pm 0.51) \times 10^{11}$ |
| 1.18 | 1.28 | $(8.21 \pm 1.15) \times 10^{10}$ | 0.84 | $(2.36 \pm 0.47) \times 10^{12}$ | 0.58 | $(4.33 \pm 0.97) \times 10^{11}$ |
| 1.31 | 1.24 | $(5.88 \pm 0.23) \times 10^{10}$ | 0.8 | $(1.49 \pm 0.47) \times 10^{12}$ | 0.54 | $(1.33 \pm 0.05) \times 10^{10}$ |
| 1.4 | 1.22 | $(5.28 \pm 1.37) \times 10^{10}$ | 0.78 | $(1.14 \pm 0.25) \times 10^{12}$ | 0.52 | $(9.42 \pm 0.56) \times 10^{10}$ |
| 1.59 | 1.18 | $(6.05 \pm 0.60) \times 10^{10}$ | 0.74 | $(1.25 \pm 1.04) \times 10^{12}$ | 0.48 | $(9.38 \pm 0.18) \times 10^{10}$ |
| 1.66 | 1.16 | $(3.49 \pm 0.17) \times 10^{10}$ | 0.72 | $(9.33 \pm 1.86) \times 10^{11}$ | 0.46 | $(3.49 \pm 0.45) \times 10^{10}$ |
| 1.84 | 1.13 | $(4.23 \pm 0.64) \times 10^{10}$ | 0.69 | $(6.27 \pm 0.87) \times 10^{11}$ | 0.43 | $(2.72 \pm 4.17) \times 10^{10}$ |
| 2.03 | 1.11 | $(3.73 \pm 0.89) \times 10^{10}$ | 0.67 | $(2.69 \pm 0.10) \times 10^{11}$ | 0.41 | $(1.56 \pm 0.23) \times 10^{10}$ |

## Appendix 5.

### Calculation of hole density of state

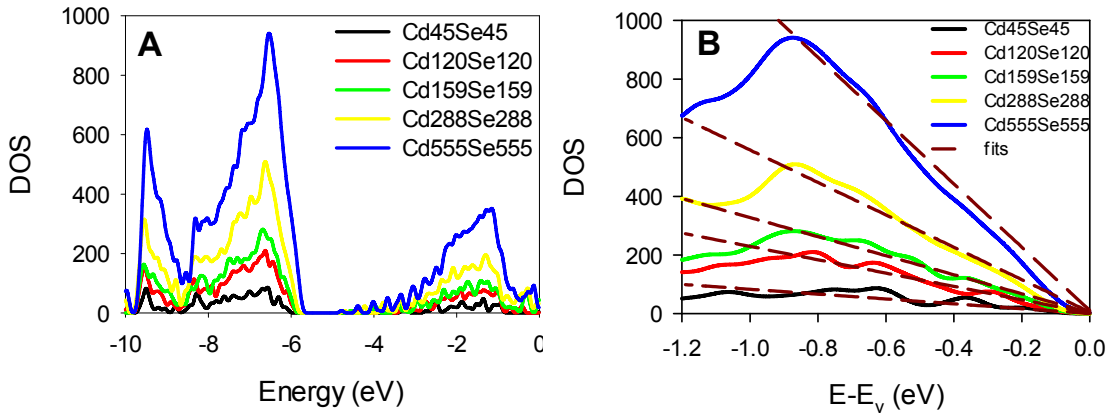

**Figure A.3.4.** (A) Calculated density of state of CdSe QDs with radius between 0.8 nm and 2 nm. (B) Density of state of hole with energy $E_h$ below the valance band edge ($E_h$ = $E-E_v$) for different CdSe QDs radius (solid lines). The dashed lines show the $E_hR^3$ fitting.

The density of state of CdX (X=S, Se, Te) QDs (radius between 0.8 nm and 2 nm) were calculated by using Siesta code with generalized-gradient approximation (GGA). Double-ζ (DZ) is used as a basis set. Only Gama point is used for k-point sample. The supercells contain a vacuum region of at least 10 Å, which is large enough to reduce the periodic interactions. The lattice parameters for CdSe (CdS/CdTe) of our calculation are a=4.419 (4.236/4.716) Å, c=7.212 (6.883/7.725) Å, and the internal parameter for CdSe (CdS/CdTe) is u=0.3757 (0.3779/0.375).

The quantum dots are cut out from the bulk wurtzite lattice by a given sphere radius. The structure is accepted only when the numbers of Cd atoms and X (S, Se, Te ) atoms are equal and the dangling bonds is no more than two. We found that the passivation atoms have negligible effect on states within the valence band. They remove the dangling bond of surface atoms and push the unoccupied surface states into the valence band. The calculated DOS for CdSe QDs are shown in Figure S6A. The hole density of states near the valance band edge for CdSe QDs are shown in Figure S6B. The hole DOS within ~1 eV of the valence band edge can be well reproduced by $DOS = N_{QD}E_hR^3$, where $N_{QD}$ is a material dependent prefactor, $E_h$ is the hole energy below the valance band edge and R is the QD radius.

# Appendix 6.

## Time-domain *ab initio* simulation of Auger-assisted ET

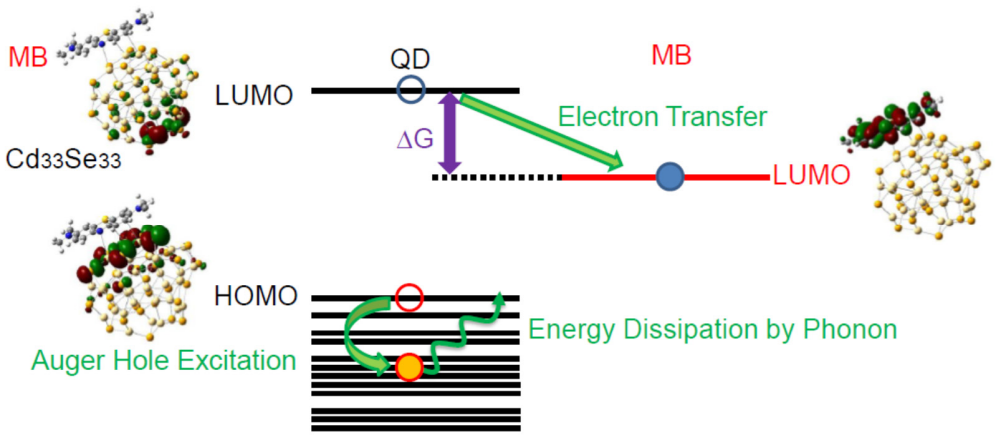


**Figure A.3.5.** Time-domain *ab initio* modeling of Auger-assisted ET from CdSe QD to MB. The QD/$MB^+$ complex is drawn with the orbital distributions of the key electronic states: QD HOMO, QD LUMO and MB LUMO.

We have performed real-time atomistic simulation of ET from the CdSe QD electron donor to the MB electron acceptor, accompanied by Auger-type excitation of the hole within the QD. The system under investigation is shown in Figure A.3.4. In order to account for the Auger excitation of the hole, accompanying the ET, we adopted an exciton representation, illustrated in Figure A.3.5. The band gap excitation of the QD is

the reactant state. The electron-phonon relaxation in the QD is significantly faster than the timescale of the current ET, allowing us to exclude higher energy QD excitons from consideration and to achieve significant computational savings. The remaining states in the exciton basis are product states with the electron transferred to the MB LUMO, indicated in Figure A.3.5 by the red line, and the hole in one of the valence band (VB) orbitals of the QD. There are 43 product states, corresponding to the number of VB states, $N_{VB}$, considered explicitly. Note that including both conduction and VB states of the QD rapidly increases the size of the exciton basis. For instance, consideration of both single and double excitons extends the basis size to hundreds of thousands for QDs of the size considered here,[65,66] and to astronomical numbers for larger QDs. The ET driving force, ΔG, is the difference between the energies of the QD LUMO and the MB LUMO, Figure A.3.5.

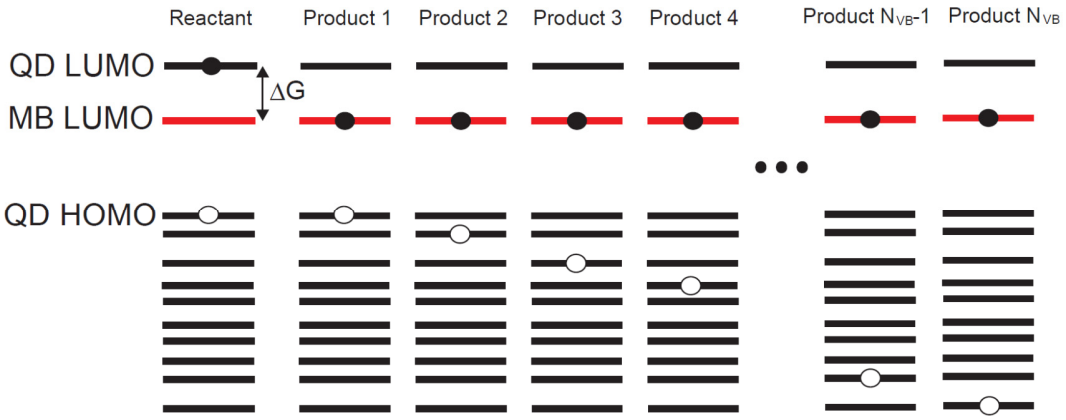

**Figure A.3.6.** Adiabatic exciton basis used in the TDDFT/NAMD simulation. The QD HOMO-LUMO exciton is the reactant state. The product states contain the electron in the MD LUMO and the hole in one of the VB orbitals of the QD.

The time-domain *ab initio* simulations are performed by combining real-time time-dependent density functional theory (TDDFT) with non-adiabatic (NA) molecular dynamics (MD). The atomic vibrational motions are treated using classical mechanics. The evolution of the electronic degrees of freedom is represented by TDDFT, which is formulated in the Kohn-Sham (KS) representation. The adiabatic KS orbitals depend on atomic coordinates, and transitions between adiabatic states occur due to the NA couplings, as explained below. The time-dependent single-electron KS orbitals, $\varphi_p(\boldsymbol{r},t)$, are evolved using the standard TDKS equations

$$i\hbar\frac{\partial\varphi_p(\boldsymbol{r},t)}{\partial t} = H\big(\varphi(\boldsymbol{r},t)\big)\varphi_p(\boldsymbol{r},t), \quad p = 1,\dots,N_\mathrm{e} \tag{S12}$$

where $N_\mathrm{e}$ is the number of electrons. The equations are coupled through the non-linear dependence of the Hamiltonian $H$ on the electron density, obtained by summing over all occupied KS orbitals, and other parameters of a chosen DFT functional, e.g. density gradient.

Expanding the time-dependent KS orbitals $\varphi_p(\boldsymbol{r},t)$ in the adiabatic KS orbital basis $\tilde{\varphi}_k(\boldsymbol{r};\boldsymbol{R})$,

$$\varphi_p(\boldsymbol{r},t) = \sum_{k=1}^{N_\mathrm{e}} c_{pk}(t)|\tilde{\varphi}_k(\boldsymbol{r};\boldsymbol{R})\rangle, \tag{S13}$$

transforms eq.(S5) into an equation for the expansion coefficients[67]

$$i\hbar \frac{\partial c_{pk}(t)}{\partial t} = \sum_{m=1}^{N_e} c_{pm}(t)(\varepsilon_m \delta_{km} - i\hbar \boldsymbol{d}_{km} \cdot \dot{\boldsymbol{R}}). \quad \text{(S14)}$$

The adiabatic KS orbitals, $\tilde{\varphi}_k(\boldsymbol{r};\boldsymbol{R})$, are obtained by solving the time-independent DFT equation for fixed atomic positions at each moment along the MD trajectory. The NA coupling,

$$\boldsymbol{d}_{km} \cdot \dot{\boldsymbol{R}} = \langle \tilde{\varphi}_k(\boldsymbol{r};\boldsymbol{R}) | \boldsymbol{\nabla}_{\boldsymbol{R}} | \tilde{\varphi}_m(\boldsymbol{r};\boldsymbol{R}) \rangle \cdot \dot{\boldsymbol{R}} = \left\langle \tilde{\varphi}_k(\boldsymbol{r};\boldsymbol{R}) \middle| \frac{\boldsymbol{\partial}}{\boldsymbol{\partial t}} \middle| \tilde{\varphi}_m(\boldsymbol{r};\boldsymbol{R}) \right\rangle, \quad \text{(S15)}$$

stems from the dependence of the adiabatic KS orbitals on the phonon dynamics, $\boldsymbol{R}(t)$, and represents electron-phonon interactions. Since the NA coupling is proportional to the nuclear velocity, $\dot{\boldsymbol{R}}$, NA transitions would never happen under the Born-Oppenheimer approximation with stationary atoms.

The exciton, two-particle, electron-hole representation of the above equations is obtained using the second quantization formulism. Starting from the ground state, $\left|\phi_g(\boldsymbol{r};\boldsymbol{R})\right\rangle$, single exciton (SE) states, $\left|\phi_{SE}^{i,j}(\boldsymbol{r};\boldsymbol{R})\right\rangle$, are defined as

$$\left|\phi_{SE}^{i,j}\right\rangle = \hat{a}_i^\dagger \hat{a}_j \ \left|\phi_g\right\rangle \quad \text{(S16)}$$

where the electron creation and annihilation operators, $\hat{a}_i^\dagger$ and $\hat{a}_j$ , generate and annihilate an electron in the *i*th and *j*th adiabatic KS orbitals, respectively. The total wave function is then expanded as

$$|\Psi(t)\rangle = C_g(t) \left|\phi_g\right\rangle + \sum_{i,j} C_{SE}^{i,j}(t) \left|\phi_{SE}^{i,j}\right\rangle. \quad \text{(S17)}$$

Similarly to eq.(S7), substitution of eq.(S10) into the TDKS equations leads to the equations of motion for the expansion coefficients appearing in eq.(S10):

$$i\hbar\frac{\partial C_X(t)}{\partial t} = C_X(t)E_X - i\hbar C_{\mathrm{g}}(t)\boldsymbol{d}_{X;\mathrm{g}}\cdot\dot{\mathbf{R}} - i\hbar\sum_{i',j'} C_{\mathrm{SE}}^{i',j'}(t)\boldsymbol{d}_{X;\mathrm{SE},i',j'}\cdot\dot{\boldsymbol{R}}. \qquad \text{(S18)}$$

Now, $X$ corresponds to either the ground state or a SE, $E_X$ is the excitation energy relative to the ground state, and the NA coupling is expressed by

$$\boldsymbol{d}_{X;Y}\cdot\dot{\boldsymbol{R}} = \langle\phi_X|\boldsymbol{\nabla_R}|\phi_Y\rangle\cdot\dot{\boldsymbol{R}} = \left\langle\phi_X\left|\frac{\partial}{\partial t}\right|\phi_Y\right\rangle. \qquad \text{(S19)}$$

The atomistic simulation of the Auger-assisted ET dynamics is performed by directly solving eq.(S20) with the time-dependent NA couplings and energies obtained from the *ab initio* MD simulation. The initial SE state is created with the electron in the QD LUMO and the hole in the QD HOMO. NA transitions lead to ET and are accompanied by electron-vibrational energy exchange.

The electronic structure and adiabatic MD are obtained within the VASP software package, using the PW91 density functional and projector-augmented-wave pseudopotentials. The geometry of the QD/MB complex is fully optimized at zero temperature. Then, the complex is heated up to an ambient temperature by repeated velocity rescaling, and a 10 ps microcanonical trajectory is calculated in the ground electronic state using the Verlet algorithm with a 1 fs time-step. 51 initial conditions are sampled from this trajectory to initiate the TDDFT/NAMD simulation. The TDKS equations are solved with a 1 as time-step. The adiabatic KS orbitals and the NA coupling are updated every MD time-step. The obtained results are presented in Figure 3.7.

# Chapter 4. Charge Separation and Recombination from CdSe/ZnS Type I Core/Shell Quantum Dots of Different Shell Thicknesses: the Study of Electronic Coupling



## 4.1. Introduction

Quantum dots (QDs) have been widely explored in bioimaging,[1,2] lasing,[3] light emitting diodes,[4,5] and solar cells[6-9] because of their size dependence properties, flexible solution processing and higher photostability compared to traditional organic dyes.[10,11] Interests in their application in solar cells have intensified in recent years, [6,9,12-20] in part because of reports of the highly controversial multi-exciton generation process in these materials.[3,21-32] However, as a light harvesting component in photovoltaic devices, the stability of core only QDs remains an issue due to photoinduced oxidation.[17,18,33] It has been reported that overcoating a wide band gap shell (such as ZnS) on bare CdSe QDs to form type I core/shell structures can greatly enhance their photostability[18] and efficiency[13-16] in QD-sensitized solar cells. The ZnS shell is thought to passivate the trap sites on the surface of core materials, increasing their fluorescence quantum yields.[34,35]

Furthermore, it insulates the holes in the core materials, preventing their photooxidation and improving their photostability.[19,34,36] However, how the ZnS shell affects the efficiency of solar cells remains poorly understood.

In solar cells based on QD sensitized oxide nanostructures, the incident-photon-to-current conversion efficiency depends on the efficiencies of many processes, including light harvesting, charge separation, recombination, and carrier collection.[37] The presence of the ZnS shell on the CdSe core is expected to slow down the rate of charge separation and recombination across the oxide/QD interface as well as to retard the regeneration rate of the neutral QD (from the oxidized form) by the redox mediators in the electrolyte. However, a quantitative measurement and understanding of the effects of the shell on these processes has not been achieved so far. Such quantitative understanding not only is needed for a rational optimization of the solar cell performance by controlling the shell materials and thickness, but also provides an opportunity to test the theoretical models for describing charge transfer processes from and to QDs.

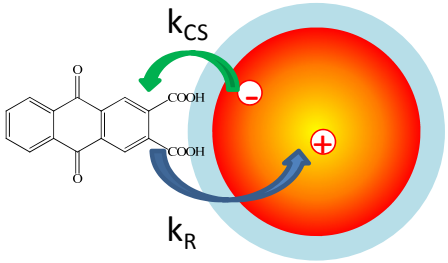


**Figure 4.1.** Photoinduced charge separation ($k_{CS}$) and recombination ($k_R$) processes in CdSe/ZnS core/shell QD – Anthraquinone complexes.

In this chapter we report a study of the effect of the ZnS shell thickness on the charge separation and recombination dynamics between CdSe/ZnS type I core/shell QDs and adsorbed electron acceptors, anthraquinone-2,3-dicarboxylic acid (AQ, see Figure 1). As will be discussed later, the estimated reduction and oxidation potentials of the QDs in the 1S exciton state are -0.87 and + 1.7 V (*vs* NHE), respectively. The reduction (oxidation) potential of AQ is -0.71 V (> +1.9 V) (*vs* NHE).[38,39] In this system, excitons in QDs cannot be quenched by energy transfer or hole transfer to the adsorbate. Optical excitation of QDs is expected to lead to electron transfer (ET, with rate constant $k_{CS}$) to AQ and the charge separated state recombines (with rate constant $k_R$) to regenerate the QD and AQ ground state, as shown in equation (1):[40,41]

$$QD^*[1S(e), 1S(h)] - AQ \rightarrow QD^+[h] - AQ^- \rightarrow QD - AQ \qquad (4.1)$$

Here QD*[1S(e),1S(h)] is the excited QD in its 1S exciton state, $QD^+[h]$ is the oxidized QD with a hole in the valence band, and $AQ^-$ is the reduced adsorbate. We measure the rates of charge separation and recombination as a function of the shell thickness by transient absorption spectroscopy. We show that these rates decrease exponentially with the ZnS shell thickness (d):

$$k(d) = k_0 e^{-\beta d} \qquad (4.2)$$

where $k_0$ is the charge separation or recombination rate for bare QDs. However, the decay constants β for charge separation (0.35 ± 0.03 per Å) is significantly smaller than that for charge recombination (0.91 ± 0.14 per Å). We show that the observed dependence can be

attributed to the decrease of the QD surface electron and hole density with the shell thickness.

## 4.2. Results and Discussion

### 4.2.1. Characterization of QDs and QD-AQ Complexes

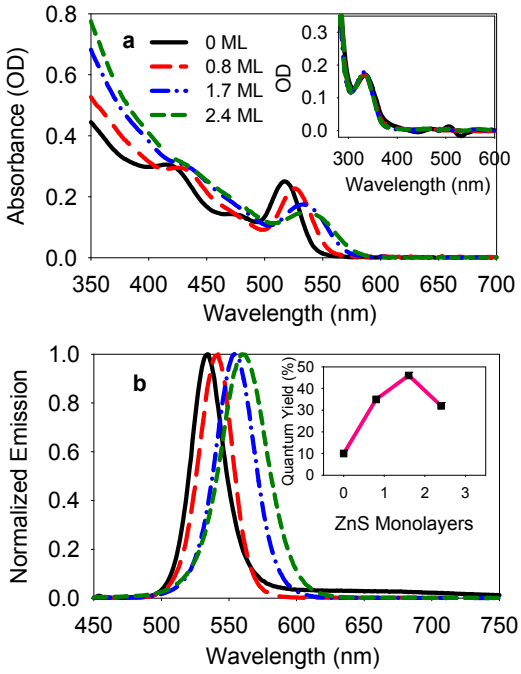


**Figure 4.2.** (a) UV-Vis absorption and b) normalized PL spectra of CdSe/ZnS QDs with 0 (black, solid), 0.8 (red, long-dash), 1.7 (blue, dash-dot) and 2.4 (green short-dash) MLs of ZnS in heptane solution. The integrated areas of the first exciton band are the same in these samples, indicating the same QD concentration. Inset in (a): Difference spectra

between free QDs and QD-AQ samples of 0 – 2.4 MLs of ZnS, showing similar amount of AQs in these samples. Inset in (b): The PL quantum yield as a function of the ZnS shell thickness.

Figure 4.2 (a) and (b) show the UV-vis absorption and photoluminescence (PL) spectra of QDs with the same CdSe core and 0, 0.8, 1.7 and 2.4 MLs of ZnS shell. With increasing shell thicknesses, both the absorption and emission of the 1S exciton band are red-shifted due to the increased leakage of exciton wave function into the ZnS shell.[35] As shown in Figure 1b inset, the ZnS coating suppresses the deep trap emission of CdSe core and increases the quantum yield from 10% in CdSe core to more than 30% in CdSe/ZnS (1.7 MLs) by passivating surface defects.[34,35] A further increase of the ZnS shell thickness leads to a reduction of the PL quantum yield, which can be attributed to an increase in the lattice-mismatch-induced defects.[35]

It was previously shown that the ET rate from QDs to adsorbed electron acceptors increases with the number of acceptors.[42] To quantify the influence of the ZnS shell thickness on the ET rate, it is essential to keep the same QD-to-AQ ratios for samples of different shell thicknesses. As shown in Figure 4.2, the four QD samples use in this study have the same integrated areas of the first exciton absorption band, indicating the same QD concentrations if the oscillator strength of the 1S exciton transition can be assumed to be independent of the shell thickness in QDs of the same core size. The concentration of AQs in these samples can be determined from the UV-vis absorption spectra of AQ, which were obtained by subtracting the absorption of free QDs from that of QD-AQ

complexes. As shown in Figure 4.2a inset, these spectra show similar AQ absorptions for the band at ~ 330 nm, indicating similar QD-to-AQ ratios in these samples. Based on the measured absorbance and published extinction coefficient of AQ ($\varepsilon_{330}$=4405 $cm^{-1}/M$)[43] and CdSe ($\varepsilon_{517}$=164456 $cm^{-1}/M$)[44], the average number of adsorbed AQ molecules per QD for these samples was estimated to be 3.5.

### 4.2.2. Exciton Dynamics in Free QDs

The femtosecond (0 - 1 ns) and nanosecond (1 ns – 6 μs) transient absorption spectra of free QDs with different shell thickness are shown in Figure 4.3 (0.8 ML) and Figure A.4.1 (0, 1.7 and 2.4 MLs). These spectra were obtained with low (14 nJ/pulse) 400 nm excitation to ensure that the average number of excitons per QD is much less than 1. The spectra show long-lived bleach of exciton bands with half-life of about 20 ns. TA signals in excited QDs can be attributed to two processes: state filling (SF) and carrier induced stark effect (SE).[45,46] Due to the Pauli exclusion principle, the occupancy of a photo-excited electron in the lowest electron, lS(e), level reduces the transitions to this level by half, thus leading to the bleach of exciton bands in the transient difference spectra.[45] In addition to the SF features, electron-hole pairs can generate a local dc electrical field which shifts the excitonic bands to longer wavelength due to dc Stark effect, and leads to derivative like features in the difference spectra.[47,48] The amplitude of the shift has been predicted to depend on the nature of the trapped carriers and the size of the QDs.[48] As shown in Figure 4.3 and A4.1, the amplitude of the SF bleach signal is

much larger than SE signal in free QDs. Therefore the 1S exciton bleach recovery time provides a direct probe of the lifetime of 1S electrons in free QDs.[45,49] For all QDs with different shells, the bleach recovers by <15 % within 1 ns. It confirms that under our experimental conditions most excited QDs have 1 exciton and the effect of exciton-exciton annihilation, which occurs on the 10s to 100s ps time scale, can be neglected.[50,51] For these QDs, excitation at 400 nm promotes an electron above the 1P(e) level, which relaxes to the 1S(e) level to give rise to the bleach in the 1S exciton transition. A fit of the 1S bleach formation kinetics reveals a rise time of ~330 fs, consistent with reported 1P - 1S electron cooling time in related QDs.[45,52,53]

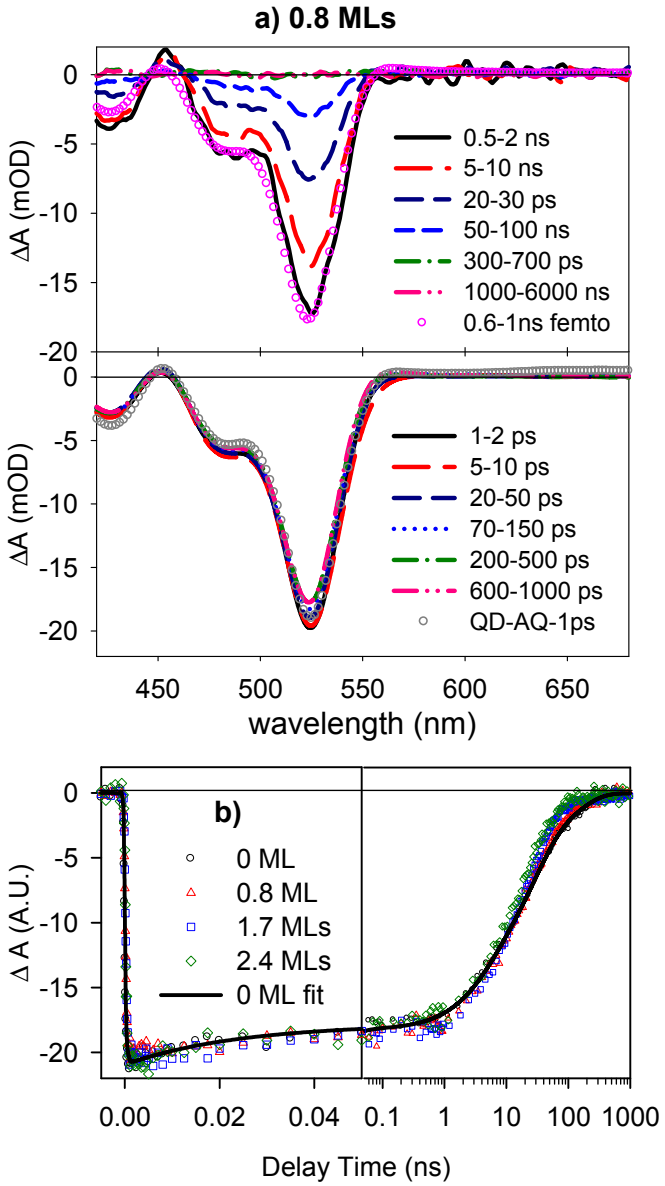


**Figure 4.3.** a) Average visible TA spectra of free CdSe/ZnS(0.8ML) QDs at indicated delay time windows after 400 nm excitation. Upper panel: 0.5 ns -6 μs, lower panel: 1 ps – 1 ns. The TA spectrum at 0.6-1 ns (open red circles) from the lower panel has been reproduced in the upper panel to show the good agreement between the spectra recorded using femtosecond and nanosecond TA spectrometers. Also shown in the lower panel is

the average TA spectrum of QD-AQ complexes at ~ 1ps (black open circles), which agrees well with that of free QDs. B) comparison of 1S exciton bleach recovery kinetics in CdSe QDs with 0, 0.8, 1.7 and 2.4 MLs of ZnS shells. The solid line is a fit to the bleach recovery of the CdSe core only QDs. The horizontal axis is in the linear scale in the left panel (0-50 ps) and in the logarithmic scale in the right panel (50 ps - 1 ns).

### 4.2.3. Charge Transfer Dynamics in QD-AQ Complexes

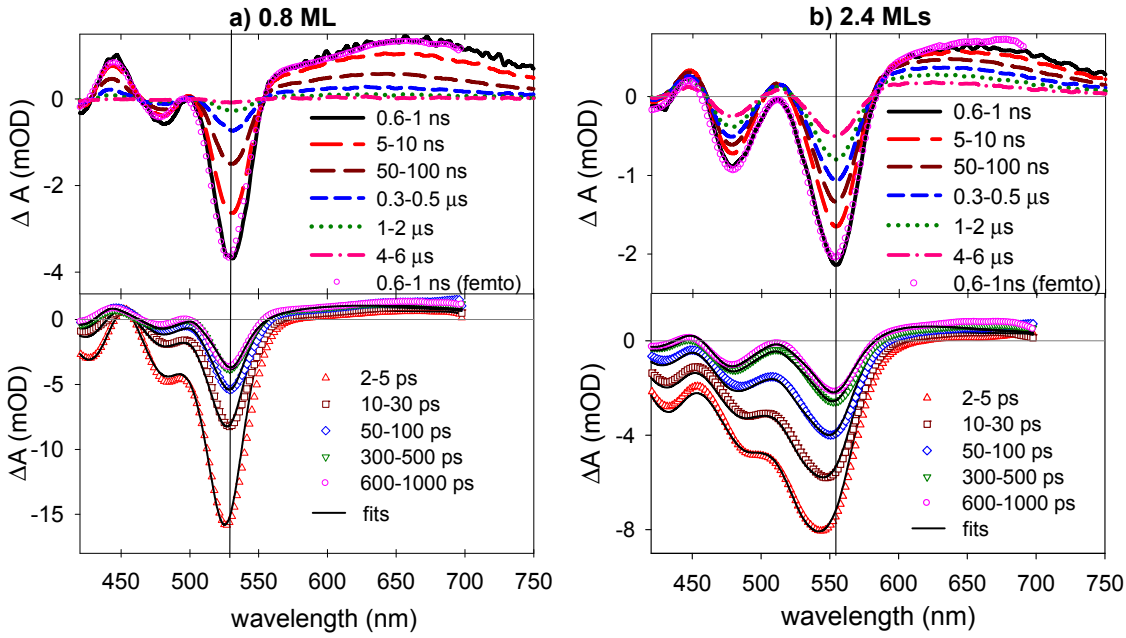


**Figure 4.4.** Average visible TA spectra of QD-AQ with (a) 0.8 ML ZnS (b) 2.4 MLs of ZnS at indicated delay time windows (0 - 1 ns: lower panels; 0.5 ns - 6 µs: upper panels) after 400 nm excitation. The vertical scale in the upper panels has been expanded to more clearly show the anion features. Solid lines in the lower panel are fits to the data (symbols)

according to equation (3) in the text. The TA spectrum at 600-1000 ps (circles) from the lower panel has been reproduced in the upper panel to show the good agreement between the spectra recorded using femtosecond and nanosecond TA spectrometers.

Visible TA spectra of QD-AQ samples with different shell thicknesses are shown in Figure 4.4 (0.8 and 2.4 MLs) and Figure A.4.2 (0 and 1.7 MLs). Femtosecond TA spectra (0.1 ps to 1 ns, lower panel) were acquired under the same conditions as those for free QDs to ensure negligible multi-exciton decay in the bleach kinetics. The nanosecond TA spectra (from 0.5 ns to 6 μs) were also recorded under similar excitation power density as the femtosecond measurement. In addition to amplitude changes, the TA spectra of QD-AQ complexes show noticeable changes of spectral shapes and clear red-shifts of the peak of the bleach band with increasing delay times between 1 ps and 1 ns. The red-shift becomes more pronounced with increasing shell thicknesses. At delay time < 1 ps, the TA spectra are dominated by the bleach signals arising from state-filling. These spectral features (designated as $A_{QD^*}(\lambda)$) are identical to those in free QDs and their spectral shape is time-independent, as shown in Figure 4.4 and A.4.2. Therefore its amplitude, $N_{QD^*}(t)$, reflects the population of excited QDs. At longer delay time (> 1 ns) the transient spectra shows derivative-like features caused by stark effect induced shift of exciton bands,[49] and a broad absorption band centered around 650 nm. This absorption band can be more clearly seen in the nanosecond TA spectra (upper panels of Figure 4.4), in which the probe wavelength is extended to 750 nm. This feature can be assigned to the one-electron reduced AQ radical, which has been reported to show an absorption band in

the region ≥ 600 nm.[41,56] Furthermore, the amplitude of the exciton bleach at 1 ns is much smaller than its initial value at ~ 1ps, suggesting the decrease of the 1S electron population. All these features suggest the transfer of electrons from the excited QDs to the AQ molecules (to form $AQ^-$) between 1ps and 1ns, as described by the first step in equation (4.1). From 1 ns to 6 μs, the shape of the transient spectra remains unchanged, as indicated by clear isosbestic points shown in Figure 4.4. These spectra, denoted as $A_{CS}(\lambda)$, can be attributed to the charge separated state ($QD^+$-$AQ^-$). The decease of the amplitude, $N_{CS}(t)$, of this spectral signature from 1 ns to 6 μs can be attributed to the charge recombination process, i.e. back ET from $AQ^-$ to the oxidized QD, to regenerate the AQ and QD in their ground states, as described by the second step in equation (4.1).

In the intermediate delay times between ~ 1 ps and ~ 1ns, the transfer of electrons from the 1S(e) level to the adsorbed AQ reduces the population of excited QDs and increases the population of the charge separated state, leading to the time-dependent red-shift of the observed TA spectra. Because of the overlap of the signals of the QD excited state and charge separated state in the exciton bleach region, these contributions have to be separated to obtain the QD excited state decay kinetics. To do so, we fit the transient spectra ($S(\lambda,t)$) in Figure 4.4 by the sum of the TA spectra of the excited QDs and charge-separated state according to equation 4.3:

$$S(\lambda, t) = N_{QD*}(t)A_{QD*}(\lambda) + N_{CS}(t)A_{CS}(\lambda) \qquad (4.3)$$

$N_{CS}(t)$ and $N_{QD*}(t)$ are the only variable parameters used in the fit. The fitted averaged spectra at indicated delay time windows between ~ 1ps and 1 ns are shown in Figure 4.5. It is clear that the TA spectra can be well reproduced by the sum of the base spectra for

the excited QD and charge-separated state with time-dependent populations, supporting the spectral assignment discussed above. $N_{CS}(t)$ is set to zero at $t < 1$ ps, and is assumed to be proportional to the amplitude of the transient spectra at $t > 1$ns. The value of $N_{QD^*}(t)$ is set to be proportional to the 1S exciton bleach amplitude before 1ps.

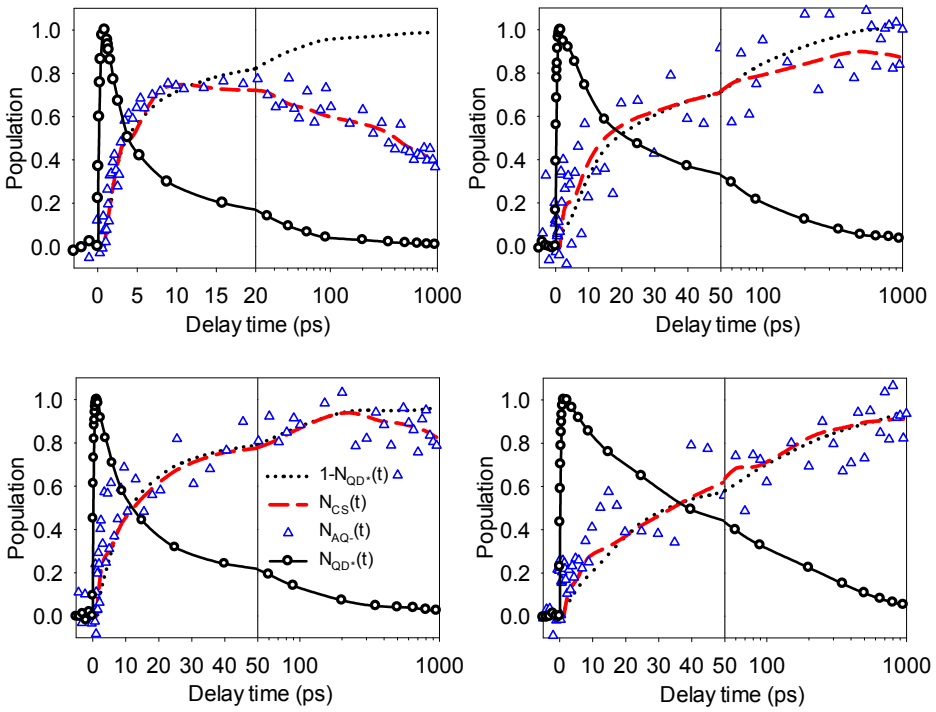


**Figure 4.5.** Comparison of the kinetics of QD excited state ($N_{QD^*}(t)$, open black circles), charge separated state ($N_{CS}(t)$, red lines) and anion ($N_{AQ^-}(t)$, open blue triangles) of QD-AQ complexes with 0.8 MLs of ZnS shells. $N_{QD^*}(t)$ and $N_{CS}(t)$ are obtained from fitting the transient data according equation (4.3). $N_{AQ^-}(t)$ is the TA signal at 640-660 nm. Also shown as the dotted lines is (1- $N_{QD^*}(t)$). Both $N_{CS}(t)$ and $N_{AQ^-}(t)$ have been scaled such that their formation kinetics agree with (1- $N_{QD^*}(t)$).

### 4.2.4. Shell Thickness Dependent Charge Separation and Recombination Kinetics

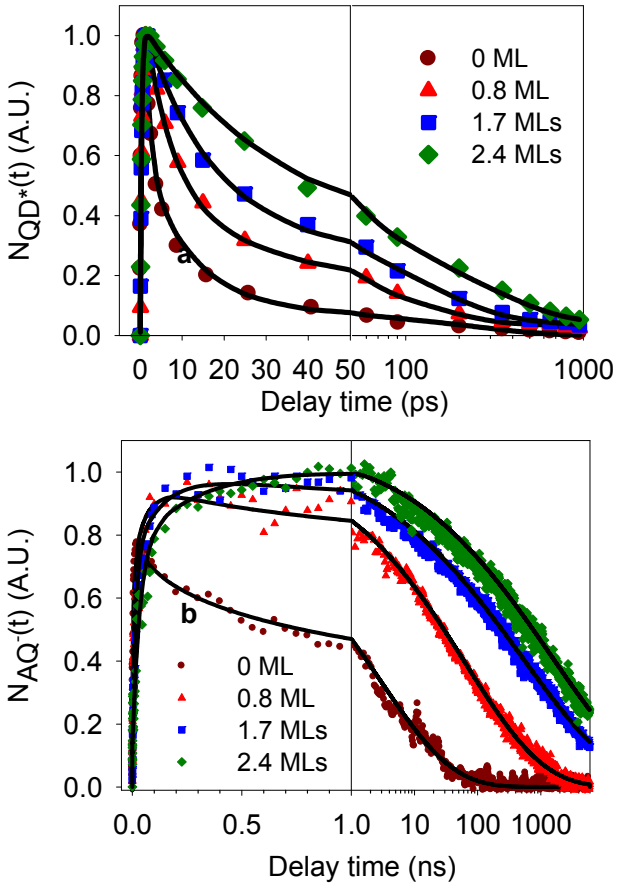


**Figure 4.6.** Comparison of QD excited state (a) and anion (b) population kinetics in QD-AQ samples of different ZnS shell thickness. The rates of charge separation and recombination, which are determined from the decay of excited state and anion populations, respectively, decrease with increasing shell thickness. Black lines are fits of the charge separation and recombination kinetics according to equation (4) and (5), respectively. The delay time in (a) is in linear scale from 0-50 ps (left) and logarithmic

scale from 10- 1000 ps (right). The delay time in (b) is in linear scale from 0-1 ns (left) and logarithmic scale from 1- 6000 ns (right).

The kinetics of the excited QD population ($N_{QD^*}(t)$) and anion population ($N_{AQ^-}(t)$) for the QD-AQ complexes with different shell thicknesses are compared in Figure 4.6. It is clear that with the increasing ZnS shell thickness, both the QD excited state and anion decay become slower, suggesting the decrease of the rates of ET from QD to AQ and the charge recombination process.

The charge separation and recombination kinetics are not single-exponential. As shown in Figure 4.6 a, the kinetics of the QD excited state can be fit according to the following equation:

$$N_{QD^*}(t) = \sum_i A_i \, e^{-k_{CS,i}t} - e^{-k_0 t} \qquad (4.4)$$

Here, $1/k_0$ (~ 330 fs) is the formation time of the 1S exciton bleach. This rise-time reflects the cooling of the conduction band electrons to the 1S(e) level, similar to those in the free QDs. Satisfactory fits to the QD decay kinetics can be obtained using three-exponential functions with amplitudes and time constants of $A_i$ *and* $k_{CS,i}$, respectively. The fitting parameters are listed in Table 4.1.

**Table 4.1.** Fitting parameters for the QD* decay kinetics in QD-AQ complexes according to equation (4.4).

| ZnS thickness | $k_0$, $ps^{-1}$ | $k_{cs,1}$, $ps^{-1}$ (A1, %) | $k_{cs,2}$, $ps^{-1}$ (A2, %) | $k_{cs,3}$, $ps^{-1}$ (A3, %) | Half life (ps) |
|---|---|---|---|---|---|
| 0 ML | 2.97 | 0.71 (67) | 0.084 (32) | 0.01 (1) | 3.4 |
| 0.8 ML | | 0.15 (67) | 0.018 (32) | 0.002 (1) | 10.5 |
| 1.7 MLs | | 0.069 (67) | 0.0081 (32) | 0.001 (1) | 23.6 |
| 2.4 MLs | | 0.032 (67) | 0.0038 (32) | $4.5*10^{-4}$ (1) | 45 |

According to equation (1), the population of the charge separated state increases with the rate of charge separation process and decays with the rate of charge recombination. The anion kinetic traces can be fit to equation (4.5):

$$[N_{AQ^-}](t) = -\sum_i A_i\, e^{-k_{CS,i}t} + e^{-(t/\tau_R)^{\alpha}} \qquad (4.5)$$

The parameters for charge separation has been determined by fitting the decay of QD excited state as discussed above. The decay of the charge separated state can be best fit by stretched exponential functions, as shown in Figure 4.6b, although they can also be fit by tri-exponential functions. The characteristics times $\tau_R$ and exponents $\alpha$, of the best stretched exponential fits are listed in Table 4.2. The stretched exponential functions suggest a broad distribution of charge recombination rates, similar to those observed previously for QDs or dye sensitized $TiO_2$ nanoparticles.[57,58]

**Table 4.2.** Fitting parameters for the anion decay kinetics of QD-AQ samples according to equation (4.5).

| ZnS thickness | $\tau_R$*, $ns^{-1}$ | $\alpha$ | Half-life (ns) |
|---|---|---|---|

| | | | |
|---|---|---|---|
| 0 ML | 2.2 | 0.38 | 0.75 |
| 0.8 ML | 63 | 0.35 | 30 |
| 1.7 MLs | 523 | 0.30 | 230 |
| 2.4 MLs | 1788 | 0.31 | 800 |

Because of the highly non-exponential charge separation and recombination kinetics, we use the half life-time for the QD excited state and anion decay to represent the charge separation and recombination times. The charge separation (and recombination) half lifetimes are 3.4 ps (0.75 ns), 10.5 ps (30 ns), 23.6 ps (230 ns), and 45.0 ps (800 ns) for QDs with 0, 0.8, 1.7 and 2.4 MLs of shells, respectively. Plots of the logarithm of the charge separation and recombination rates (the inverse of their half life-times) as a function of shell thickness yield straight lines, as shown in Figure 4.7. It suggests that both the charge separation and recombination rates decay exponentially with the shell thickness. Fitting the thickness dependence to equation (4.2) yields a slope $\beta$ of 0.35 ± 0.03 per Å and 0.91 ± 0.14 per Å for charge separation and recombination rates, respectively.

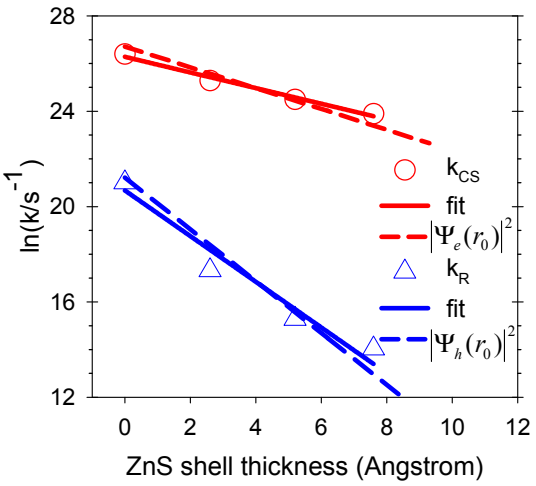


**Figure 4.7.** Plot of the logarithm of charge separation (red circles) and recombination (blue triangles) rates as a function of the ZnS shell thickness. These rates are determined from the half-lives of the QD excited state and anion decays, respectively. Best fits (red and blue solid lines) of the data according to equation (2) yield slopes (-β) of -0.35 (±0.03) and -0.91 (±0.14) per Angstrom for charge separation and recombination rates, respectively. Also shown are the calculated electron (red dashed line) and hole (blue dashed line) densities at the shell surface as a function of shell thickness. For better comparison, the electron (hole) densities for the bare QDs were normalized to the measured charge separation (recombination) rates.

The rate of nonadiabatic electron transfer processes is given by[59]

$$k_{ET}(d) = \frac{2\pi}{\hbar}\frac{|H(d)|^2}{\sqrt{4\pi\lambda k_B T}}\exp\left[-\frac{(\lambda + \Delta G(d))^2}{4\lambda k_B T}\right] \qquad (4.6)$$

where $\Delta G$ is the driving force, $H$ the electronic coupling strength, and $\lambda$ the total reorganization energy. The reorganization energy for ET from QDs can be assumed to be negligible because the delocalized 1S wave function. Thus the total reorganization energy is controlled by that of the molecule and should remain unchanged for QDs with different shell thickness. For the charge separation process, H depends on the overlap of the 1S electron wave function with the lowest unoccupied molecular orbital (LUMO) in AQ, and $\Delta G$ is given by the difference between the QD excited state oxidation potential ($V_{QD+/QD*}$) and the reduction potential of AQ. For the recombination process, H depends on the overlap of the LUMO of AQ with the hole wave function in the valence band of the QDs and $\Delta G$ is determined by the difference of the QD oxidation potential ($V_{QD+/QD}$) and the reduction potential of AQ. Both the driving force and the coupling strength can vary with the shell thickness.

To quantify the effect of ZnS shell thickness on the electron (hole) transfer rate, we calculate the eigen function and energy of the electrons and holes in CdSe/ZnS type I QDs by modeling them as particles confined in spherical wells of finite depth.[35,60] The effective masses of electrons (holes) are $m_e$*=0.13 ($m_h$*=0.45) in CdSe and 0.25 (1.3) in ZnS.[61] The conduction and valence band edge positions are -4.0 and -5.7 V in the CdSe core, -3.1 and -6.6 V in the ZnS shell, and 0 and -8.4 eV in the surrounding organic medium, as shown in Figure 7.[61,62] The Schrodinger equation of the system is solved numerically to obtain the wave function and energy of the lowest (1S) electron and hole levels.[35] The coulomb interaction between the electron and hole is treated as a first-order perturbation (the dielectric constants are $\varepsilon=10\varepsilon_0$ in CdSe and $8.9\varepsilon_0$ in ZnS), from which

the energy of the first exciton state can be calculated.[63] The reported conduction band edge position of bulk CdSe crystals varies considerably, ranging from -4.0 to -3.5 *vs* the vacuum level.[64] This uncertainty affects the calculated values of electron and hole energy levels. The values reported here (using a conduction band edge of -4.0 V) represent their lower limits. However, this uncertainty in absolute band edge position has negligible effect on the shell thickness dependence of the energy and wave function to be discussed below.

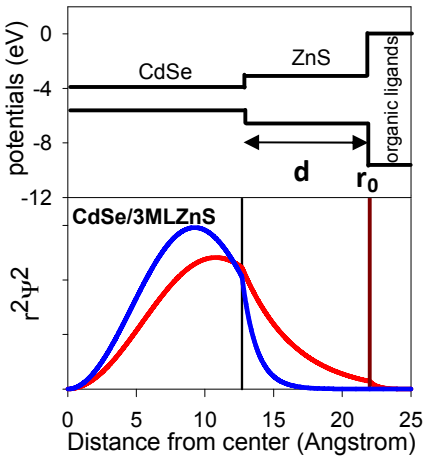


**Figure 4.8.** (top) Band alignments and (bottom) radial distribution functions for 1S electron and hole levels of CdSe/ZnS core/shell QD with a 13.7 Å CdSe core and 3 monolayers of ZnS shell (thickness d). $r_0$ indicates the outer surface of the shell. Potentials are relative to the vacuum energy level.

The calculations were performed for QDs with the same core and 0, 1, 2, and 3 monolayer(s) of ZnS shells. The core diameter was chosen to be 2.74 nm, the averaged diameter of CdSe core only QDs determined by TEM. The calculated first exciton peaks for these QDs and their shell thickness dependence are in reasonable agreement with the measured absorption spectra. For example, the calculated and measured first exciton peak positions in CdSe core only QDs are 513 and 517 nm, respectively. The calculated 1S exciton energy deceases by 100 meV from QDs with 0 to 3 MLs of ZnS shells. This value agrees well with the measured value of ~ 80 meV. From the energies of the 1S electron, hole and exciton, the redox potentials for QD 1S excited state oxidation ($V_{QD+/QD*}$), 1S excited state reduction ($V_{QD*/QD-}$) and ground state oxidation ($V_{QD+/QD}$ ) can be calculated.[10,65] The calculated values for ($V_{QD+/QD*}$, $V_{QD*/QD-}$, $V_{QD+/QD}$ ) are (-0.87, +1.73, +1.55) and (-0.86, +1.63, +1.46, V NHE) for QDs with 0 and 3 MLs of ZnS shells, respectively. Using a reduction potential of -0.70 V NHE for AQ and the calculated $V_{QD+/QD*}$, the driving force for charge separation process can be estimated to be > 0.17 V and changes negligibly with the shell thickness. The driving force for the charge recombination process is estimated to be 2.25 V and decreases by < 90 meV from core only QDs to those with 3 MLs of shells. It is clear that the energetic changes cannot account for the observed shell thickness dependent ET rates. It suggests that the shell thickness dependence is caused by the variation of the electronic coupling strength for ET.

Figure 4.8 shows the radial distribution functions of the 1S electron and hole in QDs with 3 MLs of ZnS shells. Both the electron and hole wave functions spread into the ZnS layer and their amplitudes decay exponentially with the shell thickness. The

electronic coupling strength for charge separation (recombination) should depend on the overlap integrals of the electron (hole) wave function with the LUMO of AQ. Because the AQ molecules likely bind on the outmost layer of the inorganic surface (CdSe surface in bare QDs and ZnS surface in core/shell QDs) by displacing the organic ligands or occupying uncoordinated sites, we assume that the coupling strength is proportional to the amplitude of the electron (hole) wave function $\Psi(r_0)$ at the QD/organic ligand interface. According to equation (4.6), the electron transfer rate should be proportional to the square of the coupling strength: $k_{ET} \propto |\Psi(r_0)|^2$. Under these assumptions, the relative electron (hole) density on QDs surface could be used to ascertain the relative electron (hole) transfer rate. As shown in Figure 4.8, the electron (hole) density has been scaled such that the values on the bare CdSe QDs (without shell) match their charge separation (recombination) rate. The calculated surface electron and hole densities decay exponentially with ZnS layer thickness with exponential decay factors of 0.43 $Å^{-1}$ for the electron and 1.09 $Å^{-1}$ for the hole, which are in reasonable agreement with the measured thickness dependence of ET charge separation and recombination rates. This agreement confirms that in CdSe/ZnS type I QDs, the ZnS shell serves as a tunneling barrier for the electron and hole transfer and slows down their rates by decreasing the electronic coupling with the adsorbate. Similar exponential dependence of ET rate with the thickness of insulating spacer has been extensively studied in molecular systems and in dye-sensitized oxide nanoparticles.[66-69]

It is interesting to note that with increasing shell thicknesses, the charge recombination rate decays much faster than charge separation rate. With 2.4 MLs of ZnS

shells, the measured charge separation rate decreases by a factor of 15, whereas the recombination rate is reduced by a factor of 1000. According to the model calculation described above, this difference can be attributed to the larger effective mass of the hole than the electron in the ZnS shell. Considering the fast charge separation rate (~3.4 ps) in CdSe-AQ complexes and the long intrinsic exciton lifetimes of these QDs (~ 20 ns), it is possible to maintain high charge separation yield while greatly prolong the lifetime of the charge separated state by increasing the shell thickness. In fact, for QD-AQ, both the peak population and the lifetime of the charge separated state increases with the shell thickness because of the retardation of the charge recombination process (see Figure 4 and S4). The highest percentage of charge separated state population (near unity at its peak) and the longest charge separation lifetime (half life of ~ 0.8 μs) was achieved with the largest shell thickness (2.4 MLs of ZnS) examined in this study. Thus, by tuning the shell thickness and changing the shell materials in type I QDs, it is possible to design more efficient and stable QD based photovoltaic devices.

## 4.3. Conclusion

In summary, we have investigated how the shell thickness affects the charge separation and recombination dynamics of CdSe/ZnS type I core/shell QDs. We have demonstrated that the excitons in the QDs can be dissociated by electron transfer to the adsorbed AQ, which is followed by charge recombination on a much slower time scale.

For core only CdSe QDs, the half lifetimes for charge separation and recombination are 3.4 ps and 0.75 ns, respectively. With the increasing shell thickness, both the charge separation and recombination rates decrease exponentially with exponential factors of 0.35±0.03 per Å and 0.91±0.14 per Å, respectively. Model calculations of these core/shell QDs show that the trends in charge separation and recombination rates agree well with the exponential decreases of the electron and hole densities at the QD surface with the shell thickness. The faster exponential decay of recombination rate with the shell thickness can be attributed to the steeper decrease of the surface hole density, which is caused by the larger hole effective mass (than electron) in the ZnS shell. The results of this study suggest possible ways of optimizing the charge separation yield and lifetime by controlling the thickness and nature of the shell materials, achieving more efficient and stable QD based solar cells.

## References

(1) Chan, W. C. W.; Nie, S. *Science* **1998**, ***281***, 2016.

(2) Bruchez, M.; Moronne, M.; Gin, P.; Weiss, S.; Alivisatos, A. P. *Science* **1998**, *281*, 2013.

(3) Klimov, V. I. *Journal of Physical Chemistry B* **2006**, *110*, 16827.

(4) Colvin, V. L.; Schlamp, M. C.; Alivisatos, A. P. *Nature* **1994**, *370*, 354.

(5) Steckel, J. S.; Snee, P.; Coe-Sullivan, S.; Zimmer, J. P.; Halpert, J. E.; Anikeeva, P.; Kim, L.-A.; Bulovic, V.; Bawendi, M. G. *Angew. Chem., Int. Ed.* **2006**, *45*, 5796.

(6) Kamat, P. V. *Journal of Physical Chemistry C* **2008**, *112*, 18737.

(7) Huynh, W. U.; Dittmer, J. J.; Alivisatos, A. P. *Science* **2002**, *295*, 2425.

(8) Gur, I.; Fromer Neil, A.; Geier Michael, L.; Alivisatos, A. P. *Science* **2005**, *310*, 462.

(9) Sargent, E. H. *Nature Photonics* **2009**, *3*, 325.

(10) Brus, L. E. *J. Chem. Phys.* **1984**, *80*, 4403.

(11) Alivisatos, A. P. *Science* **1996**, *271*, 933.

(12) Robel, I.; Subramanian, V.; Kuno, M.; Kamat, P. V. *J. Am. Chem. Soc.* **2006**, *128*, 2385.

(13) Shen, Q.; Kobayashi, J.; Diguna, L. J.; Toyoda, T. *J. Appl. Phys.* **2008**, *103*.

(14) Mora-Seró, I. n.; Giménez, S.; Fabregat-Santiago, F.; Gómez, R.; Shen, Q.; Toyoda, T.; Bisquert, J. *Acc. Chem. Res.* **2009**, *42*, 1848.

(15) Diguna, L. J.; Shen, Q.; Kobayashi, J.; Toyoda, T. *Appl. Phys. Lett.* **2007**, *91*, 023116.

(16) Barea, E. M.; Shalom, M.; Giménez, S.; Hod, I.; Mora-Seró, I. n.; Zaban, A.; Bisquert, J. *J. Am. Chem. Soc.* **2010**, *132*, 6834.

(17) Peng, X. G.; Schlamp, M. C.; Kadavanich, A. V.; Alivisatos, A. P. *J. Am. Chem. Soc.* **1997**, *119*, 7019.

(18) Sambur, J. B.; Parkinson, B. A. *J Am Chem Soc* **2010**, *132*, 2130.

(19) Xie, R.; Kolb, U.; Li, J.; Basche, T.; Mews, A. *J. Am. Chem. Soc.* **2005**, *127*, 7480.

(20) Tachibana, Y.; Akiyama, H. Y.; Ohtsuka, Y.; Torimoto, T.; Kuwabata, S. *Chem. Lett.* **2007**, *36*, 88.

(21) Nozik, A. J. *Physica E* **2002**, *14*, 115.

(22) Klimov, V. I. *Appl. Phys. Lett.* **2006**, *89*, 123118/1.

(23) Schaller, R. D.; Klimov, V. I. *Phys. Rev. Lett.* **2004**, *92*, 186601.

(24) Ellingson, R. J.; Beard, M. C.; Johnson, J. C.; Yu, P.; Micic, O. I.; Nozik, A. J.; Shabaev, A.; Efros, A. L. *Nano Lett.* **2005**, *5*, 865.

(25) Luther, J. M.; Beard, M. C.; Song, Q.; Law, M.; Ellingson, R. J.; Nozik, A. J. *Nano Lett.* **2007**, *7*, 1779.

(26) Schaller, R. D.; Sykora, M.; Pietryga, J. M.; Klimov, V. I. *Nano Lett.* **2006**, *6*, 424.

(27) Trinh, M. T.; Houtepen, A. J.; Schins, J. M.; Hanrath, T.; Piris, J.; Knulst, W.; Goossens, A. P. L. M.; Siebbeles, L. D. A. *Nano Lett.* **2008**, *8*, 1713.

(28) Nair, G.; Bawendi, M. G. *Phys. Rev. Lett.* **2007**, *76*, 081304.

(29) Pijpers, J. J. H.; Hendry, E.; Milder, M. T. W.; Fanciulli, R.; Savolainen, J.; Herek, J. L.; Vanmaekelbergh, D.; Ruhman, S.; Mocatta, D.; Oron, D.; Aharoni, A.; Banin, U.; Bonn, M. *J. Phys. Chem. C* **2007**, *111*, 4146.

(30) Ben-Lulu, M.; Mocatta, D.; Bonn, M.; Banin, U.; Ruhman, S. *Nano Lett.* **2008**, *8*, 1207.

(31) McGuire, J. A.; Joo, J.; Pietryga, J. M.; Schaller, R. D.; Klimov, V. I. *Acc. Chem. Res.* **2008**, *41*, 1810.

(32) Pijpers, J. J. H.; Ulbricht, R.; Tielrooij, K. J.; Osherov, A.; Golan, Y.; Delerue, C.; Allan, G.; Monn, M. *Nat. Phys.* **2009**, *5*, 811.

(33) Spanhel, L.; Haase, M.; Weller, H.; Henglein, A. *J. Am. Chem. Soc.* **1987**, *109*, 5649.

(34) Hines, M. A.; Guyot-Sionnest, P. *J. Phys. Chem.* **1996**, *100*, 468.

(35) Dabbousi, B. O.; RodriguezViejo, J.; Mikulec, F. V.; Heine, J. R.; Mattoussi, H.; Ober, R.; Jensen, K. F.; Bawendi, M. G. *J. Phys. Chem. B* **1997**, *101*, 9463.

(36) Nazzal, A. Y.; Wang, X.; Qu, L.; Yu, W.; Wang, Y.; Peng, X.; Xiao, M. *J. Phys. Chem. B* **2004**, *108*, 5507.

(37) Hagfeldt, A.; Gratzel, M. *Chem. Rev.* **1995**, *95*, 49.

(38) Cao, Y.; Rabinowitz, D. J.; Dixon, D. W.; Netzel, T. L. *Synthetic Commun.* **2009**, *39*, 4230

(39) Maia, G.; Maschion, F.; Tanimoto, S.; Vaik, K.; Mäeorg, U.; Tammeveski, K. *J. Solid State Electr.* **2007**, *11*, 1411.

(40) Burda, C.; Link, S.; Mohamed, M.; El-Sayed, M. *J. Phys. Chem. B* **2001**, *105*, 12286.

(41) Burda, C.; Green, T. C.; Link, S.; El-Sayed, M. A. *J. Phys. Chem. B* **1999**, *103*, 1783.

(42) Boulesbaa, A.; Issac, A.; Stockwell, D.; Huang, Z.; Huang, J.; Guo, J.; Lian, T. *J. Am. Chem, Soc.* **2007**, *129*, 15132.

(43) Du, H.; Fuh, R. A.; Li, J.; Corkan, A.; Lindsey, J. S. *Photochem. Photobiol.* **1998**, *68*, 141.

(44) Jasieniak, J.; Smith, L.; Embden, J. v.; Mulvaney, P.; Califano, M. *J. Phys. Chem. C* **2009**, *113*, 19468.

(45) Klimov, V. I. *Annu. Rev. Phys. Chem.* **2007**, *58*, 635.

(46) Klimov, V. I.; McBranch, D. W. *Phys. Rev. B* **1997**, *55*, 13173.

(47) Norris, D. J.; Sacra, A.; Murray, C. B.; Bawendi, M. G. *Phys. Rev. Lett.* **1994**, *72*, 2612.

(48) Wang, Y.; Suna, A.; McHugh, J.; Hilinski, E. F.; Lucas, P. A.; Johnson, R. D. *J. Chem. Phys.* **1990**, *92*, 6927.

(49) Huang, J.; Stockwell, D.; Huang, Z.; Mohler, D. L.; Lian, T. *J. Am. Chem. Soc.* **2008**, *130*, 5632.

(50) Nozik, A. J. *Annu. Rev. Phys. Chem.* **2001**, *52*, 193.

(51) Klimov, V. I.; Mikhailovsky, A. A.; McBranch, D. W.; Leatherdale, C. A.; Bawendi, M. G. *Science* **2000**, *287*, 1011.

(52) Huang, J.; Huang, Z.; Yang, Y.; Zhu, H.; Lian, T. *J. Am. Chem. Soc.* **2010**, *132*, 4858.

(53) Cooney, R. R.; Sewall, S. L.; Dias, E. A.; Sagar, D. M.; Anderson, K. E. H.; Kambhampati, P. *Phys. Rev. B* **2007**, *75*, 245311/1.

# Appendix 1.

## Femtosecond TA spectra of free QDs

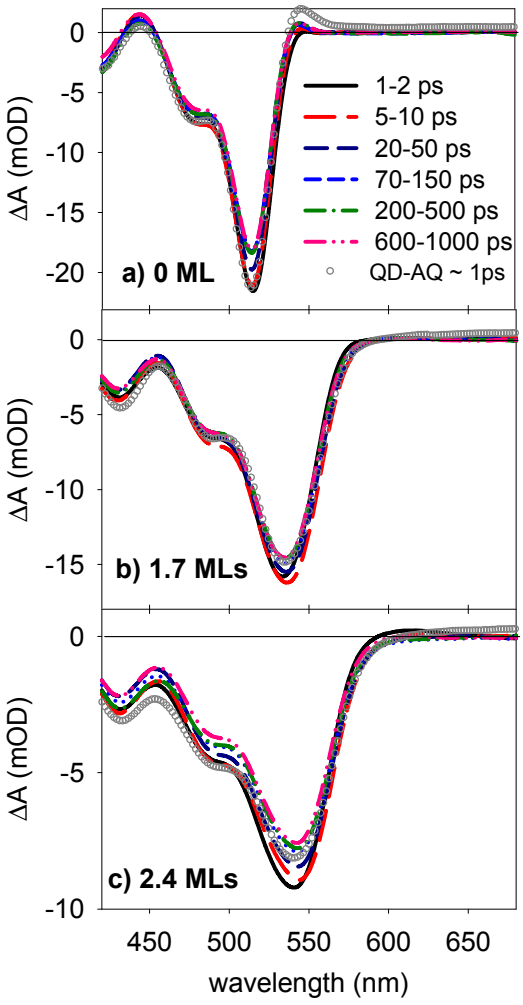


**Figure A.4.1.** Average visible TA spectra of free CdSe/ZnS QDs (lines) with (a) 0, (b) 1.7, and (c) 2.4 MLs of ZnS shells at indicated delay time windows after 400 nm

excitation. Also shown are TA spectra of correspond QD-AQ complexes at ~ 1ps (open circles).

# Appendix 2.

## Transient spectra of QD-AQ complexes

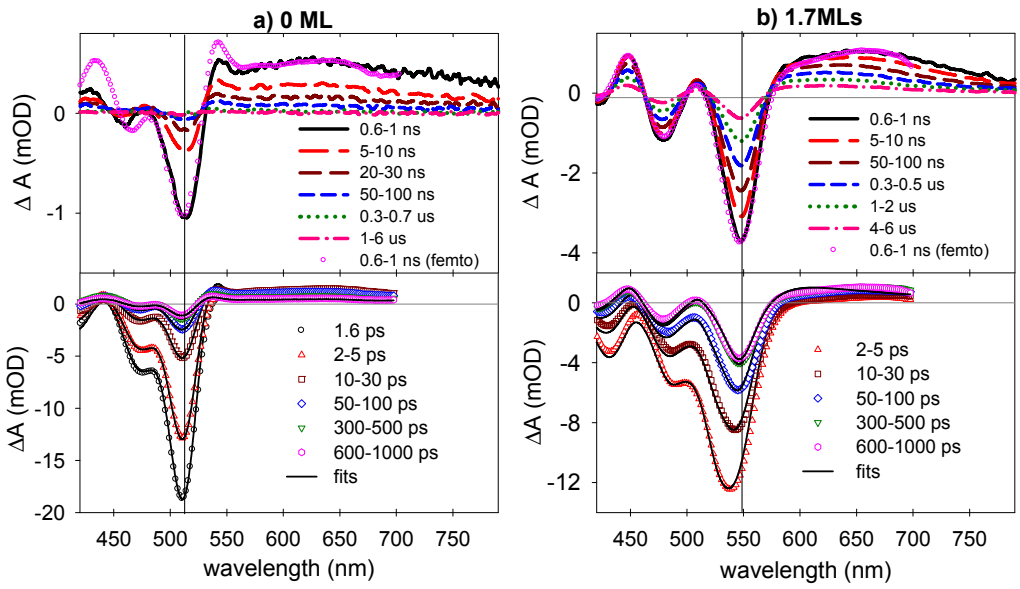


**Figure A.4.2.** Averaged visible TA spectra of QD-AQ complexes with (a) 0 ML and (b) 1.7 MLs of ZnS shells at indicated delay time windows (0 - 1 ns: lower panels, 0.5 ns - 6 μs: upper panels) after 400 nm excitation. The vertical scale in upper panels has been expanded to more clearly show the anion features. Solid lines in the lower panel are fits to the data (symbols) according to equation 4.3 in the text. The TA spectrum at 600-1000

ps (pink circles) from the lower panel has been reproduced in the upper panel to show the agreement between the TA spectra recorded using femtosecond and nanosecond spectrometers.

# Chapter 5. Charge Separation and Recombination from CdTe/CdSe Type II Core/Shell Quantum Dots: the Idea of Wavefunction Engineering



## 5.1. Introduction

The size dependent optical and electronic properties of semiconductor quantum dots (QDs)[1-5] have been explored in a wide range of applications from solar energy conversion[6-10] to biological imagining.[11-14] In recent years, the effect of quantum confinement on the excited state dynamics of QDs has also been extensively studied,[15-19] leading to the report of novel phenomena, such as long lived hot carriers[20] and muliexciton generation (MEG).[21-24] These findings have intensified interests in QDs as light harvesting materials because they may provide new approaches for improving the power conversion efficiency in QD-based photovoltaics.[25-29] The mechanism and efficiency of MEG has been a subject of intense recent debates, and the latest reports suggest that the MEG efficiencies in PbS and PbSe QDs are similar to those in bulk semiconductors at the same excitation wavelength.[21-24] In addition to the need to further

improve MEG efficiency for practical applications, efficient utilization of multiple excitons requires their extraction prior to annihilation by Auger recombination on the 10 - 100 ps time scale.[15,30] With regard to the latter requirement, QDs offer the potential advantage because of the ability to dissociate excitons on the picosecond and faster time scale by interfacial charge transfer to surface adsorbed acceptors.[27-29,31-35] Unlike in bulk semiconductors, ultrafast interfacial charge transfer in strongly quantum confined QDs can be expected because of the larger amplitude of exciton wave function at the surface the semiconductors, enhancing electronic coupling with adsorbed acceptors. Indeed, recent proof-of-principle experiments have demonstrated that up to three[28] and four[36] excitons per CdSe QDs (generated by multiple photon absorption) can be dissociated by ultrafast electron transfer (ET) to adsorbed electron acceptors. Furthermore, hot electron injection from PbSe QDs to $TiO_2$[29] and MEG enhanced incident photon-to-current conversion efficiency in PbS QD sensitized $TiO_2$ solar cells[27] have also been reported.

Despite these reports of hot electron transfer as well as ultrafast single and multiple exciton dissociation, the factors controlling the rate of charge transfer from and to quantum dots remain poorly understood. Furthermore, the effective utilization of excitons in QDs requires not only fast charge separation but also a long-lived interfacial charge separated state (or slow recombination) such that the separated charge carriers can be efficiently extracted to the external circuit in photovoltaic devices or used for photocatalysis. In a recent report, we show that in CdSe/ZnS core/shell QDs adsorbed with anthraquinone (as electron acceptors), both the rates of electron transfer from the QD to the acceptor and the subsequent recombination decrease with increasing shell

thickness.[37] However, because the charge separation rate decreases much slower with the shell thickness than the recombination rate, it is possible to increase the yield as well as lifetime of the charge separated state by optimizing the shell thickness, offering an approach for engineering core/shell structures for efficient charge transfer application. The CdSe/ZnS core/shell structure has a type I band alignment, as shown in Figure 5.1 upper panel, in which both the lowest energy electrons and holes are localized in the CdSe core. The ZnS shell acts as a tunneling barrier, slowing down both the electron transfer and recombination (or hole transfer) processes. As a result, these type I structures would not be ideal for extracting hot carriers or multiple excitons, which require ultrafast exciton dissociation rates (to compete with hot electron relaxation and exciton-exciton annihilation, respectively). [27-29,31-35]

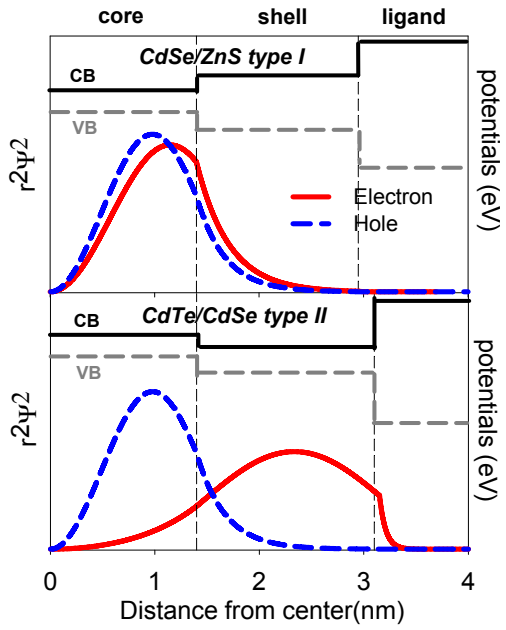


**Figure 5.1.** Radial distribution function of lowest energy (1S) conduction band electron (solid red lines) and valence band hole (dashed blue lines) levels of CdSe/ZnS type I

(upper panel) and CdTe/CdSe type II (lower panel) core/shell QDs. Both structures have a 1.4 nm core and 5 monolayers of shell. Vertical dashed lines indicate core/shell and shell/ligand interfaces. Also shown are relative bulk conduction band (CB, solid black lines) and valance band (VB, dashed grey lines) edge positions in these materials.

One possible way to simultaneously enable ultrafast charge separation and retard charge recombination is to use core-shell QDs with staggered type II band alignment, as shown in Figure 5.1 lower panel, in which the lowest energy conduction band electron and valence band hole wave functions can be preferentially localized largely in the shell and core, respectively. It has been shown that by selecting core/shell materials with appropriate band edge positions and tuning the degree of quantum confinement by core size and shell thickness, type II band alignment can be achieved and the spatial distributions of electron and hole wave functions can be tuned in core-shell QDs, such as CdTe/CdSe, CdSe/CdS, CdS/ZnSe.[38-48] The spatially separated electron and hole wave-functions also have beneficial effects on the absorption and excited state dynamics of these type II QDs. In addition to the absorption bands within the core and shell materials, the charge transfer transitions between the core and shell extend the absorption of the type II core/shell materials to longer wavelength, offering an additional approach to enhance the spectral response. The reduced electron hole overlap extends the single exciton lifetime,[45-48] reduces exciton spin relaxation rate,[49,50] and decreases Auger recombination rates. The latter leads to longer hot carrier[20] and multiexciton lifetimes,[38,51-54] enhanced optical gain[43,55,56] and reduced blinking behavior in QDs.[57-59]

All these properties suggest that type II semiconductor heterostructures should be ideal light harvesting materials for photovoltaic and photocatalytic applications.

In this chapter, we study the effect of type II band alignment on charge separation and recombination processes in CdTe/CdSe type II core/shell QDs adsorbed with the electron acceptor, anthraquinone-2,3-dicarboxylic acid (AQ). As shown in Figure 5.2, because of the type II band alignment, photoexcitation of the CdTe core is followed by an internal electron transfer (with a rate constant $k_{IET}$) from the CdTe to CdSe conduction band, while the hole remains in the CdTe core, forming $CdTe^{+}/CdSe^{-}$-AQ. The 1S electron in CdSe shell can then undergo external electron transfer (with a rate constant $k_{EET}$) to the adsorbed AQ to form the charge separated state ($CdTe^{+}/CdSe$-$AQ^{-}$), competing with the electron-hole recombination process (rate constant $k_R$). The electron in $AQ^{-}$ can eventually recombine with the hole in the CdTe core (with a rate constant $k_{CR}$) to regenerate the QD and AQ ground state (CdTe/CdSe-AQ). The rates of these expected internal/external charge separation and recombination processes were measured with transient absorption (TA) spectroscopy. As a comparison, relevant charge separation and recombination processes in CdTe-AQ complexes are also studied. A comparison of these rates with those previously reported for CdSe-AQ and CdSe/ZnS (type I core/shell)-AQ complexes [37] shows that the unique spatial distribution of the shell-localized electron and core localized hole in the type II core/shell QDs enables ultrafast charge separation while simultaneously retards charge recombination.

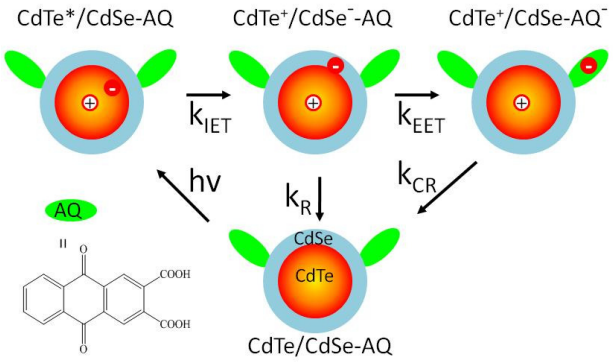


**Figure 5.2.** Relevant species involved in the photoinduced charge separation and recombination processes in CdTe/CdSe-AQ complexes.

## 5.2. Results and Discussion

### 5.2.1. Characterization of CdTe/CdSe Type II QDs

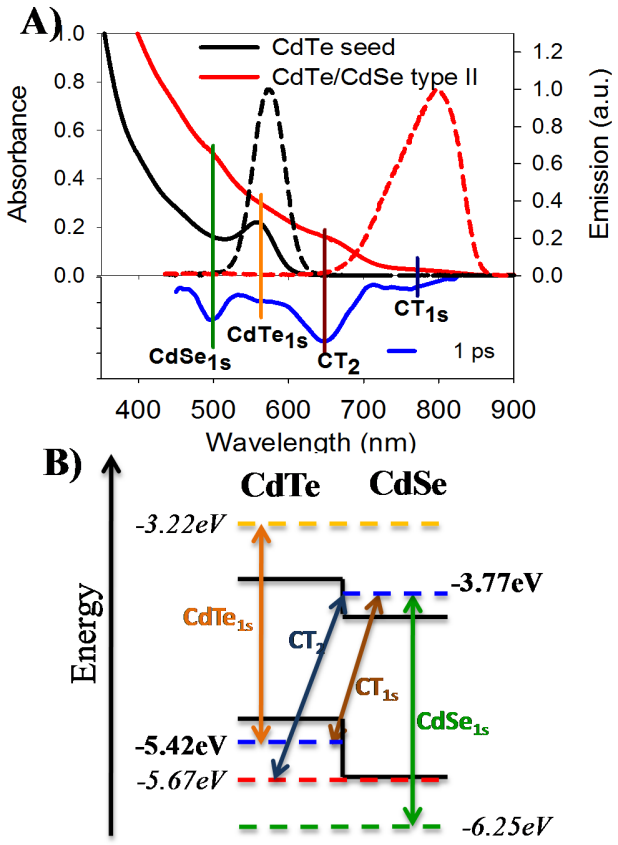


**Figure 5.3.** (a) UV-Vis absorption (solid) and emission (dashed) spectra of CdTe seed (black) and corresponding CdTe/CdSe core/shell type II QDs (red). Also shown is a TA spectrum of CdTe/CdSe QDs at 1ps delay time, which clearly shows four absorption bands (vertical dotted lines). (b) Energetic diagram of CdTe/CdSe type II QDs based on calculated lowest energy electron and hole levels and measured transition energies. B1 is assigned to the lowest energy charge transfer exciton absorption band (with a 1S hole in the CdTe core and 1S electron in the CdSe shell). $B_2$ and $B_3$ are transitions from higher valence band levels to the 1S electron level in the CdSe shell from high valence band levels. C is attributed to the lowest energy core localized exciton absorption band.

The UV-Vis absorption and emission spectra of CdTe core-only QDs (or seeds) and corresponding CdTe/CdSe core/shell type II QDs in heptane are shown in Figure 5.3 (a). The CdTe seed QD exhibits typical absorption and emission features with a distinctive first (1S) exciton peak at ~560 nm. In the CdTe/CdSe core/shell QD, the 1S exciton absorption peak becomes much less pronounced and a new band at ~ 650 nm and a broad absorption tail extending into the near-IR are formed. Furthermore, its emission peak position (~ 800 nm) is significantly red-shifted from that of the CdTe core-only QD (~580 nm). The emission spectrum of the CdTe/CdSe QD was measured at low QD concentration with negligible re-absorption effect. Therefore, the absence of emission features in the < 650 nm region suggests negligible emission from the CdTe core or CdSe shell and there is a fast internal charge transfer across the core/shell interface. These absorption and emission spectral features suggest the existence of a type II band alignment in the CdTe/CdSe core/shell QD.

Typically, in type II heterostructures (core/shell QDs[46,50,57], nanorods[48,49,60] or tetrapods[61,62]), the absorption spectrum exhibits transitions of both constituent materials and charge transfer (CT) bands between them, while the emission is centered at the lowest energy CT band due to the radiative recombination of the spatially separated lowest energy electron-hole pairs. As shown in Figure 5.3a, four absorption bands, $B_1$, $B_2$, $B_3$, and C (centered at ~ 770, 650, 500, 560 nm, respectively), can be indentified in the absorption spectrum of CdTe/CdSe QDs. These bands are seen more clearly in the TA spectrum at the initial delay times (such as 1ps), which shows bleaches at these bands. As will be further explained later, these bleaches can be attributed to the filling of the

conduction band electron levels associated with these transitions. The lowest energy absorption band ($B_1$, centered at ~770 nm) is near the emission peak position of this type II QD and can be assigned to the charge transfer transition from the CdTe valance band edge ($1S_h$) to CdSe conduction band edge ($1S_e$). The TA spectra (see below) show that $B_1$, $B_2$ and $B_3$ transitions have exactly the same bleach formation and decay kinetics, suggesting that these transitions share the same electron level (i. e. the $1S_e$ in the CdSe shell). The C band is assigned to the lowest energy CdTe core localized exciton transition. It is interesting to note that it is at the same energy as the lowest energy 1S exciton transition of the CdTe seed (from which the core/shell QDs were prepared). These assignments are further supported by the TA study of exciton dynamics and the effective mass calculation to be discussed below.

To support the assignments discussed above, we calculated the wave function and energy of the lowest energy conduction band electron and valence band hole in the CdTe seed and CdTe/CdSe type II QDs by treating them as particles confined in spherical wells of finite depth.[46,63,64] The effective mass of electrons (holes) are $m_e^*$=0.1 ($m_h^*$=0.35) in CdTe[65,66] and 0.13 (0.45) in CdSe.[67,68] The bulk conduction and valance band edge positions are -3.67 and -5.17 V (relative to vacuum) in the CdTe core, -4.04 and -5.74 V in the CdSe shell, and 0 and -8.4 V in the surrounding organic medium.[69,70] The Coulomb interaction between the electron and hole is treated as a first-order perturbation to the energy of the 1S exciton state in the CdTe core only QD (the dielectric constant is $\varepsilon$=10 $\varepsilon_0$ in CdTe).[65] This correction was neglected in the CdTe/CdSe type II QDs because of the much smaller overlap of the electron and hole wavefunctions. For CdTe core only

QDs with diameter of 2.86 nm, the calculated 1S exciton peak position (550 nm) agrees well with the measured value of 560 nm, suggesting the validity of the effective mass calculation for these materials.[46,50,63,64]

The calculation shows that the lowest energy electron ($1S_e$) and hole ($1S_h$) levels are largely localized in the CdSe conduction band and CdTe valence band, respectively, as shown in Figure 5.3b, confirming the type II band alignment in the CdTe/CdSe QD. From the calculated $1S_e$ and $1S_h$ levels (at -3.77 V and -5.42 V, respectively), the $B_1$ band center is estimated at 1.65 V, agreeing well the measured value of ~1.61 V and confirming the assignment of this transition. The energies of the valence band levels associated with transitions $B_2$ and $B_3$ are estimated to be -5.67 and -6.25 V, respectively. From the calculated $1S_h$ level position and the measured band center, the conduction level involved in transition C is estimated to be at -3.22 V. Considering the HOMO (more negative than -6.61 V) and LUMO ( -4 V) levels of AQ[37], only electron transfer from the excited QD to AQ is energetically possible.

### 5.2.2 Exciton Dynamics in Free CdTe/CdSe Type II QD

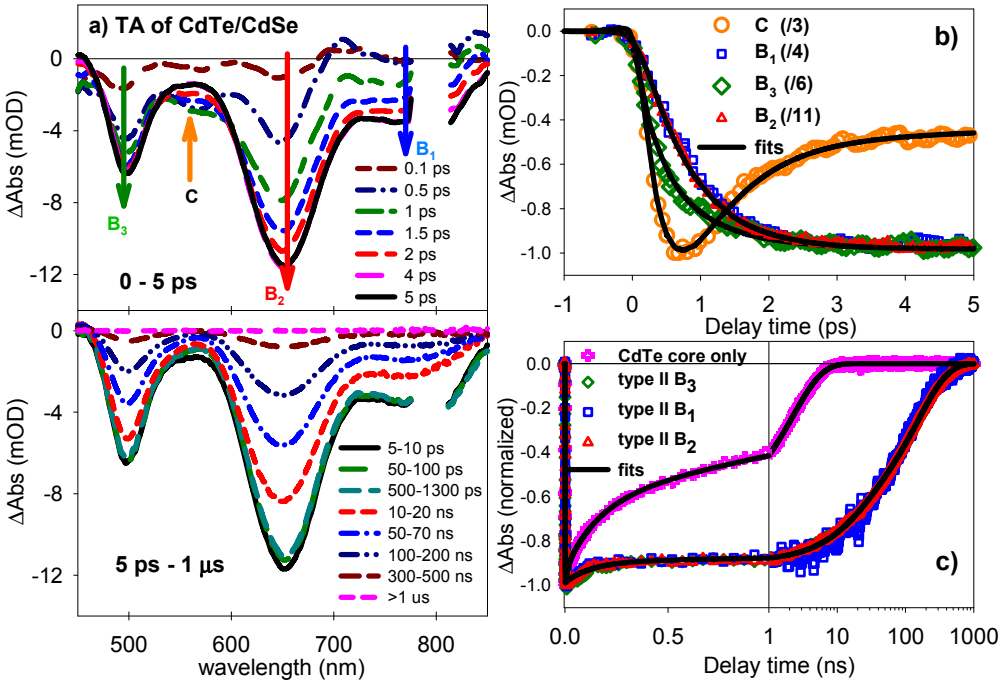


**Figure 5.4.** TA spectra and kinetics in CdTe/CdSe type II core/shell QDs. (a) Average TA spectra of free CdTe/CdSe QDs at indicated delay time windows after 400 nm excitation: upper panel, 0 -5 ps; lower panel, 5 ps - 1 µs. As indicated by the arrows in the upper panel, the decay of the bleach at band C leads to the growth of the bleach at $B_1$, $B_2$ and $B_3$ transitions. This is attributed to the internal electron transfer from the CdTe core to CdSe shell conduction band in the first 5 ps. (b) Formation and decay kinetics of the bleaches at C (560 nm), $B_3$(500 nm), $B_1$(770 nm) and $B_2$ (650 nm) bands from 0 to 5 ps. These signals have been scaled by factors indicated in the legend for better comparison. c) Comparison of the normalized bleach recovery kinetics of $B_1$, $B_2$ and $B_3$ bands in the CdTe/CdSe QDs with the 1S exciton bleach recovery kinetics of the CdTe seed. The slower bleach recovery kinetics in the CdTe/CdSe QD is attributed to the longer 1S electron lifetime, consistent with type II band alignment in this material. The horizontal

axis is in linear scale in the left panel (0-1 ns) and logarithmic scale in the right panel (1-1000 ns). The solid lines in b) and c) are fits to these kinetic according to eq. 5.1- 5.3 in the main text.

Transient absorption spectra of free CdTe/CdSe QDs after 400 nm excitation are shown in Figure Figure 5.4a upper (0- 5 ps) and lower (5 ps-1 μs) panels. These spectra were obtained with low pump power (20 nJ/pulse) to ensure that the average number of excitons per QD is much less than one and the effect of multiexcitons on carrier relaxation dynamics is negligible. Previous studies of CdSe core only QDs have shown that TA signals in these materials are dominated by the bleach of the 1S exciton band, which is caused by the filling of the 1S electron level.[17,18,71] Due to the Pauli exclusion principle, the occupancy of 2-fold degenerate 1S electron level reduces the transition probability to this level by half, giving rise to the bleach of 1S exciton band in the TA spectrum. Interestingly, there lacks a similar bleach due to the presence of holes, which has been attributed to the higher degeneracy and closely spaced energy levels (due to higher hole effective mass) in the valance band, as well as dark exciton states (caused by electron-hole exchange interaction).[17,18,33,72] In addition to state filling, photoexcited elelctron-hole pair can generate a local electrical field, which shifts of exciton transition by Stark effect and lead to derivative-like features in the TA spectra.[73-76] This feature is not observed in free CdTe/CdSe core/shell QDs. Therefore, the formation and decay of bleach signals can be attributed to the dynamics of electrons in the corresponding conduction band levels in the CdTe/CdSe QD.

In the first 5 ps (Figure 5.4a upper panel), the spectra show four separate bleaching bands centered at 500, 560, 650 and 770 nm, assigned to C, $B_3$, $B_2$ and $B_1$ transitions, respectively. The bleach of C band forms with a time constant of ~300 fs (see below) and decays within ~ 4 ps. Its decay leads to the growth of the bleach signals of $B_1$, $B_2$ and $B_3$ transitions. This relationship is clearly shown by two isosbestic points (at 532 nm and 599 nm) in Figure 5.4a upper panel, as well as in the kinetics shown in Figure 5.4b. The formation of bleach features at $B_1$, $B_2$, $B_3$ transitions indicates the arrival of electrons in the $1S_e$ level in the CdSe conduction band. This spectral evolution can be attributed to the internal electron transfer from the CdTe to CdSe conduction band within the type II core/shell QD, as shown in Figure 2. The bleach formation kinetics of $B_2$ and $B_1$ transitions are identical, confirming that these transitions involve the same 1S electron level in the CdSe shell. After ~ 5ps, when the internal electron transfer process from the CdTe to the CdSe conduction band is completed, the TA spectra consist of bleaches of $B_1$, $B_2$, $B_3$ transitions (Figure 5.4a lower panel). These bleaches recover with the same kinetics (Figure 5.4c), reflecting the depopulation of the shell localized 1S electron through recombination with the holes in the core and/or relaxation to defect states. These electron decay kinetics were found to be the same as the QD fluorescence decay (results not shown), suggesting that the lifetime of the conduction band electrons is controlled by the electron-hole recombination process.

The kinetics of the bleach formation and decay in CdTe/CdSe QDs can be fit to obtain the rates of IET and recombination. The kinetics of C, $B_1$, $B_2$, and $B_3$ bleaches are fit by the following model:

$$\Delta A(B_1, B_2) = -[\sum_{i=3} a_i e^{-k_{Ri}t} - e^{-k_{IET}t}] \quad (5.1)$$

$$\Delta A(B_3) = -[\sum_{i=3} a_i e^{-k_{Ri}t} - e^{-k_{IET}t}] - c_2[e^{-k_{IET}t} - e^{-k_0 t}] \quad (5.2)$$

$$\Delta A(C) = -[e^{-k_{IET}t} - e^{-k_0 t}] - c_1[\sum_{i=3} a_i e^{-k_{Ri}t} - e^{-k_{IET}t}] \quad (5.3)$$

Here, $k_0$ is the 1S exciton bleach formation rate in the CdTe core. $k_{IET}$ is the internal electron transfer rate from the CdTe to CdSe conduction band. $a_i$ and $k_{Ri}$ *(i=1-3)* are the amplitudes and time constants of the multiple-exponential function that describes the decay of the 1S electron in the CdSe shell. The bleach kinetics of the C and $B_3$ transitions are complicated by their spectral overlap. The last term in equation (5.3) accounts for the contribution of $B_3$ transition (with amplitude $c_1$) at the C band. Similarly, the last term in equation (5.2) corrects for the contribution of transition C (amplitude $c_2$) at the $B_3$ band.

As shown in Figure 5.4b and c, global fitting of these kinetics by equation (5.1-5.3) yields satisfactory fits to all kinetics traces, supporting the assignment of these transitions as well as the internal charge separation and recombination processes described above. The fitting parameters are listed in Table 5.1. The best fit value for the C bleach formation rate, $k_0 = 3.3$ ps$^{-1}$, reflects the relaxation of the initially exited electron to the lowest energy level in the CdTe core. This relaxation time is similar to that in CdTe (see below) and CdSe core only QDs of similar sizes.[18,28] The best fit yields $k_{IET} = 1.3$ ps$^{-1}$ (or an internal charge separation time of 0.77 ps), which is in good agreement with the $k_{IET}$ rate in similar CdTe/CdSe type II QDs determined in a previous fluorescence up conversion measurement.[77] Similar ultrafast intra-QD charge separation dynamics have also been reported in other type II materials.[60,62,78,79] From the multiple exponential fit

parameters ($a_i$ *and* $k_{Ri}$), we calculate a half-life ($\tau_{1/2,R}$) of 62 ns for the 1S electron in the CdSe shell of the CdTe/CdSe core/shell QDs.

**Table 5.1.** Fitting parameters for the C, $B_1$, $B_2$ and $B_3$ exciton bleach formation and recovery kinetics in free CdTe/CdSe QDs according to eq. 5.1-5.3.

| | $k_0$, $ps^{-1}$ | $k_{IET}$, $ps^{-1}$ | $c_1$ | $c_2$ | $k_{R1}$, $ns^{-1}$ ($a_1$) | $k_{R2}$, $ns^{-1}$ ($a_2$) | $k_{R3}$, $ns^{-1}$ ($a_3$) |
|---|---|---|---|---|---|---|---|
| $B_1$, $B_2$ | NA | 1.31±0.11 | NA | NA | 6.58±0.58 (0.097±0.012) | 0.051±0.015 (0.206±0.031) | 0.006±0.002 (0.697±0.051) |
| C | 3.25±0.22 | | 0.33±0.07 | NA | | | |
| $B_3$ | | | NA | 0.47±0.06 | | | |

It should be mentioned that both the CdTe core and CdSe shell based transitions can be exited at 400 nm. The direct excitation of the CdSe shell should lead to a faster (similar to $k_0$, ~ 300 fs) bleach formation of $B_2$ and $B_1$ bands because of the faster relaxation within the conduction band levels in the shell. This is not observed in the current system. It is possible that the absorption at this excitation wavelength is dominated by CdTe core based transitions with negligible contribution of the direct excitation of the CdSe shell. It is also possible that in CdTe/CdSe type II QDs, there may exist ultrafast (< 300 fs) energy transfer between the core and shell, leading to relaxation of all excitations to the lowest energy non-charge transfer excitonic state (giving rise the

bleach at the C band), prior to the internal charge separation process.[49] This ultrafast energy transfer process may be too fast to be resolved in the current measurement. Nevertheless, it does not influence the determination of the internal charge transfer rate $k_{IET}$ discussed above or the external electron transfer rate to molecular acceptors to be discussed later.

As a comparison, we have also studied the exciton decay dynamics of the CdTe core only QDs after 400 nm excitation. The TA spectra (Figure A.5.1) show the bleach of the 1S exciton band that can be attributed to the filling of the 1S electron level. The 1S exciton bleach recovery kinetics in CdTe QDs is compared with the bleach recovery kinetics in CdTe/CdSe core/shell QDs in Figure 5.4. The formation of the 1S exciton bleach in CdTe can be fit by a single exponential function with a rate constant, $k_0$, of 3.3 $ps^{-1}$. The recovery of the exciton bleach can be well fit by a three exponential function, from which a half-life of 0.62 ns is obtained for the 1S electron in the CdTe QD. This lifetime is 100 times shorter than that in CdTe/CdSe, consistent with the slower electron-hole recombination rate expected in the type II core/shell QDs.

### 5.2.3. Charge Transfer Dynamics in QD-AQ Complex

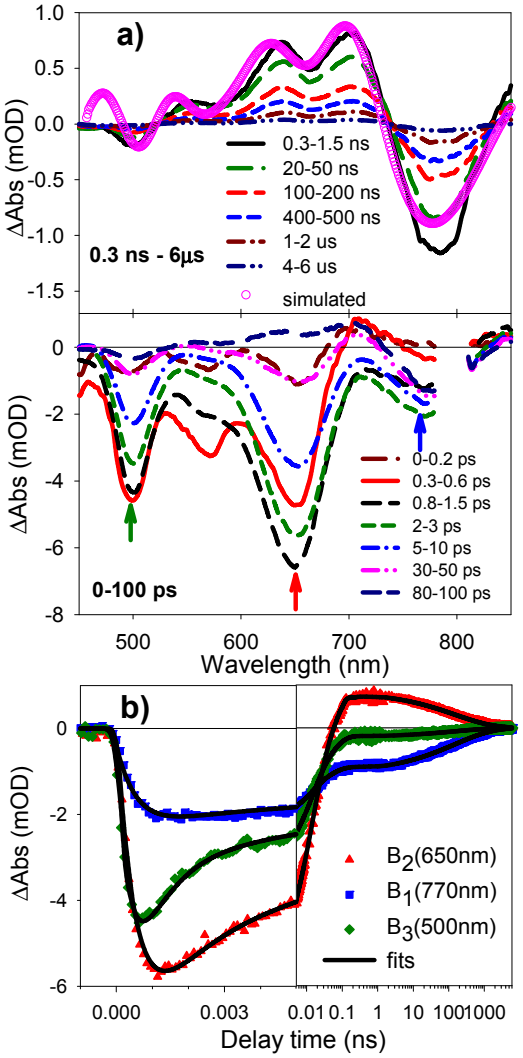


**Figure 5.5.** Transient spectra and kinetics of CdTe/CdSe-AQ complexes. (a) Average TA spectra of CdTe/CdSe-AQ at indicated delay time windows (0-100 ps, lower panel; 0.3 ns-6 µs, upper panel) after 400 nm excitation. The vertical scale in the upper panel has been expanded to show more clearly the spectra of the charge separated state. The simulated charge separated state spectrum (pink circles) is also shown in the upper panel. (b) Transient absorption kinetics at $B_3$ (500 nm), $B_2$ (650 nm) and $B_1$ (770 nm) bands

(indicated by arrows in a) in CdTe/CdSe-AQ complexes. Black lines are fits according to eq (4). The delay time is in a linear scale for 0-5 ps (left) and logarithmic scale for 5 ps - 6μs (right).

TA spectra of CdTe/CdSe-AQ complex, shown in Figure 5.5(a), were acquired under the same excitation conditions as those for free CdTe/CdSe. With low excitation power density, the average number of excions in QDs is much less than 1 and the measured TA features can be attributed to the dynamics of single exciton states. Within the first 5 ps, the TA features are similar to those in free QDs. It shows the initial formation of bleach at C band and its subsequent decay that leads to the growth of the bleaches of $B_1$, $B_2$ and $B_3$ transitions. These features can be attributed to the internal electron transfer from the CdTe to CdSe conduction band with a rate constant $k_{IET}$ that is assumed to be the same as that in free CdTe/CdSe QDs.

Unlike free CdTe/CdSe QDs, the $B_1$, $B_2$ and $B_3$ bleaches in CdTe/CdSe-AQ complexes recover more rapidly to form a new spectral feature. The shape of this feature remains unchanged but its amplitude decreases between 150 ps and 6 μs, as shown in Figure 5.5(a) upper panel. This spectral feature ($A_{cs}(\lambda)$) can be attributed to the externally-charge separated state $CdTe^{+}$/CdSe-$AQ^{-}$ (see scheme 1), in which the electron in the CdSe shell has been transferred to AQ. The $A_{cs}(\lambda)$ spectrum can be qualitatively described by the sum of the spectrum of $AQ^{-}$ (a broad positive absorption band around 650 nm) and a Stark effect induced TA spectrum of the CdTe/CdSe QD. The former was obtained in CdS/ZnS-AQ complexes, in which the photoexcitation leads to a long-lived

charge separated state, $CdS^{+}/ZnS\text{-}AQ^{-}$. Because the exciton bands of CdS/ZnS QDs are below 400 nm, the TA spectra in the visible region can be attributed to the absorption of $AQ^{-}$. Similar Stark-effect induced TA features caused by external charge separation were previously observed in CdSe/ZnS-AQ complexes.[37] This spectral feature is also similar to the Stark-effect induced spectra in CdSe quantum dots, caused by either a surface trapped charge or externally applied DC field.[73,75,80] The spatially separated electron and hole in the charge separated state ($CdS^{+}/ZnS\text{-}AQ^{-}$) produces a local electrical field that modulates the absorption spectrum of QDs because of the different electric dipole moments and polarizabilities between the QD ground and excited states.[73,75,80] On the basis of these spectral assignment, the TA spectral evolution shown in Figure 4a indicates that after the initial internal charge separation within the core/shell QDs, the electron in the CdSe shell is transferred to the adsorbed AQ molecule (to form $AQ^{-}$) in the first 150 ps, which is then followed by the recombination of the electron in $AQ^{-}$ with the hole in the CdTe core in the > 150 ps time scale, as shown in Figure 5.2.

The kinetics of the external charge separation and recombination can be monitored at $B_1$ and $B_2$ transitions, as shown in Figure 5.5b. At these wavelengths, the TA signals contain both the contributions of internally charge-separated QD excited state ($CdTe^{+}/CdSe^{-}$ -AQ, with TA spectra $A_{QD^*}(\lambda)$) and the externally charge-separated state ($CdTe^{+}/CdSe\text{-}AQ^{-}$, with TA spectra $A_{CS}(\lambda)$). The kinetics of these TA signals at the peak of $B_1$ and $B_2$ transitions can be described by the following equation.

$$\Delta A(\lambda, t) = A_{QD^*}(\lambda)(-e^{-k_{IET}t} + \sum_{i=3} b_i e^{-k_{EETi}t}) + A_{CS}(\lambda)(-\sum_{i=3} b_i e^{-k_{EETi}t} + e^{-\left(\frac{t}{\tau}\right)^{\alpha}}) \quad (5.4)$$

Here, $b_i$ and $k_{EETi}$ are the amplitudes and rate constants of a multiple exponential fit to the external charge separation process. $\tau$ and $\alpha$ are the characteristic time and exponent of the stretch exponential function used to describe the charge recombination process. $k_{IET}$ and $A_{QD*}(\lambda)$ have already been determined in the measurement of free CdTe/CdSe QDs under the same conditions, as shown in Figure 5.4. $A_{CS}(\lambda)$ is given by the TA spectra after 150 ps.

The bleach kinetics of $B_2$ ($\lambda$=650 nm) and $B_1$ ($\lambda$=770nm) bands are fit according to eq 5.4 with $b_i$, $k_{EETi}$, $\tau$, $\alpha$ as fitting parameters. Similarly, the kinetics of the $B_3$ bleach ($\lambda$=500 nm) can be described by the same model after accounting for the overlap with the C transition according to eq. (5.2). As shown in Figure 5.5b, these kinetics are well described by the model and the fitting parameters are listed in Table 5.2. The best fit to the external charge separation process requires at least three exponentials, from which we calculate a half-lifetime ($\tau_{1/2,CS}$) of 2.7 ps to represent the average external charge separation time. The charge recombination kinetics can be best fit by a stretched exponential function with $\tau = 181$ ns and $\alpha = 0.42$, from which a half-lifetime ($\tau_{1/2,CR}$) of 92 ns is calculated to represent the average charge recombination time.

**Table 5.2.** Fitting parameters for TA kinetics at $B_3$($\lambda$=500 nm), $B_2$($\lambda$=650 nm) and $B_1$($\lambda$=770 nm) transitions in CdTe/CdSe-AQ complex according to equation 5.4.

| | $A_{QD^*}(\lambda)$ | $A_{CS}(\lambda)$ | $k_{EET1}$, $ps^{-1}$ ($b_1$) | $k_{EET2}$, $ps^{-1}$ ($b_2$) | $k_{EET3}$, $ps^{-1}$ ($b_3$) | $\tau$, ns | $\alpha$ |
|---|---|---|---|---|---|---|---|

| | | | | | | | |
|---|---|---|---|---|---|---|---|
| $B_2$ | -0.013±0.003 | 0.0007±0.0002 | 0.602±0.068 | 0.088±0.017 | 0.026±0.005 | 181.5±8.3 | 0.42±0.03 |
| $B_1$ | -0.004±0.001 | -0.0009±0.0002 | (0.55±0.08) | (0.35±0.05) | (0.10±0.02) | | |
| $B_3$ | -0.007±0.001 | -0.0002±0.0001 | | | | | |

As a comparison, the charge separation and recombination of CdTe-AQ complexes were also investigated by transient absorption spectroscopy. The details of their TA spectra, kinetics and analysis can be found in the Appendix 1. The half-lifetimes of charge separation ($\tau_{1/2,CS}$) and recombination ($\tau_{1/2,CR}$) processes are 0.85 ps and 0.89 ns, respectively. These time constants are compared with those in CdTe/CdSe QDs in Table 5.3. Also compared are the charge separation and recombination times previously reported for CdSe-AQ and CdSe/ZnS (2ML)-AQ complexes.[37]

**Table 5.3.** Half-life time for charge separation ($\tau_{1/2,CS}$) and recombination ($\tau_{1/2,CR}$) in CdTe-AQ, CdTe/CdSe-AQ, CdSe-AQ and CdSe/ZnS (2ML)-AQ complexes as well as the conduction band electrons ($\tau_{1/2,R}$) in corresponding free QDs. (*The time constant for CdSe-AQ and CdSe/ZnS-AQ are taken from published paper [37].)

| | $\tau_{1/2,CS}$, ps | $\tau_{1/2,CR}$, ns | $\tau_{1/2,R}$, ns |
|---|---|---|---|
| CdTe-AQ | 0.85±0.07 | 0.89±0.03 | 0.62±0.02 |
| CdSe-AQ* | 3.4 | 0.75 | 15 |
| CdTe/CdSe (type II)-AQ | 2.7±0.3 | 92±6 | 62±4 |
| CdSe/ZnS | 23.6 | 230 | 13 |

| | | | |
|---|---|---|---|
| (type I)-AQ* | | | |

### 5.2.4. Comparison between CdSe, CdTe, CdTe/CdSe (type II) and CdSe/ZnS (type I) QDs

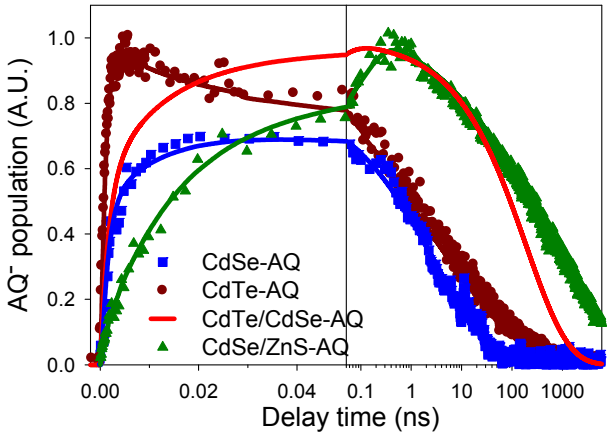


**Figure 5.6.** Comparison of $AQ^-$ anion population kinetics in CdTe-AQ, CdTe/CdSe-AQ, CdSe-AQ, CdSe/ZnS(2MLs)-AQ samples. The kinetics for CdTe/CdSe-AQ and CdTe-AQ complexes are extracted from eqs. (5.4) and (A.5.2), respectively. The $AQ^-$ poplation kinetics for CdSe-AQ and CdSe/ZnS-AQ complexes have been published[37] and are replotted here. The amplitudes of these kinetics have been scaled to represent the transient quantum yields of $AQ^-$ formation (see main text).

To investigate their dependence on the structures of the QDs, we compared the charge separation and recombination kinetics in core only (CdSe and CdTe), type I

core/shell (CdSe/ZnS) and type II core/shell (CdTe/CdSe) QDs. For all data shown in Figure 5.6, the QD-AQ ratios are similar, which enables a meaningful direct comparison of ET rates. In previous studies, we have shown that electron transfer rates from QDs increase linearly with the number of adsorbed acceptors.[32,81,82] The kinetics of the formation and decay of the charge separated state in CdTe/CdSe-AQ complexes are obtained from the fit to the raw kinetics shown in Figure 5.5. Because of well separated $AQ^-$ and QD absorption features, the $AQ^-$ kinetics in CdTe-AQ complexes can be obtained at ~ 650 nm (Figure A.5.1) and is used directly for comparison. Similar kinetics of $AQ^-$ formation and decay for CdSe-AQ and CdSe/ZnS-AQ complexes have been published previously,[37] and are replotted here. The type I core/shell sample with ~2 ZnS MLs is chosen for this comparison since it is commonly used in solar cell study.[83-85] These kinetics have been scaled such that their time-dependent amplitude represents the transient quantum yield of $AQ^-$ formation.[37] In all samples, the rates of charge separation are much faster than the intrinsic electron-hole recombination time in free QDs. Therefore all excited electrons are transferred to the adsorbates. However, due to the competition of heterogeneous charge separation and recombination processes, the transient quantum yield of the charge separated state is time-dependent and may not reach 100% in some cases.

For CdTe/CdSe-AQ complex, the charge separation rate is three times slower than CdTe-AQ and is similar to CdSe-AQ, while the charge recombination rate is ~ 100 times slower than core-only (CdTe and CdSe) QDs. This comparison suggests that the type II band alignment enables ultrafast charge separation while retards charge recombination.

As shown in Figure 5.6, the highest yield of charge separated state in CdSe core-only QDs is ~ 70%, due to the fast charge recombination process. By maintaining the charge separation rate and greatly slowing down the recombination rate in type II QDs, a higher transient yield (~100% at the peak) and longer lifetime of the charge separated state can be achieved. In principle, this property of the type II QDs should allow more efficient extraction of the separated charge carriers for either electricity generation in solar cells or photocatalysis in solar-to-fuel conversion devices.

The variations of charge separation rates in these materials can be understood within the frame work of the Marcus theory of electron transfer, according to which, the electron transfer rate depends on the free energy change, electronic coupling strength and reorganization energy.[86] Due to the delocalized electron wave functions in the QDs, the reorganization energy for the ET process is dominated by the contribution of adsorbates, and can be assumed to be same in these samples. The estimated 1S electron energy in CdTe/CdSe, CdTe seed, and CdSe (with first exciton peak at ~520 nm) QDs is -3.77, -3.10 and -3.63 V (vs. vacuum level), respectively. Thus, ET from CdTe/CdSe and CdSe core only QDs to AQ have similar driving forces and any difference in rate can be attributed to variations in the electronic coupling strength. In a previous study of type I core/shell CdSe/ZnS-AQ complexes, we showed that the electronic coupling strength for the charge separation and recombination processes is proportional to the surface 1S electron and hole densities, respectively.[37] As shown in Figure 5.1 lower panel, the type II band alignment in CdTe/CdSe QDs leads to the localization of the 1S electron in the CdSe shell. The calculated electron densities at the surface for CdSe core-only and

CdTe/CdSe QDs (0.115 and 0.053 $nm^{-3}$, respectively) are within a factor two despite two times larger radius of the core/shell QDs. Their similar electron densities account for the similar electronic coupling strengths and ET rates from these materials.

The rate for the charge recombination from $AQ^-$ is determined by the energy and surface density of the hole level in the QD. The calculated surface densities and energy are 0.104, 0.173 and $1.63*10^{-4}$ $nm^{-3}$ and -6.2, -5.51 and -5.42 V, respectively, for the lowest energy valence band hole in CdSe, CdTe and CdTe/CdSe QDs. The calculated surface hole density in the type II core/shell structure is 1000 times smaller than core-only QDs. This large difference can be attributed to the CdTe core localized valence band hole in CdTe/CdSe, for which the CdSe shell acts as a tunneling barrier, reducing its density at the surface. We believe that the large reduction of the surface hole density is the main reason for the much slower charge recombination rate in the type II core/shell structures. Unfortunately, a quantitative comparison the charge recombination rates in various QDs is difficult because the exact nature of the hole involved in the recombination process is unknown. The transient visible spectra probe the state filling of the 1S electron level and provide no direct information of the hole level. It is possible that the valence band hole can be trapped at some yet-to-be-characterized defect sites prior to the charge recombination process, affecting its energy and wave function. It should be noted that, the CdSe shell, which acts as a hole tunneling barrier, should reduce the surface amplitudes of the wave functions for both the valence band and trapped holes in the CdTe core. Thus type II core/shell structures, with shell localized electrons and core localized holes, enable ultrafast charge separation and retard charge recombination by

selectively reducing the coupling strength for recombination without decreasing the coupling strength for charge separation.

It is also interesting to compare type I and type II core/shell structures. In a previous study we showed that both the charge separation and recombination rates are reduced in CdSe/ZnS type I core/shell structures, because both the 1S electron and hole wave functions are localized in the core, as shown in Figure 5.1. However, because of the difference in the shell-thickness dependence of the electron and hole wave functions (determined by their effective masses and band off-sets), a judicious choice of the shell materials, such as ZnS, can lead to a much faster decreases of the recombination than separation rates with the shell thickness. As long as the charge separation time is shorter than the intrinsic exciton lifetimes in QDs, it is possible to increase the charge separation yield and lifetime by using type I core/shell architecture, as shown in Figure 5.6. Unlike the type I QDs, the type II core/shell QDs can retard the charge recombination rate without reducing the charge separation rate. Additionally, type II QDs offer extra advantages as light harvest materials for charge transfer applications because of the long single and multiple exciton lifetimes in these materials. Compared to core-only QDs and type I QDs, both the single and multiple exciton lifetimes increases in type II heterostructures because of reduced electron-hole overlap.[38,45-48,51-54] For example, in CdTe/CdSe-AQ both the single exciton lifetime (~62 ns) and biexciton lifetime (~600 ps)[51] are much longer than interfacial charge separation time (~ 3 ps) to AQ, suggesting the possibility of efficient dissociation of single and multiple excitons from these materials.

## 5.3. Conclusion

We have investigated charge separation and recombination kinetics in core-only (CdTe-AQ) and type II core/shell (CdTe/CdSe-AQ) QD-electron acceptor complexes, and compared them with the kinetics of similar processes in CdSe-AQ and type I core/shell CdSe/ZnS-AQ complexes. Optical excitation of these QDs generates long-lived single excitons, which can be dissociated by electron transfer to the adsorbed anthraquinone. In type II CdTe/CdSe QDs, the initial intra-QD charge separation step leads to the ultrafast transfer of the conduction band electron from the CdTe core to the CdSe shell in ~ 0.77 ps with the hole remaining in the CdTe core. The half-lifetimes of external electron transfer to the adsorbed acceptor (AQ) and the subsequent recombination of the transferred electron (in $AQ^-$) with the valence band hole are 2.7 ps and 92 ns, respectively. Comparing with CdSe-AQ or CdTe-AQ, the charge separation rates are similar, whereas the charge recombination is retarded by 100 times in the CdTe/CdSe-AQ complexes. This differs from type I CdSe/ZnS core/shell QDs, in which the ZnS shell slows down both the charge separation and recombination rates. The advantageous charge separation property of type II QDs can be attributed to the shell localized conduction band electron and the core localized valence band hole, maintaining the electronic coupling strength for charge separation while reducing the coupling strength for charge recombination. This study demonstrates that type II heterostructures, with the ability to control both the compositions and dimensions of the constituent

(core/shell) materials, offer an exciting opportunity to engineer the electron and hole wave function distributions to achieve ultrafast charge separation and ultraslow charge recombination. This unique ability, coupled with long single and multiple exciton lifetimes as well as extended absorption spectra (compared to constituent materials), suggests that type II heterostructures are promising light harvesting materials for solar energy conversion.

## References

(1) Alivisatos, A. P. *Science* **1996**, *271*, 933.

(2) Brus, L. E. *J. Chem. Phys.* **1983**, *79*, 5566.

(3) Brus, L. E. *J. Chem. Phys.* **1984**, *80*, 4403.

(4) Norris, D. J.; Efros, A. L.; Rosen, M.; Bawendi, M. G. *Phys. Rev. B* **1996**, *53*, 16347.

(5) Efros, A. L.; Rosen, M. *Annu. Rev. Mater. Sci.* **2000**, *30*, 475.

(6) Gur, I.; Fromer Neil, A.; Geier Michael, L.; Alivisatos, A. P. *Science* **2005**, *310*, 462.

(7) Huynh, W. U.; Dittmer, J. J.; Alivisatos, A. P. *Science* **2002**, *295*, 2425.

(8) Kamat, P. *J. Phys. Chem. C* **2008**, *112*, 18737.

(9) Kamat, P. V.; Tvrdy, K.; Baker, D. R.; Radich, J. G. *Chem. Rev.* **2010**, *110*, 6664.

(10) Pattantyus-Abraham, A. G.; Kramer, I. J.; Barkhouse, A. R.; Wang, X.; Konstantatos, G.; Debnath, R.; Levina, L.; Raabe, I.; Nazeeruddin, M. K.; Gratzel, M.; Sargent, E. H. *ACS Nano* **2010**, *4*, 3374.

(11) Bruchez Jr, M.; Moronne, M.; Gin, P.; Weiss, S.; Alivisatos, A. *Science* **1998**, *281*, 2013.

(12) Chan, W. C. W.; Nie, S. M. *Science* **1998**, *281*, 2016.

(13) Kim, S.; Lim, Y. T.; Soltesz, E. G.; De Grand, A. M.; Lee, J.; Nakayama, A.; Parker, J. A.; Mihaljevic, T.; Laurence, R. G.; Dor, D. M.; Cohn, L. H.; Bawendi, M. G.; Frangioni, J. V. *Nat Biotech* **2004**, *22*, 93.

(14) Michalet, X.; Pinaud, F. F.; Bentolila, L. A.; Tsay, J. M.; Doose, S.; Li, J. J.; Sundaresan, G.; Wu, A. M.; Gambhir, S. S.; Weiss, S. *Science* **2005**, *307*, 538.

(15) Klimov, V. I.; Mikhailovsky, A. A.; McBranch, D. W.; Leatherdale, C. A.; Bawendi, M. G. *Science* **2000**, *287*, 1011.

(16) Guyot-Sionnest, P. *Structure and Bonding (Berlin, Germany)* **2005**, *118*, 59.

(17) Klimov, V. I. *J. Phys. Chem. B* **2000**, *104*, 6112.

(18) Klimov, V. I. *Annu. Rev. Phys. Chem.* **2007**, *58*, 635.

(19) Zhang, J. *J. Phys. Chem. B* **2000**, *104*, 7239.

(20) Pandey, A.; Guyot-Sionnest, P. *Science* **2008**, *322*, 929.

(21) Pijpers, J. J. H.; Ulbricht, R.; Tielrooij, K. J.; Osherov, A.; Golan, Y.; Delerue, C.; Allan, G.; Bonn, M. *Nat. Phys.* **2009**, *5*, 811.

(22) McGuire, J. A.; Sykora, M.; Joo, J.; Pietryga, J. M.; Klimov, V. I. *Nano letters* **2010**, *10*, 2049.

(23) Beard, M. C.; Midgett, A. G.; Hanna, M. C.; Luther, J. M.; Hughes, B. K.; Nozik, A. J. *Nano letters* **2010**, *10*, 3019.

(24) Nair, G.; Geyer, S. M.; Chang, L.-Y.; Bawendi, M. G. *Physical Review B* **2008**, *78*, 125325.

(25) Nozik, A. J. *Physica E: Low-Dimensional Systems & Nanostructures (Amsterdam, Netherlands)* **2002**, *14*, 115.

(26) Nozik, A. J. *Nano letters* **2010**, *10*, 2735.

(27) Sambur, J. B.; Novet, T.; Parkinson, B. A. *Science* **2010**, *330*, 63.

(28) Huang, J.; Huang, Z.; Yang, Y.; Zhu, H.; Lian, T. *Journal of the American Chemical Society* **2010**, *132*, 4858.

(29) Tisdale, W. A.; Williams, K. J.; Timp, B. A.; Norris, D. J.; Aydil, E. S.; Zhu, X.-Y. *Science* **2010**, *328*, 1543.

(30) Nozik, A. J. *Annu. Rev. Phys. Chem.* **2001**, *52*, 193.

(31) Huang, J.; Stockwell, D.; Huang, Z.; Mohler, D. L.; Lian, T. *J. Am. Chem. Soc.* **2008**, *130*, 5632.

(32) Boulesbaa, A.; Issac, A.; Stockwell, D.; Huang, Z.; Huang, J.; Guo, J.; Lian, T. *J. Am. Chem. Soc.* **2007**, *129*, 15132.

(33) Sykora, M.; Petruska, M. A.; Alstrum-Acevedo, J.; Bezel, I.; Meyer, T. J.; Klimov, V. I. *J. Am. Chem. Soc.* **2006**, *128*, 9984.

(34) Burda, C.; Link, S.; Mohamed, M.; El-Sayed, M. *J. Phys. Chem. B* **2001**, *105*, 12286.

(35) Robel, I.; Kuno, M.; Kamat, P. V. *J. Am. Chem. Soc.* **2007**, *129*, 4136.

(36) Matylitsky, V. V.; Dworak, L.; Breus, V. V.; Basche, T.; Wachtveitl, J. *J. Am. Chem. Soc.* **2009**, *131*, 2424.

(37) Zhu, H.; Song, N.; Lian, T. *J. Am. Chem. Soc.* **2010**, *132*, 15038.

(38) Sitt, A.; Sala, F. D.; Menagen, G.; Banin, U. *Nano Lett.* **2009**, *9*, 3470.

(39) Ivanov, S. A.; Piryatinski, A.; Nanda, J.; Tretiak, S.; Zavadil, K. R.; Wallace, W. O.; Werder, D.; Klimov, V. I. *J. Am. Chem. Soc.* **2007**, *129*, 11708.

(40) Donega, C. d. M. *Chem. Soc. Rev.* **2011**, *40*, 1512.

(41) Peter Reiss, M. P., Liang Li, *Small* **2009**, *5*, 154.

(42) Chuang, C.-H.; Lo, S. S.; Scholes, G. D.; Burda, C. *J. Phys. Chem. Lett.* **2010**, 2530.

(43) García-Santamaría, F.; Chen, Y.; Vela, J.; Schaller, R. D.; Hollingsworth, J. A.; Klimov, V. I. *Nano Lett.* **2009**, *9*, 3482.

(44) Smith, A. M.; Mohs, A. M.; Nie, S. *Nat. Nanotechnol.* **2009**, *4*, 56.

(45) Lee, D. C.; Robel, I. n.; Pietryga, J. M.; Klimov, V. I. *J. Am. Chem. Soc.* **2010**, *132*, 9960.

(46) Kim, S.; Fisher, B.; Eisler, H. J.; Bawendi, M. *J. Am. Chem. Soc.* **2003**, *125*, 11466.

(47) Chen, C.-Y.; Cheng, C.-T.; Lai, C.-W.; Hu, Y.-H.; Chou, P.-T.; Chou, Y.-H.; Chiu, H.-T. *Small* **2005**, *1*, 1215.

(48) Kumar, S.; Jones, M.; Lo, S. S.; Scholes, G. D. *Small* **2007**, *3*, 1633.

(49) He, J.; Lo, S. S.; Kim, J.; Scholes, G. D. *Nano Lett.* **2008**, *8*, 4007.

(50) He, J.; Zhong, H.; Scholes, G. D. *Physical Review Letters* **2010**, *105*, 046601/1.

(51) Oron, D.; Kazes, M.; Banin, U. *Phys. Rev. B* **2007**, *75*, 035330.

(52) Gachet, D.; Avidan, A.; Pinkas, I.; Oron, D. *Nano Letters* **2009**, *10*, 164.

(53) Osovsky, R.; Cheskis, D.; Kloper, V.; Sashchiuk, A.; Kroner, M.; Lifshitz, E. *Phys. Rev. Lett.* **2009**, *102*, 197401.

(54) Htoon, H.; Malko, A. V.; Bussian, D.; Vela, J.; Chen, Y.; Hollingsworth, J. A.; Klimov, V. I. *Nano Lett.* **2010**, *10*, 2401.

(55) Klimov, V. I.; Ivanov, S. A.; Nanda, J.; Achermann, M.; Bezel, I.; McGuire, J. A.; Piryatinski, A. *Nature* **2007**, *447*, 441.

(56) Nanda, J.; Ivanov, S. A.; Htoon, H.; Bezel, I.; Piryatinski, A.; Tretiak, S.; Klimov, V. I. *J. Appl. Phys.* **2006**, *99*, 034309.

(57) Chen, Y.; Vela, J.; Htoon, H.; Casson, J. L.; Werder, D. J.; Bussian, D. A.; Klimov, V. I.; Hollingsworth, J. A. *J. Am. Chem. Soc.* **2008**, *130*, 5026.

(58) Mahler, B.; Spinicelli, P.; Buil, S.; Quelin, X.; Hermier, J. P.; Dubertret, B. *Nat. Mater.* **2008**, *7*, 659.

(59) Spinicelli, P.; Buil, S.; Quelin, X.; Mahler, B.; Dubertret, B.; Hermier, J. P. *Phys. Rev. Lett.* **2009**, *102*, 136801.

(60) Dooley, C. J.; Dimitrov, S. D.; Fiebig, T. *Journal of Physical Chemistry C* **2008**, *112*, 12074.

(61) Milliron, D. J.; Hughes, S. M.; Cui, Y.; Manna, L.; Li, J. B.; Wang, L. W.; Alivisatos, A. P. *Nature* **2004**, *430*, 190.

(62) Peng, P.; Milliron, D. J.; Hughes, S. M.; Johnson, J. C.; Alivisatos, A. P.; Saykally, R. J. *Nano Lett.* **2005**, *5*, 1809.

(63) Oron, D.; Kazes, M.; Banin, U. *Phys. Rev. B* **2007**, *75*, 035330.

(64) Haus, J. W.; Zhou, H. S.; Honma, I.; Komiyama, H. *Phys. Rev. B* **1993**, *47*, 1359.

(65) Pellegrini, G.; Mattei, G.; Mazzoldi, P. *J. Appl. Phys.* **2005**, *97*, 073706.

(66) Masumoto, Y.; Sonobe, K. *Phys. Rev. B* **1997**, *56*, 9734.

(67) Berger, L. I. *Semiconductor materials*; CRC Press, 1997.

(68) Peng, X. G.; Schlamp, M. C.; Kadavanich, A. V.; Alivisatos, A. P. *J. Am. Chem. Soc.* **1997**, *119*, 7019.

(69) Salomon, A.; Boecking, T.; Seitz, O.; Markus, T.; Amy, F.; Chan, C.; Zhao, W.; Cahen, D.; Kahn, A. *Adv. Mater.* **2007**, *19*, 445.

(70) Wei, S.-H.; Zunger, A. *Appl. Phys. Lett.* **1998**, *72*, 2011.

(71) Blackburn, J. L.; Selmarten, D. C.; Ellingson, R. J.; Jones, M.; Micic, O.; Nozik, A. J. *J. Phys. Chem. B* **2005**, *109*, 2625.

(72) Huang, J.; Huang, Z.; Jin, S.; Lian, T. *J. Phys. Chem. C* **2008**, *112*, 19734.

(73) Colvin, V. L.; Alivisatos, A. P. *J. Chem. Phys.* **1992**, *97*, 730.

(74) Empedocles, S. A.; Bawendi, M. G. *Science* **1997**, *278*, 2114.

(75) Norris, D. J.; Sacra, A.; Murray, C. B.; Bawendi, M. G. *Phys. Rev. Lett.* **1994**, *72*, 2612.

(76) Hewa-Kasakarage, N. N.; Kirsanova, M.; Nemchinov, A.; Schmall, N.; El-Khoury, P. Z.; Tarnovsky, A. N.; Zamkov, M. *J. Am. Chem. Soc.* **2009**, *131*, 1328.

(77) Chou, P. T.; Chen, C. Y.; Cheng, C. T.; Pu, S. C.; Wu, K. C.; Cheng, Y. M.; Lai, C. W.; Chou, Y. H.; Chiu, H. T. *ChemPhysChem* **2006**, *7*, 222.

(78) Chen, C.-Y.; Cheng, C.-T.; Yu, J.-K.; Pu, S.-C.; Cheng, Y.-M.; Chou, P.-T.; Chou, Y.-H.; Chiu, H.-T. *J. Phys. Chem. B* **2004**, *108*, 10687.

(79) Hewa-Kasakarage, N. N.; El-Khoury, P. Z.; Tarnovsky, A. N.; Kirsanova, M.; Nemitz, I.; Nemchinov, A.; Zamkov, M. *ACS Nano* **2010**, *4*, 1837.

(80) Sacra, A.; Norris, D. J.; Murray, C. B.; Bawendi, M. G. *J. Chem. Phys.* **1995**, *103*, 5236.

(81) Boulesbaa, A.; Huang, Z.; Wu, D.; Lian, T. *J. Phys. Chem. C* **2010**, *114*, 962.

(82) Song, N.; Zhu, H.; Jin, S.; Zhan, W.; Lian, T. *ACS Nano* **2011**, *5*, 613.

(83) Sambur, J. B.; Parkinson, B. A. *J. Am. Chem. Soc.* **2010**, *132*, 2130.

(84) Makhal, A.; Yan, H.; Lemmens, P.; Pal, S. K. *J. Phys. Chem. C* **2010**, *114*, 627.

(85) Dabbousi, B. O.; RodriguezViejo, J.; Mikulec, F. V.; Heine, J. R.; Mattoussi, H.; Ober, R.; Jensen, K. F.; Bawendi, M. G. *J. Phys. Chem. B* **1997**, *101*, 9463.

(86) Marcus, R.; Sutin, N. *Biochim. Biophys. Acta* **1985**, *811*, 265.

# Appendix 1.

## TA spectra and kinetics of free CdTe seed and CdTe-AQ complex

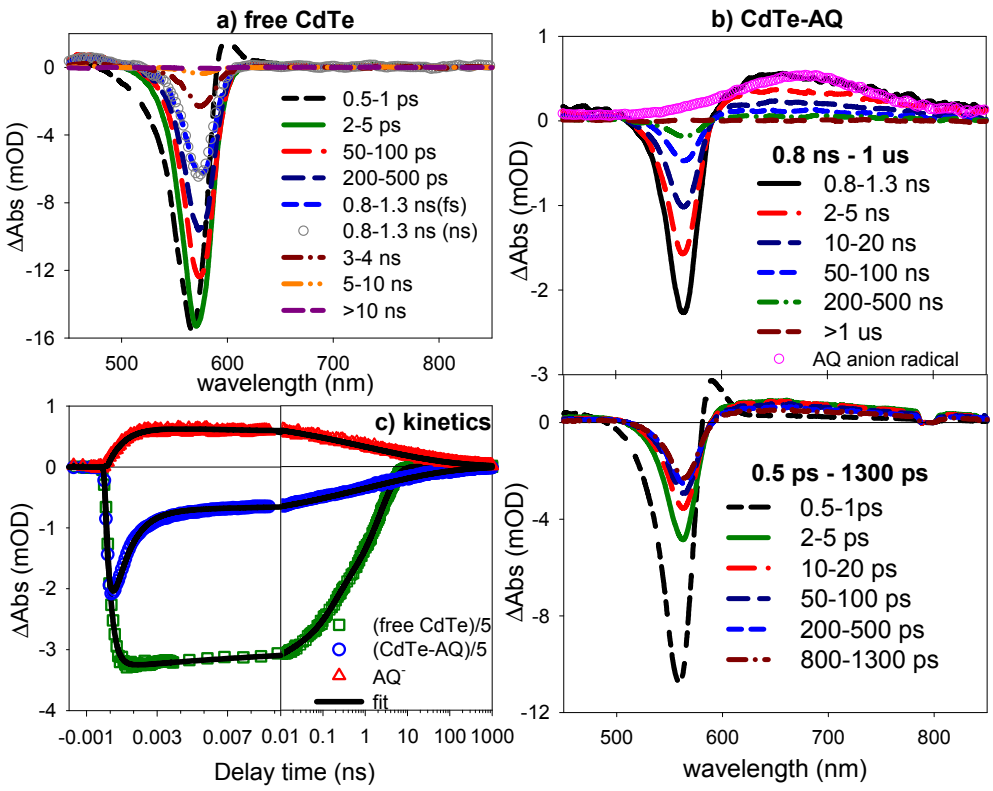


**Figure A.5.1.** Averaged TA spectra of free CdTe (a) and CdTe-AQ complexes (b) at indicated delay time windows after 400 nm excitation. The vertical scale in the upper panel (0.8 ns-2 μs) in b) has been expanded relative to the lower panel (0.5 to 1300 ps) to clearly show the spectra of the charge separated state. A TA spectrum of $AQ^-$ (pink open circles) is also shown in b). (c) Comparison of the kinetics of 1S exciton bleach in free CdTe QDs (green circles), and the 1S exciton bleach (blue circles) and $AQ^-$ absorption

(red triangle) in CdTe-AQ complexes. The horizontal axis is in linear scale in the left panel (0-0.01 ns) and logarithmic scale in the right panel (0.01-1000 ns). The signal size of the 1S exciton bleach in CdTe and CdTe-AQ has been reduced by a factor of 5 for better comparison with the kinetics of $AQ^-$. The solid lines are fits according to eq. A.5.1-A.5.2.

For comparison, exciton dynamics in CdTe QDs and charge separation and recombination kinetics in CdTe-AQ complexes are also studied by TA spectroscopy. As shown in Figure A.5.1a, the bleach of 1S exciton band (~560 nm) in free CdTe QDs is fully formed within 500 fs afternoon 400 nm excitation and recovers completely within 10 ns. As discussed in the main text, the bleach signal can be attributed to the state filling of the 1S electron level in the conduction band. To follow the formation and decay of the 1S electron, we have plotted the kinetics of 1S exciton bleach (at 560 nm) of free CdTe in Figure A.5.1c. It can be well fitted by a single-exponential rise and three-exponential decay (equation A.5.1). From the best fit parameters, listed in Table A.5.1, the rise time ($1/k_0$) is determined to be 300 fs, which reflects the cooling time of initially excited higher energy electron to the 1S level in the conduction band. The half-life of the 1S electron in the free CdTe QDs is calculated to be 0.62 ns.

$$\Delta A(\lambda) = A_{QD^*}(\lambda)[\sum_{i=3} a_i e^{-k_i t} - e^{-k_0 t}] \qquad \text{(A.5.1)}$$

As shown in Figure A.5.1b, the 1S exciton bleach in CdTe-AQ complexes shows an ultrafast recovery (with rate $k_{ET}$) in the first ~5 ps, indicating a much shorter-lived 1S electron in the CdTe conduction band. In addition, there is also a broad positive

absorption band at around 650 nm, which can be assigned to one electron reduced AQ radical ($AQ^-$). These features suggest a fast electron transfer from CdTe to AQ. The TA spectra of the charge-separated state, $CdTe^+(h)$-$AQ^-$, consist of a bleach in the 1S exciton band due to charge separation induced stark effect and the $AQ^-$ absorption. These signals decay with the same kinetics, as indicated by the clear isosbestic point (at ~590 nm) in Figure A.5.1b. This decay can be attributed to the charge recombination process, which regenerates the CdTe and AQ ground state.

The kinetics at 650 nm (due to $AQ^-$ only) and at 560 nm (both 1S exciton bleach and $AQ^-$) are shown in Figure A.5.1C. These kinetics are fitted according to equation A.5.2

$$\Delta A(\lambda, t) = A_{QD^*}(\lambda)(-e^{-k_0 t} + e^{-k_{ET} t}) + A_{CS}(\lambda)(-e^{-k_{ET} t} + e^{-\left(\frac{t}{\tau}\right)^{\alpha}}) \qquad (A.5.2)$$

The first part of eq A.5.2 accounts for the formation and decay of 1S electron, in which $k_0$, the hot electron relaxation rate, is assumed to be the same as in free CdTe QDs (1/3.3 $ps^{-1}$) and $k_{ET}$ is the transfer rate of the 1S electron (to AQ). The second term accounts for the growth and decay of the TA spectral features of the charge separated state. The growth process is attributed to charge separation with rate constant $k_{ET}$. The decay process can be attributed to charge recombination, which can be best described by a stretch exponential function with a time constant ($\tau$) and exponent ($\alpha$). This model satisfactorily fit the kinetics at 560 nm and 650 nm, as shown in Figure A.5.1c. The fitting parameters are listed in Table A.5.1.

**Table A.5.1.** Fitting parameters for free CdTe, CdTe-AQ kinetics according to eq. A.5.1-A.5.2.

| free CdTe | $A_{QD}$* | $k_0$, $ps^{-1}$ | $k_{R1}$, $ns^{-1}$ ($a_1$) | $k_{R2}$, $ns^{-1}$ ($a_2$) | $k_{R3}$, $ns^{-1}$ ($a_3$) |
|---|---|---|---|---|---|
| ΔA(560nm) | -0.0034±0.0001 | 3.25±0.27 | 50±4 (0.08±0.02) | 6.2±0.1 (0.26±0.05) | 0.46±0.08 (0.66±0.08) |
| CdTe-AQ | $A_{QD}$* | $A_{CS}$ | $k_{ET}$, $ps^{-1}$ | τ, $ns^{-1}$ | α |
| ΔA(560 nm) | -0.0037±0.0004 | -0.0009±0.0001 | 1.04±0.24 | 1.08±0.18 | 0.21±0.02 |
| ΔA(650 nm) | 0 | 0.00085±0.00016 | | | |

# Chapter 6. Multiexciton Annihilation and Dissociation from CdSe/CdS Quasi-type II Quantum Dots: the Effect of Band Alignment



## 6.1. Introduction

Direct solar-to-fuel conversion is a promising approach for generating renewable clean energy.[1] Many desirable solar fuel forming reactions require multiple reduction and oxidation steps.[2-4] For example, the oxidation of water ( $2H_2O \rightarrow O_2 + 4H^+ + 4e^-$ ) requires the removal of four electrons and the formation of $H_2$ from protons ( $2H^+ + 2e^- \rightarrow H_2$ ) needs the addition of two electrons. Thus solar-to-fuel conversion devices require not only efficient catalysts to accelerate the reactions, but also a machinery to accumulate multiple electrons/holes needed in the catalytic centers through sequential single photon absorption and single electron transfer events in light harvesting components. In photosynthetic systems in nature, the four oxidative equivalents needed to oxidize water are accumulated by the use of Z-scheme, in which finely tuned protein arrays with specific spatial distributions and energetic gradients enable eight sequential

single photon induced long distance single electron transfers while suppressing charge recombination.[5,6] Most molecular chromophores, like the ones used in natural photosynthetic systems, change their absorption properties dramatically upon excitation or redox events, often losing the ability to harvest additional solar photons until returning to its initial state.[7] Due to delocalized electrons and continuous electronic levels in the conduction and valence bands, semiconductor nanomaterials can continue to absorb efficiently after accumulation of electrons and/or holes, a unique property that may provide an alternative approach to construct simpler artificial photosynthetic systems.

Using semiconductor nanocrystals or quantum dots (QDs) as light harvesting and charge separation materials in solar energy conversion devices have been a subject of intense recent interest.[8-11] Semiconductor nanocrystals can generate and accumulate multiple excitons through either direct multi-exciton generation (MEG) by one high energy photon or multiple photons absorption (MPA).[12-16] In bulk semiconductors, diffusion of electrons/holes from the interior to the surface attached catalysts can be inefficient because of their limited surface areas and competitive electron-hole recombination processes.[17] In semiconductor QDs and related nanostructures, in addition to the increased catalyst concentration afforded by the large effective surface area (due to larger surface area/volume ratio), the confinement of electrons and holes lead to enhanced amplitudes of their wave functions at the surface, enabling direct and efficient dissociation of excitons by interfacial electron or hole transfer to surface adsorbed acceptors or catalysts.[11,18-24] Unfortunately, the small volume of quantum dots enhances exciton Auger recombination process, wherein an electron-hole pair (exciton) nonradiatively recombines by transferring its energy to a third carrier (Figure 6.1).[25-27]

The Auger recombination occurs on the 10-100 ps time scale for biexcitons in CdSe QDs, and its rate becomes faster with increased number of excitons, competing with the extraction of multiple electrons and holes needed to drive photocatalytic reactions.[26,28] Furthermore, efficient photocatalysis requires not only fast interfacial charge separation but also slow charge recombination (back reaction). In small nanoparticles, both the amplitudes of electron and hole wave functions at the surface are enhanced, speeding up both the initial charge separation and the subsequent charge recombination processes.[20,29] Therefore, in QDs, both the enhanced exciton Auger recombination and interfacial recombination of the separated charges hinder their applications as multi-electron/hole transfer centers in photocatalytic systems (Figure 6.1).

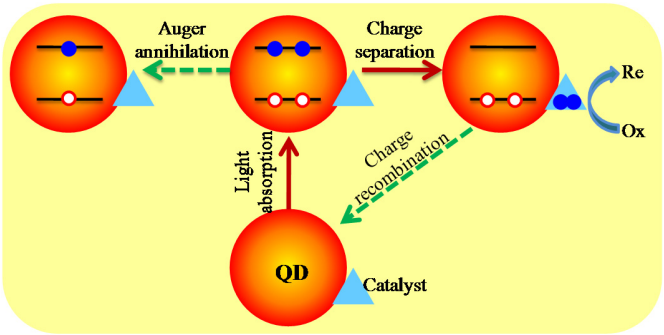


**Figure 6.1.** The competition of multi-exciton dissociation and catalysis with exciton annihilation and charge recombination processes in quantum dot-catalyst complexes.

In colloidal heteronanostructures (core/shell QDs or nanorods), the relative conduction band (CB) and valence band (VB) positions of the component materials can be chosen to tailor the electron and hole distributions (i.e. wave function engineering) to

control the single and multiple exciton lifetimes within the nanostructure as well as to optimize the rate and efficiency of interfacial charge transfer to external acceptors.[30-36] It has been shown that in type II or quasi-type II core/shell QDs, such as CdTe/CdSe and CdSe/CdS QDs, respectively, the spatially separated 1S electron and hole wave functions reduced their Coulomb interaction, increasing the lifetimes of single and multiple exciton states.[31,37-39] Type II core/shell QDs with shell-localized 1S electrons and core-localized 1S holes can achieve ultrafast electron transfer (ET) to adsorbed acceptors while simultaneously retard the charge recombination process.[18,19] The combined properties of long multi-exciton lifetimes as well as efficient charge separation and slow recombination in (quasi-) type II heterostructures suggest that these may be ideal materials for delivering multiple electrons to catalysts or redox mediators in artificial photosynthetic systems.

In this chapter, we investigate the capability of CdSe/CdS quasi type II core/shell QDs for storing multiple excitons and transferring multiple electrons to surface adsorbed methylviologen ($MV^{2+}$) molecules (a widely used electron acceptor and mediator). We show that compared with CdSe or CdS core only QDs, the delocalized electron wave function in CdSe/CdS QDs maintains ultrafast electron transfer to $MV^{2+}$ whereas the strongly core confined hole wave function greatly slows down the interfacial charge recombination process. The efficient charge separation and lengthened multi-exciton lifetime in these materials enables efficient photo-driven multiple electron transfer to adsorbed $MV^{2+}$ molecules. As many as nineteen excitons can be generated in one CdSe/CdS QD under 400 nm excitation, and in the presence of adsorbed $MV^{2+}$, all

nineteen excitons can be dissociated by interfacial electron transfer. This result demonstrates the feasibility of using nano-heterostructures as multi-electron transfer centers for photocatalytic reactions.

## 6.2. Results and Discussion

### 6.2.1. Characterization of CdTe/CdSe Type II QDs

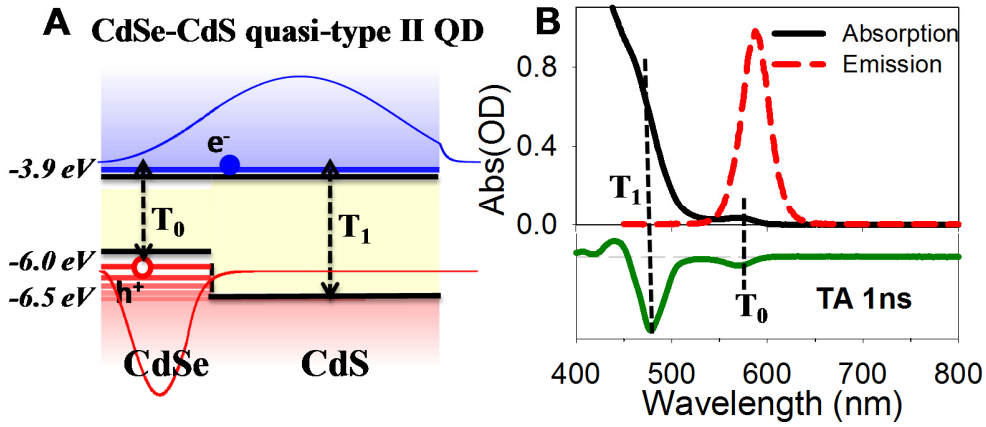


**Figure 6.2.** (A) Schematic energy level diagram and lowest energy electron and hole wave functions in CdSe/CdS (core/shell) quasi-type II QDs. According to an effective mass calculation (see SI3), the electron wave function (blue solid line) is delocalized and hole wave function (red solid line) is localized in the core. The black dashed vertical arrows connect the levels involved in the $T_0$ and $T_1$ transitions and the curved arrows indicate the electron and hole relaxation processes after 400 nm excitation (blue arrow).

(B) Static absorption (black solid line) and static emission (red dashed line) and transient absorption (at 1ns, green line) spectra of CdSe/CdS QDs.

The prepared CdSe/CdS core/shell QD has a CdSe core of ~1.2 nm radius and a CdS shell with thickness ~2.2 nm. As shown in Figure 6.2B, the static ultraviolet and visible (UV-vis) absorption spectrum of CdSe/CdS core/shell QDs exhibits a peak at 575 nm (denoted as $T_0$) and a much more intense bulk-like continuous absorption band with an onset at ~475 nm (denoted as $T_1$), which is more clearly seen in the transient absorption (TA) spectrum. The $T_0$ band is close to the emission peak at 590 nm (Figure 2B) and can be assigned to the transition between the lowest energy CB electron ($1S_e$) and VB hole ($1S_h$) levels in the core/shell structure ($1S_e$-$1S_h$). As shown in the transient absorption (TA) spectrum at 1 ns (Fig. 2B), the formation of 1S exciton state leads to bleaches at both the $T_1$ and $T_0$ bands, suggesting that these transitions involve the same $1S_e$ level. Therefore, the $T_1$ band is assigned to the transition between the delocalized $1S_e$ level and the lowest energy hole level above the VB band edge of the CdS shell. The transitions between the quasi continua of higher energy electron and hole levels give rise to the bulk-like absorption feature seen in Figure 6.2B.

To support the assignment of the $T_0$ and $T_1$ transitions and the band alignment in the CdSe/CdS QDs, we conducted effective mass calculation to determine the energies and wave functions of the lowest energy (1S) electron and hole levels.[18,19,36-38,40] The effective mass of electrons (holes) is $m_e^* = 0.13$ ($m_h^* = 0.45$) in CdSe and 0.2 (0.7) in CdS and the bandgap energy of CdSe and CdS are 1.7 eV and 2.5 eV.[36,38,40] The bulk

conduction (CB) and valance (VB) band edge positions are -4 V and -5.7 V relative to vacuum and 0 and -8.4 in the surrounding organic medium.[41] The conduction band offset ($\Delta E_c$) between CdSe and CdS is not well established, ranging from 0.3 eV (the band offset of bulk semiconductors) to 0 eV (when considering lattice strain at the interface).[32,33,42,43] Assuming $\Delta E_c$=0 (or CdS CB edge at -4 V and VB edge at -6.5 V), the calculated 1S electron/hole radial probability distributions clearly show a delocalized CB electron (throughout the core and shell) and a CdSe core confined VB hole as shown in Figure 6.2A, consistent with a quasi-type II band alignment. The calculated confinement energies (and energy relative to the vacuum level) for the 1S electron and hole are 0.1 (-3.9) and 0.3 (-6.0) eV, respectively. This yields a band gap of 2.1 eV, which agrees well with the measured $T_0$ transition energy of 2.15 eV. The calculated energy between the 1S electron level and CdS valance band edge is 2.6 eV which also agrees well with the $T_1$ transition energy (2.61 eV). This calculation confirms the assignment of $T_0$ ($1S_e$ - $1S_h$) and $T_1$ ($1S_e$ - $VB_{CdS}$) transitions. Our calculation also shows that assuming a band offset $\Delta E_c$ of 0.3 eV, the core/shell structure still maintains a Quasi-type II band alignment and the calculated $T_0$ and $T_1$ transition energies decrease by 0.06 and 0.15 eV, respectively, which agrees less well with the experimental values.

To further confirm the nature of $T_0$ and $T_1$ transitions and examine carrier relaxation dynamics within the core/shell structure, we conducted an excitation wavelength dependence study of CdSe/CdS QDs, as shown in figure 6.3. These measurements were carried out with excitation power density of (~27 $\mu W/cm^2$), under which the signal is dominated by single exciton states with negligible contribution of

multi-exciton dynamics. In TA spectra of CdX (X=S,Se, Te) QDs, transient bleach of optical transitions are caused by the state filling of the conduction band electron levels.[44,45] Upon 565 nm excitation (near the $T_0$ transition), both the bleach at the $T_0$ and $T_1$ transitions are formed instantaneously (<50 fs risetime) and show negligible decay on the picoseconds and longer time scale. It confirms that the lowest energy $1S_e$ is involved in both transitions as depicted in Figure 6.2A.

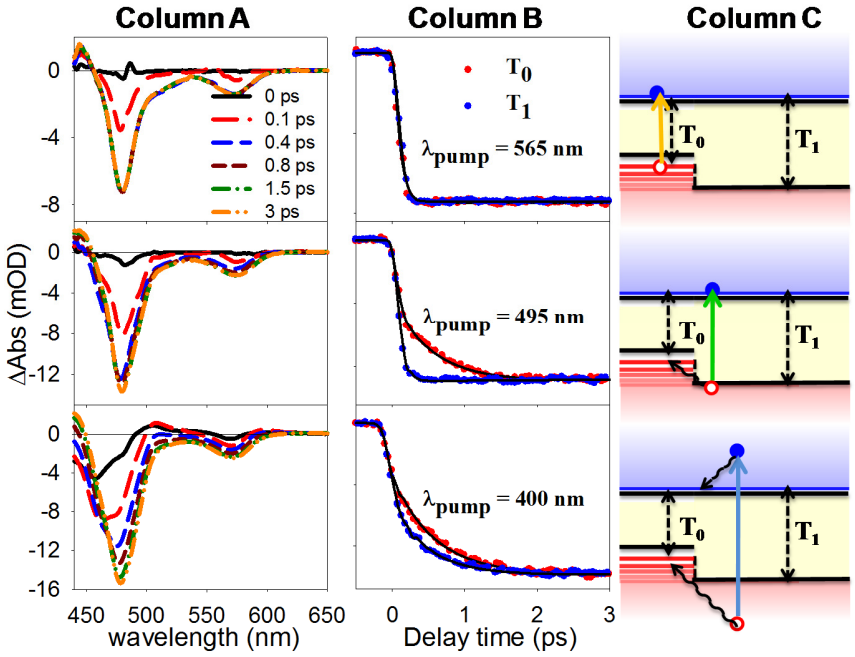


**Figure 6.3.** Column A: early time (0-3 ps) transient absorption spectra of CdSe/CdS under different excitation wavelength (565nm, 495nm and 400nm from upper to lower panels); Column B: Transient bleach recovery of $T_0$ (575 nm) and $T_1$ (475 nm) bands at indicated txcitation wavelength, revealing the nature of electron and hole levels involved

in these transitions. Column C: schematic depiction of electron and hole relaxation processes under different excitation wavelengths.

Upon excitation at 495 nm, which directly populates an electron/hole pair in CdS shell based $T_1$ transition ($1S_e$ - $VB_{CdS}$), the bleach at $T_1$ band forms instantaneously while the bleach at $T_0$ shows a clear biphasic formation feature (an instantaneous formation and a slower growth). The instantaneous rise corresponds to direct electron occupation at $1S_e$ state which leads to the bleaches in both $T_0$ and $T_1$ while the slower rise in $T_0$ is attributed to the hole localization process from the CdS shell to CdSe core valance band and consistent with the quasi type II band alignment in these core/shell QDs. Interestingly, the relaxation of the hole doesnot result in a decay of the $T_1$ bleach. We also show that in the presence of electron acceptors both the $T_1$ and $T_0$ bleach recover completely, suggesting that these signals are dominated by the state filling of the 1S electron level. It suggests that the hole localization process likely affect the electron distribution in the 1S level, leading to an increase in the $T_0$ bleach signal.

Under 400 nm excitation, (which creates both the electron and hole above the CdS band edges), the bleach of the $T_1$ transition region appears initially at higher energy and shows a time dependent continuous red-shift to the final $T_1$ band position, corresponding to the relaxation of the initially excited hot electrons to the $1S_e$ level. This relaxation process leads to a growth of the bleach at $T_0$ band, but no change in the spectral shape was observed, indicating this transition involves only the $1S_e$ and $1S_h$ level. The growth

of the $T_0$ bleach also contains the hot hole localization dynamics, giving rise to a slower formation time.

To extract the carrier relaxation dynamics, we conducted a global fitting to the excitation wavelength dependent kinetics of $T_0$ and $T_1$:

565nm: $A_{T_0,T_1}(t) = -\exp(-k_{ins}t) + \exp(t/\tau_{rec})$ (6.1a)

495nm: $A_{T_1}(t) = -\exp(-k_{ins}t) + \exp(t/\tau_{rec})$ (6.1b)

$$A_{T_0}(t) = -a_e * \exp(-k_{ins}t) - (1-a_e)\exp(-k_{hr'}t) + \exp(t/\tau_{rec}) \quad (6.1c)$$

400nm: $A_{T_1}(t) = -\exp(-k_{er}t) + \exp(t/\tau_{rec})$ (6.1d)

$$A_{T_0}(t) = -a_e * \exp(-k_{er}t) - (1-a_e)\exp(-k_{hr''}t) + \exp(t/\tau_{rec}) \quad (6.1f)$$

In these equations, $k_{rec}$ is the exciton recombination rate which is much longer than 1 ns; $k_{er}$ is the electron relaxation rate at 400 nm excitation and is same for both $T_0$ and $T_1$; $k_{hr'}$ and $k_{hr''}$ are the hole localization rates at 495 nm and 400 nm excitation, respectively. (1- $a_e$ ) is the amplitude of the kinetic component corresponding to the hole localization process. As shown in Figure 6.3, this model yields satisfactory fits to the kinetics. The fitting parameters are listed in Table S1. From the fit, we determined a hot electron relaxation rate of 1.97 ± 0.08 $ps^{-1}$ (or ~0.5 ps) and hole localization rate of 1.61 ± 0.07 $ps^{-1}$ (or ~0.7 ps) upon 400 nm excitation.

**Table 6.1.** Fitting parameters for the $T_0$ and $T_1$ bleach formation kinetics.

| $a_e$ | $k_{er}$ | $k_{hr'}$ | $k_{hr''}$ | $\tau_{rec}$ |
|---|---|---|---|---|
| 0.56±0.02 | 1.97±0.08 $ps^{-1}$ | 1.61±0.07 $ps^{-1}$ | 1.50±0.06 $ps^{-1}$ | >> 1ns |

### 6.2.2. Single Exciton Charge Separation and Recombination Kinetics in CdSe/CdS QDs

The TA spectra of free CdSe/CdS QDs and CdSe/CdS-$MV^{2+}$ complexes at 5 ps are compared in Figure 6.4A and the corresponding kinetics at $T_0$, $T_1$ and 630 nm in the first 5 ps are compared in Figure 6.4B. These spectra were recorded under the same single exciton excitation conditions. In QD-$MV^{2+}$ complexes, the adsorption of $MV^{2+}$ reduces the exciton lifetime, as indicated by the completely quenching of QD emission (data not shown) and ultrafast recovery of the exciton bleaches in the transient absorption spectra. The bleaches at the $T_1$ and $T_0$ bands show much smaller initial amplitudes and almost completely recovery in the first 5 ps when free QDs do not show any decay(Figure 6.4B & C), suggesting an ultrafast (hot) electron transfer from the QD to $MV^{2+}$and the injection yield is unity. Concomitant with the QD exciton bleach recovery, a positive absorption band above 600 nm and forms and reaches maximum in 5 ps (Figure 6.4D), which matches well with the absorption spectrum of $MV^{+}$ radicals (Figure 6.4A inset). In addition, a derivative feature shows up below 600 nm after charge separation, which can be attributed to the shift of the QD exciton band by charge separation induced electric field.[18,19] Both positive $MV^{+}$ radical and charge separated

state induced shiftting confirm the ultrafast electron transfer from CdSe/CdS QDs to $MV^{2+}$ molecules. The growth and decay of the $MV^{+}$ radical signal at 630 nm can be fitted by multiple-exponential and stretched exponential functions, respectively. From the fit, we determine a half-life time of 0.18 ± 0.02 ps and 425 ± 20 ns for the charge separation and charge recombination processes, respectively.

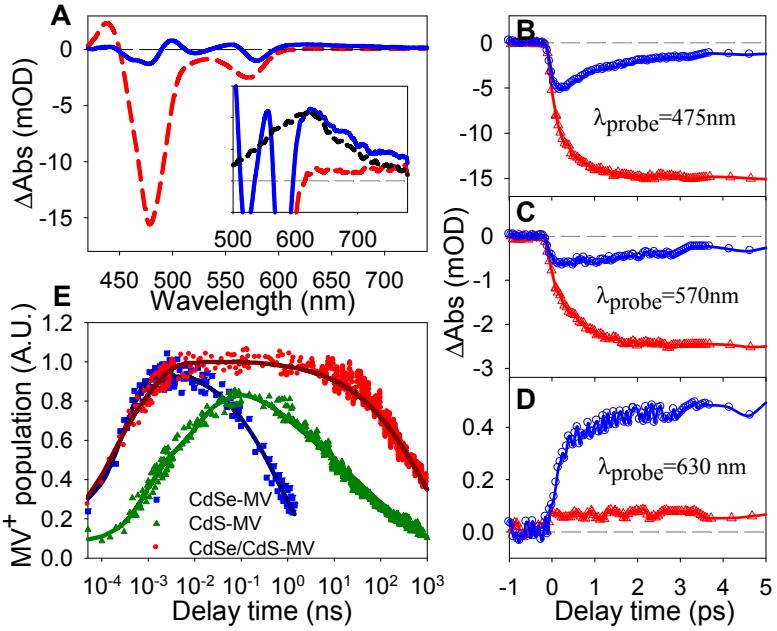


**Figure 6.4.** (A) TA spectra of free CdSe/CdS QDs (red dashed line) and CdSe/CdS-$MV^{2+}$ complexes (blue line) at 5 ps after 400nm excitation under single exciton conditions (~ 27 μW/cm$^2$). (Inset) An expanded view of the spectra at 500-750 nm and a comparison with $MV^{+}$ radical spectrum (dashed black line), showing photo-generated $MV^{+}$ radicals in the QD-$MV^{2+}$ complexes. (B, C, D) Comparison of TA kinetics probed at (B) 475 nm ($T_1$), (C) 570 nm ($T_0$) and (D) 630 nm ($MV^{+}$ radical) in free CdSe/CdS

QDs (red circle) and CdSe/CdS-$MV^{2+}$ complexes (blue triangle). (E) Comparison of normalized $MV^{+}$ radical formation and decay kinetics in QD-$MV^{2+}$ complexes of CdSe (blue), CdS (green) and CdSe/CdS (red) after 400 nm excitation.

As a comparison, the charge separation and recombination kinetics in CdSe-$MV^{2+}$ and CdS-$MV^{2+}$ complexes were also investigated. The details of their TA spectra, kinetics and analysis can be found in Appendix 6.1 and Appendix 6.2. The kinetics of $MV^{+}$ radical formation measured at ~ 630 nm in CdSe, CdS and CdSe/CdS QDs are compared in Figure 6.4E. The actual reason for the relatively slower charge separation and recombination from CdS QDs than CdSe QDs in QD-MV complex is not clear to us and requires further investigation. Obviously, compared to CdSe core only QDs, CdSe/CdS core/shell quasi type II QDs maintain a similar ultrafast charge separation rate but slow down the charge recombination process by ~ 1000 times. This much improved charge separation property can be attributed to the electron and hole distributions in the quasi-type II material: the delocalization of the CB electron maintains a large amplitude of electron wave function at the shell surface, enabling an ultrafast electron transfer to the adsorbates, whereas the strongly core confined VB hole reduces electronic coupling strength for the charge recombination process, resulting in a much longer lived charge separated state.[19]

### 6.2.3. Multi-Exciton Dyanmics in CdSe/CdS QDs

To investigate the exciton-exciton annihilation dynamics and quantify the average number of excitons generated in CdSe/CdS QDs, we recorded TA spectra in free QDs as a function of excitation intensities from ~27 to ~4250 μW/cm$^2$ (see Appendix 3). A representative set of TA spectra of CdSe/CdS QDs recorded at the highest excitation intensities (4250 μW/cm$^2$) is shown in Figure 6.5A. In addition to the bleaches at $T_1$ and $T_0$ bands, the transient spectra show two broad photoinduced absorption (PA) bands centered at ~ 640 nm ($PA_1$) and 825 nm ($PA_2$). The $PA_1$ feature extends into the $T_0$ band, but its contribution can be subtracted to reveal the kinetics of $T_0$ bleach only, which are shown in Figure 5A.[44] As shown in Figure 6.6, under the presence of electron acceptor Benzoquinone (BQ), these PA bands were shown to remain unchanged when the 1S electrons were transferred to electron acceptors. Therefore, the PA signal can be attributed to transitions involving the VB hole in the QD. At all excitation intensities, the amplitudes of these features ($T_0$, $T_1$, PA) initially grow and reach a maximum at $t_{max}$ due to the initial hot electron and hole cooling process. The value of $t_{max}$ ranges from 0.3 to 2 ps, becoming shorter with increasing excitation intensity, reflecting the carrier density dependent hot electron and hole relaxation time.[45]

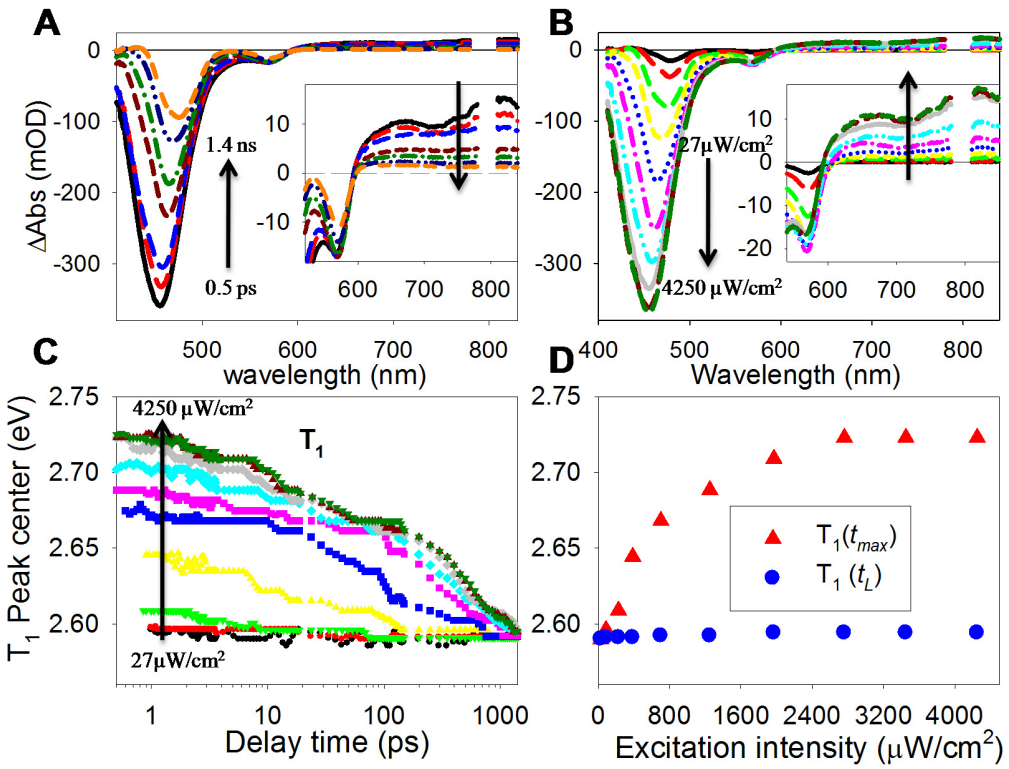


**Figure 6.5.** (A) TA spectra of CdSe/CdS QDs from 0.5 ps to 1.4 ns (0.5 ps, 3 ps, 10 ps, 50 ps, 100 ps, 500 ps, 1.4 ns from lower to upper) at the highest 400 nm excitation intensity (~4250 μW/cm$^2$) (B) TA spectra at $t_{max}$ (when the bleach amplitudes are largest) under different excitation intensities (from 27 to 4250 μW/cm$^2$). The spectra between 500-840 nm are expanded in the inset of A) and B) to more clearly show the photoinduced absorption features at > 600 nm. (C) The time evolution of the $T_1$ bleach peak position at different excitation intensities. (D) $T_1$ bleach peak positions at $t_{max}$ and $t_L$ =1.4 ns as a function of the excitation intensity.

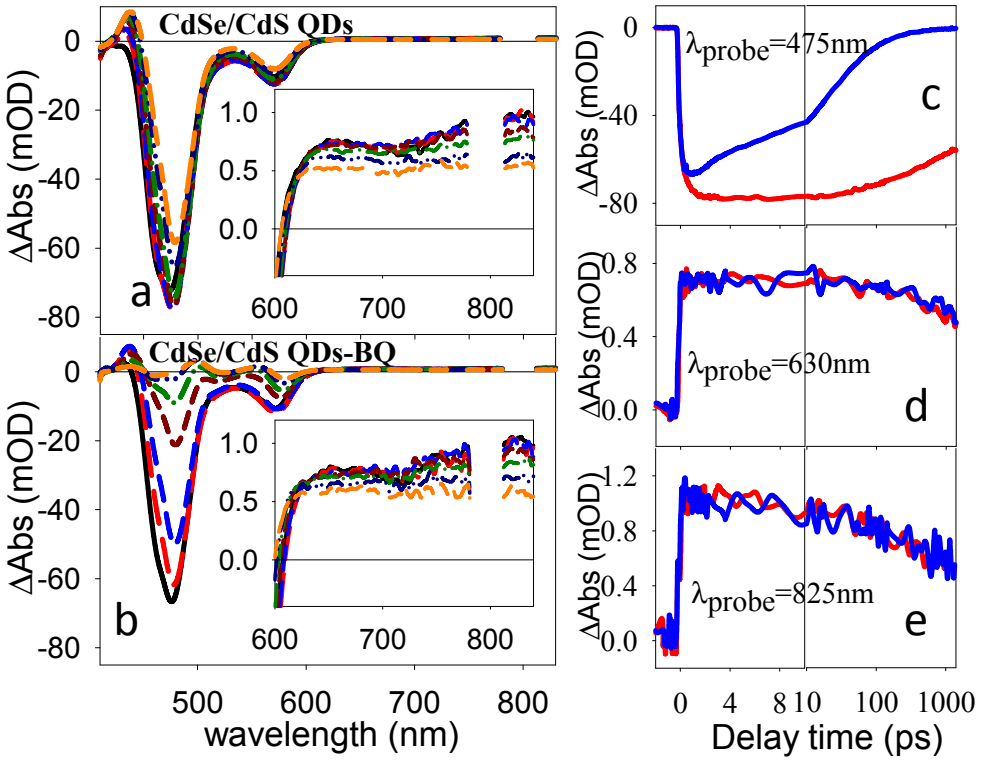


**Figure 6.6.** Left column: TA spectra of CdSe/CdS QDs without (a) and with (b) adsorbed BQ. The curves from black to orange correspond to delay time windows of 0.5-1 ps, 2-3 ps, 5-10 ps, 30-50 ps, 70-150 ps, 200-600 ps, 800-1400 ps after 400 nm excitation. The data from 600-850 nm are expanded in the insets of a) and b). Right column: comparison of bleach recovery kinetics at c) $T_1$ (475nm) and d) $PA_1$ (630nm) and 3) $PA_2$ 825nm) bands. The horizontal axis is in linear scale in the left panel (0- 10 ps) and in logarithmic scale in the right panel (10ps -1.4 ns) The much faster bleach recovery of $T_1$ indicates electron transfer in QDs-BQ complex while PA shows identical kinetics in QD and QD-BQ, indicating the these signals can be attributed to hole transitions.

At the lowest excitation intensity, there are negligible changes in the peak position and amplitude of these features ($T_1$, $T_0$, $PA_1$ and $PA_2$) between $t_{max}$ and 1.4 ns, indicating that the signal is dominated by the long-lived single exciton state, as discussed previously. At higher excitation intensities, these features show fast decay components (Figure 6.5A and 6.5B) caused by fast exciton-exciton annihilation processes. At all excitation intensities, the transient spectra and kinetics after 1.4 ns ($t_L$) become identical to those at the lowest excitation intensity, suggesting the completion of multi-exciton annihilation at this delay time and negligible sample degradation under all excitation intensities. However, between $t_{max}$ and 1.4 ns ($t_L$), these features exhibit different excitation intensity dependence in their amplitudes, peak positions and decay kinetics. For example, the $T_0$ bleach amplitude recovery kinetics become independent of the excitation intensity after 1250 $\mu W/cm^2$ (Figure 6.5A), while the $PA_2$ kinetics (amplitude and kinetics) and $T_1$ bleach (amplitude and peak shift) saturates at higher excitation intensity (3450 $\mu W/cm^2$). As will be discussed below, these variations indicate different dependence on the number of excitons and reflect the different degeneracy of these transitions.

We first compare the TA spectra at $t_{max}$ (Figure 6.5B) and the peak positions (Figure 6.5C) as a function of delay time for the $T_1$ bleach at all excitation intensities. At higher excitation intensities, the amplitude of $T_1$ bleach (at $t_{max}$) increases, its width broadens, and peak position shifts to higher energy. These features suggest the filling of more and higher energy CB electron levels at higher excitation intensities, similar to the band filling induced dynamic Burstein-Moss shift observed in many semiconductor

materials.[46-48] We model the observed intensity dependence of $T_1$ bleach spectra by assuming a bulk like density of states for $T_1$ and higher energy transitions (see Appendix 4 for details).[47] As shown in Figure A.6.4, the calculated spectra reproduce the blue shift, broadening and amplitude increase of the $T_1$ bleach band at higher excitation intensities. The qualitative agreement suggests a quasi-continuum of conduction band states in the CdSe/CdS QDs, consistent with the bulk-like UV-vis absorption features above the $T_1$ transition and the calculated weekly confined electron levels. We note that the initial peak position appears to no longer increase after the excitation intensity reaches 3450 μW/cm$^2$ (figure 6.5D), suggesting the saturation of the number of excitons generated in the QDs.

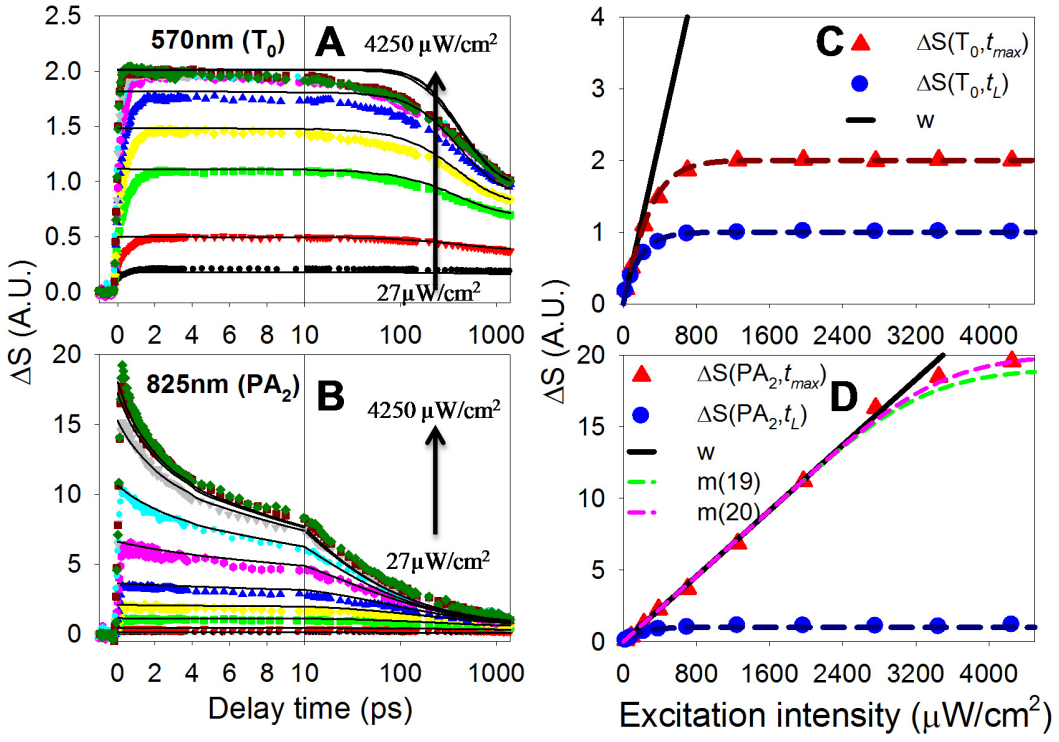

**Figure 6.7.** (Left column) Normalized transient kinetics (open symbols) at T0 (A) and PA2 (B) bands at different excitation intensities. The solid lines are fits to a stochastic multi-carrier annihilation model described in the main text. (Right column) Normalized TA signal of T0 (C) and PA2 (D) at tmax (red circles) and tL (blue triangles) as a function of excitation intensities. The solid and dashed lines in C and D are fits to equations (6.3)-(6.5).

To quantify the number of excitons in the QD at any given excitation intensity level, we analyze the intensity dependence of the TA signal at $T_0$ and $PA_2$ bands. Excitation at 400 nm (or 3.2 eV) creates electron and hole pairs at 1 eV above the band edge. We assume that the probability of a QD encountering *n* photons, *f(n)*, within the laser pulse duration is governed by the Poisson statistics: $f(n) = \frac{w^n e^{-w}}{n!}$.[21,42] Here *w* is the average number of encountered photons, which scales with the excitation pulse energy (*I*), *i.e.* $w = C \bullet I$ . The scaling factor C, dependent on the absorption cross section as well as the pump and probe beam geometries and overlaps, cannot be accurately calculated. Instead, we will rely on the fitting procedure to be discussed below to determine its value, which will enable the determination of the average number of excitons at any given excitation intensity. We assume that there is a maximum number ($N_{max}$) of excitons that can be generated in each QD under our 400nm laser pulse excitation condition. Only excitons with energy covered by 400 nm pulse can be excited and the upper limit is reached when exciton states within 400 nm excitation energy range are all excited. Prior

to $N_{max}$, every QD-photon encounter leads to the absorption of one photon and the generation of one exciton. After that, the random encounter no longer leads to a photon absorption and exciton generation event. At early delay time (t = $t_{max}$, prior to the exciton-exciton annihilation process), the number of excitons (n) generated in a QD can be assumed to obey the Poisson distribution ( $P(n,t_{\max}) = f(n) = \frac{w^n e^{-w}}{n!}$ ) at $n < N_{\max}$ , and saturates at $n=N_{max}$, *i.e.* $P(N_{\max},t_{\max}) = 1 - \sum_{n=0}^{N_{\max}-1} f(n)$. The average number of excitons in the QDs ($m$) is given by:

$$m(N_{\max}) = \sum_{n=0}^{N_{\max}} P(n,t_{\max}) \bullet n \qquad (6.2)$$

It predicts that $m(N_{\max}) = w = C \bullet I$ when $m << N_{max}$, but saturates when $m$ approaches $N_{max}$.

As discussed above, at $t_L$= 1.4 ns, all multiple excitons have annihilated and only single exciton states remain. Therefore, at $t_L$= 1.4 ns, the transient signal amplitudes, $\Delta A(\lambda,t_L)$ , at $T_0$ and $PA_2$ bands are proportional to the number of excited QDs: $\Delta A(\lambda,t_L) = \alpha(\lambda)[1 - P(0,t_{\max})]$ , where $\alpha(\lambda)$ is a wavelength dependent scaling factor that is proportional to the extinction coefficients of these transitions. We define a normalized transient signal:

$$\Delta S(\lambda,t_L) = \Delta A(\lambda,t_L) / \alpha(\lambda) = 1 - P(0,t_{\max}) = 1 - e^{-w} \qquad (6.3)$$

These normalized transient absorption signals represent the probability of finding excited QDs in the ensemble. At high excitation intensities, when all QDs are excited, $\Delta S(\lambda, t_L)$ approaches one, from which we can determine the normalization factor $\alpha(\lambda)$. The transient signals at other delay times are also normalized by the same scaling factor to obtain normalized transient signals, $\Delta S(\lambda, t) = \Delta A(\lambda, t)/\alpha(\lambda)$, which are shown in the kinetics traces in Figure 6.7 A and B.

The transient bleach signal at $T_0$ band is determined by the state filling of the 1S electron level. Because of the 2 fold spin degeneracy of this level, we assume that the $T_0$ bleach amplitude in QDs with multiple ($n \geq 2$) excitons is twice as large as that with a single exciton. Therefore, the initial normalized transient bleach signal at $t_{max}$ is given by:

$$\Delta S(T_0, t_{\max}) = P(1, t_{\max}) + 2[1 - P(0, t_{\max}) - P(1, t_{\max})] = 2 - (2 + w)e^{-w} \qquad (6.4)$$

It predicts that at $w$>>1, when all QDs have two or more excitons, $\Delta S(T_0, t_{\max})$ approaches 2.

The transient absorption signal $PA_2$ appears to increase linearly with excitation power (or the average number of excitons). The corresponding normalized transient signal at $t_{max}$ is:

$$\Delta S(PA_2, t_{\max}) = \sum_n nP(n, t_{\max}) = m \qquad (6.5)$$

The normalized transient signals, $\Delta S(\lambda, t_L)$ and $\Delta S(\lambda, t_{\max})$, at $T_0$ and $PA_2$ bands are plotted as a function of excitation intensities in Figure 6.7 C and D. These data can be fit by equations (6.3)-(6.5) with the scaling factor C (=I/$w$) and $N_{max}$ as the only fitting

parameters. These data are well fit by this model, from which the average number of excitons ($m$) at all excitation powers can be obtained. The normalized transient absorption signal $\Delta S(PA_2, t_{\max})$ (or $m$) increases linearly with the excitation intensity until $m$> 16. At higher excitation intensity, the signal saturates, deviating from a linear dependence on the excitation intensity. Similar saturation behavior was observed in the $T_1$ bleach position (Fig. 6.7D) indicating that there is an upper limit to the number of excitons in the QD. The saturation behavior can be best fit with $N_{max}$=20. Our result suggests that these QDs can achieve a maximum of 20 excitons per QD at our 400 nm laser pulse excitation condition because of pumping saturation. At the highest excitation intensity (4250 μW/cm$^2$) used in this study, the average number of excitons per QD reaches 19 in our sample.

The decay of the normalized transient signals at $T_0$ and $PA_2$ from the initial distribution of multiple excitons states, $\Delta S(\lambda, t_{\max})$, to the final single exciton states, $\Delta S(\lambda, t_L)$, is governed by the multiple exciton decay dynamics. The kinetics at $T_0$ and $PA_2$ are different due to their different dependence on the number of excitons as discussed above. The normalized transient signals at $T_0$ and $PA_2$ transition at delay time $t$ are given by:

$$\Delta S(T_0, t) = P(1,t) + 2[1 - P(0,t) - P(1,t)] \qquad (6.6)$$

$$\Delta S(PA_2, t) = \sum_n nP(n,t) \qquad (6.7)$$

where $P(n,t)$ is the probability of finding QDs with n excitons at time $t$. Assuming that n-exciton state can only decay sequentially (to $n$-1 exciton state) by auger recombination

(with time constant $\tau_n$), the time-dependent distribution of multi-exciton states in QDs is described by a set of coupled rate equations:[26,49,50]

$$\frac{dP(n,t)}{dt} = \frac{P(n+1,t)}{\tau_{n+1}} - \frac{P(n,t)}{\tau_n} \qquad (6.8)$$

The single exciton state lifetime is assumed to be 30 ns. Because it is >> 1.4 ns, it does not significantly influence the kinetics shown in Figure 6.7A and 6.7B. The initial exciton distribution, P(n,$t_{max}$), at a certain excitation power has been obtained from fitting the early time and longer time transient signal amplitudes shown in Figure 6.7C and 6.7D. The Auger recombination time of n-exciton states have been reported to obey quadratic $\tau_n^{-1} \propto n^2$, cubic $\tau_n^{-1} \propto n^3$ or statistical $\tau_n^{-1} \propto n^2(n-1)$ scaling laws, depending on the materials and size.[26,28] From the calculated *P(n,t),* fits to the normalized kinetics at $T_0$ and $PA_2$ can be obtained using equation (6.6) and (6.7), respectively. As shown in Figure 6.7A and B, the kinetics of both $T_0$ and $PA_2$ at most excitation intensities can be well fit by this model with the biexciton lifetime ($\tau_2$) as the only fitting parameter. The statistical scaling law yields the best fit, from which, we obtained thebiexction lifetime and deduced lifetimes of all other higher order-exciton states ($\tau_2 \approx 440$ ps, $\tau_{19} \approx 270$ fs). As a comparison, the biexciton lifetime in the CdSe core only QD (1.2 nm radius, without the CdS shell) is ~6 ps,[26] or 80 times shorter. The biexciton lifetime in a CdSe QDs of the same size (3.4 nm radius) can be estimated to be ~130 ps from a volume scaling law,[25] which is about 4 times shorter. The prolonged biexciton lifetime in CdSe/CdS QDs can be attributed to reduced electron-hole wave function overlap in this quasi-type II structure[37] and possibly to alloy formation at the core/shell interface.[39] The fits deviate

substantially from the experimental data at high exciton number (m > 12) per QDs, the reason for which is yet to be understood. It may suggest the failure the statistical scaling law, which assumes that all electrons and holes are equal in the Auger recombination process, and/or the presence of other recombination pathways at high carrier densities.

### 6.2.4. Multi-Exciton Charge Separation and Recombination

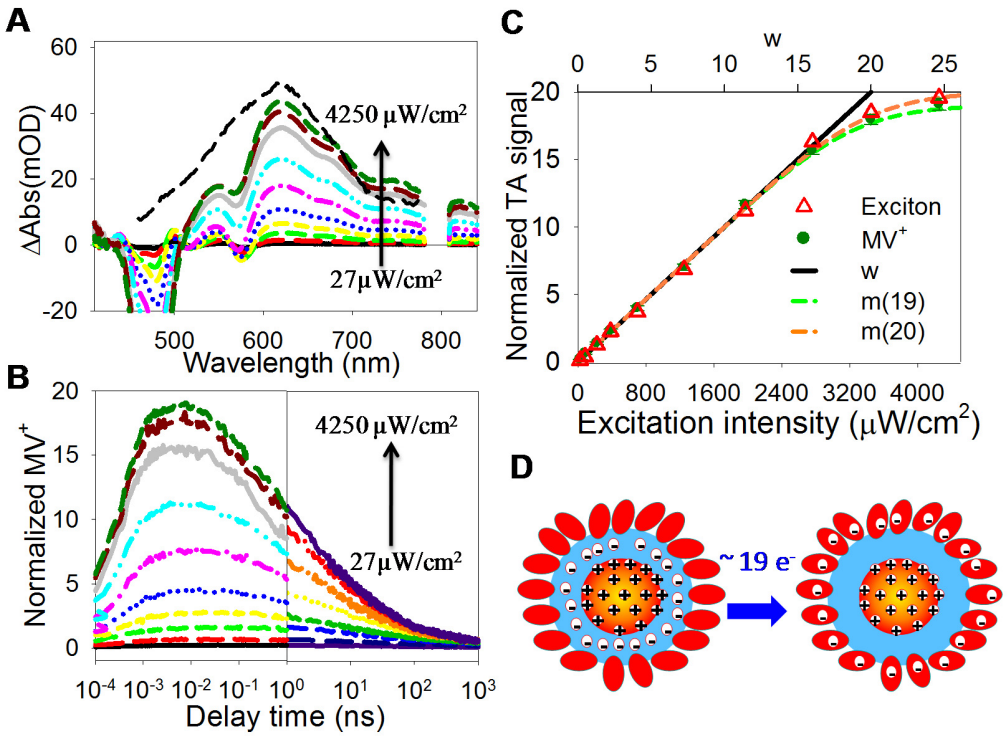


**Figure 6.8.** (A) Average TA spectra of QD-$MV^{2+}$ complexes at 8-10 ps (when the $MV^{+}$ radical signal has reached maximum) at indicated excitation intensities. (B) Kinetics of normalized $MV^{+}$ radical TA signal at 630 nm in QD-$MV^{2+}$ complexes. The normalized

$MV^+$ radical signal represents the average number of $MV^+$ radicals per QD (see the main text for details). (C) Normalized $MV^+$ radical signal (at 8-10 ps) in QD-$MV^{2+}$ complexes as a function of excitation intensities. (D) Schematic depiction of ultrafast transfer of 19 electrons from CdSe/CdS QDs to adsorbed $MV^{2+}$ molecules.

We conducted TA measurement on QD-$MV^{2+}$ complexes as a function of excitation intensities under the same conditions as those for free QDs. Because $MV^{2+}$ molecules do not absorb at 400 nm, the average number of excitons generated in the QD-$MV^{2+}$ complex at a given excitation intensity should be the same as in free QDs and have been quantified above. By measuring the average number of $MV^+$ radicals generated under these conditions, the average number of dissociated excitons can be determined. The complete set of transient spectra at different excitation intensities are shown in Appendix 3. It shows the formation of $MV^+$ radical absorption band at 630 nm and the corresponding recovery of the QD exciton bleach at early delay times. The TA spectra at ~ 8-10 ps, when the amplitude of $MV^+$ radical absorption band reaches the maximum, are compared in Figure 6.8A for all excitation intensities. The comparison shows that the amplitude of $MV^+$ radical absorption increases with excitation intensity until it saturates at 3450 μW/cm$^2$ when the average number of excitons per QD also saturates.

The amplitude of $MV^+$ radicals TA absorption signals $\Delta A(MV^+)$ is proportional to the average number of radicals per QD ( $S_{MV^+}$ ): $S_{MV^+} = \Delta A(MV^+)/\alpha(MV^+)$ . Here $\alpha(MV^+)$ is a scaling factor that depends on the extinction coefficients $MV^+$ radical and

QD concentration. As discussed above, at the lowest excitation intensity (when multiple excitons are negligible), every exciton dissociates by electron transfer to $MV^{2+}$ to generate a $MV^{+}$ radical, i.e. $S_{MV^+} = m$. Therefore, we scaled the $MV^{+}$ signal at 630 nm (at 8-10 ps) by a factor $\alpha(MV^+)$ such that it equals to *m* at this low excitation intensity. The same scaling factor is applied to all the measured $MV^{+}$ signal amplitudes (at 8-10 ps) at higher excitation intensities. Thus, the normalized $MV^{+}$ signal represents the average number of $MV^{+}$ radicals (or dissociated excitons) per QD. We note that the TA signal at 630 nm contains a small portion (14% - 18%) of QDs PA signal, which has been determined in the free QD samples and subtracted from the total signal in QD-$MV^{2+}$ complexes to obtain the $MV^{+}$ radical signal. The normalized $MV^{+}$ radical signals at 8-10 ps as a function of excitation intensity are plotted in Figure 6.8C (dark green dot). It shows that the average number of $MV^{+}$ radicals per QD ($S_{MV^+}$) closely follows the average number of excitons generated (*m*) in the free QD --- all excitons generated in the QDs under 400 nm illumination can be dissociated by electron transfer to $MV^{2+}$ to produce $MV^{+}$ radicals with nearly 100% quantum yield. At the highest excitation intensity (4250 μW/cm$^2$), on average, 19 excitons were generated and dissociated from each QD to produce 19.09±0.45 $MV^{+}$ radicals.

To follow the fate of the multiple-charge separated state, we have plotted the normalized $MV^{+}$ radical signals (i.e. the average number of $MV^{+}$ radicals per QD) as a function of time from femtoseconds to microseconds in Figure 6.8B. The data before and after 1.4 ns were acquired at different instruments with different excitation intensities. The kinetics traces acquired at the highest excitation intensities connects smoothly

because the average number of dissociated excitons (and hence $MV^+$ radicals) saturates to the same value in the QDs. Below saturation, these kinetics don't connect well because different excitation intensities. It is interesting to note that the exciton dissociation rates remain ultrafast even when 19 excitons were dissociated. The enhanced electron-electron repulsion and weakened electron-hole attraction in this kind of quasi-type II structures[37,41] may account for this ultrafast multi-electron transfer rates. With increasing number of dissociated excitons, the $MV^+$ radical kinetics shows a faster decay, suggesting a faster charge recombination process (of the holes in the QDs and electrons in $MV^+$ radicals), which is consistent with bimolecular nature of this process. Nevertheless, the half-life times of charge separated states with two and nineteen dissociated excitons in one QD are ~ 80 ns and ~2.3 ns, respectively, in this core/shell structure, suggesting the possibility of driving multi-electron catalytic reactions.

## 6.3. Conclusion

Semiconductor nanomaterials can continue to absorb photons at excited or charged states, offering the possibility to deliver multiple electrons/holes needed in solar-to-fuel conversion devices. The quantum confinement of electron and hole in semiconductor nanocrystals enhances ultrafast charge separation rate, but it also enhances the rates of charge recombination and exciton-exciton annihilation (by Auger recombination), hindering the efficient extraction of multiple carriers. In nano-

heterostructures with type II or quasi type II band alignment, it is possible to tailor the distributions of electron and hole wave functions to selectively control these rates. Using CdSe/CdS quasi-type II core shell QDs, we demonstrate that ultrafast charge separation, ultraslow charge recombination and slow exciton Auger annihilation can be simultaneously achieved. With adsorbed methylviologen molecules as model electron acceptors, nineteen excitons per QD can be dissociated with unity yield by electron transfer to the adsorbed $MV^{2+}$ and the lifetime of the multiple-charge separated state is lengthened considerably compared to core only QDs.

Our study demonstrates that type II nano-heterostructures can be used as potential light harvesting and charge separation components in artificial photosynthetic systems to enhance multiple excitons dissociation efficiencies. For practical applications, it is desirable to remove the valence band holes efficiently by external circuit or other electron sources, which can be facilitated in linear or branched type II heterostructures where both carriers are exposed to charge collection network.[51,52] Furthermore, efficient exciton dissociation would need to be coupled with schemes of generating multiple excitons. Direct MEG by one high energy photon has been reported in type II materials with threshold energy below that for each constituent material.[53] Alternatively, methods to enhance light harvesting rates of nano-heterostructures by plasmonic enhancement[54] and by building large QD-antenna complexes should also be explored.

## References

(1) Lewis, N. S.; Nocera, D. G. *Proc. Natl. Acad. Sci.* **2006**, *103*, 15729.

(2) Gratzel, M. *Nature* **2001**, *414*, 338.

(3) Esswein, A. J.; Nocera, D. G. *Chem. Rev.* **2007**, *107*, 4022.

(4) Walter, M. G.; Warren, E. L.; McKone, J. R.; Boettcher, S. W.; Mi, Q.; Santori, E. A.; Lewis, N. S. *Chem. Rev.* **2010**, *110*, 6446.

(5) Hill, R.; Bendall, F. A. Y. *Nature* **1960**, *186*, 136.

(6) Mitchell, P. *Biol. Rev. Cambridge Philosophic. Soc.* **1966**, *41*, 445.

(7) Bach, U.; Lupo, D.; Comte, P.; Moser, J. E.; Weissortel, F.; Salbeck, J.; Spreitzer, H.; Gratzel, M. *Nature* **1998**, *395*, 583.

(8) Kamat, P. V.; Tvrdy, K.; Baker, D. R.; Radich, J. G. *Chem. Rev.* **2010**, *110*, 6664.

(9) Gur, I.; Fromer, N. A.; Geier, M. L.; Alivisatos, A. P. *Science* **2005**, *310*, 462.

(10) Brown, K. A.; Dayal, S.; Ai, X.; Rumbles, G.; King, P. W. *J. Am. Chem. Soc.* **2010**, *132*, 9672.

(11) Sambur, J. B.; Novet, T.; Parkinson, B. A. *Science* **2010**, *330*, 63.

(12) Nair, G.; Chang, L.-Y.; Geyer, S. M.; Bawendi, M. G. *Nano Lett.* **2011**, *11*, 2145.

(13) Nozik, A. J. *Nano Lett.* **2010**, *10*, 2735.

(14) Beard, M. C. *J. Phys. Chem. Lett.* **2011**, *2*, 1282.

(15) McGuire, J. A.; Joo, J.; Pietryga, J. M.; Schaller, R. D.; Klimov, V. I. *Acc. Chem. Res.* **2008**, *41*, 1810.

(16) Pijpers, J. J. H.; Ulbricht, R.; Tielrooij, K. J.; Osherov, A.; Golan, Y.; Delerue, C.; Allan, G.; Bonn, M. *Nat. Phys.* **2009**, *5*, 811.

(17) Landsberg, P. T. *Recombination in semiconductors*; Cambridge University Press: Cambridge, 2003.

(18) Zhu, H.; Song, N.; Lian, T. *J. Am. Chem. Soc.* **2010**, *132*, 15038.

(19) Zhu, H.; Song, N.; Lian, T. *J. Am. Chem. Soc.* **2011**, *133*, 8762.

(20) Tisdale, W. A.; Williams, K. J.; Timp, B. A.; Norris, D. J.; Aydil, E. S.; Zhu, X.-Y. *Science* **2010**, *328*, 1543.

(21) Huang, J.; Huang, Z.; Yang, Y.; Zhu, H.; Lian, T. *J. Am. Chem. Soc.* **2010**, *132*, 4858.

(22) Matylitsky, V. V.; Dworak, L.; Breus, V. V.; Basche, T.; Wachtveitl, J. *J. Am. Chem. Soc.* **2009**, *131*, 2424.

(23) Dworak, L.; Matylitsky, V. V.; Breus, V. V.; Braun, M.; Basché, T.; Wachtveitl, J. *J. Phys. Chem. C* **2011**, *115*, 3949.

(24) Morris-Cohen, A. J.; Frederick, M. T.; Cass, L. C.; Weiss, E. A. *J. Am. Chem. Soc.* **2011**, *133*, 10146.

(25) Robel, I.; aacute; Gresback, R.; Kortshagen, U.; Schaller, R. D.; Klimov, V. I. *Phys. Rev. Lett.* **2009**, *102*, 177404.

(26) Klimov, V. I.; Mikhailovsky, A. A.; McBranch, D. W.; Leatherdale, C. A.; Bawendi, M. G. *Science* **2000**, *287*, 1011.

(27) Efros, A. L.; Kharchenko, V. A.; Rosen, M. *Solid State Commun.* **1995**, *93*, 281.

(28) Klimov, V. I.; McGuire, J. A.; Schaller, R. D.; Rupasov, V. I. *Phys. Rev. B* **2008**, *77*, 195324.

(29) Tisdale, W. A.; Zhu, X.-Y. *Proc. Natl. Acad. Sci.* **2011**, *108*, 965.

(30) Cragg, G. E.; Efros, A. L. *Nano Lett.* **2010**, *10*, 313.

(31) Zavelani-Rossi, M.; Lupo, M. G.; Tassone, F.; Manna, L.; Lanzani, G. *Nano Lett.* **2010**, *10*, 3142.

(32) Müller, J.; Lupton, J. M.; Lagoudakis, P. G.; Schindler, F.; Koeppe, R.; Rogach, A. L.; Feldmann, J.; Talapin, D. V.; Weller, H. *Nano Lett.* **2005**, *5*, 2044.

(33) Borys, N. J.; Walter, M. J.; Huang, J.; Talapin, D. V.; Lupton, J. M. *Science* **2010**, *330*, 1371.

(34) Pandey, A.; Guyot-Sionnest, P. *Science* **2008**, *322*, 929.

(35) Zhu, H.; Yang, Y.; Song, N.; Rodríguez-Cordoba, W.; Lian, T. *Proc. SPIE* **2011**, *8098*, 809802.

(36) Brovelli, S.; Schaller, R. D.; Crooker, S. A.; García-Santamaría, F.; Chen, Y.; Viswanatha, R.; Hollingsworth, J. A.; Htoon, H.; Klimov, V. I. *Nat. Commun.* **2011**, *2*, 280.

(37) Oron, D.; Kazes, M.; Banin, U. *Phys. Rev. B* **2007**, *75*, 035330.

(38) García-Santamaría, F.; Chen, Y.; Vela, J.; Schaller, R. D.; Hollingsworth, J. A.; Klimov, V. I. *Nano Lett.* **2009**, *9*, 3482.

(39) García-Santamaría, F.; Brovelli, S.; Viswanatha, R.; Hollingsworth, J. A.; Htoon, H.; Crooker, S. A.; Klimov, V. I. *Nano Lett.* **2011**, *11*, 687.

(40) Sitt, A.; Sala, F. D.; Menagen, G.; Banin, U. *Nano Lett.* **2009**, *9*, 3470.

(41) Salomon, A.; Boecking, T.; Seitz, O.; Markus, T.; Amy, F.; Chan, C.; Zhao, W.; Cahen, D.; Kahn, A. *Adv. Mater.* **2007**, *19*, 445.

(42) Luo, Y.; Wang, L.-W. *ACS Nano* **2009**, *4*, 91.

(43) Steiner, D.; Dorfs, D.; Banin, U.; Della Sala, F.; Manna, L.; Millo, O. *Nano Lett.* **2008**, *8*, 2954.

(44) Klimov, V. I. *J. Phys. Chem. B* **2000**, *104*, 6112.

(45) Klimov, V. I. *Annu. Rev. Phys. Chem.* **2007**, *58*, 635.

# Appendix 1.

## Charge separation and recombination processes in CdSe QD-$MV^{2+}$ complex

As a comparison, we also studied charge separation and recombination processes of CdSe core only QDs adsorbed with $MV^{2+}$ molecules. CdSe -$MV^{2+}$ complexes were prepared in the same way as CdSe/CdS-$MV^{2+}$ complexes As shown in Figure S7, free CdSe QDs without $MV^{2+}$ shows a main bleach peak at 500 nm and this bleach has negligible decay in 1.4 ns. In CdSe -$MV^{2+}$ complexes under the same single exciton excitation conditions, the initial amplitude of the bleach at 500 nm is much smaller and it decays quickly. At the same time, a new positive absorption band from 570 nm to 700 nm was formed (within 2 ps) and eventually decays on a much longer (ns) time scale. This positive feature matches the spectra of $MV^{+}$ radical, confirming that excitons in CdSe QDs dissociate by ET to $MV^{2+}$ molecules.

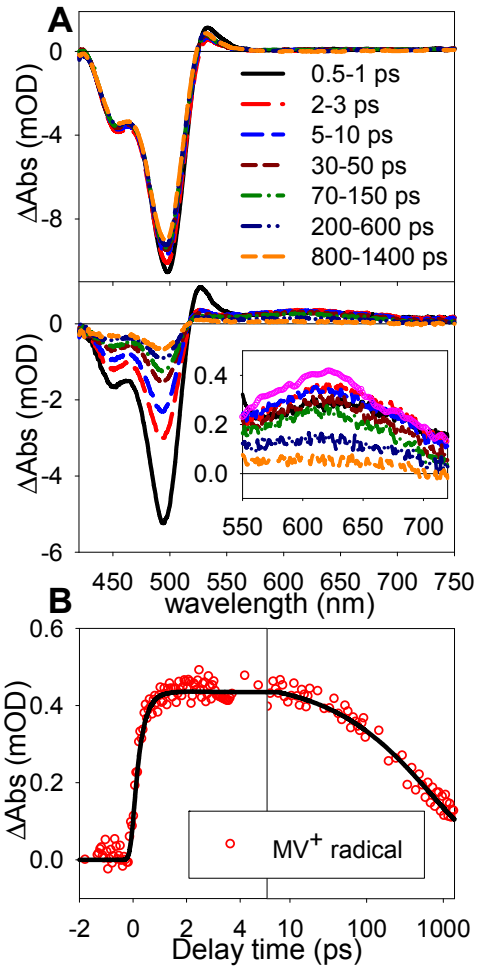


**Figure A.6.1.** (A) TA spectral of CdSe core only QDs with (lower panel) and without (upper panel) adsorbed $MV^{2+}$. The spectra from 550 nm to 750 nm are expanded in the inset of the lower panel, showing that they match the $MV^{+}$ radical spectrum (pink circles). (B) $MV^{+}$ radical rise (charge separation) and decay (charge recombination) kinetics (red circles) and its fit (black line). The horizontal axis is in linear scale (0- 5 ps) in the left panel and in logarithmic scale (5 ps- 1.4 ns) in the right panel.

The $MV^+$ radical kinetics can be well fit by a biexponential rise and a stretched exponential decay function, $A(t)_{MV^+} = A_{MV^+}[-a\exp(-k_1 t)-(1-a)\exp(-k_2 t)+\exp(-(t/\tau)^{\alpha})]$, as shown in Figure A.6.1). The fitting parameters are listed in Table A.6.1 and the half-life times for charge separation and recombination processes are 0.16 ± 0.02 ps and 390 ± 30 ps, respectively.

**Table A.6.1.** Fitting parameters for $MV^+$ radical formation and decay kinetics in CdSe-$MV^{2+}$ complexes

| $A_{MV+}$ (mOD) | a | $k_1$ $ps^{-1}$ | $k_2$ $ps^{-1}$ | τ ps | α |
|---|---|---|---|---|---|
| 0.47 ± 0.02 | 0.74 ± 0.03 | 6.4 ± 0.3 | 0.9 ± 0.1 | 600 ± 40 | 0.59 ± 0.03 |

# Appendix 2.

## Charge separation and recombination process in CdS QD-$MV^{2+}$ complex

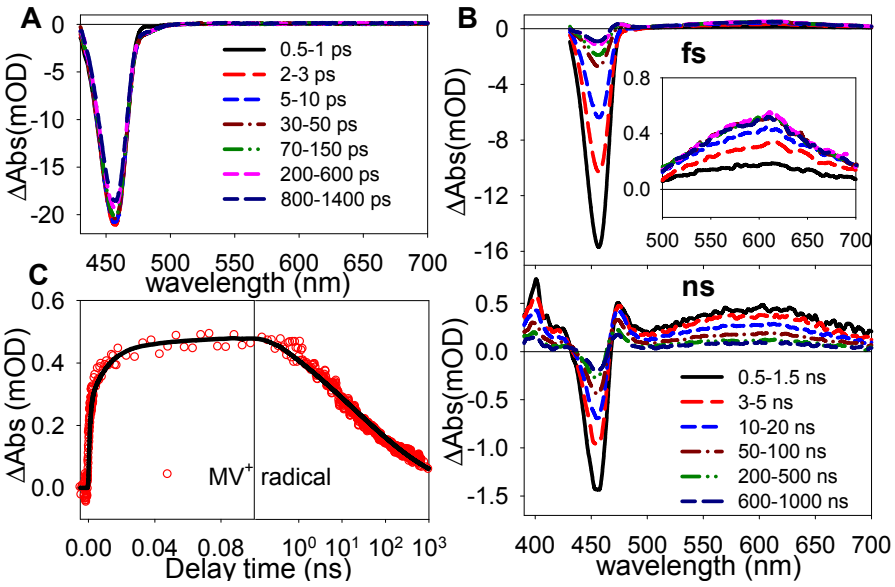


**Figure A.6.2.** TA spectral of CdS core only with (A) and without (B) adsorbed $MV^{2+}$. The upper panel in (B) shows spectra between 0 and 1.4 ns and the lower panel shows the spectra from 1,4 ns to 1 μs. Inset in (B) upper panel expands the spectra from 500 nm to 700 nm, showing clearly the $MV^{+}$ radical formation. (C) The kinetics of $MV^{+}$ radical (~620 nm). The horizontal axis in C is in linear scale (0- 100 ps) in the left panel and in logarithmic scale (100 ps - 1μs) in the right panel.

As a comparison, we also studied charge separation and recombination processes in CdS QDs (460 nm) adsorbed $MV^{2+}$. The sample was prepared in the same way as CdSe/CdS-$MV^{2+}$ complexes. As shown in Figure A.6.2, after 400 nm excitation, free CdS QDs (without $MV^{2+}$) show a distinct 1S exciton bleach peak at 460 nm. This bleach has negligible recovery in 1.4 ns, confirming the single exciton excitation conditions. In CdS-$MV^{2+}$ samples, the 1S exciton bleach recovers quickly to generate the MV+ radical

absorption band (500 nm to 700 nm). The $MV^+$ radical kinetics by a biexponential rise and a stretched exponential decay function, $A(t)_{MV^+} = A_{MV^+}[-a\exp(-k_1 t) - (1-a)\exp(-k_2 t) + \exp(-(t/\tau)^{\alpha})]$ , as shown in Figure A.6.2. The fitting parameters are listed in Table A.6.2 and the half lifetimes for charge separation and recombination processes are 2.9 ± 0.2 ps and 8.3 ± 0.4 ns, respectively.

**Table A.6.2.** Fitting parameters for $MV^+$ radical formation and decay kinetics in CdS-$MV^{2+}$ complexes

| $A_{MV+}$ (mOD) | a | $k_1$ $ps^{-1}$ | $k_2$ $ps^{-1}$ | τ ns | α |
|---|---|---|---|---|---|
| 0.58 ± 0.03 | 0.53 ± 0.02 | 1.1 ± 0.1 | 0.09 ± 0.02 | 18.9 ± 0.2 | 0.22± 0.03 |

# Appendix 3.

## Femtosecond transient absorption spectra of CdSe/CdS QDs with and without $MV^{2+}$ at different excitation powers

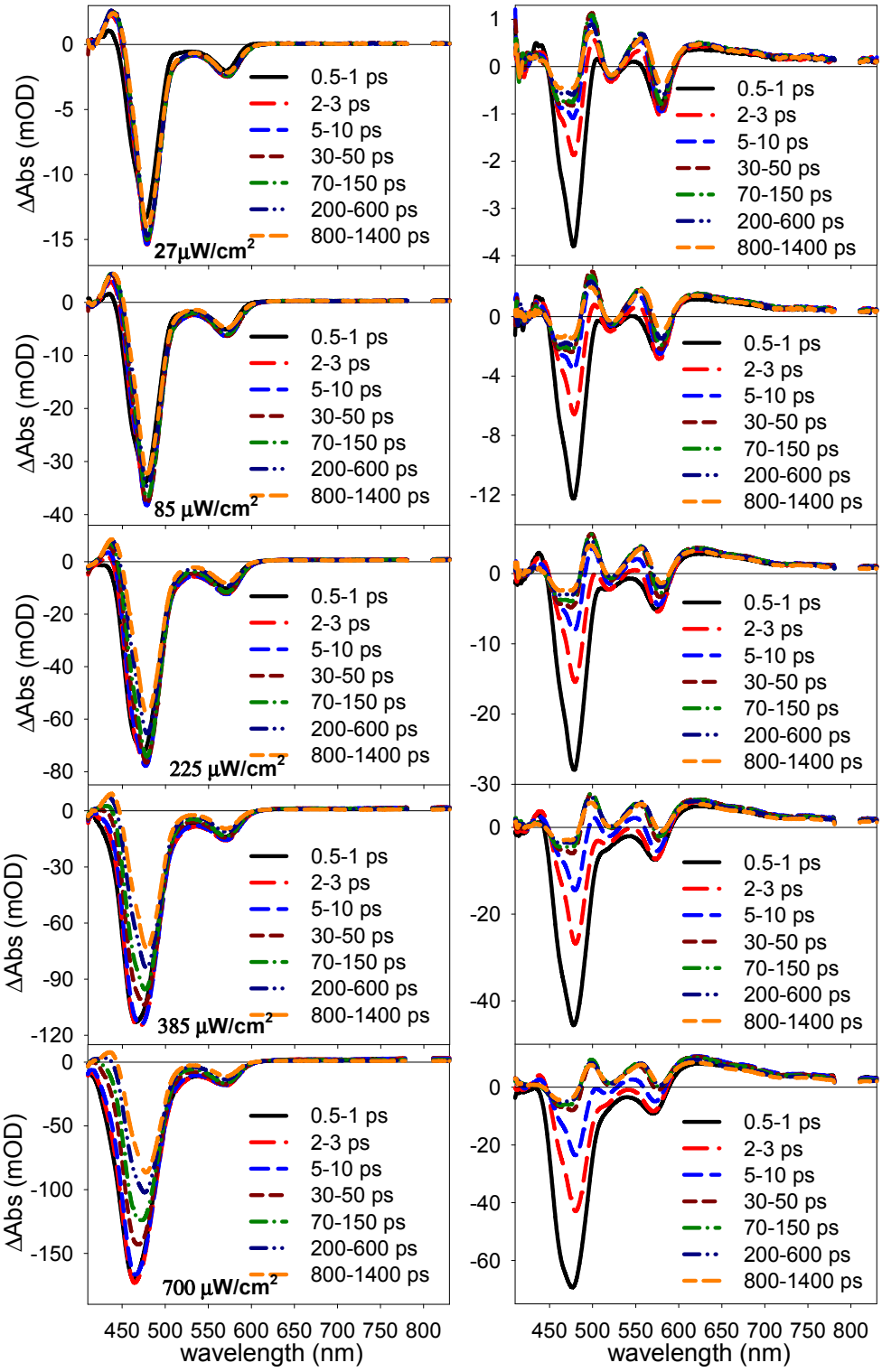
ΔAbs (mOD)
0.5-1 ps
2-3 ps
5-10 ps
30-50 ps
70-150 ps
200-600 ps
800-1400 ps
27μW/cm²
85 μW/cm²
225 μW/cm²
385 μW/cm²
700 μW/cm²
450 500 550 600 650 700 750 800
wavelength (nm)

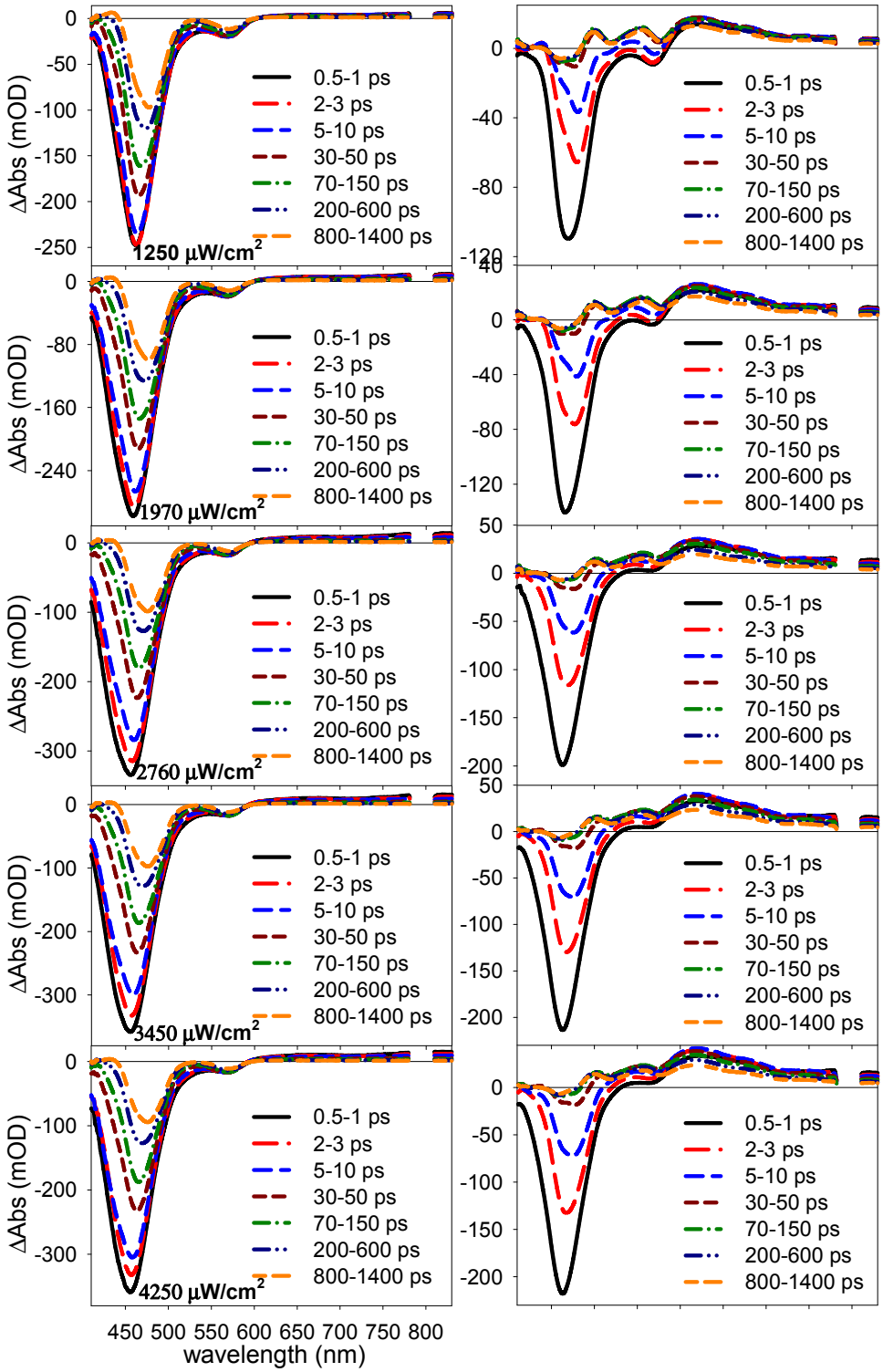
ΔAbs (mOD)
0.5-1 ps
2-3 ps
5-10 ps
30-50 ps
70-150 ps
200-600 ps
800-1400 ps
1250 μW/cm2
1970 μW/cm2
2760 μW/cm2
3450 μW/cm2
4250 μW/cm2
450 500 550 600 650 700 750 800
wavelength (nm)

**Figure A.6.3.** TA spectra of CdSe/CdS (left column) and CdSe/CdS- $MV^{2+}$ complexes (right column) at indicated excitation intensities (pulse energies).

# Appendix 4.

## Modeling of the T1 bleach by dynamic Burstein-Moss shift

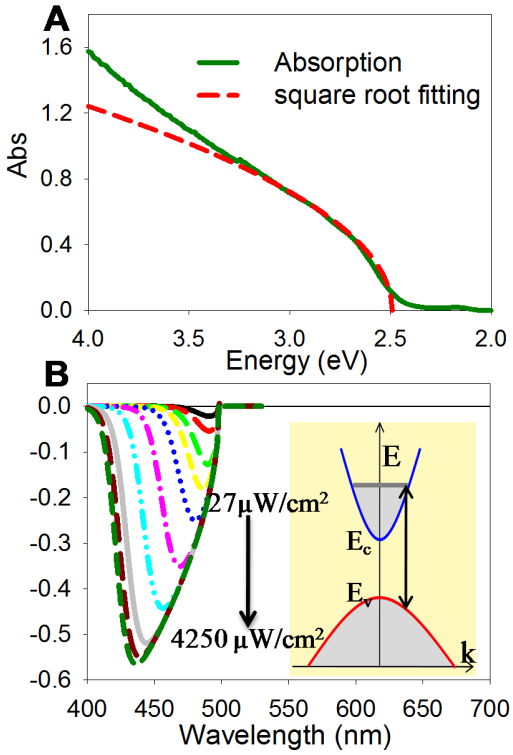


**Figure A.6.4.** (A) Absorption spectra of CdSe/CdS QDs (green) and a fit to a bulk-like density of states (red). (B) The calculated initial bleach spectra of CdS band caused by the dynamic Burstein-Moss effect. We have assumed a bulk like parabolic density of

states for the CdSe shell based transitions. Inset: A schematic depiction of band filling by the presence of multiple excitons.

Because of the rapid intraband relaxation (faster than carrier annihilation), the carrier distribution in the conduction band can be approximately modeled by a Fermi-Dirac distribution with a quasi-Fermi level for the electron. The average number of excitons (m) in each QDs at all excitation intensities was obtained from fitting the normalized $T_0$ and $PA_2$ amplitudes as a function of the excitation intensities (described in main text and shown in Figure 5). From the average QD volume determined from the TEM images, we can calculate the average initial (at $t_{max}$) conduction band electron density (n) in each QD after 400 nm excitation. The quasi-Fermi level ($E_f$, related to CB edge) at each excitation intensity is given by

$$n = 2(\frac{m_e kT}{2\pi\hbar^2})^{3/2} * \frac{2}{\sqrt{\pi}} \int_0^\infty \frac{\sqrt{x}}{1+\exp(x-\frac{E_f}{kT})} dx \qquad \text{(A.6.1)}$$

Because of momentum conservation during optical transition, at each probe wavelength, the energy difference between the probed electron level and the CB edge is given by:

$$\Delta E = (E_{probe} - E_g)(\frac{1}{1+m_e/m_h}) \qquad \text{(A.6.2)}$$

The electron occupation probability at this energy is governed by the Fermi-Dirc distribution:

$$f_e(E_{probe}) \cong \frac{1}{1+\exp(\frac{\Delta E - E_f}{kT})} \tag{A.6.3}$$

As shown in Figure S11A, the steady state adsorption spectrum of the CdSe/CdS QDs can be approximately described by a bulk-like square root dependent absorption coefficient at transition energy above the $T_1$ band, reflecting its dependence on the density of states:

$$DOS \propto \sqrt{E - E_g} \tag{A.6.4}$$

The effective band gap is extracted from the fit. Because transient bleach signal of CdSe/CdS is due to the filling of electron levels, it can be described as the product of electron occupation probability at a given energy level and the corresponding density of state:

$$A(E_{probe}) = A_0 \sqrt{E - E_g} f(E_{probe}) \tag{A.6.5}$$

The calculated transient absorption spectra at different excitation intensities are shown in Figure A.6.4 B.

# Chapter 7. Multiexciton Annihilation and Dissociation from One-dimensional CdSe Nanorods: the Effect of Nanocrystal Shape



## 7.1. Introduction

Quantum confined colloidal semiconductor nanocrystals (NCs) has been a subject of intense interests because of their size dependent optical and electronic properties, processing versatility and low cost. In addition, these NCs can generate and accommodate multiple excitons (e-h pairs) through either optical or electric current pumping. Therefore, NCs can potentially be used in advanced optoelectronic devices ranging from high power light emitting diodes,[1,2] low-threshold lasing media,[3,4] and multi-photon source[5,6] to highly sensitive and efficient photodetectors and photovoltaic/catalytic cells.[7-9] The development and improvement of these NC-based devices requires the understanding of multiple exciton dynamics in NCs and their efficient conversion to emitted photons (for emission applications) or separated external charges (for photovoltaic/catalytic applications) before exciton-exciton annihilate.[10-12]

Multiexcitons can annihilate through Auger recombination, wherein an electron−hole pair nonradiatively recombines by transferring its energy to another carrier or exciton. This process occurs on the 10−100 ps time scale for biexciton states in typical CdSe QDs. The Auger recombination in QDs involves three particle collisions and the lifetime ($\tau_n$) for $n$-exciton state decreases rapidly with n: $\frac{1}{\tau_n} = \frac{C_3}{2} n^2(n-1)$, where $C_3$, the three molecular Auger recombination rate constant, is related to the biexciton state recombination rate ($C_3 = 1 / 2\tau_2$).[13-16] Previous proof-of-principle experiments have demonstrated that up to three[17] and four[18] excitons per CdSe QDs (generated by the absorption of multiple photons) can be dissociated by interfacial charge separation to adsorbed electron acceptors. The number of dissociated excitons is limited by the competition between interfacial electron transfer and exciton-exciton annihilation. To achieve high multiexciton dissociation (MED) efficiency, it is highly desirable to facilitate the interfacial charge separation while slow down the Auger annihilation process in NCs. We previously investigated an approach for improving MED efficiency by utilizing quasi-type II CdSe/CdS core/shell QDs.[19] The reduced electron-hole overlap in the quasi-type II structure decreases the Auger recombination rate constant $C_A$, lengthening the lifetime of the multiple-exciton states. Furthermore, the carrier distribution also enables ultrafast electron transfer to the acceptor. As a result, up to 19 excitons can be dissociated from these QDs with methylviologen ($MV^{2+}$) as the electron acceptor.[19]

In this chapter, we report a new approach for enhancing MED efficiency by using one dimensional (1D) quantum rods (QRs). The synthesis and photovoltaic/photocatalytic

applications QRs and associated heterostructures have attracted intense interest in recent years.[20-25] Unlike QDs, in quantum confined nanorods (NRs) and nanowires (NWs), the e-h Coulomb interaction is dramatically enhanced by the dielectric contrast effect, leading to the formation of strongly bound 1D excitons.[26-30] One consequence of the 1D exciton structure is the highly polarized emission along the direction of the rod, which has been observed in the pioneering studies of quantum rods.[20,31-34] As another consequence, the Auger recombination is expected to occur through bimolecular exciton-exciton collision, which has been suggested and probed in both CdSe QRs and NWs.[15,35-37] In principle, the lifetime ($\tau_n$) for *n*-exciton state in a bimolecular recombination process can be generalized as $\frac{1}{\tau_n} = \frac{C_2}{2} n(n-1)$, where bimolecular Auger recombination rate constant $C_2 = 1 / \tau_2$.[15,38] Unfortunately, the experimental support for this scaling law remains incomplete because of the difficulties in extracting the lifetimes of higher order ($n \geq 3$) exciton states in these previous studies.[14,35] The expected slower increase of exciton annihilation rate with exciton number suggests the possibility of enhanced MED efficiency in QRs. Motivated by this expectation and reported ultrafast charge separation in CdSe QR-electron acceptor complexes,[39] we investigate the 1D exciton annihilation and dissociation dynamics in CdSe QRs by transient absorption (TA) spectroscopy. We first examine the 1D excitonic states and assign the spectral signatures of electrons and holes. We show that the multiexciton Auger recombination process in CdSe QR is governed by exciton-exciton bimolecular annihilation dynamics with $\frac{1}{\tau_n} = \frac{C_A}{2} n(n-1)$, and the multi-exciton lifetime is significantly lengthened compared with CdSe QDs. With methylviologen ($MV^{2+}$) as a model electron acceptor, we demonstrate ultrafast exciton

dissociation by interfacial electron transfer (~59 fs) from the CdSe QR to the adsorbed $MV^{2+}$ due to quantum confinement in the radial direction. The ultrafast charge separation and lengthened multiexciton lifetimes enable the dissociation of over 21 excitons from one CdSe QR at high excitation intensity, greatly exceeding the MED efficiency of CdSe QDs.[18]

## 7.2. Results and Discussion

### 7.2.1. Spectral Signature and Assignment of 1D Excitons

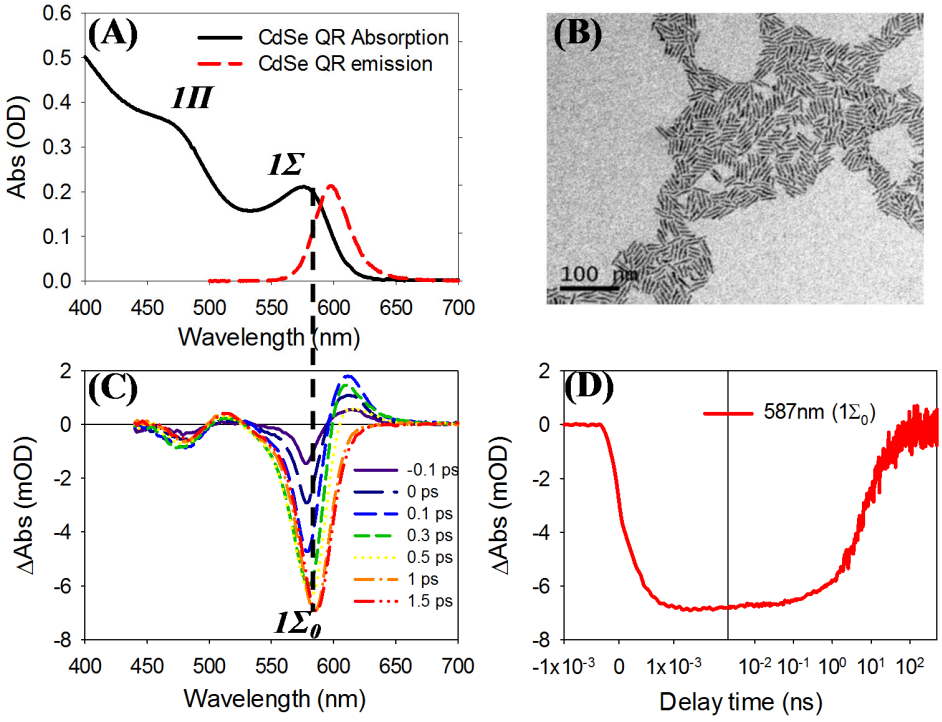

**Figure 7.1.** (A) Absorption and emission spectra and (B) TEM image of CdSe QRs. (C) Transient absorption spectra of CdSe QR at indicated delay times (-0.1 - 1.5 ps) after 400 nm excitation (at lowest intensity, 7 $\mu J \cdot cm^{-2}$). (D) $1\Sigma_0$ (587 nm) bleach formation and decay kinetics. The left panel (-1 to 2 ps) is in linear scale and the right panel (2 ps to 1000 ns) is in logarithmic scale.

From the TEM image (Figure 7.1 B), the CdSe QR is determined to be 3.2 ± 0.2 nm in diameter and 28.9 ± 3.1 nm in length (aspect ratio ~ 9). The absorption spectrum of the QR shows distinct exciton bands at 575 and 457 nm and the exciton emission peak is centered at 600 nm with 7% quantum yield. Considering the bulk exciton Bohr radius of CdSe (~ 5.6 nm), the motion of electron and holes is quantum confined only in the radial direction, leading to discrete electron and hole levels, $1\sigma$, $1\pi$,…….[26,27,30] Because of dielectric contrast between the rod and surrounding medium, the electron-hole binding energy is significantly enhanced, giving rise to an effective Coulomb potential that depends on their separation along the long axis of the QR. This 1D potential between the $1\sigma$ ($\pi$) electron and hole forms bound $1\Sigma$ ($\Pi$) exciton states.[26,27,30] The density of the 1D exciton states in those bands increases quickly with energy but the oscillator strength is largely concentrated on the lowest energy exciton state ($1\Sigma_0$).[26,27] Following these theoretical models,[26,27,30] the exciton bands at 575 and 457 nm in the steady state absorption spectrum are assigned to $1\Sigma$ and $1\Pi$ exciton manifolds, respectively.

The transient absorption (TA) spectra (-0.1 - 1.5 ps) of CdSe QR at the lowest excitation intensity (7 $\mu J \cdot cm^{-2}$ at 400 nm) are shown in Figure 7.1C. Under this excitation

intensity, the average number of excitons per QR is ~ 0.08 (see analysis below). Upon 400 nm excitation, higher energy exciton states are populated, which is followed by rapid intraband relaxation to the lowest energy levels indicated by the formation and decay of positive biexciton peak at ~ 610 nm and progressive red-shift and growth of the 1Σ bleach peak (Figure 7.1C).[40-42] At ~1 ps, the bleach signal is dominated by the state filling of the lowest energy ($1\Sigma_0$) exciton state at 587 nm.[40] A single exponential fit to the kinetics at 587 nm yields a rise time of 0.5 ps, which represents the hot carrier relaxation time (Figure 7.1D). The subsequent bleach recovery, reflecting the decay of the $1\Sigma_0$ exciton population, has a half-life time of about 4.9 ns (see Figure 7.1D). This 1D exciton lifetime in CdSe QRs is ~3 times shorter than that of the 0D excitons in CdSe QDs of similar exciton energy (~15 ns), which is consistent with the predicted accelerated electron-hole recombination in QRs.[26,27] At 1.2 ns, $1\Sigma_0$ bleach decays by 17% (thus the percentage of the remaining signal $\gamma$=0.83) due to single exciton recombination. The absence of any fast decay component on this time scale confirms negligible multiexciton population under such excitation conditions.

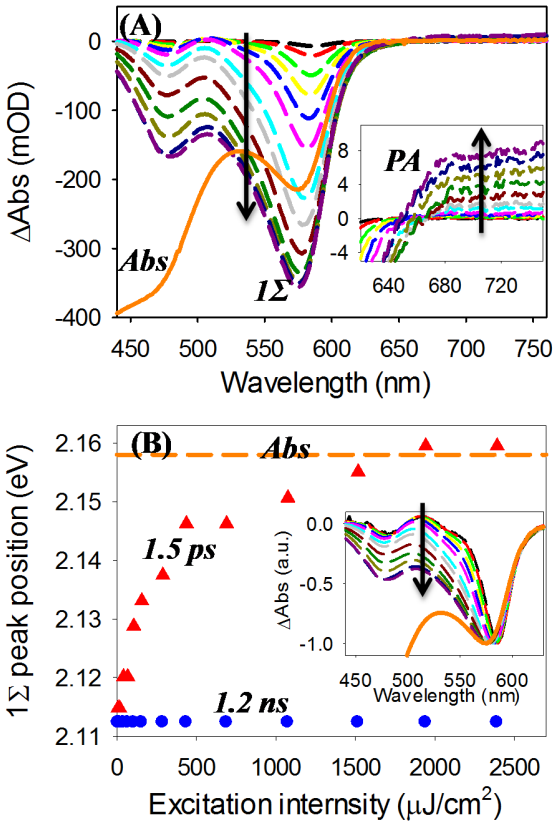


**Figure 7.2.** (A) TA spectra of CdSe QRs at 1.5 ps under different excitation intensities (from 7 to 2390 $\mu J \cdot cm^{-2}$). Also shown is the steady state absorption spectrum of CdSe QRs (orange circles, inverted). (Inset) Expanded view of the spectra from 600 - 770 nm, showing the photoinduced absorption (PA) feature. (B) The 1Σ bleach peak position at 1.5 ps (red triangles) and 1.2 ns (blue circles) as a function of the excitation intensity. The peak position of the steady-state absorption spectrum is indicated by the solid orange line. (Inset) normalized comparison of the transient and steady state absorption spectra shown in (A).

The TA spectra of CdSe QR at 1.5 ps under different excitation intensities (7 ~ 2390 $\mu J \cdot cm^{-2}$) are compared in Figure 7.2A. The complete sets of TA spectra as a function of time (0-1.2 ns) are shown in Appendix 1. At 1.5 ps, when hot carrier relaxation is completed and exciton-exciton annihilation is negligible, the 1Σ bleach in the TA spectra reflects the occupancy of exciton states. In addition to the 1Σ bleach, the TA spectra of excited CdSe QR also show broad and weak photoinduced absorption (PA) features at > 650 nm (Figure 7.2A inset). The PA signal shows identical kinetics in the 650-770 nm spectral region after ~ 1 ps. Before 1 ps, the kinetic traces at different wavelengths contain varying amplitudes of the biexciton peak shift signal shown in Figure 2A. In order to identify the contributions of electrons and holes to the $1\Sigma_0$ and PA spectral signatures, selective charge transfer studies are performed on CdSe QRs. The TA kinetics of $1\Sigma_0$ and PA features with different acceptors can be seen in Figure 7.3. Without electron or hole acceptors, the $1\Sigma_0$ and PA signals have identical and long-lived kinetics within 1.2 ns. In the presence of benzoquinone (BQ), an electron acceptor,[43,44] the $1\Sigma_0$ bleach shows an ultrafast and nearly complete decay while the PA signal remains unaffected, indicating that the $1\Sigma_0$ bleach is solely due to the state filling of the $1\sigma$ electron level, while the PA feature can be attributed to the transition of holes. The selective removal of hole by phenothiazine (PTZ), a hole acceptor,[45,46] leads to slightly longer-lived $1\Sigma_0$ bleach signal and shorter-lived PA signal, further confirming the spectral assignment of these species. (see Figure 7.3)

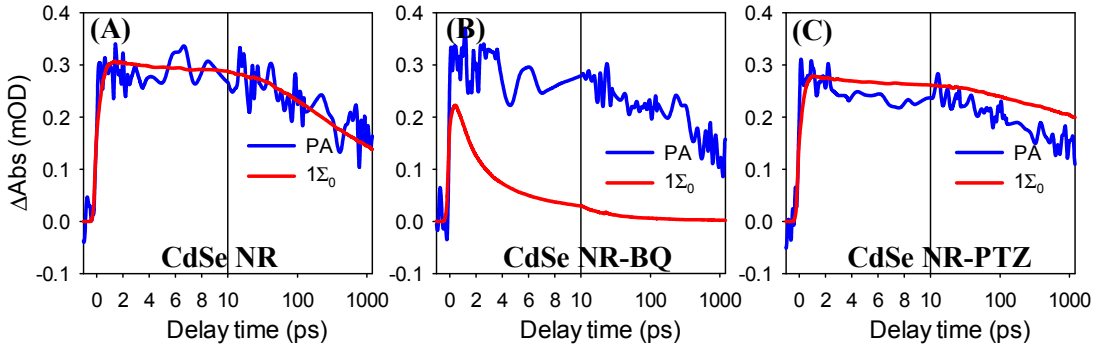


**Figure 7.3.** Transient kinetics at $1\Sigma_0$ (red line) and PA (blue line) of free CdSe QRs (A), CdSe QR-BQ complexes (B) and CdSe QR-PTZ complexes (C). All three samples have the same absorbance at excitation wavelength (400 nm). The $1\Sigma_0$ kinetics in all three samples have been scaled by the same factor such that in free CdSe QRs, the $1\Sigma_0$ kinetics agrees with PA.

In free QRs, the PA signal forms with a rise time of ~0.06 ps (result not shown) and decays with the same kinetics as the $1\Sigma_0$ bleach. The latter indicates that the CB electron decays mainly by recombination with the hole that is responsible for the PA signal. The lack of clear rise process suggests that the PA signal can be attributed to the photoexcited valence band (VB) hole (with negligible trapping in <1.2 ns), trapped hole (with < 0.06 ps trapping time) or both the trapped and VB holes (with indistinguishable PA spectral feature). Although there has been reports of the hole trapping process in CdSe QD or QR on the 10-100 ps time scale, it is unclear whether similar trapping time can be expected in our QRs.[47,48] The small fluorescence quantum yields of the QRs suggest that the holes are likely trapped and the PA signal is dominated by the trapped

holes. Despite the uncertainty in the nature of the hole (VB *vs* trapped) and the transitions involved in the PA signal, we will show below that its amplitude scales linearly with the number of excitons and can be used to follow the exciton dynamics.[16,19]

### 7.2.2. Multi-exciton Dynamics in CdSe QRs.

As shown in Figure 7.2A, the 1Σ bleach amplitude increases at higher excitation intensity, indicating the creation of more excitons in the CdSe QR. Associated with the amplitude increase, the peak of the 1Σ bleach shifts to higher energy, which can be better seen in the comparison of normalized TA spectra (Figure 7.2B inset) and the comparison of 1Σ bleach peak positions at 1.5 ps and 1.2 ns (Figure 7.2B). At the lowest excitation intensity, when single exciton states dominate, the bleach peak position remains unchanged at 1.5 ps and 1.2 ns, agreeing well with the $1\Sigma_0$ peak position and red-shifted from the steady state 1Σ peak . With increasing excitation intensity, when more excitons are created in each QR, the 1Σ bleach at 1.5 ps shows increased amplitude on the higher energy side, broadened line width and blue-shifted peak position. At the highest excitation intensity (2390 $\mu J \cdot cm^{-2}$), the transient spectra gradually approaches the steady state absorption spectrum of the 1Σ band. The observed excitation intensity dependence is consistent with the presence of a manifold of 1D exciton states.[26,27] With increasing number of excitons in the QR, 1D exciton states of higher energies are occupied, blue-shifting and broadening the bleach spectra. When all 1D exciton states in the 1Σ band are occupied, the 1Σ bleach spectrum resembles the steady state absorption spectrum, which

is the sum of all optically active transitions. At later delay time $t_L$ (1.2 ns), the 1Σ bleach peak positions under all excitation intensities merge to the same energy as the $1\Sigma_0$ exciton, indicating the completion of the exciton-exciton annihilation in the QR and formation of the long-lived $1\Sigma_0$ single exciton state.

It should be noted that the observed excitation intensity dependent transient spectral evolution of the 1Σ bleach in CdSe QRs is similar to the band filling induced dynamic Burstein−Moss shift observed in semiconductor materials with bulk-like continuous densities of state.[19,41,49] It is different from the excitation intensity dependence of the two-fold degenerate 1S exciton bleach in CdSe QDs.[17,19] As a comparison, the excitation intensity dependent spectral evolution and steady state absorption spectrum of CdSe QDs with similar lowest exciton energy (1S peak at 574 nm) are shown in Appendix 2. With increased number of excitons per QD, the initial amplitudes of the 1S bleach (at 1.5 ps) increases until it reaches saturation. More importantly, the 1S bleach peak shows negligible excitation intensity dependent peak shift and broadening and the bleach spectrum closely resembles the steady state absorption spectrum at all excitation intensities. The power dependence of 1S exciton bleach amplitude can be well modeled by assuming a two-fold degenerate exciton state with an initial Poisson distribution of the number of excitons in QDs, as previously reported.[17,19]

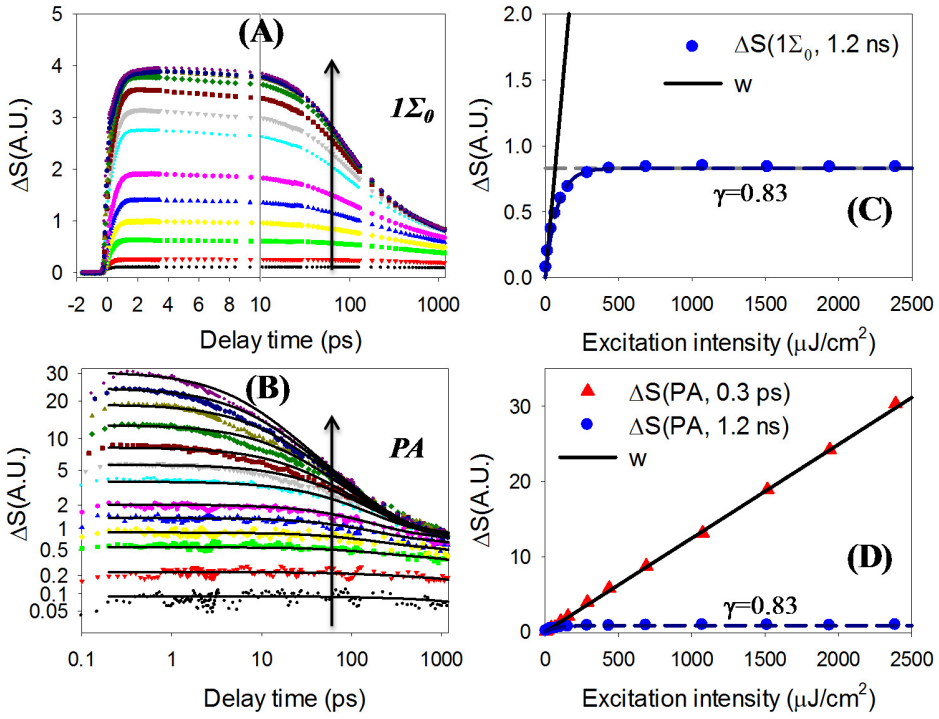


**Figure 7.4.** (Left column) Normalized transient kinetics (symbols) at $1\Sigma_0$ (A) and PA (B) under different excitation intensities. The solid lines in (B) are fits to a stochastic multicarrier annihilation model described in the main text. (Right column) Normalized TA signal of $1\Sigma_0$ (C) and PA (D) at indicated delay times as a function of excitation intensities. The solid and dashed lines are fits according to eqs 7.1-7.3.

To quantify the exciton distribution and multiexciton Auger annihilation dynamics, we analyze the excitation intensity dependent $1\Sigma_0$ and PA kinetics shown in Figure 7.4 A and B. Let $P(n,t)$ be the probability of having QRs with $n$ excitons at delay time $t$. Because 400 nm excitation creates electron and hole pairs well above the band

edge, the number of excitons ($n$) per QR at early time ( $t_E$ = 0.3 ps, after thermal relaxation and before annihilation) can be assumed to obey the Poisson distribution

$$P(n, t_E) = f(n) = w^n e^{-w} / n! \qquad (7.1)$$

where $f(n)$ is the probability of having CdSe QRs with $n$ excitons and $w$ is the average number of excitons per QR. The latter is proportional to the excitation intensity (I), $w = C * I$. The scaling factor $C$ depends on the CdSe QR absorption crossing section at the excitation wavelength and pump/probe beam geometries and overlap. Accurate determination of C is difficult experimentally.[17,19,40] Instead, we determine the average number of excitons by fitting the excitation intensity dependence of the signal amplitude (see below), which has been successfully applied to CdSe and CdSe/CdS QDs.[17,19,40]

With increasing excitation intensities, both $1\Sigma_0$ and PA kinetics show larger amplitudes of fast decay components, consistent with the creation and annihilation of multiple excitons in the QR. After 1.2 ns ($t_L$), the $1\Sigma_0$ kinetics under all excitation intensities agree well with single exciton decay kinetics (SI3 and SI4), indicating that the signal at $t_L$ = 1.2 ns is solely due to single exciton state. Therefore, at that time, the transient signal amplitudes $\Delta A(\lambda, t_L)$ ($\lambda$= $1\Sigma_0$ and PA) are proportional to the number of excited QRs: $\Delta A(\lambda, t_L) = \alpha(\lambda)\gamma[1 - f(0)]$, where $\alpha(\lambda)$ is a scaling factor proportional to the extinction coefficients at that wavelength and $\gamma$ = 0.83 accounts for the decay of single exciton states in 1.2 ns. We define a normalized transient signal $\Delta S(\lambda, t_L)$ that represents the probability of finding excited QRs at $t_L$ in the ensemble:

$$\Delta S(\lambda, t_L) = \Delta A(\lambda, t_L) / \alpha(\lambda) = \gamma[1 - f(0)] \qquad (7.2)$$

$\Delta S(\lambda, t_L)$ should approach $\gamma$ (= 0.83) when all QRs are excited, from which we can determine the scaling factor $\alpha(\lambda)$ for $1\Sigma_0$ and PA signals, respectively. The transient signal at other delay times, $\Delta A(\lambda, t)$ are then normalized by the same scaling factor and the normalized kinetics $\Delta S(\lambda, t) = \Delta A(\lambda, t) / \alpha(\lambda)$ are shown in Figure 7.4 A and B.

Because of the intensity dependent width broadening and peak shifting of the 1Σ band, the bleach amplitude does not scale linearly with the number of excitons. A quantitative analysis of this signal would require a detailed model of the structure and transition strength of the 1D exciton states within the 1Σ manifold, which has not been attempted here. However, similar to CdSe[16] and CdSe/CdS core/shell QDs[19], the PA signal in the CdSe QRs increases linearly with the excitation intensity (or the average number of excitons). Therefore, the normalized transient PA signal at early time can be defined as

$$\Delta S(PA, t_E) = \sum_n nf(n) = w \qquad (7.3)$$

The normalized transient signals $\Delta S(1\Sigma_0, t_L)$, $\Delta S(PA, t_L)$, and $\Delta S(PA, t_E)$ are plotted as a function of excitation intensities in Figure 7.4 C and D. These transient signals can be simultaneously fitted by eqs 7.1-7.3 with the scaling factor C as the only fitting parameter. This model describes well the experimental data, from which the scaling factor C and, thus, the average number of excitons at any excitation intensity can be obtained. As can be seen in Figure 7.4D, the normalized PA signal at early time follows the average number of excitons, *w*. At the highest excitation intensity (2390 $\mu J \cdot cm^{-2}$), as many as 30 excitons in each CdSe QR are generated by multiphoton absorption and accommodated by the densely spaced 1D exciton states.

Since the PA signal is proportional to the average number of excitons per QR under all excitation intensities, the kinetics of the normalized PA signal $\Delta S(PA,t)$ directly reflects the multiple exciton Auger annihilation process. At delay time t,

$$\Delta S(PA,t) = \sum_n nP(n,t) \qquad (7.4)$$

Assuming sequential multiexciton annihilation process ($n \rightarrow n\text{-}1 \ldots \rightarrow 2 \rightarrow 1$) in QRs and denoting the rate constant for the transition from $n$ to $n\text{-}1$ exciton states by $1/\tau_n$, the time dependent probability $P(n,t)$ can be described by a set of coupled rate equations[13-16,50]

$$\frac{dP(n,t)}{dt} = \frac{P(n+1,t)}{\tau_{n+1}} - \frac{P(n,t)}{\tau_n} \qquad (7.5)$$

The Auger decay rate of an n-exciton state $1/\tau_n$ (n>1) is expected to be (i) $\frac{1}{\tau_n} = \frac{C_A}{2} n(n-1)$ according to the excitonic model, in which the electrons and holes are bound as excitons and the Auger recombination occurs through exciton-exciton bimolecular collision; or (ii) $\frac{1}{\tau_n} = \frac{C_A}{2} n^2(n-1)$ according to the independent carrier model, in which the electrons and holes are independent carriers and the Auger recombination involves three-carrier collisions.[14-16,50]

The normalized PA decay kinetics (Figure 7.4B) are fitted with eqs 7.4-7.5 according to the two Auger rate scaling models. The fit requires the single exciton ($\tau_1$) and bi-exciton ($\tau_2$) lifetimes and the initial distribution of excitons. The initial distribution $P(n,t_E)$ of exciton states can be calculated using eq 7.1 for any given excitation intensities. Under the lowest excitation intensity (7 uJ$\cdot$ cm$^{-2}$), the excited QRs (n≥1) are mostly in the single exciton state (97%) and show long-lived single exciton decay

kinetics. Although the single exciton decay is non-single exponential (Figure 1D), the $1\Sigma_0$ bleach recovery kinetics within the first 1.2 ns, the relevant time window for the kinetics shown in Figure 7.4B, can be well represented by a single exponential decay with $\tau_1 = 7$ ns. When the excitation intensity increases from 7 uJ· $cm^{-2}$ to 17.6 uJ· $cm^{-2}$, the excited QR is still dominated by single exciton states (90.5 %) with a small amount of biexciton state population (9.0%). The $1\Sigma_0$ shows a fast decay component corresponding to the biexciton Auger annihilation. Subtraction of the normalized (at 1.2 ns) $1\Sigma_0$ kinetics under these two lowest excitation intensities yields the biexciton decay kinetics, from which we obtain the biexciton lifetime $\tau_2$ of 201 ps. This biexciton lifetime is close to the values reported previously in similar CdSe QRs.[48,51] It is about four times longer than that of 0D biexcitons in CdSe QDs (~ 50 ps) with similar confinement energies,[13,17] which can be attributed to the much bigger volume along the axial direction in CdSe QRs.

The numerically simulated kinetics assuming the excitonic model are shown in Figure 7.4B (black lines) and the results assuming independent carrier behavior are plotted in Figure A.7.3. It is clear that the excitonic model yields a much better fit to the experimental results than the independent carrier model, indicating that the Auger recombination in 1D QRs is dominated by excition-excition bimolecular annihilation. It is consistent with the formation of strongly bound 1D excitons in CdSe QRs. The agreement is remarkable considering that there are no fitting parameters in the simulation. At high average exciton numbers, the simulated decay kinetics is slower than the experimental result. The reason for the deviation is not clear. It may suggest a weakened Coulomb attraction for very high order exciton states and/or spatially separated e-h pairs

in some portions of CdSe QR because of wurtzite/zinc blende phase disorder.[36,52] As shown in Figure A.7.3B, A fit that includes a mixture of QR populations following excitonic (93%) and independent carrier (7%) Auger recombination models leads to a better agreement with the experimental results. The lifetimes of n-exciton states in CdSe QR calculated from the excitonic model are plotted in Figure 7.7B. Because of the reduced Auger rate constant due to their larger volume and the weaker dependence on *n*, QRs show a much longer-lived multiexciton states (~ two orders of magnitude) than typical QDs and the difference become larger for higher order exciton states.

Earlier studies on Auger decay rates in CdSe QDs (and QRs) were based on the 1S (1Σ) exciton bleach recovery kinetics and a bulk semiconductor kinetic model which neglects the distribution of exciton numbers in an ensemble.[13,35] An elaborated subtraction scheme was used to extract the second and third order exciton state lifetimes and the ratio between them provides an initial sense of the multiexciton state lifetime scaling law. Because of the saturation of the two-fold degenerate 1S bleach in QDs and shifting and broadening of densely spaced 1Σ bleach in QRs as well as the quantized nature of the exciton number in a given NC, the validity of such approach for obtaining the lifetimes of higher order ($\geqslant$ 3) exciton states has been questioned.[14,15] Furthermore, our simulation result suggests that both the excitonic (Figure 7.4B) and independent carrier (Figure A.7.3A) models describe the kinetics reasonably well when the population of high order exciton states and average number of excitons per QD are small. Therefore, a rigorous test of the validity of these models requires the decay kinetics of higher order exciton states, as shown in Figure 7.4B and A.7.3A. Unlike the 1S or 1Σ interband

transitions, the broad PA signal, whose amplitude depends linearly on the exciton number, offers a simple way to monitor the decay kinetics of higher order excitons. A similar approach has been recently applied to the multiexciton decay kinetics of 0D excitons in QDs, which was found to be well described by the $n^2(n-1)$ Auger rate scaling law.[16,19]

### 7.2.3. Single and Multiple Exciton Dissociation from CdSe QRs

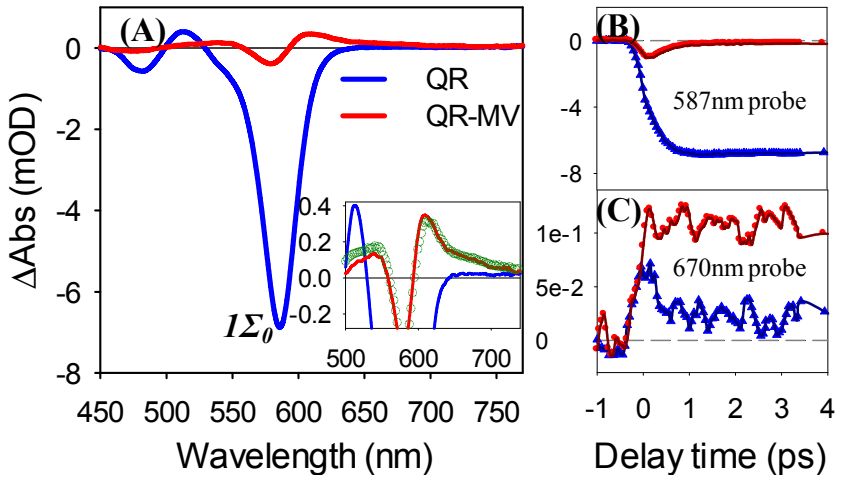


**Figure 7.5.** (A) Transient absorption spectrum of free CdSe QRs (blue) and CdSe QR-$MV^{2+}$ complexes (red) at 1.5 ps after 400 nm excitation (intensity: 7 μJ·$cm^{-2}$). Inset: An expanded view of the spectrum at 500−750 nm and a simulated spectrum of the charge separated state (green circles) of the QR-$MV^{2+}$ complex. Comparison of TA kinetics probed at (B) 587 nm ($1\Sigma_0$) and (C) 670nm ($MV^{+\bullet}$ radicals) in free CdSe QRs (blue triangles) and CdSe-$MV^{2+}$ complexes (red circles).

To examine the effect of 1D exciton structure on single and multiple-exciton dissociation dynamics in CdSe QRs, we chose methylviologen ($MV^{2+}$), a widely-used electron mediator for photocatalytic reactions, as a model electron acceptor. The transient absorption spectra of CdSe QRs with and without $MV^{2+}$ are compared in Figure 7.5A (at 1.5 ps) and SI2 (0 – 1.2 ns). These spectra were taken at the lowest excitation intensity (7 $\mu J \cdot cm^{-2}$) to ensure that the signal is dominated by single exciton states. Comparison of transient kinetics in free QRs and QR-$MV^{2+}$ complexes at 587 nm ($1\Sigma_0$) and 670 nm ($MV^+$ radical) are shown in Figure 7.5 B and C, respectively. As discussed above, $1\Sigma_0$ bleach of free CdSe QRs is long-lived, reflecting the long-lived single exciton state. In QR-$MV^{2+}$ complexes, the $1\Sigma_0$ bleach grows to a much smaller initial amplitude and decays rapidly in the first 1 ps (Figure 7.5B), suggesting ultrafast (hot) electron transfer from the CdSe QR to adsorbed $MV^{2+}$. Concomitant with $1\Sigma_0$ bleach recovery, a spectrum with derivative-like feature below 650 nm and a positive absorption band above 650 nm is formed (Figure 7.5A inset). This spectrum can be attributed to the charge separated state of CdSe QR-$MV^{2+}$ complexes in which the electron is transferred to the adsorbed $MV^{2+}$ molecules and the hole remains in the CdSe QR. The buildup of the electric field shifts the excitonic transition in CdSe QRs through Stark effect, leading to the derivative-like features in the TA spectrum.[53,54] Such charge separation induced Stark effect spectrum of QR can be clearly resolved in QR-benzoquinone (BQ) complex in which $BQ/BQ^-$ doesn't show any spectral signature in visible range. In QR-$MV^{2+}$, the stark effect spectrum extends until 650 nm and beyond that, the positive absorption band can be assigned to $MV^{+\bullet}$ radicals and a small amount (15% ~ 20%) of QR PA signal. The spectrum of the charge separated state in CdSe QR-$MV^{2+}$ complexes can be very well

simulated by adding the TA spectrum of QR-BQ complexes (containing Stark effect and PA signal) and the $MV^{+\bullet}$ radical signal (from CdS QD-$MV^{2+}$ complexes), confirming the spectral assignment.

The $MV^{+}$ radical kinetics can be monitored at 670 nm (Figure 7.5C), where the TA signal consists of $MV^{+\bullet}$ radical absorption and a small amount of QR PA signal. As shown in Figure 7.5C, free CdSe QRs also show a positive absorption feature that decays within 1 ps and the long lived PA absorption. The fast decay component corresponds to the red shift of the 1Σ exciton band caused by hot carriers generated with 400 nm excitation (biexciton effect),[40,55] which can be clearly seen in Figure 7.1C. Indeed, with excitation near the band edge (~590 nm), the transient kinetics of free CdSe QRs at 670 nm does not show this hot carrier signature and the corresponding kinetics of the CdSe-$MV^{2+}$ can be fit to yield a $MV^{+\bullet}$ formation time, i.e. the electron transfer (ET) time, of ~59 fs, as shown in Figure A.7.4. This ET rate is much faster than hot electron cooling process in the QR, which suggests that the majority of electrons go through ultrafast hot electron transfer to $MV^{2+}$ prior to the relaxation to the 1σ level.[39] This is consistent with the much smaller initial amplitude of the 1Σ exciton bleach (Figure 7.5B). It is also interesting to point out that this ET rate is comparable to or even faster than that in CdSe QD-$MV^{2+}$ complexes.[18,19,39,56] Although the CdSe QR has a much bigger volume than typical QDs, it is still quantum confined in the radial direction. This ensures a large amplitude of electron wave function at the surface, enabling ultrafast electron transfer to the adsorbed electron acceptors.[53]

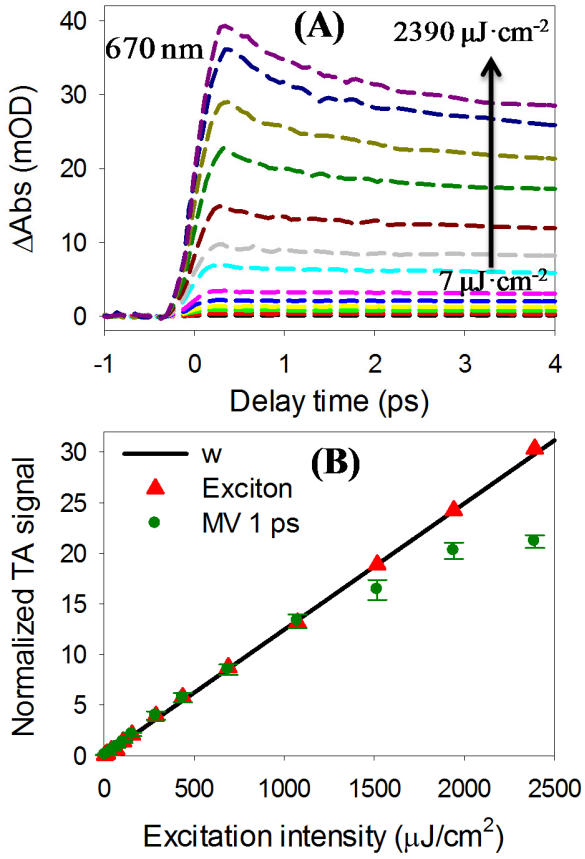


**Figure 7.6.** (A) Kinetics of $MV^{+\bullet}$ radicals at 670 nm and (B) Normalized $MV^{+\bullet}$ radical signal at 1 ps as a function of excitation intensity in CdSe QR-$MV^{2+}$ complexes.

This fast ET rate, coupled with slow multiexciton Auger annihilation, suggests the possibility of efficient dissociation of multiple excitons from CdSe QRs. To determine the MED efficiency, transient absorption measurements were conducted on CdSe QR-$MV^{2+}$ complex under the same excitation intensities as in free CdSe QRs. The complete sets of TA spectra under different excitation intensities are shown in Figure A.7.1. Because of the negligible absorption of $MV^{2+}$ at the excitation wavelength (400 nm), the

average numbers of excitons per QR created in the CdSe QR-$MV^{2+}$ complex should be the same as those in the free CdSe QR, which have been determined above. As shown in Figure 7.6A, the $MV^{+\bullet}$ radical forms quickly and reaches maximum at ~ 0.3 ps under all excitation intensities. With increasing excitation intensities, the initial amplitude of 670 nm signal increases and the decay due to bimolecular charge recombination process becomes faster, indicating more $MV^{+}$ radicals are generated from each QR.[17,19]

In order to determine the average number of $MV^{+\bullet}$ radicals generated per QR, we defined a normalized $MV^{+\bullet}$ radical signal: $S_{MV^+}(I,t) = \Delta A(MV^+, I, t) \,/\, \alpha(MV^+)$, where $\Delta A(MV^+, I, t)$ is the $MV^{+\bullet}$ radical signal size at intensity $I$ at delay time $t$ and $\alpha(MV^+)$ is a scaling factor.[19] As discussed above, at the lowest three excitation intensities ($I$ = 7.0, 17.6, 42.1 μJ·cm$^{-2}$), the excited QR population is dominated by single exciton states with minor biexciton states. Because the lifetimes of the single and bi- exciton states are much longer than the ET time, every exciton in the QR is assumed to be dissociated to generate one $MV^{+}$ radical. This is consistent with the complete recovery of the 1Σ exciton bleach in QR-$MV^{2+}$ complexes. Furthermore, because the $MV^{+\bullet}$ radical kinetics under these low excitation intensities show negligible recombination loss in the first 5 ps, normalized $MV^{+\bullet}$ radical signal should equal to the average number of excitons: $S_{MV^+}(I, 1ps) = w$. From the measured TA signal at the three lowest excitation intensities, a scaling factor $\alpha(MV^+)$ was determined. The same scaling factor is applied to all $MV^{+\bullet}$ radical signals $\Delta A(MV^+, I, 1ps)$ under different excitation intensities. We have chosen transient signal at 1 ps to avoid any contamination from the hot carrier induced exciton absorption signal. Furthermore, it has to be noted that the TA signal at 670 nm contains a small amount

(15~20 %) of PA signal from the holes in the QRs. The PA signal amplitude should be the same as that in free QRs, and has been subtracted to yield the $MV^{+\bullet}$ radical absorption signal shown in Figure 7.6B.

The normalized $MV^{+}$ radical signal $S_{MV^+}(I, 1ps)$ represents the average number of $MV^{+}$ radicals (or dissociated excitons) per QR. As shown in Figure 7.6B, at low excitation intensities (< 1200 μJ·cm$^{-2}$) where charge recombination and Auger annihilation loss is negligible in the first 1 ps, the normalized $MV^{+\bullet}$ radical signal closely follows the average number of excitons per QR ($w$). At higher intensities, the normalized $MV^{+\bullet}$ radical signal becomes smaller than $w$, because of charge recombination and the Auger annihilation loss. At highest excitation intensity (2390 μJ·cm$^{-2}$), the number of excitons per QR that can be dissociated is 21.2 ± 0.6. The error bar reflects the standard deviation of two measurements.

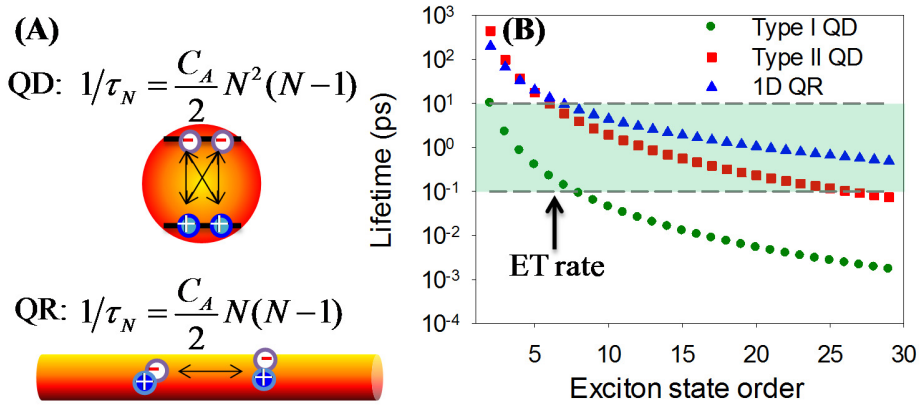


**Figure 7.7.** (A) Schematic depiction of multiexciton Auger annihilation process and the Auger rate scaling law in QDs (upper) and QRs (lower), (B) The lifetime of n-exciton

states (n=1 to 30) of CdSe QDs (green circles)[18], quasi-type II CdSe/CdS QDs (red square)[19] and CdSe QRs (blue triangles). Typical electron transfer times from quantum dots and quantum rods to molecular adsorbates (100 fs ~ 10 ps) are indicated in the shaded area, suggesting that more efficient multiple exciton dissociation can be achieved in CdSe QRs and CdSe/CdS core/shell QDs than in CdSe QDs.

It is interesting to compare the multiple exciton dissociation efficiency in CdSe QRs with CdSe QDs and CdSe/CdS core/shell QDs.[20,25,26] Using $MV^{2+}$ as electron acceptors, the multiexciton dissociation efficiency in CdSe QRs reported here is much higher than that in CdSe QDs (~ 4 excitons).[18] The efficiency of multiexciton dissociation depends on the competition between interfacial charge separation and multiexciton Auger annihilation. As shown in Figure 7.5, the quantum confinement in the radial direction in the QR facilitates ultrafast electron transfer to $MV^{2+}$, with a rate comparable to or even faster than that in QD-$MV^{2+}$ complexes.[18,19,39,56] Compared to QDs, the elongation along the axial direction increases the volume of the QR, which greatly reduces the Auger rate constant. Furthermore, the formation of strongly bound 1D exciton modifies the multiexciton Auger annihilation rate scaling law (Figure 7.7A), which further lengthens the n-exciton state lifetime in QRs compared to QDs, as shown in Figure 7.7B. Thus the reduced Auger recombination rate is responsible for the enhanced MED efficiency in CdSe QRs compared to CdSe QDs. Although Auger recombination rate can also be decreased in type II CdSe/CdS core/shell QDs by reducing the electron/hole overlap, compared to QRs, the n-exciton state lifetime decreases much more rapidly with *n* in

core/shell QDs due to different scaling law, reducing the efficiency of multiple exciton dissociation.[19]

## 7.3. Conclusion

In summary, by transient absorption spectroscopy, we show the formation of bound 1D exciton states in CdSe QRs. Furthermore, the lifetime of n-exciton states is controlled by Auger recombination, which occurs primarily through an exciton-exciton bimolecular collision process with rates proportional to $n(n-1)$, in contrast to the $n^2(n-1)$ dependence in CdSe QDs. This weaker dependence on $n$ and the larger volume in CdSe QRs greatly lengthen their multiexciton lifetimes compared to CdSe QDs of a similar optical gap. In the presence of electron acceptors, such as methylviologen, excitons can be dissociated by ultrafast interfacial electron transfer. Because of quantum confinement along the radial direction of the rod, the electron transfer rate from QRs is comparable to that in CdSe QDs. The combination of ultrafast electron transfer and reduced Auger recombination rates significantly enhances multiexciton dissociation efficiency in CdSe QRs. Under high excitation intensity, more than 21 electrons can be transferred from one CdSe quantum rod to adsorbed methylviologen molecules, greatly exceeding the MED efficiency of CdSe QDs. Our findings, together with large absorption cross section, improved charge transport and enhanced multiexciton generation reported in these materials,[25,31,52,57] suggest that quantum confined 1D nanomaterials (NR and NW) are

promising light harvesting and multielectron transferring materials for photocatalytic and optoelectronic devices.

## References

(1) Coe, S.; Woo, W.-K.; Bawendi, M.; Bulovic, V. *Nature* **2002**, *420*, 800.

(2) Colvin, V. L.; Schlamp, M. C.; Alivisatos, A. P. *Nature* **1994**, *370*, 354.

(3) Klimov, V. I.; Ivanov, S. A.; Nanda, J.; Achermann, M.; Bezel, I.; McGuire, J. A.; Piryatinski, A. *Nature* **2007**, *447*, 441.

(4) Kambhampati, P. *Acc. Chem. Res.* **2010**, *44*, 1.

(5) Fisher, B.; Caruge, J. M.; Zehnder, D.; Bawendi, M. *Phys. Rev. Lett.* **2005**, *94*, 087403.

(6) Osovsky, R.; Cheskis, D.; Kloper, V.; Sashchiuk, A.; Kroner, M.; Lifshitz, E. *Phys. Rev. Lett.* **2009**, *102*, 197401.

(7) Sukhovatkin, V.; Hinds, S.; Brzozowski, L.; Sargent, E. H. *Science* **2009**, *324*, 1542.

(8) Sambur, J. B.; Novet, T.; Parkinson, B. A. *Science* **2010**, *330*, 63.

(9) Semonin, O. E.; Luther, J. M.; Choi, S.; Chen, H.-Y.; Gao, J.; Nozik, A. J.; Beard, M. C. *Science* **2011**, *334*, 1530.

(10) Debnath, R.; Bakr, O.; Sargent, E. H. *Energy Environ. Sci.* **2011**, *4*, 4870.

(11) Chan, W.-L.; Ligges, M.; Jailaubekov, A.; Kaake, L.; Miaja-Avila, L.; Zhu, X.-Y. *Science* **2011**, *334*, 1541.

(12) Nair, G.; Chang, L.-Y.; Geyer, S. M.; Bawendi, M. G. *Nano Lett.* **2011**, *11*, 2145.

(13) Klimov, V. I.; Mikhailovsky, A. A.; McBranch, D. W.; Leatherdale, C. A.; Bawendi, M. G. *Science* **2000**, *287*, 1011.

(14) Klimov, V. I.; McGuire, J. A.; Schaller, R. D.; Rupasov, V. I. *Phys. Rev. B* **2008**, *77*, 195324.

(15) Barzykin, A. V.; Tachiya, M. *J. Phys.: Condens. Matter* **2007**, *19*, 065105.

(16) Ueda, A.; Tayagaki, T.; Kanemitsu, Y. *J. Phys. Soc. Jpn.* **2009**, *78*, 083706.

(17) Huang, J.; Huang, Z.; Yang, Y.; Zhu, H.; Lian, T. *J. Am. Chem. Soc.* **2010**, *132*, 4858.

(18) Matylitsky, V. V.; Dworak, L.; Breus, V. V.; Basche, T.; Wachtveitl, J. *J. Am. Chem. Soc.* **2009**, *131*, 2424.

(19) Zhu, H.; Song, N.; Rodríguez-Córdoba, W.; Lian, T. *J. Am. Chem. Soc.* **2012**, *134*, 4250.

(20) Hu, J.; Li, L.-s.; Yang, W.; Manna, L.; Wang, L.-w.; Alivisatos, A. P. *Science* **2001**, *292*, 2060.

(21) Kan, S.; Mokari, T.; Rothenberg, E.; Banin, U. *Nat. Mater.* **2003**, *2*, 155.

(22) Yu, H.; Li, J.; Loomis, R. A.; Gibbons, P. C.; Wang; Buhro, W. E. *J. Am. Chem. Soc.* **2003**, *125*, 16168.

(23) Amirav, L.; Alivisatos, A. P. *J. Phys. Chem. Lett.* **2010**, *1*, 1051.

(24) Tang, M. L.; Grauer, D. C.; Lassalle-Kaiser, B.; Yachandra, V. K.; Amirav, L.; Long, J. R.; Yano, J.; Alivisatos, A. P. *Angew. Chem. Int. Ed.* **2011**, *50*, 10203.

(25) Tang, J.; Huo, Z.; Brittman, S.; Gao, H.; Yang, P. *Nat Nano* **2011**, *6*, 568.

(26) Shabaev, A.; Efros, A. L. *Nano Lett.* **2004**, *4*, 1821.

(27) Bartnik, A. C.; Efros, A. L.; Koh, W. K.; Murray, C. B.; Wise, F. W. *Phys. Rev. B* **2010**, *82*, 195313.

(28) Slachmuylders, A. F.; Partoens, B.; Magnus, W.; Peeters, F. M. *Phys. Rev. B* **2006**, *74*, 235321.

(29) Muljarov, E. A.; Zhukov, E. A.; Dneprovskii, V. S.; Masumoto, Y. *Phys. Rev. B* **2000**, *62*, 7420.

(30) Vietmeyer, F.; McDonald, M. P.; Kuno, M. K. *J. Phys. Chem. C* **2012**, *116*, 12379.

(31) Protasenko, V.; Bacinello, D.; Kuno, M. *J. Phys. Chem. B* **2006**, *110*, 25322.

(32) Chen, X.; Nazzal, A.; Goorskey, D.; Xiao, M.; Peng, Z. A.; Peng, X. *Phys. Rev. B* **2001**, *64*, 245304.

(33) Carey, C. R.; LeBel, T.; Crisostomo, D.; Giblin, J.; Kuno, M.; Hartland, G. V. *J. Phys. Chem. C* **2010**, *114*, 16029.

(34) Giblin, J.; Kuno, M. *J. Phys. Chem. Lett.* **2010**, *1*, 3340.

(35) Htoon, H.; Hollingsworth, J. A.; Dickerson, R.; Klimov, V. I. *Phys. Rev. Lett.* **2003**, *91*, 227401.

(36) Robel, I.; Bunker, B. A.; Kamat, P. V.; Kuno, M. *Nano Lett.* **2006**, *6*, 1344.

(37) Vietmeyer, F.; Frantsuzov, P. A.; Janko, B.; Kuno, M. *Phys. Rev. B* **2011**, *83*, 115319.

(38) Barzykin, A. V.; Tachiya, M. *Phys. Rev. B* **2005**, *72*, 075425.

(39) Jiang, Z.-J.; Kelley, D. F. *J. Phys. Chem. C* **2011**, *115*, 4594.

(40) Klimov, V. I. *Annu. Rev. Phys. Chem.* **2007**, *58*, 635.

(41) Puthussery, J.; Lan, A.; Kosel, T. H.; Kuno, M. *ACS Nano* **2008**, *2*, 357.

(42) Mohamed, M. B.; Burda, C.; El-Sayed, M. A. *Nano Lett.* **2001**, *1*, 589.

(43) Burda, C.; Link, S.; Mohamed, M.; El-Sayed, M. *J. Phys. Chem. B* **2001**, *105*, 12286.

(44) McArthur, E. A.; Morris-Cohen, A. J.; Knowles, K. E.; Weiss, E. A. *J. Phys. Chem. B* **2010**, *114*, 14514.

(45) Huang, J.; Huang, Z.; Jin, S.; Lian, T. *J. Phys. Chem. C* **2008**, *112*, 19734.

(46) Song, N.; Zhu, H.; Jin, S.; Lian, T. *ACS Nano* **2011**, *5*, 8750.

(47) Knowles, K. E.; McArthur, E. A.; Weiss, E. A. *ACS Nano* **2011**, *5*, 2026.

(48) Taguchi, S.; Saruyama, M.; Teranishi, T.; Kanemitsu, Y. *Phys. Rev. B* **2011**, *83*, 155324.

(49) Burstein, E. *Physical Review* **1954**, *93*, 632.

(50) Wang, F.; Dukovic, G.; Knoesel, E.; Brus, L. E.; Heinz, T. F. *Phys. Rev. B* **2004**, *70*, 241403.

(51) Jiang, Z.-J.; Kelley, D. F. *J. Phys. Chem. C* **2010**, *114*, 17519.

(52) Kuno, M. *Phys. Chem. Chem. Phys.* **2008**, *10*, 620.

(53) Zhu, H.; Song, N.; Lian, T. *J. Am. Chem. Soc.* **2010**, *132*, 15038.

(54) Zhu, H.; Song, N.; Lian, T. *J. Am. Chem. Soc.* **2011**, *133*, 8762.

(55) Klimov, V. I. *J. Phys. Chem. B* **2000**, *104*, 6112.

(56) Morris-Cohen, A. J.; Frederick, M. T.; Cass, L. C.; Weiss, E. A. *J. Am. Chem. Soc.* **2011**, *133*, 10146.

(57) Cunningham, P. D.; Boercker, J. E.; Foos, E. E.; Lumb, M. P.; Smith, A. R.; Tischler, J. G.; Melinger, J. S. *Nano Lett.* **2011**, *11*, 3476.

# Appendix 1.

## Femtosecond TA spectra of CdSe NRs and NR-$MV^{2+}$ complexes under different excitation intensities.

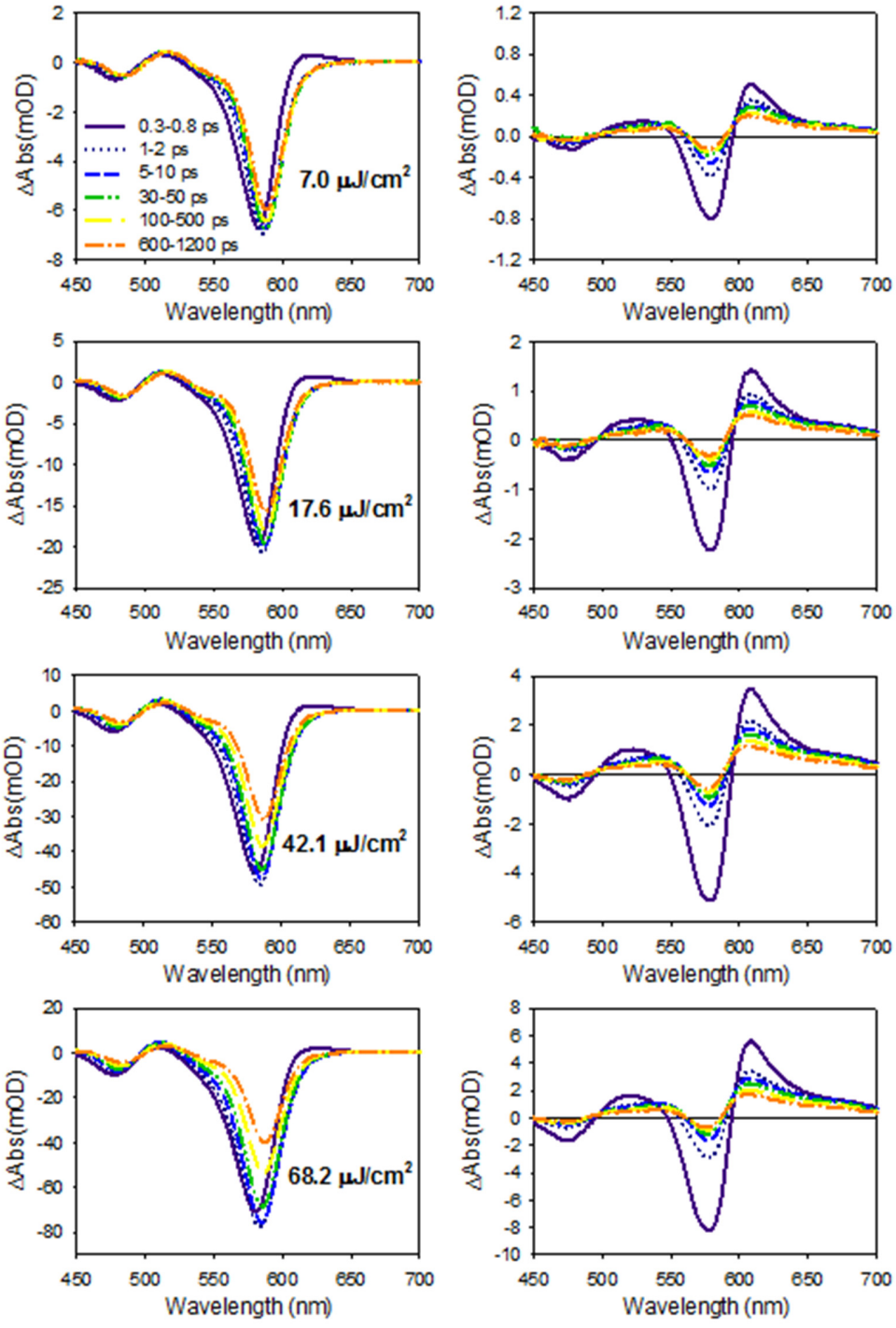
0.3-0.8 ps
1-2 ps
5-10 ps
30-50 ps
100-500 ps
600-1200 ps
7.0 µJ/cm²
17.6 µJ/cm²
42.1 µJ/cm²
68.2 µJ/cm²
ΔAbs(mOD)
Wavelength (nm)

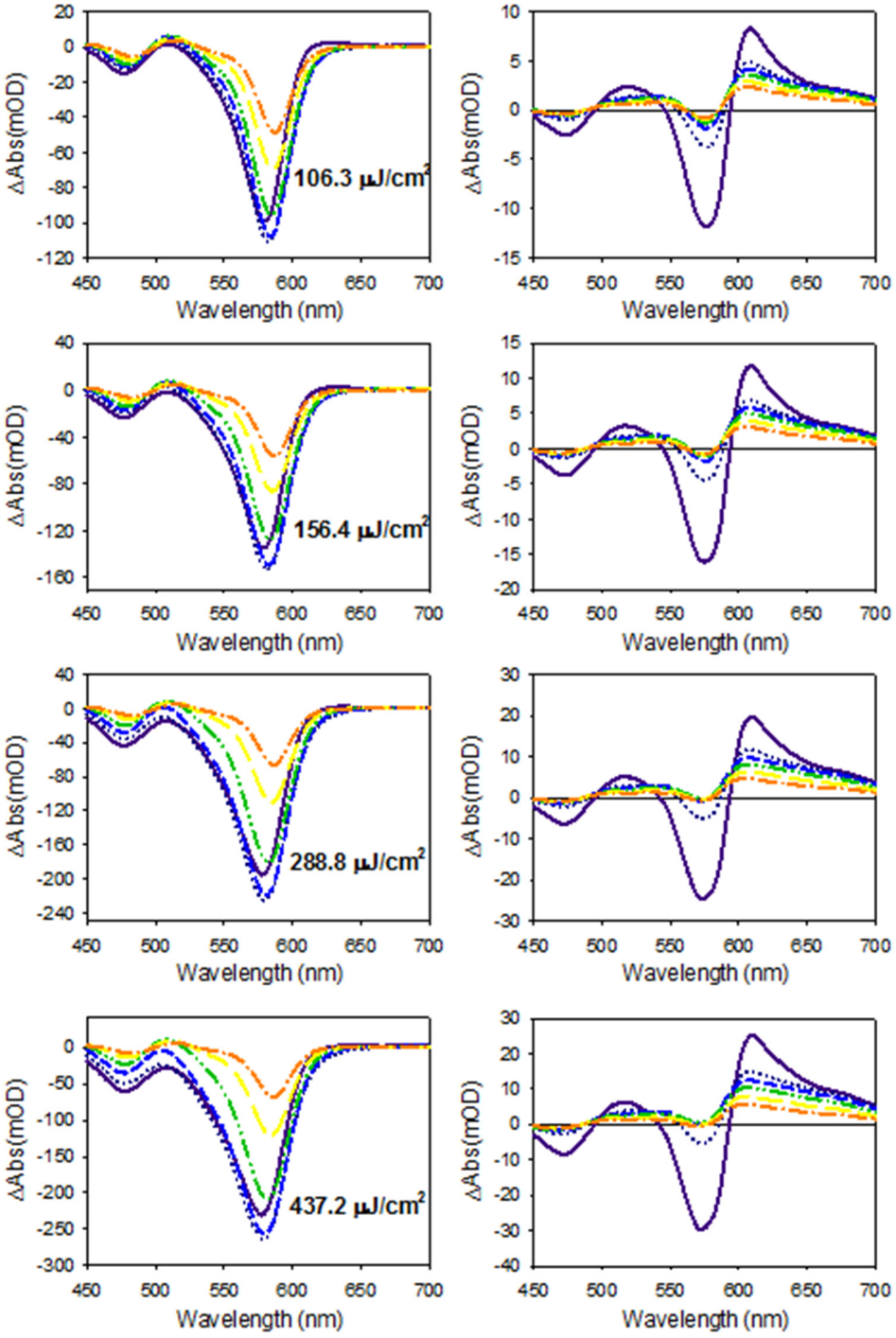
106.3 μJ/cm²
156.4 μJ/cm²
288.8 μJ/cm²
437.2 μJ/cm²
ΔAbs(mOD)
Wavelength (nm)

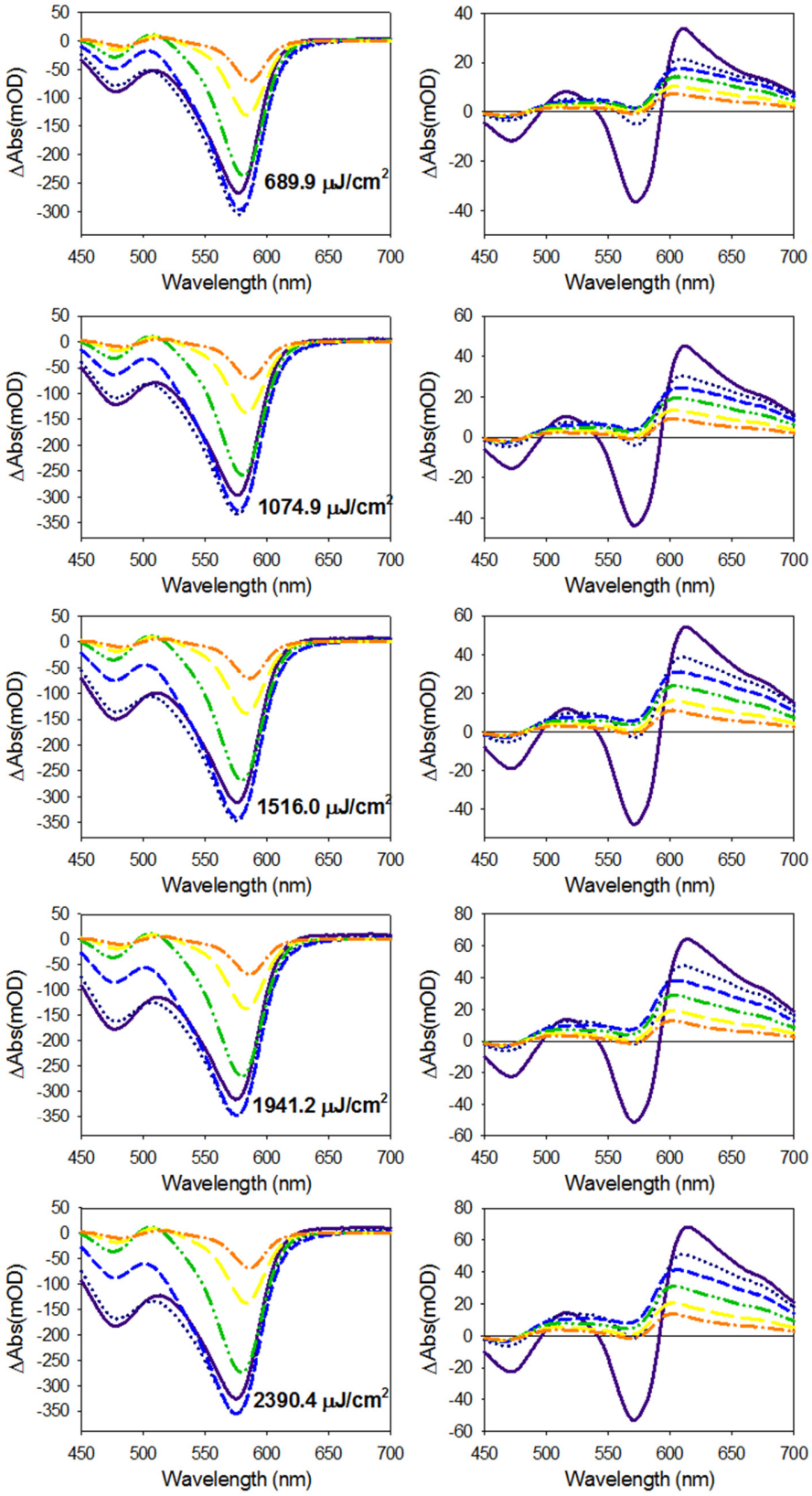
ΔAbs(mOD)
Wavelength (nm)
689.9 μJ/cm2
1074.9 μJ/cm2
1516.0 μJ/cm2
1941.2 μJ/cm2
2390.4 μJ/cm2

**Figure A.7.1.** Femtosecond TA spectra of CdSe QR (left column) and CdSe QR-$MV^{2+}$ complex (right column) at 400 nm excitation at indicated excitation intensities.

# Appendix 2.

## Excitation intensity dependent TA spectra and kinetics of CdSe QDs.

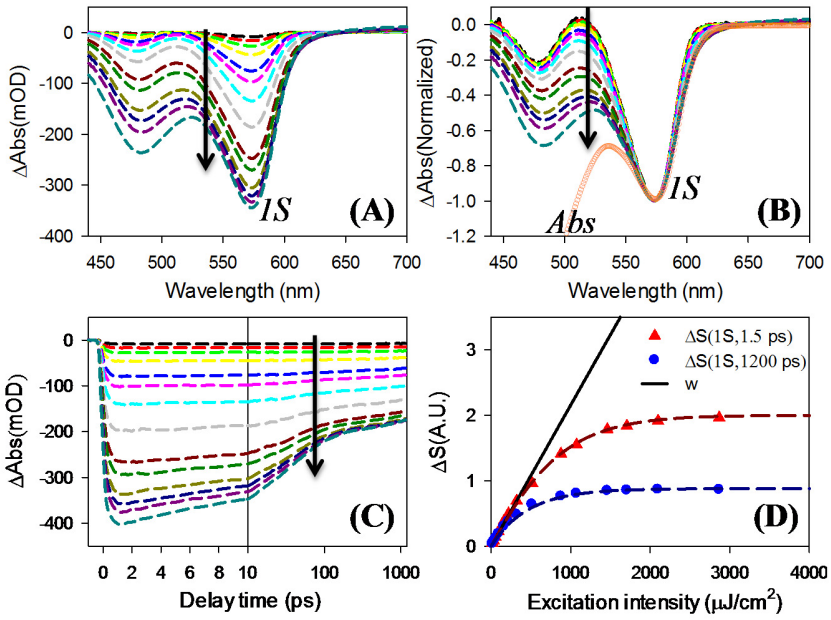


**Figure A.7.2.** (A) TA spectra of CdSe QDs at 1.5 ps under different excitation intensities (from 19.4 to 2869 μJ/$cm^2$). (B) Normalized comparison of TA spectra in (A). These spectra have been normalized to the same amplitude at the peak of 1S exciton bleach (574nm). Also shown is the steady state absorption spectrum of CdSe QDs (orange

circles). (C) Transient 1S exciton decay kinetics of CdSe QDs under different excitation intensities. (D) Normalized 1S peak signal at early time (1.5 ps) and later time (1200 ps) as a function of excitation intensity. The solid lines are fits according to Poisson distribution model for a 2 fold degenerate transition

# Appendix 3.

## Simulation of normalized PA decay kinetics

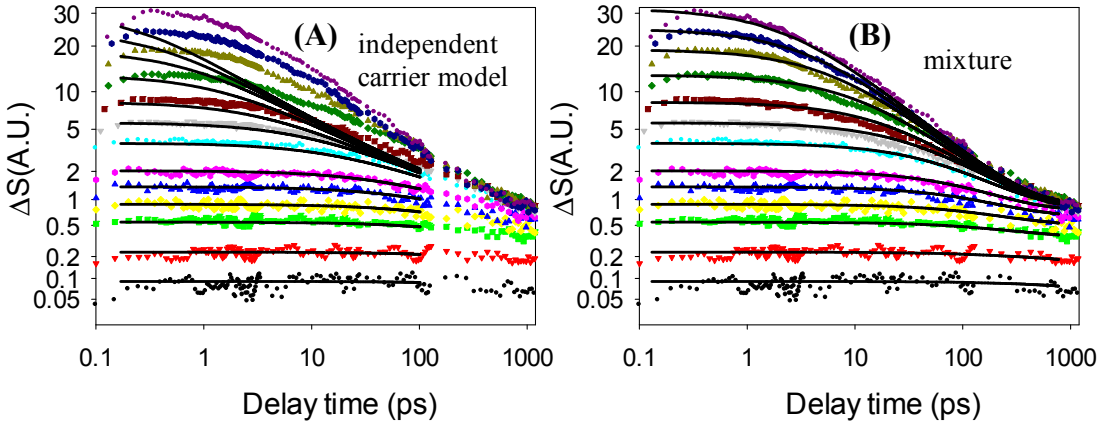


**Figure A.7.3.** Measured normalized PA decay kinetics (open circles) and simulated kinetics (sold lines) obtained by assuming (A) an independent carrier model and (B) a mixture of populations following excitonic (93 %) and independent carrier (7%) models. The details of these models are described in the main text. Clearly the independent carrier model does not agree with the experimental results.

# Appendix 4.

## Comparsion of 670 nm kinetics between CdSe QRs and CdSe QR-$MV^{2+}$ complexes under ~590nm excitation

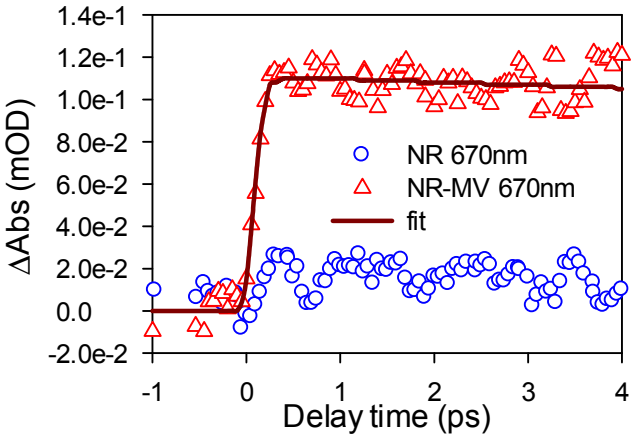


**Figure A.7.4.** Comparison of TA kinetics of CdSe QRs (blue circles) and CdSe QR-$MV^{2+}$ complexes (red triangles) at 670 nm under 590 nm band edge excitation. The signal of free QRs can be attributed to PA. The larger signal in QR-$MV^{2+}$ complexes can be attributed to the formation of $MV^{+\bullet}$ radicals. A single exponential fit of the $MV^{+}$ radical formation kinetics (dark red line) yields an electron transfer time ~59 fs.

# Chapter 8. Redox Mediator Photoreduction and $H_2$ Evolution Using CdSe/CdS Dot-in-rod Nanorod



## 8.1. Introduction

Direct solar-to-fuel conversion has been intensely investigated in recent years as a potential approach for solar energy conversion and storage.[1] The overall process consists of two half reactions: the oxidation of water to $O_2$ ($2H_2O \rightarrow 2O_2 + 4H^+ + 4e^-$) and the reduction of $CO_2$ or water ($2H^+ + 2e^- \rightarrow 2H_2$) to form fuel. A general photoreduction scheme, depicted in Fig. 8.1A, involves i) the absorption of light by the sensitizer (with efficiency $\phi_{LH}$), ii) the charge separation and reduction of the catalyst *via* direct electron transfer or redox mediators (with efficiency $\phi_{col}$), and iii) the turnover of the substrates to fuel by the reduced catalyst (with efficiency $\phi_{cat}$). The efficiencies of these processes determine the overall external quantum efficiency of solar-to-fuel conversion, defined as the ratio of products to incident photons, $\Phi = \phi_{LH} \times \phi_{col} \times \phi_{cat}$. Therefore, the advancement of solar-to-fuel conversion technologies requires the development of

efficient catalysts (increasing $\phi_{cat}$) for $H_2$ evolution and $CO_2$ reduction as well as better materials and approaches for light harvesting and charge separation (increasing $\phi_{LH}$, $\phi_{col}$).

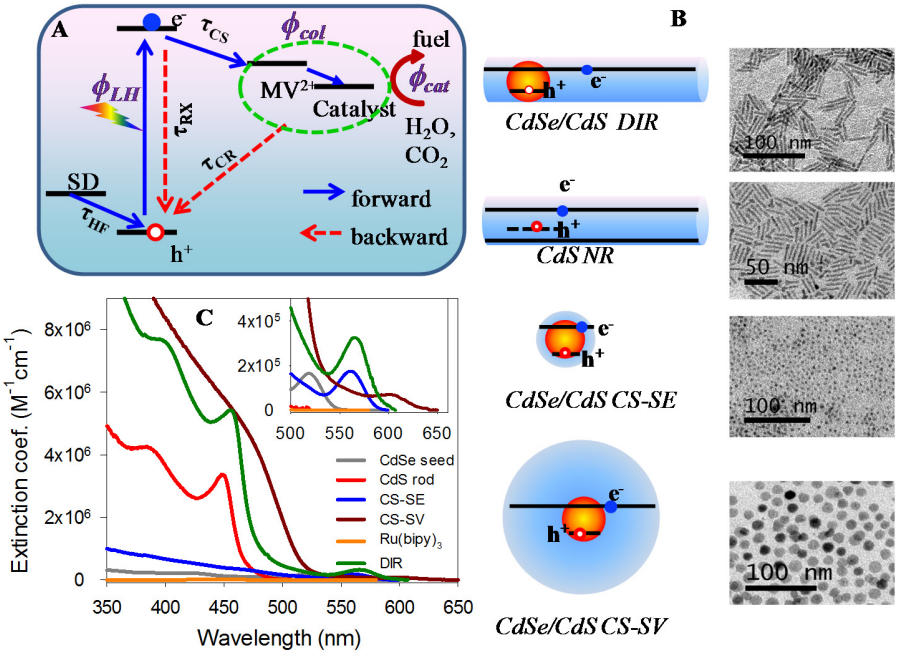


**Figure 8.1.** (A) Schematic depiction of relevant processes in a solar-to-fuel conversion system containing sacrificial electron donor (SD), sensitizer, redox mediator ($MV^{2+}$) and catalyst. The competitions between the forward (electron transfer and hole filling, with time constant $\tau_{CS}$ and $\tau_{HF}$, respectively) and backward (electron – hole and charge recombination, with time constants $\tau_{RX}$ and $\tau_{CR}$, respectively) reactions determine the charge collection efficiency ($\phi_{col}$). (B) Schematic structures (left) and TEM images (right) of CdSe/CdS dot-in-rod (DIR) nanorods (NRs) as well as CdS NRs of similar dimensions, CdSe/CdS core/shell QDs of similar lowest exciton energy (CS-SE), and CdSe/CdS core/shell QDs of similar volume (CS-SV) as the DIR. The horizontal lines in the

schematic structures indicate the extent of delocalization of the lowest energy conduction band electron and valence band hole. (C) Extinction coefficient spectra of CdSe/CdS DIR, CdSe seed, CdS NR, CdSe/CdS CS-SE, CdSe/CdS CS-SV and $Ru(bipy)_3^{2+}$. Inset: expanded view of the lowest energy exciton bands.

Quantum-confined semiconductor nanocrystals (NCs) have many characteristics that are ideal for light harvesting and charge separation applications.[2-4] Compared to molecular chromophores,[5-8] these NCs offer unique size-dependent absorption properties, large extinction coefficients over a broad spectral range, long exciton lifetimes, possibility of generating multiple excitons by single photons, and enhanced photostability.[3,4,9] The surface of NCs can be readily modified for specific functional targets and/or reaction environments.[10-12] Recent advances in the synthesis of nano-heterostructures consisting of two or more materials provide additional control of the electron and hole wave functions in these materials (i. e. wave function engineering) for optimizing charge separation and photocatalytic properties.[4,13-16] Furthermore, some of these nano-heterostructures have built-in directional charge separation and catalytic units,[17,18] resembling the well-studied molecular dyads and triads.[19-21]

Many solar-to-fuel conversion processes, such as $H_2$ evolution or $CO_2$ reduction, require the transfer of multiple electrons. Because a single photon absorption event results in the excitation and transfer of one electron in most light harvesting materials, effective schemes for accumulating multiple electrons at the catalyst while simultaneously suppressing charge recombination processes are also required. In nature,

one-electron redox mediators/relays can be used to sequentially deliver the electrons from the light harvesting units to the catalytic centers.[22] It has been reported that $MV^{2+/+}$ couple (-0.45 vs NHE in aqueous solution) can act as an effective one-electron mediator for multi-electron photocatalytic reactions, such as $H_2$ evolution (with Pt[5,23,24] and hydrogenase[25,26]), $CO_2$ reduction (with formate dehydrogenase[27] and Pd[28]) and other reductase-dependent reactions.[29-32] Thus, efficient solar-to-fuel conversion can be realized if a scheme for efficient light-driven photoreduction of $MV^{2+}$ or other redox mediators can be developed. Although electron transfer from semiconductor NCs to $MV^{2+}$ has been observed,[33,34] charge recombination is also rapid in NC-$MV^{2+}$ complexes (*via infra*). As a result, an efficient system for photogeneration of $MV^{+\bullet}$ radicals and photocatalysis has yet to be developed.[35,36]

In this chapter, we report a colloidal quasi-type II[16,37] nanorod (NR) based system for the photogeneration of $MV^{+\bullet}$ radicals with near-unity quantum efficiency over a broad $MV^{2+}$ concentration range (0.040 - 125 mM). The system consists of a simple mixture of 3-mercaptopropionic acid (MPA) caped water-soluble CdSe/CdS dot-in-rod (DIR) NRs, $MV^{2+}$ and excess MPA in aqueous solution. Addition of Pt nanoparticles (NPs) into the above system leads to direct conversion of solar energy to $H_2$ with a ~14% internal quantum efficiency, demonstrating the applicability of this highly efficient and flexible $MV^{+\bullet}$ radical generation system for solar-to-fuel conversion. To understand the origin of the unprecedented high steady-state $MV^{2+}$ photoreduction efficiency, we compare the quantum efficiencies and transient kinetics of the CdSe/CdS DIR with a commonly used molecular chromophore, $Ru(bipy)_3^{2+}$, and related nanostructures of different shapes and

dimensions (Fig. 8.1B). These NCs include CdSe seed quantum dots (QDs) used to prepare the DIR, CdS NRs of similar dimensions (diameter and length), CdSe/CdS core/shell QDs of similar lowest exciton energy (CS-SE), and giant CdSe/CdS core/shell QDs of similar volume (CS-SV). These comparisons show that the electron and hole wave functions in the CdSe/CdS quasi-type II DIR enable ultrafast electron transfer to $MV^{2+}$, ultrafast hole filling by MPA, and ultraslow charge recombination, resulting in the near-unity quantum yield of $MV^{+\bullet}$ radical generation. Our study demonstrates the possibility of using wave function engineering to enhance light harvesting and charge separation properties of quantum confined nano-heterostructures.

## 8.2. Results and Discussion

### 8.2.1. $MV^{2+}$ Photoreduction

The CdSe/CdS DIR, CdSe/CdS CS-SE, and CdSe/CdS CS-SV heterostructures used in this study are grown from the same CdSe seed QDs. Starting from TOPO-capped CdSe seed with a lowest exciton peak at 520 nm ( 2.6 nm in diameter[39]), TOPO-capped CdSe/CdS DIR with 3.1 ± 0.2 nm in diameter and 35.3 ± 2.3 nm in length (Figure 8.1B) was prepared. After ligand exchange, mercaptopropionic acid (MPA)-capped water soluble NRs were obtained. It should be noted that CdS NR, CdSe/CdS DIR and CdSe/CdS CS-SV have similar volumes and surface areas (within a factor of 2~3). The

extinction coefficient (EC) spectra of CdSe seed, CdS rod, CdSe/CdS DIR, CdSe/CdS CS-SE, CdSe/CdS CS-SV and $Ru(bipy)_3^{2+}$ are compared in Figure 8.1C. The EC spectra of CdSe seed and $Ru(bipy)_3^{2+}$ are deduced from literature values[6,39] and the EC spectra of all other NCs are estimated from their UV-Vis absorption spectra by assuming that their concentrations are the same as those of the CdSe seed used to start the growth process. Because of the loss of NCs in the synthesis and purification process, the estimated ECs should be considered as a lower limit with ~20% error. All semiconductor NCs have much higher ECs over a broader spectral range than $Ru(bipy)_3^{2+}$. CdSe/CdS heterostructures exhibit the absorption properties of both the CdSe seed and CdS shell or rod, as well as new CdSe-to-CdS transitions, thus exhibiting improved light harvesting ability compared to single component nanomaterials (CdSe seed or CdS rod).

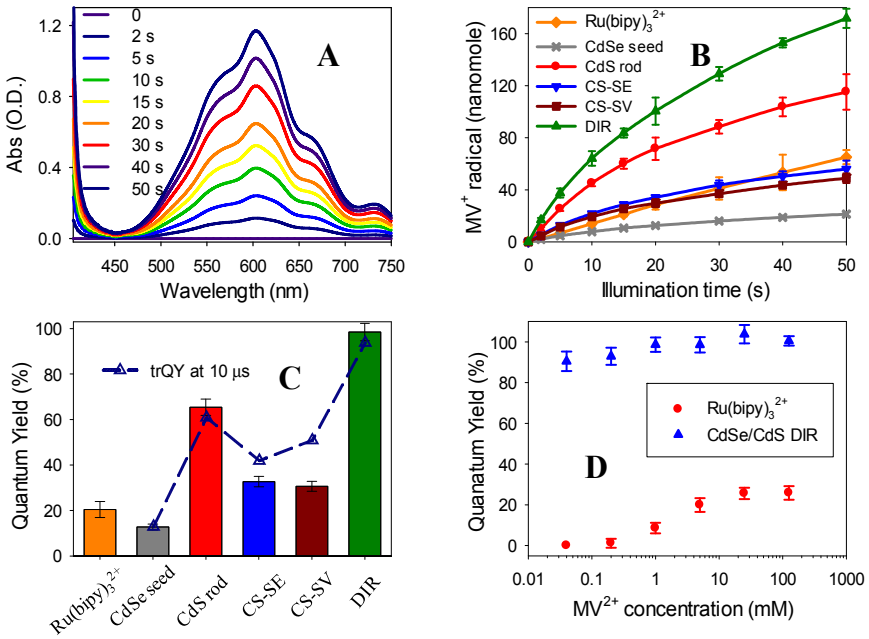

**Figure 8.2.** Steady-state photoreduction of $MV^{2+}$. (A) UV-Vis difference spectra (after-before irradiation) of a solution containing CdSe/CdS DIR, $MV^{2+}$ and MPA after indicated time of irradiation, showing the generation of $MV^{+\bullet}$ radicals. Similar spectra using other NCs are shown in Figure A.8.1. Experiment conditions: light source (wavelength - 455 nm, power - 2.4 mW, beam diameter at sample ~0.4 cm), absorbance of sensitizers at 455 nm (1.1 OD), sacrificial electron donor (50 mM MPA for NCs and 50 mM TEOA for $Ru(bipy)_3^{2+}$), 5 mM $MV^{2+}$, 50 mM pH 7.8 phosphate buffer, total reaction volume (2 mL). (B) $MV^{+\bullet}$ radical generation kinetics using different sensitizers. (C) Initial quantum yields of $MV^{+\bullet}$ radical generation using different sensitizers (bars). Also plotted are the transient quantum yields (open triangles) at 10 μs obtained from transient absorption measurements. (D) Dependence of the initial quantum yield on $MV^{2+}$ concentration (0.040 ~ 125 mM) for $Ru(bipy)_3^{2+}$ and CdSe/CdS DIR.

Photoreduction of $MV^{2+}$ was performed by mixing sensitizers, $MV^{2+}$ (5.0 mM) and sacrificial electron donors in anaerobic pH=7.8 aqueous solutions where all NCs were well dissolved to form a homogeneous system. Excess (50 mM) MPA and triethanolamine (TEOA) were used as sacrificial electron donors for NCs and $Ru(bipy)_3^{2+}$, respectively. The sensitizer (MPA-capped NC or $Ru(bipy)_3^{2+}$) concentrations were adjusted to ensure that all solutions have the same absorbance at the illumination wavelength (1.1 OD at 455 nm). Under these conditions, the CdSe/CdS DIR concentration (~0.2 μM) is ~500-fold smaller than $Ru(bipy)_3^{2+}$. Upon illumination of a solution containing CdSe/CdS DIR, $MV^{+\bullet}$ radicals form quickly, as indicated by the

growth of distinct 605 nm band in the difference spectra shown in Figure 8.2A. This feature can be attributed to $MV^{+\bullet}$ radicals because MPA and $MV^{2+}$ have negligible absorption in this spectral range. Complete sets of steady state UV-Vis difference spectra for all sensitizers are shown in Figure A.8.1. In the absence of sensitizers or illumination, no $MV^{+\bullet}$ radicals were observed, indicating that these reactions are indeed photo-driven. Using the reported extinction coefficient (13700 ± 300 $M^{-1}cm^{-1}$ at 605 nm),[40] the concentrations of $MV^{+\bullet}$ radicals can be calculated to obtain the radical formation kinetics, which are shown in Fig. 8.2B. Because these solutions have same illumination intensity and same absorbance at illumination wavelength thus same photon absorption rates, the $MV^{+\bullet}$ radical formation rates, which is the slope of formation kinetics in Figure 8.2B, reflect the charge separation efficiencies using these sensitizers. Clearly, CdSe/CdS DIR shows the best $MV^{2+}$ photoreduction performance among the tested sensitizers.

To quantify the performance of these sensitizers, we compare their photon-to-$MV^{+\bullet}$ conversion quantum yields defined as: $\Phi_{MV} = \Delta(MV^{+\bullet})/ \Delta(\hbar v)$, where $\Delta(MV^{+\bullet})$ is the $MV^{+\bullet}$ generation rate and $\Delta(\hbar v)$ is the photon absorption rate of the reaction solution, respectively. The latter can be calculated from illumination light intensity and UV-Vis absorption spectrum. The $MV^{+\bullet}$ generation rate is the slope of $MV^{+\bullet}$-*vs*-time plots shown in Fig. 8.2B. It is largest at the beginning of the reaction and decreases slowly with time because of ongoing photoreduction. For this reason, only the slope of initial linear range (first three points, 0, 2s, 5s) are used to calculate quantum yields (defined as initial quantum yields) and the values for different sensitizers are compared in Fig. 8.2C and Table 8.1.

Under our experiment conditions, $Ru(bipy)_3^{2+}$ shows a 20.4 ± 3.5 % initial quantum yield for $MV^{+\bullet}$ radical generation, in agreement with the reported value for the same sensitizer under similar conditions.[41-43] The initial quantum yield for the CdSe seed is relatively low (11.4 ± 1.3 %). However, for CdSe/CdS DIR, the yield increases by one order of magnitude to near-unity (98.2 ± 3.8 %), indicating that nearly every absorbed photon leads to the reduction of one $MV^{2+}$ molecule with negligible loss. The initial quantum yields for other sensitizers (CdS NR, CdSe/CdS CS-SE and CdSe/CdS CS-SV) fall between the values of CdSe seed and CdSe/CdS DIR.

The quantum yields reported above were measured in solutions with 5 mM $MV^{2+}$. Under these conditions, less than 2% of the $MV^{2+}$ was reduced after 50 s of illumination. It has been pointed out that as an electron mediator, a high concentration of $MV^{2+}$ is undesirable in some photocatalytic systems because of either reversed transformation of the product to reactant, such as $MV^{2+} + \frac{1}{2}H_2 + OH^- \overset{Pt}{\leftrightarrow} MV^{+\cdot} + H_2O$, or the adsorption of $MV^{2+}$ on catalysts, blocking the active sites.[44-46] We compare the initial quantum yields of $MV^{2+}$ photoreduction as a function of $MV^{2+}$ concentration for $Ru(bipy)_3^{2+}$ and CdSe/CdS DIR in Fig. 8.2D. In this experiment, the $MV^{2+}$ concentration was varied between 40 μM and 125 mM, while other experimental conditions remain the same as those used in Figure 8.2A. The kinetics for $MV^{+\bullet}$ radical formation at all $MV^{2+}$ concentrations can be found in Appendix 2. For $Ru(bipy)_3^{2+}$, the initial quantum yield is strongly dependent on $MV^{2+}$ concentration, which is < 0.1% (below the detection limit) at 40 μM and saturates at 26 ± 3% at 25 mM. This is consistent with the expected bimolecular quenching between the excited $Ru(bipy)_3^{2+}$ and $MV^{2+}$, whose quantum yield

decreases at lower $MV^{2+}$ concentrations.[43] Therefore, undesirably high $MV^{2+}$ concentrations are sometimes used in catalytic systems employing $Ru(bipy)_3^{2+}$ sensitizers.[45,47] For CdSe/CdS DIR, the quantum yield remains high (> 90%) over the evaluated concentration range (0.040 - 125 mM). The weaker $MV^{2+}$ concentration dependence indicates the formation of NC-$MV^{2+}$ complexes, likely facilitated by the electrostatic interaction between $MV^{2+}$ cations and the negatively charged NCs surface (such as deprotonated carboxylic group or uncapped, negatively charged surface atoms). The presence of NC-$MV^{2+}$ complexes is further confirmed by the observation of ultrafast electron transfer from excited NCs to $MV^{2+}$, which will be discussed below. Thus, the easily-controlled surface properties of NCs enable the formation of sensitizer/quencher complexes through electrostatic interaction, providing a simple method for constructing efficient redox mediator photoreduction systems.

### 8.2.2. $H_2$ Evolution Coupled with Pt as Catalyst

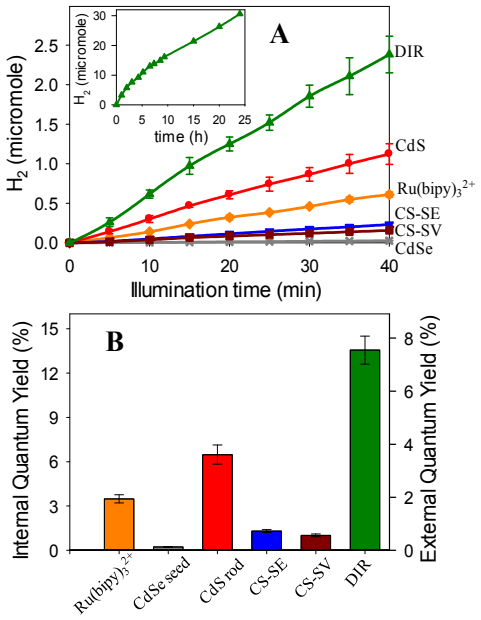


**Figure 8.3.** (A) Kinetics of $H_2$ formation from water reduction using different sensitizers in the first 40 minutes. Inset: the $H_2$ formation kinetics using CdSe/CdS DIR up to 24 hours. Conditions: $MV^{2+}$, MPA and NCs concentrations (same as in Figure 8.2A caption); 50 mM pH=6.2 phosphate buffer; $H_2$ evolution catalyst (0.8 mM Pt nanoparticles); and illumination light (8 mW, 455 nm). (B) Internal (left axis) and external (right axis) quantum yields of $H_2$ evolution using different sensitizers.

$MV^{+\bullet}$ radicals are known to drive water or $CO_2$ reduction in the presence of catalysts.[2, 21,27] To demonstrate the utility of the NC-based $MV^{2+}$ photoreduction systems for solar-to-fuel conversion applications, we added colloidal Pt nanoparticles (0.8 mM, capped by polyvinyl alcohol) as the catalyst for $H_2$ generation and Pt nanoparticles were uniformly dispersed in solution. The NC, MPA and $MV^{2+}$ concentrations are the same as those reported in Figure 8.2A. It has been reported efficient $H_2$ evolution from $MV^{+\bullet}$

radical using colloidal Pt catalyst requires acidic pH condition and indeed we didn't see $H_2$ generation under pH=7.8, therefore, a pH=6.2 phosphate buffer for all the sensitizers instead of pH=7.8 was used here to increase the $H_2$ generation rate.[44]. Because of the protonation of MPA (the thiol group) at the acidic conditions, the ligand partially dissociated from the NC surface and led to the precipitation of some NCs.[48] To overcome this problem, the hydrogen evolution experiment was performed under rigorous stirring, which generated a NC suspension. Upon illumination, the amount of photogenerated $H_2$ increases linearly with time in the experiment period (40 minutes) for all sensitizers (Figure 8.3A). Control experiments show that all the three components, $MV^{2+}$, Pt and light illumination, were necessary for $H^2$ generation; No $H_2$ was detected under the absence of any of them. The quantum yield of $H_2$ generation can be calculated by $\Phi_{H2} = 2\Delta(H_2)/\Delta(h\nu)$ where $\Delta(H_2)$ is the $H_2$ generation rate and the factor of 2 accounts for the requirement of two electrons per $H_2$ molecule. An external quantum yield of 7.5 ± 0.6 % is obtained for CdSe/CdS DIR. After correction for Pt absorption and cell reflection, an internal quantum yield of 13.6 ± 1.0% was estimated for CdSe/CdS DIR. These internal and external quantum yields are compared in Figure 8.3B for different sensitizers. The values for internal quantum yields represent a lower limit because the scattering loss of the suspension has not been taken into account. The trend of $H_2$ generation efficiencies agrees well with that of $MV^{+\bullet}$ radical generation efficiencies, suggesting that the modest overall $H_2$ generation quantum efficiencies are limited mainly by the low catalytic efficiency of the Pt NPs used in this study. The efficiency can be improved with optimization of the experimental conditions and the use of more efficient $H_2$ evolution catalysts (e. g. hydrogenase). The $H_2$ turnover number for each CdSe/CdS nanorod

reaches 82500 during a 24 hour test period without significant loss of activity (Fig. 8.3A inset), indicating the stability and applicability of the DIR-based $MV^{+\bullet}$ photogeneration system for solar-to-fuels conversion.

### 8.2.3. Mechanism for Efficient $MV^{2+}$ Photoreduction

As illustrated in Figure 8.1A, the overall $MV^{+\bullet}$ radical generation quantum yield depends on the rates of charge separation, charge recombination and hole filling processes in the system. To understand the origin of the different $MV^{2+}$ photoreduction performances for the nanostructures discussed above, we used time resolved transient absorption and fluorescence decay spectroscopy to directly measure the rates of these steps. We first conducted transient absorption measurement on the complete photoreduction systems under conditions similar to those for the steady-state $MV^{2+}$ photoreduction described in Fig. 8.2A. The NC concentrations have been increased by ~ 4 times to allow measurement in a thinner cell needed to maintain ultrafast time-resolution (~ 150 fs). The transient spectra and exciton bleach recovery kinetics of samples with and without $MV^{2+}$ are compared in Figure 8.4. In the absence of $MV^{2+}$, the lowest energy exciton bleach is long-lived, indicating long-lived conduction band electrons in these NCs. In the presence of $MV^{2+}$, the transient bleach of the exciton band undergoes fast and complete recovery (Figure 8.4F). After the bleach recovery, the TA spectra consist of derivative-like features of the exciton bands and the broad absorption of $MV^{+\bullet}$ radicals centered at 605 nm. The former can be attributed to the Stark-effect

induced exciton peak-shift of the NC-$MV^{2+}$ complexes in the charge separated state ($NC^{+}$- $MV^{+\bullet}$).[13,14] The formation of these spectral features and the recovery of exciton bleach confirm the transfer of electrons from NCs to $MV^{2+}$.

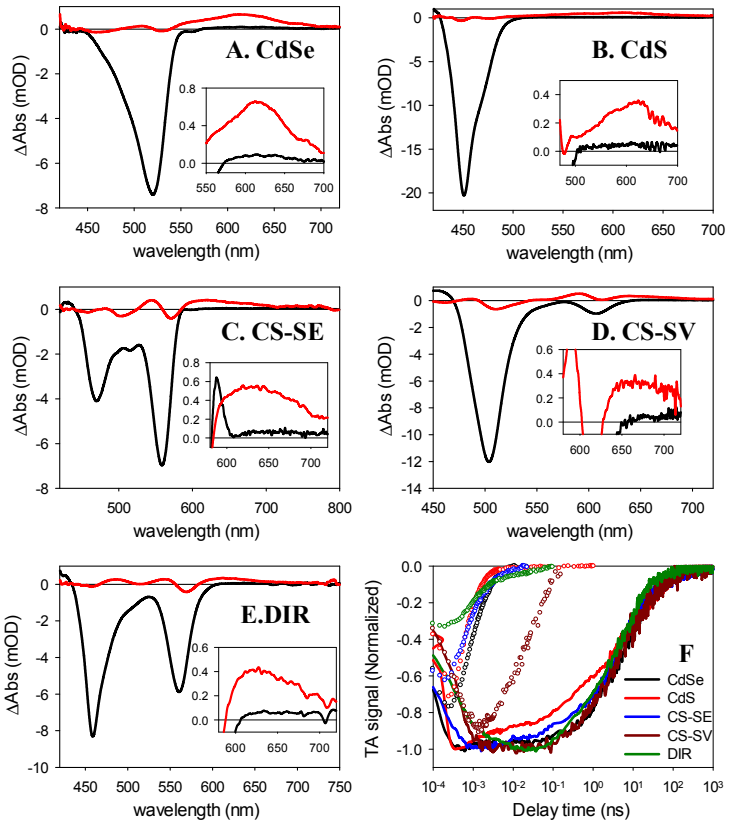


**Figure 8.4.** (A-E)TA spectra of free NCs (black line) and NC-$MV^{2+}$ complexes (red line) for ((A) CdSe seed (10-15 ps), (B) CdS NR (20-30 ps), (C) CdSe/CdS CS-SE (20-30 ps), (D) CdSe/CdS CS-SV (500 ps) and (E) CdSe/CdS DIR (10-20 ps) at indicated delay times (in parentheses) after 400 nm excitation. The $MV^{+}$ radical absorption reaches maximum at these delay times in the MPA-NC-$MV^{2+}$ complexes. Insets: expanded views of the TA spectra showing the photo-generated $MV^{+\bullet}$ radical absorption band at >600 nm.

(F) Transient bleach recovery kinetics of the lowest energy exciton bands in MPA-NCs with (circles) and without (lines) $MV^{2+}$, showing long-lived conduction band electrons in free NCs and ultrafast electron transfer in NC-$MV^{2+}$ complexes. For comparison, the transient kinetics of each NC with and without $MV^{2+}$ were taken under same excitation intensity. The transient kinetics of free NCs (without $MV^{2+}$) were normalized to 1 at the maximum signal size and the kinetics for each NC with $MV^{2+}$ were normalized accordingly using the same scaling factors for free NC.

The kinetics of the formation and decay of $MV^{+\bullet}$ radicals can be monitored at 605 nm (650 nm for CdSe/CdS CS-SV), where NCs have negligible absorption as shown in Figure 8.4. The normalized $MV^{+\bullet}$ radical kinetics for all the NCs are compared in Figure 8.5A, from which we determined the half-life time for $MV^{+\bullet}$ radical formation to represent the effective charge separation time ($\tau_{CS}$ in Table 8.1). The electron transfer times from all NCs to $MV^{2+}$ are ultrafast (~ 0.4 – 0.5 ps) except for CdSe/CdS CS-SV (~ 20 ps). These rates are similar to those measured in QD-$MV^{2+}$ complexes formed in organic solvents (Figure A.8.3)[34] and significantly faster than the diffusion-limited bimolecular quenching rate (estimated to be $5\times10^6$ $s^{-1}$ from reported rate constant of $\sim10^9$ $M^{-1}$ $s^{-1}$ and $MV^{2+}$ concentration of 5 mM).[41] These ultrafast electron transfer rates and the negligible concentration dependent radical formation quantum yields discussed above suggest that electron transfer occurs within the NC-$MV^{2+}$ complexes formed in aqueous solutions.

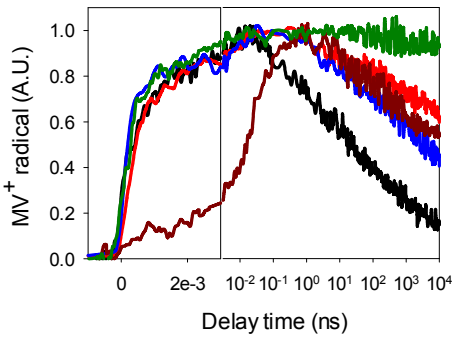


**Figure 8.5.** Comparison of the formation and decay kinetics of $MV^{+\bullet}$ radicals generated by 400 nm excitation of aqueous solutions containing different NCs: CdSe seed (black), CdSe/CdS CS-SE (blue), CdSe/CdS CS-SV (dark red), CdS rod (red) and CdSe/CdS DIR (green). The amplitude represents the transient quantum yield of $MV^{+\bullet}$ radicals (see main text for details).

**Table 8.1.** Measured and estimated time constants and yields for processes shown in Figure 1: charge separation ($\tau_{CS}$), excited state relaxation ($\tau_{RX}$), charge recombination ($\tau_{CR}$), hole filling ($\tau_{HF}$), steady-state $MV^{+\bullet}$ radical generation yield ($\Phi_{MV}$) and transient quantum yield at 9-10 μs ($\Phi_{TA}$)

| Sensitizer type | $\tau_{CS}$ (ps) | $\tau_{RX}$ (ps) | $\tau_{CR}$ (ns) | $\tau_{HF}$ (ns) | $\Phi_{TA}$ (%) | $\Phi_{MV}$ (%) |
|---|---|---|---|---|---|---|
| CdSe seed | 0.4 | > 1000 | 0.14 | 0.15 | 13 | 11.4 ± 1.3 |
| CdS NR | 0.5 | | 20 | 0.62 | 61 | 65.3 ± 3.6 |
| CdSe/CdS CS-SE | 0.4 | | 4 | 0.36 | 42 | 32.6 ± 2.3 |
| CdSe/CdS CS-SV | 20 | | 2250 | >> 100 | 51 | 30.6 ± 4.2 |
| CdSe/CdS DIR | 0.4 | | 320 | 0.31 | 94 | 98.2 ± 3.8 |

The ultrafast and complete bleach recovery and ultrafast $MV^{+\bullet}$ radical formation (Figure 8.4) suggests that the initial charge separation yield is 100% in all NC-$MV^{2+}$ complexes. Therefore, the amplitude of the normalized kinetics in Figure 8.5 represents the transient quantum yield, $\Phi_{TA}(t)$, of $MV^{+\bullet}$ radical generation. Interestingly, as shown in Table 8.1 and Fig. 8.2C, the average transient quantum yields at 9-10 μs for NCs closely follow those of steady-state $MV^{+\bullet}$ generation quantum yields. These results suggest that that the steady-state quantum yields in these systems are limited by the extent of charge recombination, which is determined by the relative rates of hole filling ($\tau_{HF}$) by the sacrificial electron donor (MPA) *vs* the charge recombination ($\tau_{CR}$) between the hole in the NC and the electron in $MV^{+\bullet}$ radicals. These rates can also be independently determined.

To measure the charge recombination rate, we investigated NC-$MV^{2+}$ complexes in chloroform in the absence of MPA using TOPO capped (water insoluble) NCs. As shown in Figure A.8.3, the $MV^{+}$ radicals are formed within hundreds of femtoseconds for all NCs except for CdSe/CdS CS-SV (20 ps), similar to MPA-capped NCs in aqueous solution (Figure 8.5). However, these kinetics show much faster decay of $MV^{+\bullet}$ radicals, reflecting the charge recombination process on the sub-nanosecond to microsecond time scale. These recombination kinetics traces are non-single-exponential. Therefore, we list the half-lifetimes in Table 8.1 to approximately represent the charge recombination time ($\tau_{CR}$) in NC-$MV^{2+}$ complexes.

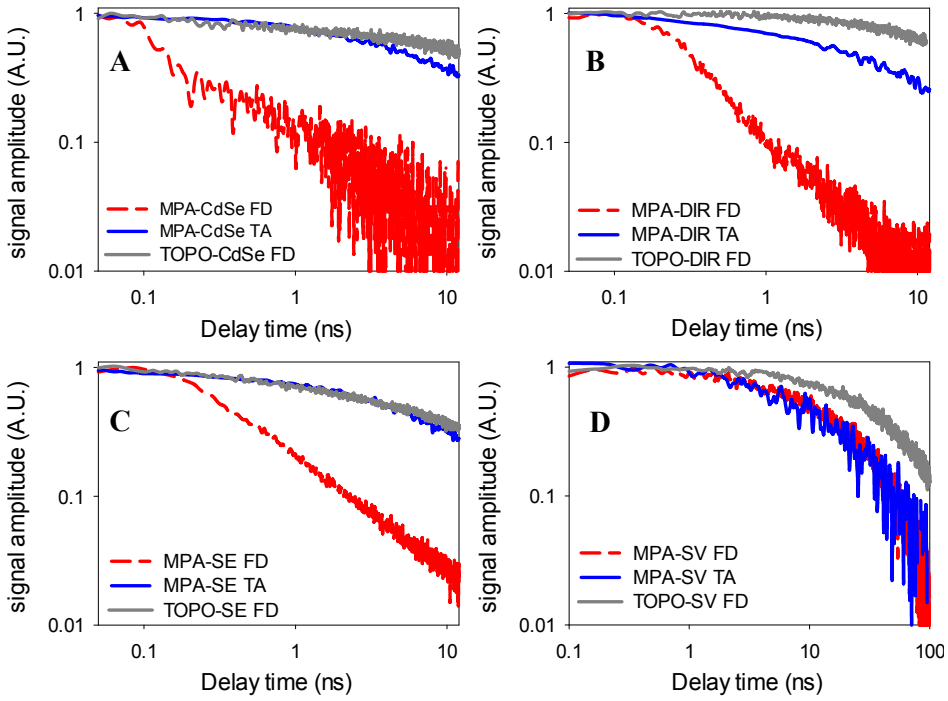


**Figure 8.6.** Comparison of fluorescence decay (red) and transient bleach recovery (blue) of the lowest energy exciton absorption band in MPA-capped NCs and fluorescence decay of TOPO-capped NCs (grey) for CdSe seed (A), CdSe/CdS DIR (B), CdSe/CdS CS-SE (C), and CdSe/CdS CS-SV (D).

To measure the hole transfer rate, we investigated MPA-capped NCs in aqueous solutions with excess MPA and without $MV^{2+}$. Under these conditions, the hole can be removed by trapping within the NC, transferring to MPA and recombining with the conduction band electron. The dynamics of the conduction band electron can be independently probed by transient bleach kinetics of the exciton bands, as mentioned above, while the fluorescence decay reflects the depopulation of the electron and/or hole. Therefore, hole transfer to MPA and/or trapping increases the NC fluorescence decay rate

without affecting the transient bleach recovery kinetics, while electron-hole recombination leads to correlated decay of fluorescence and exciton bleach recovery. For CdSe seed, CdSe/CdS CS-SE and CdSe/CdS DIR, the fluorescence decay is much faster than the transient bleach recovery (Figure 8.6), suggesting that holes decay by either trapping or transfer to MPA. Furthermore, TOPO capped NCs (before ligand exchange by MPA) shows negligible fluorescence decay on the same time scale (Figure 8.6), indicating negligible electron or hole trapping in the observed time window. Assuming that ligand exchange from TOPO to MPA does not significantly increase the hole trapping rates, these results suggest that hole transfer to MPA is the main pathway for the ultrafast emission decay in the MPA-NC complexes. The half lifetimes of these fluorescence decay curves are determined to represent the hole filling time ($\tau_{HF}$, Table 8.1). For CdSe/CdS CS-SV, the transient bleach recovery and fluorescence decay have the same kinetics (Figure 8.6D), suggesting that hole filling is much slower than the intrinsic electron-hole recombination. Therefore, the hole filling time is estimated to be >>100 ns in these giant QDs. For CdS NRs, the holes are trapped within the instrument response time of this measurement and the trapped hole can also be filled by MPA with a half-life of 0.62 ns (Figure A.8.4). Because of the limited instrument response time of the fluorescence decay measurements, faster decay component (<100 ps) may be missed and the estimated hole transfer lifetimes in Table 8.1 should be considered as a upper limit.

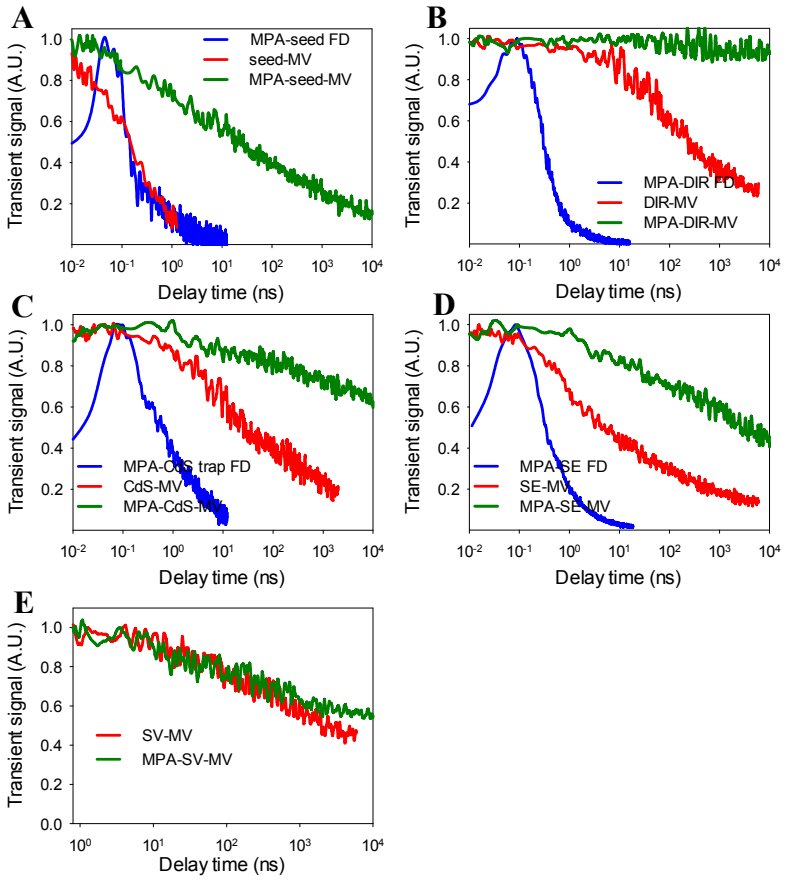


**Figure 8.7.** Comparison hole filling and charge recombination kinetics in different NCs: (A) CdSe seed and (B) CdSe/CdS DIR (C) CdS NR (D) CdSe/CdS CS-SE (E) CdSe/CdS CS-SV. The hole filling time is measured by fluorescence decay kinetics of MPA-NCs in water (blue line), except for CdSe/CdS CS-SV which shows negligible hole filling process during its intrinsic lifetime period. The charge recombination time is monitored by the $MV^{+\bullet}$ decay kinetics of NC-$MV^{2+}$ complexes in chloroform (red line). Also shown for comparison is the $MV^{+\bullet}$ decay kinetics of MPA-NC-$MV^{2+}$ complexes in water (green line). In the presence of MPA, the lifetime of $MV^{+\bullet}$ becomes longer due to the removal of the hole by MPA.

The results presented here show that the steady-state quantum yields of $MV^{+\bullet}$ radical generation in NC-based photoreduction systems depend sensitively on the composition and shape of the NCs. In all MPA-NC-$MV^{2+}$ complexes the initial charge separation is 100% because the charge separation rates are much faster than the intrinsic electron-hole recombination rates in all NCs (i.e. $\tau_{CS} << \tau_{RX}$). However, the charge recombination ($\tau_{CR}$) and hole filling ($\tau_{HF}$) rates differ in these materials, giving rise to the variation in $MV^{2+}$ photoreduction efficiencies. For CdSe seed, both the charge recombination and the hole filling are fast (Figure 8.7A), leading to a relatively small yield of radical generation. Coating the CdSe seed by a CdS shell creates quasi-type II core/shell structures in which the electron is delocalized in both the core and shell while the hole is localized in the core.[49] For CdSe/CdS CS-SE (with a thin CdS shell), the quasi-type II band alignment enables similarly fast charge separation as in CdSe seed while it retards the charge recombination process by 30 times.[13,14] For reasons yet to be understood, the hole filling time is only slowed down by a factor 2. One possibility may be the reduction of hole trap states in the CdSe surface with the epitaxially grown CdS shell. Thus, the more competitive hole filling process in these quasi-type II core/shell structures increases the overall yield of $MV^{+\bullet}$ radical generation. Further growth of a thicker CdS shell slows down both the charge recombination and hole filling rate, resulting in negligible improvement of the steady-state radical generation yield.

Unlike the spherical CdSe/CdS core/shell QDs, the CdSe/CdS DIR NRs reduce the charge recombination rate without decreasing the hole removal rate (Figure 8.7B). It

has been shown that CdSe/CdS DIR with small CdSe seed forms a quasi-type II structure with the hole confined in CdSe and the electron delocalized in the rod, as indicated in Figure 8.1B.[50,51] The delocalized conduction band electron in the rod is quantum-confined in the direction perpendicular to the long axis of the rod, which extends its wave function to the NR surface and facilitates ultrafast electron transfer to $MV^{2+}$.[13] The hole wave function, localized in the CdSe dot, can also extend to the surface in the radial direction, which enables fast hole removal by sacrificial electron donors. Furthermore, the electron and hole are separated along the NR axis, slowing down the electron-hole ($\tau_{CX}$) and charge ($\tau_{CR}$) recombination rates. Thus, these nanorod heterostrucutures offer the unique ability to vary the composition as well as radial and axial dimensions to simultaneously enhance the rates of forward processes and slow down the rates of backward processes shown in Figure 8.1.

It is interesting to note that the steady-state $MV^{+\bullet}$ radical generation yield in CdS NRs is higher than the spherical QDs. A comparison of the transient exciton bleach recovery and fluorescence decay of free CdS NRs (without $MV^{2+}$ or MPA) indicates ultrafast (<100 ps, instrument-response limited) intrinsic hole trapping in CdS NRs while the conduction band electron is long lived (see Appendix 4). Similar ultrafast hole trapping processes have also been reported previously in CdS QDs.[52,53] Thus in the CdS NRs, the hole is localized in the trap and spatially separated from the electron, similar to the electron and hole distributions in quasi-type II CdSe/CdS NRs. These charge distributions in CdS NRs enable ultrafast interfacial electron transfer and hole filling, and slows down charge recombination, leading to an improved $MV^{+\bullet}$ radical generation yield

compared to spherical QDs. However, the recombination rate is about 15 times faster and hole filling rate is about 2 times slower than those CdSe-CdS DIRs, which may account for the lower overall $MV^{+\bullet}$ radical generation yield using CdS NRs.

## 8.3. Conclusion

In conclusion, through controlling the composition, size and shape of nano-heterostructures, near-unity quantum yield of light-driven methylviologen radical generation has been achieved using colloidal quasi-type II CdSe/CdS dot-in-rod NRs as the light harvesting and charge separation components and MPA as the sacrificial hole acceptor. The quantum yield remains > 90% over a broad $MV^{2+}$ concentration range (0.040 -125 mM), due to $MV^{2+}$-NR complex formation. Coupled with Pt nanoparticles, this system can efficiently reduce water to form $H_2$ using solar energy. Because methylviologen is a common redox mediator for many catalytic reactions, including $H_2O$ and $CO_2$ reduction, this novel system provides a flexible approach for efficient redox mediator-based solar-to-fuel conversion. Comparison of the steady-state mediator photoreduction quantum yields and transient kinetics of different nanocrystals suggests that the dot-in-rod nanostructures facilitate interfacial electron transfer to the mediator and interfacial hole transfer to the hole acceptor while simultaneously retarding the charge recombination process. These advantageous properties can be attributed to the electron and hole wave function distributions in this material. Our finding suggests that

wave function engineering in quantum-confined nano-heterostructures provides a new avenue for developing novel light harvesting and charge separation materials for direct solar-to-fuel conversion.

## References

(1) Lewis, N. S.; Nocera, D. G. *Proc. Natl. Acad. Sci.* **2006**, *103*, 15729.

(2) Gur, I.; Fromer, N. A.; Geier, M. L.; Alivisatos, A. P. *Science* **2005**, *310*, 462.

(3) Nozik, A. J.; Beard, M. C.; Luther, J. M.; Law, M.; Ellingson, R. J.; Johnson, J. C. *Chem. Rev.* **2010**, *110*, 6873.

(4) Talapin, D. V.; Lee, J.-S.; Kovalenko, M. V.; Shevchenko, E. V. *Chem. Rev.* **2009**, *110*, 389.

(5) Kiwi, J.; Gratzel, M. *Nature* **1979**, *281*, 657.

(6) Kalyanasundaram, K. *Coord. Chem. Rev.* **1982**, *46*, 159.

(7) Darwent, J. R.; Douglas, P.; Harriman, A.; Porter, G.; Richoux, M.-C. *Coord. Chem. Rev.* **1982**, *44*, 83.

(8) O'Regan, B.; Gratzel, M. *Nature* **1991**, *353*, 737.

(9) Kamat, P. V.; Tvrdy, K.; Baker, D. R.; Radich, J. G. *Chem. Rev.* **2010**, *110*, 6664.

(10) Alivisatos, A. P.; Gu, W.; Larabell, C. *Annu. Rev. Biomed. Eng.* **2005**, *7*, 55.

(11) Wu, X. Y.; Liu, H. J.; Liu, J. Q.; Haley, K. N.; Treadway, J. A.; Larson, J. P.; Ge, N. F.; Peale, F.; Bruchez, M. P. *Nat. Biotechnol.* **2003**, *21*, 41.

(12) Mirkin, C. A.; Letsinger, R. L.; Mucic, R. C.; Storhoff, J. J. *Nature* **1996**, *382*, 607.

(13) Zhu, H.; Song, N.; Lian, T. *J. Am. Chem. Soc.* **2010**, *132*, 15038.

(14) Zhu, H.; Song, N.; Lian, T. *J. Am. Chem. Soc.* **2011**, *133*, 8762.

(15) Cozzoli, P. D.; Pellegrino, T.; Manna, L. *Chem. Soc. Rev.* **2006**, *35*, 1195.

(16) Zhu, H.; Song, N.; Rodríguez-Córdoba, W.; Lian, T. *J. Am. Chem. Soc.* **2012**, *134*, 4250.

(17) Amirav, L.; Alivisatos, A. P. *J. Phys. Chem. Lett.* **2010**, *1*, 1051.

(18) Tang, M. L.; Grauer, D. C.; Lassalle-Kaiser, B.; Yachandra, V. K.; Amirav, L.; Long, J. R.; Yano, J.; Alivisatos, A. P. *Angew. Chem. Int. Ed.* **2011**, *50*, 10203.

(19) Gust, D.; Moore, T. A.; Moore, A. L. *Acc. Chem. Res.* **2001**, *34*, 40.

(20) Holten, D.; Bocian, D. F.; Lindsey, J. S. *Acc. Chem. Res.* **2002**, *35*, 57.

(21) Magnuson, A.; Anderlund, M.; Johansson, O.; Lindblad, P.; Lomoth, R.; Polivka, T.; Ott, S.; Stensjö, K.; Styring, S.; Sundström, V.; Hammarström, L. *Acc. Chem. Res.* **2009**, *42*, 1899.

(22) Vignais, P. M.; Billoud, B. *Chem. Rev.* **2007**, *107*, 4206.

(23) Harriman, A.; Porter, G.; Richoux, M.-C. *J. Chem. Soc., Faraday Trans. 2* **1981**, *77*, 833.

(24) Brugger, P. A.; Cuendet, P.; Graetzel, M. *J. Am. Chem. Soc.* **1981**, *103*, 2923.

(25) Peck, H. D.; Gest, H. *J. Bacteriol.* **1956**, *71*, 70.

(26) Okura, I.; Kim-Thuan, N.; Takeuchi, M. *Angew. Chem. Int. Ed. Engl.* **1982**, *21*, 434.

(27) Parkinson, B. A.; Weaver, P. F. *Nature* **1984**, *309*, 148.

(28) Willner, I.; Mandler, D. *J. Am. Chem. Soc.* **1989**, *111*, 1330.

(29) Willner, I.; Riklin, A.; Lapidot, N. *J. Am. Chem. Soc.* **1990**, *112*, 6438.

(30) Willner, I.; Lapidot, N.; Riklin, A.; Kasher, R.; Zahavy, E.; Katz, E. *J. Am. Chem. Soc.* **1994**, *116*, 1428.

(31) Koga, H.; Hamada, T.; Sakaki, S. *Dalton Trans.* **2003**, 1153.

(32) Burai, T. N.; Panay, A. J.; Zhu, H.; Lian, T.; Lutz, S. *ACS Catalysis* **2012**, *2*, 667.

(33) Morris-Cohen, A. J.; Frederick, M. T.; Cass, L. C.; Weiss, E. A. *J. Am. Chem. Soc.* **2011**, *133*, 10146.

(34) Matylitsky, V. V.; Dworak, L.; Breus, V. V.; Basche, T.; Wachtveitl, J. *J. Am. Chem. Soc.* **2009**, *131*, 2424.

(35) Gratzel, M.; Moser, J. *Proc. Natl. Acad. Sci. U. S. A.* **1983**, *80*, 3129.

(36) Harris, C.; Kamat, P. V. *ACS Nano* **2010**, *4*, 7321.

(37) Sitt, A.; Sala, F. D.; Menagen, G.; Banin, U. *Nano Lett.* **2009**, *9*, 3470.

(38) Carbone, L.; Nobile, C.; De Giorgi, M.; Sala, F. D.; Morello, G.; Pompa, P.; Hytch, M.; Snoeck, E.; Fiore, A.; Franchini, I. R.; Nadasan, M.; Silvestre, A. F.; Chiodo, L.; Kudera, S.; Cingolani, R.; Krahne, R.; Manna, L. *Nano Lett.* **2007**, *7*, 2942.

(39) Yu, W. W.; Qu, L. H.; Guo, W. Z.; Peng, X. G. *Chem. Mater.* **2003**, *15*, 2854.

(40) Watanabe, T.; Honda, K. *J. Phys. Chem.* **1982**, *86*, 2617.

(41) Kalyanasundaram, K.; Kiwi, J.; Grätzel, M. *Helv. Chim. Acta* **1978**, *61*, 2720.

(42) Crutchley, R. J.; Lever, A. B. P. *J. Am. Chem. Soc.* **1980**, *102*, 7128.

(43) Mandal, K.; Hoffman, M. Z. *J. Phys. Chem.* **1984**, *88*, 5632.

(44) Harriman, A.; Porter, G. *J. Chem. Soc., Faraday Trans. 2* **1982**, *78*, 1937.

(45) Kiwi, J.; Graetzel, M. *J. Am. Chem. Soc.* **1979**, *101*, 7214.

(46) Ebbesen, T. W. *J. Phys. Chem.* **1984**, *88*, 4131.

(47) Du, P.; Schneider, J.; Jarosz, P.; Eisenberg, R. *J. Am. Chem. Soc.* **2006**, *128*, 7726.

(48) Aldana, J.; Lavelle, N.; Wang, Y. J.; Peng, X. G. *J. Am. Chem. Soc.* **2005**, *127*, 2496.

(49) García-Santamaría, F.; Chen, Y.; Vela, J.; Schaller, R. D.; Hollingsworth, J. A.; Klimov, V. I. *Nano Lett.* **2009**, *9*, 3482.

(50) Luo, Y.; Wang, L.-W. *ACS Nano* **2009**, *4*, 91.

(51) Rainò, G.; Stöferle, T.; Moreels, I.; Gomes, R.; Kamal, J. S.; Hens, Z.; Mahrt, R. F. *ACS Nano* **2011**, *5*, 4031.

(52) Klimov, V.; Bolivar, P. H.; Kurz, H. *Phys. Rev. B* **1996**, *53*, 1463.

(53) Garrett, M. D.; Dukes Iii, A. D.; McBride, J. R.; Smith, N. J.; Pennycook, S. J.; Rosenthal, S. J. *J. Phys. Chem. C* **2008**, *112*, 12736.

# Appendix 1.

## Steady-state difference UV-Vis spectra of $MV^{2+}$ photo-reduction

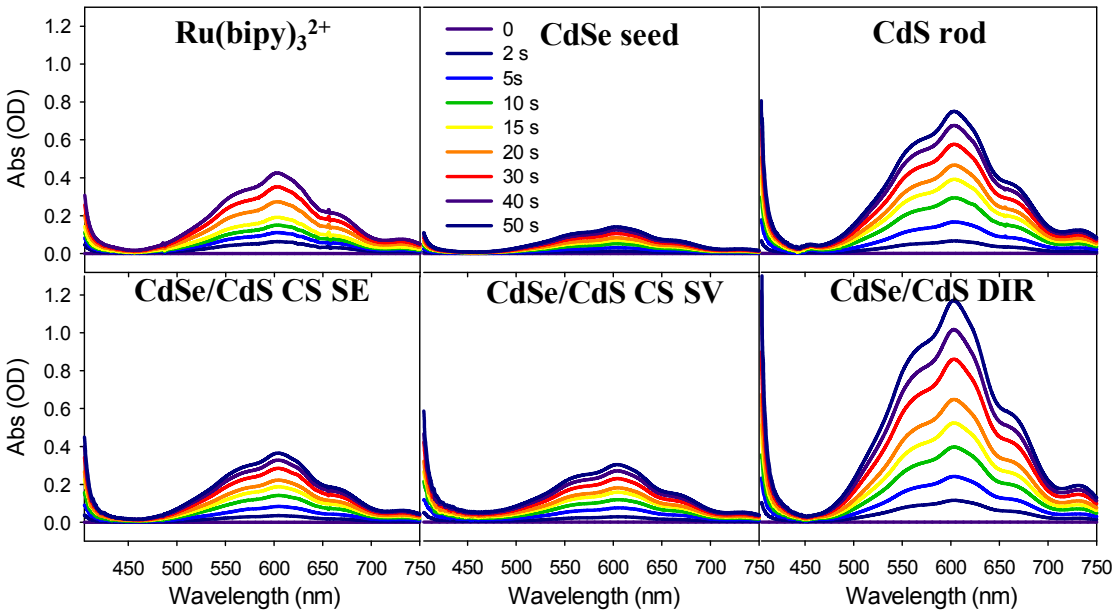


**Figure A.8.1.** Steady state UV-Vis difference spectra （0-50 s） showing MV2+ photoreduction processes using different sensitizers.

# Appendix 2.

**$MV^{+}$ radical generation kinetics under different $MV^{2+}$ concentrations**

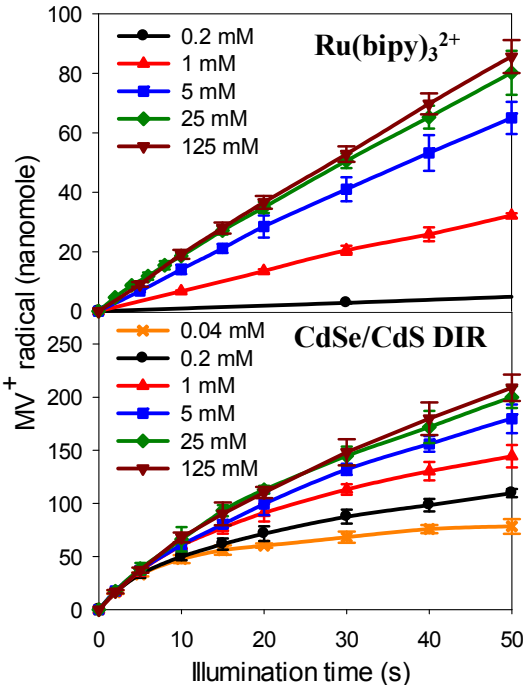


**Figure A.8.2.** $MV^{+}$ radical generation kinetics in the first 50 s using indicated $MV^{2+}$ concentrations for $Ru(bipy)_3^{2+}$ (upper panel) and CdSe/CdS DIR (lower panel). The amount of $MV^{+\bullet}$ radicals generated for $Ru(bipy)_3^{2+}$ using 0.04 μM $MV^{2+}$ is below the detection limit

.

# Appendix 3.

**Charge recombination kinetics of NC-$MV^{2+}$ complexes in chloroform**

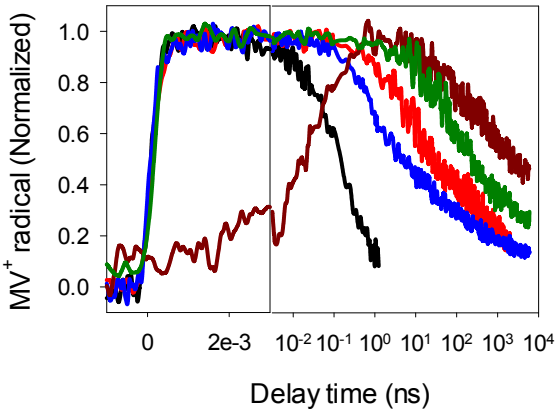


**Figure A.8.3.** Normalized $MV^{+\bullet}$ radical formation and decay kinetics of NC-$MV^{2+}$ complexes in chloroform: CdSe seed (black), CdSe/CdS CS-SE (blue), CdS NR (red), CdSe/CdS DIR (dark green) and CdSe/CdSe CS-SV(dark red).

# Appendix 4.

## Hole trapping and transfer in CdS nanorod

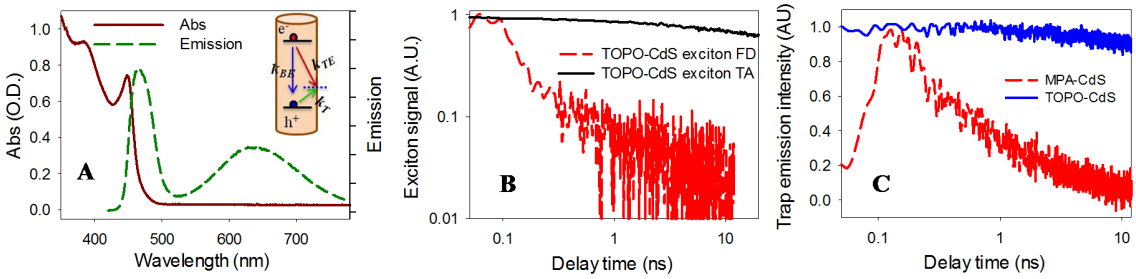

**Figure A.8.4.** (A) UV-Vis absorption and emission spectra of CdS NRs. The mission spectrum shows both a band edge and trap state emission. Inset: the competition of band edge ($k_{BE}$) and trap state ($k_{TE}$) emission due to the hole trapping process ($k_T$) (B) Comparison of transient bleach recovery kinetics (black line) and fluorescence decay (red dashed line) of the 1Σ exciton band of CdS NRs. The long-lived conduction band electron and ultrafast exciton emission decay indicates ultrafast trapping of the valence band hole. (C) Comparison of CdSe NR trap emission decay in the absence (blue, in $CHCl_3$) and presence of MPA (red, in water), showing a much faster decay in the latter due to the filling of trapped holes by MPA.

Unlike other NCs described above, CdS NRs show two distinct emission bands with comparable intensity. The band centered at 466 nm can be assigned to CdS band edge emission and the broad band from 500 to 800 nm can be assigned to trap state emission. The band edge emission shows an instrument response limited (<100 ps) decay (red line in Fig. S8 B) while the transient absorption bleach recovery of the lowest energy exciton has a half-life time of ~ 100 ns, indicating a long lifetime for the conduction band electrons.[12] Thus, the ultrafast fluorescence decay indicates an ultrafast trapping of the valance band hole. To measure the filling of the trapped hole by MPA, we compare the trap emission in CdS NRs in the presence and absence of MPA, as shown in Figure A.8.4. The fast trap emission decay in the presence of MPA indicates the transfer of the trapped hole to MPA.

# Chapter 9. Redox Mediator Photoreduction Using ZnSe/CdS Dot-in-rod Nanorod: Wavelength Dependent Quantum Yield

## 9.1. Introduction

The advancement of solar-to-fuel conversion technologies requires not only efficient $H_2$ evolution or $CO_2$ reduction catalysts but also better materials and approaches for light harvesting and charge separation. In recent years, because of their tunable chemical, optical and electronic properties, quantum confined semiconductor nanocrystals have received intense interests as light harvesting and charge separation components in photocatalytic systems.[1-7] Compared with conventional single composition quantum dots (QDs), semiconductor nanoheterostructures, which combines two or more materials in one nanoscale system, have provided additional opportunities for controlling their functionalities, including their charge transfer properties.[1,8-11] Among them, anisotropic one-dimensional nanorod (NR) heretostructures, e.g. ZnSe/CdS, CdSe/CdS dot-in-rod (DIR) NRs, have been extensively investigated in solar energy conversion applications because of well developed synthetic protocols for the preparation of these materials and their unique charge separation properties.[7,12-17]

The carrier distribution and dynamics in nanoheretostructures dictates their charge transfer properties and performance. Compared with single component or core/shell quantum dots, these properties in nanorod heretostructures are much more complicated

and intriguing. They are sensitive not only to the conduction and valence band offsets of constituent materials, geometries and dimensions, but also the local structural and energetic heterogeneities. For example, in CdSe/CdS nanorods, the lowest energy hole wavefunction is mostly localized inside CdSe seed because of large valence band offset between CdSe and CdS, whereas the band alignment and spatial distribution of the lowest energy conduction band electron has been a subject of intense debate. Although negligible conduction band offset and delocalized electron have been assumed previously,[18-25] recent experimental and theoretical studies indicates a substantial conduction band offset (~ 0.3 eV) in CdSe/CdS nanorod[26,27] and electron wavefunction is largely localized in CdSe seed.[26-31] Furthermore, recent experimental studies reveal the presence of multiple long-lived exciton species in CdSe/CdS nanorod due to surface trapping.[30,31]On the other hand, in a recent study, we show near unity redox mediator ($MV^{2+}/MV^{\cdot+}$) generation and efficient $H_2$ evolution with CdSe/CdS nanorods, significantly higher than other nanostructures including CdSe/CdS core/shell QDs.[12] The high performance of CdSe/CdS nanorods was shown to be due to effective suppression of charge recombination and fast hole removal (by sacrificial electron donor). It remains unclear how the carrier distribution and dynamics in the nanorods affect these processes.

In this chapter, we investigated the $MV^{2+}$ photocatalytic reduction using ZnSe/CdS nanorod under different excitation conditions. As in our recent study, we choose $MV^{2+}/MV^{\cdot+}$ because it is a practical redox mediator which can be further coupled with $H_2$ evolution[12,32,33] or $CO_2$ reduction[34,35] catalysts for direct solar-to-fuel conversion. ZnSe/CdS nanorod, in which the carrier distribution has been much less studied

experimentally, has a well established type II band alignment because of large conduction and valence band offsets.[26,36-38] We found the ground state exciton in ZnSe/CdS nanorod is hole confined in ZnSe seed, with electron localized in CdS shell surrounding ZnSe seed without extending into CdS rod, despite the representative type II band alignment. Under CdS rod excitation condition, majority of excitons (83%) are localized into the ground exciton state near seed location and the rest are trapped in CdS rod region. Under steady state illumination conditions, ZnSe/CdS nanorod shows dramatic wavelength dependent $MV^{2+}$ photoreduction quantum yield (~ 90% at 415nm and ~ 34% at 550 nm). With TA spectroscopy measuring the carrier dynamics in reaction solution, we found the charge separated state from seed region localized exciton has a larger charge recombination loss and lower quantum yield due to short electron-hole spatial separation. Under CdS rod excitation condition, majority of the excitons undergo ultrafast electron transfer from CdS rod to surface adsorbed $MV^{2+}$ and subsequent hole localization into ZnSe seed, due to the cascade valence band alignment. The large electron-hole spatial separation leads to suppressed charge recombination loss and much higher $MV^{2+}$ photoreduction quantum yield.

## 9.2. Results and Discussion

### 9.2.1. Static Absorption and Emission Spectra

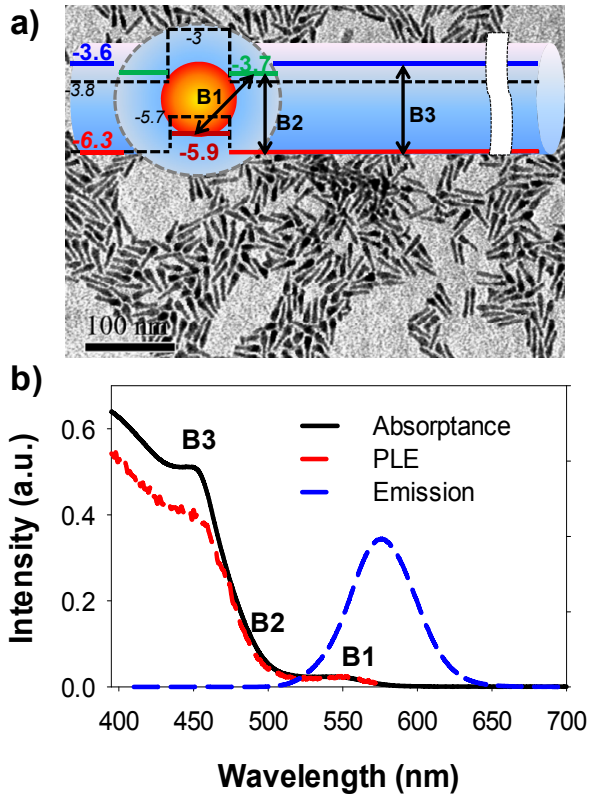


**Figure 9.1.** a) TEM image of ZnSe/CdS nanorods with average length of 20.3 ± 2.5 nm. Inset: Schematic energy level diagram and key transitions in ZnSe/CdS NRs b) UV-vis absorption spectrum (black solid line), PLE spectrum (red dashed line) and emission spectrum of ZnSe/CdS NRs in toluene solution. The y-axis is in the units of absorptance (the ratio of absorbed to incident light) in the absorption spectrum and intensity in the PLE and emission spectra. The PLE spectrum and absorption spectrum have been normalized to B1 maximum.

Figure 1a shows a representative transmission electron microscopy (TEM) image of ZnSe/CdS NRs used in this study. From the TEM image, the ZnSe/CdS NRs have an

average length of 20.3 ± 2.5 nm and a non-uniform diameter: a thinner rod (with diameter ~ 3.7 nm) with a significant thicker part ("bulb") near one end (with diameter ~5.8 nm). This bulb feature has been generally observed in seeded-grown ZnSe/CdS[36,37] and CdSe/CdS nanorod,[30,39] and has been attributed to the growth of CdS shell surrounding the seed.[26,36,39]

The static UV-Vis absorption (y axis in unit of absorptance) and emission spectra of ZnSe/CdS nanorod dispersed in toluene are displayed in Figure 9.1b. The ZnSe/CdS nanorod shows a lowest energy exciton absorption peak at 550 nm with emission centered at 575 nm. This peak is well below the bandgap of either ZnSe or CdS and can be safely assigned to the unique lowest energy interfacial charge transfer (CT) exciton from lowest energy hole level ($1S_h$) in ZnSe seed to lowest energy electron level in CdS in type II nanoheterostructure.[38,40-42] We have assumed here that confinement potentials for electrons and holes in CdSe seed and CdS bulb region still have spherical symmetry and the lowest energy electron and hole level can be labeled as $1S_e$, and $1S_h$ respectively. We'll show later the lowest energy electron level for CT band is $1S_e$ level in surrounding bulb like CdS shell, depicted as B1 in Figure 9.1a inset. The absorption spectrum also exhibits a clear exciton peak at ~ 457 nm, which can be attributed to quantum confined 1Σ excitonic transition in the CdS rod (B3 in Figure 9.1a inset).[30,43] In addition to these two pronounced excitonic transitions, there is also an absorption feature at ~ 480 nm, which can be clearly observed from the transient absorption spectra (see below). This transition has a lower energy (~130 meV) than 1Σ peak in CdS rod region and can be assigned to the lowest energy transition in the CdS shell within the bulb region (B2 in

Figure 9.1a inset). A similar bulb feature was observed previously in CdSe/CdS dot-in-rod NRs.[30,39] Because of its larger diameter (approaching CdS Bohr exciton radius), the transition in the bulb region is lower in energy due to reduced confinement energy. Its strength is small in static absorption spectrum because of its relatively small volume compared to the CdS rod. From the TA spectra measured with direct excitation of the B1 transition at 555nm (see below), this 480 nm feature shows the same instantaneous formation and long-lived decay kinetics as the B1 bleach, indicating that these two transitions share the same electron level, i.e. the $1S_e$ level in the CdS shell in bulb region. From the B3 and B2 transition energy difference and electron/hole effective masses in CdS bulk material, we estimate that the lowest energy electron level in CdS rod is ~ 100 meV higher than that in the CdS bulb. Therefore, instead of extending throughout the whole rod, the lowest energy electron level for ZnSe/CdS nanorod, localize in the CdS shell in the bulb region, surrounding the ZnSe seed. Based on conduction/valence band edges of bulk ZnSe and CdS material[8] (black dashed lines in Figure 9.1a inset) and the energies of B1, B2 and B3 transitions, the lowest energy electron and hole levels throughout the nanorod can be deduced, which are shown in Figure 9.1a. We have neglected the electron-hole Columbic binding energy in this estimation.

The photoluminescence excitation (PLE) spectrum (detected at the emission peak maximum at 575 nm) of ZnSe/CdS nanorods is also shown in Figure 9.1b and compared with its absorption spectrum. Such comparison allows direct visualization of exciton localization efficiency from higher energy states to the lowest energy B1 exciton state.[30,36,44] It should be noted that the absorption spectra region above B2 is dominated

by CdS rod because of its much larger volume and electric field enhancement due to dielectric confinement effect.[45-47] As seen from Figure 9.1b, the normalized PLE spectra is about 17% smaller than the absorption spectra in CdS rod absorption region, indicating 83% of excitons created in CdS nanorod get relaxed to B3 exciton state while rest 17% don't. The smaller yield of exciton relaxation can be either due to exciton trapped at the CdS rod surface[30,31] and/or the presence of nanorods without seed.[36] These assignments will be further confirmed by transient absorption measurement below.

### 9.2.2. Carrier Localization Dynamics in ZnSe/CdS Nanorod

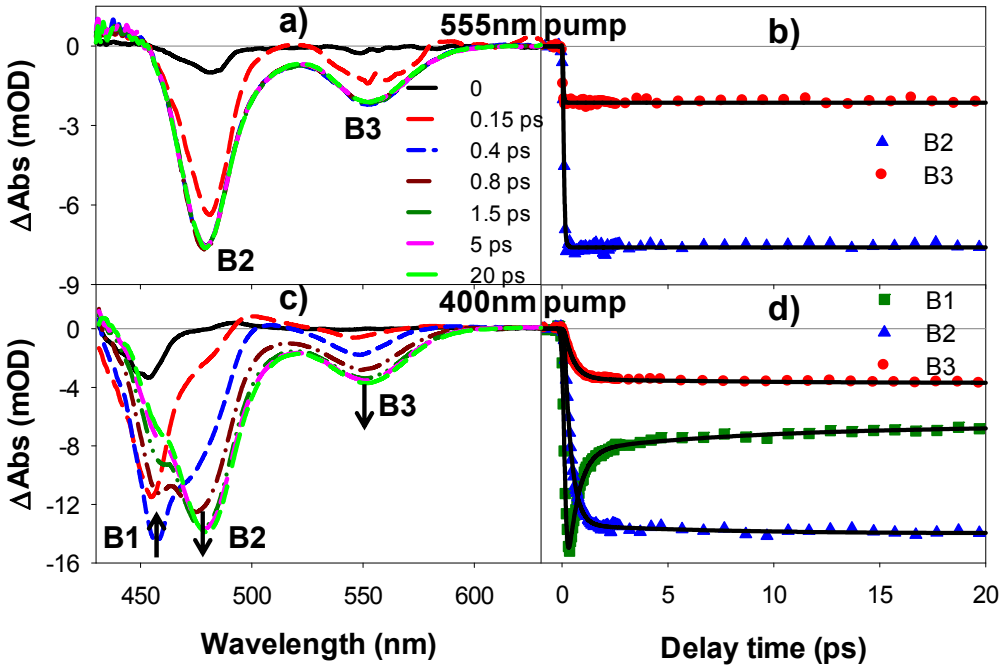

**Figure 9.2.** TA spectra and kinetics of ZnSe/CdS NRs in toluene at early delay time (0 - 20 ps) after 550 nm (upper panel) and 440 nm (lower panel) excitations. TA spectra at indicated delay times (a, c) and formation and decay kinetics of bleaches at B1 (green squares), B2 (blue triangles), and B3 (red circles) transitions (b, d). The black solid lines are fits according to a model described.

To support the above assignment and gain more insights into the carrier distribution and dynamics, we performed femtosecond TA measurements on ZnSe/CdS nanorods using different excitation wavelengths. This proves to be an effective way to reveal the electronic structures and carrier dynamics in semiconductor nanoheterostructures.[20,30,48-52] TA signals of excited semiconductor nanocrystals contain two contributions: the state filling induced bleach of exciton bands (main component) and carrier induced Stark effect signals (minor component) that are derivatives of exciton features.[53,54] Similar to CdX (X=S, Se, Te) nanocrystals, the state filling induced TA signal in ZnSe/CdS nanorod is dominated by conduction band electrons with negligible hole contributions because of much denser hole states and valence band fine structures.[53,54] This assignment will be further validated by electron transfer study described below. The TA spectra and kinetics of ZnSe/CdS NRs at early delay times (0-20 ps) after 555 nm and 400 nm excitations are displayed in Figure 9.2 upper (a, b) and lower panel (c, d), respectively. Under 555 nm excitation, which is in resonance with lowest energy CT excition transition (B3) in bulb region, both B3 and B2 bleach features form instantaneously within the instrument response limit and decay in same way in ns

timescale (not shown), confirming that these transitions share the same lowest energy electron level ($1S_e$) in the conduction band. It is interesting to note that the occupation of electrons in the $1S_e$ level doesn't lead to B1 bleach, indicating this lowest energy electron wavefunction is localized in bulb region without extending into the CdS rod, despite well-established type II band alignment between ZnSe and CdS.[26]

Under 400 nm excitation, which generates excitons in CdS rod domain, B1 bleach forms quickly (~ 50 fs formation time, see below) and then decays in the next few ps. Its decay leads to the growth of B2 and B3 bleach, indicating electron transport and localization from the lowest energy $1\sigma_e$ level in the CdS rod to the $1S_e$ level in CdS bulb region. This electron localization process is clearly shown by the kinetics in Figure 9.2d. These kinetics can be well fitted by a multiexponential model described below.

The B2 and B3 kinetics under 555 nm excitation (Figure 9.2b) can be fitted by a single exponential rise with instrument limited time (~150 fs) and a much slower decay.

Under 400 nm excitation condition (Figure 9.2d), the 550 nm and 480 nm kinetics were fit by a two exponential rise and a much slower decay process, using following equations:

$$\Delta A(550nm,t) = A_{B3}(550nm)[\alpha \exp(-t/\tau_{r1}) + (1-\alpha)\exp(-t/\tau_{r2}) - 1] \quad (9.1)$$

$$\Delta A(480nm,t) = A_{B2}(480nm)[\alpha \exp(-t/\tau_{r1}) + (1-\alpha)\exp(-t/\tau_{r2}) - 1] \quad (9.2)$$

The number 1 here accounts for the much slower decay component (>>20 ps ).

The 455nm kinetics can be fit using the following equation:

$$\Delta A(455nm,t) = A_{B1}(455nm)[\exp(-t/\tau_{r0}) - \beta[\alpha\exp(-t/\tau_{d1}) + (1-\alpha)\exp(-t/\tau_{d2})] - (1-\beta)] + \Delta A_{B2}(455nm,t) \quad \text{(S3)}$$

The second term $\Delta A_{B2}(455nm,t)$ accounts the contribution of B2 bleach at 455nm, which has been fitted using equation S2 with B2 amplitude ratio between at 455 nm and at 480 nm determined from TA spectra at 555 nm excitation as following:

$$\Delta A_{B2}(455nm,t) = 0.15\Delta A_{B2}(480nm,t) \quad \text{(S4)}$$

$\beta$ represents the portion that localize in early time while $(1-\beta)$ represents the portion that is trapped and decays much slower.

The fitted results are shown in Figure 9.2d black line and the fitting parameters are listed in table 9.1:

**Table 9.1.** Fitting parameters for TA kinetic in Figure 9.2d.

| | | $\tau_{r1}$ | $\tau_{r2}$ | α | |
|---|---|---|---|---|---|
| 550nm (B3) | | 0.487±0.061 ps | 9.70±0.82 ps | 0.91±0.02 | |
| 480nm (B2) | | 0.417±0.042 ps | 9.02±1.25 ps | 0.92±0.03 | |
| | $\tau_{r0}$ | $\tau_{d1}$ | $\tau_{d2}$ | α | β |
| 455nm (B1) | 0.053±0.011 ps | 0.498±0.057 ps | 9.09±1.02 ps | 0.89±0.03 | 0.81±0.04 |

From the fitting, both B2 and B3 bleach shows a biphasic rise with a ~ 90% fast component (~ 420 fs for B2 and ~ 490 fs for B3) and a ~ 10 % slower component (~ 9 ps for B2 and ~ 10 ps for B3), and a much slower decay on nanosecond time scale. From the

fitting, the B1 bleach shows a ~50 fs formation time, which is assigned to the electron relaxation process from the initially excited 1π to 1σ level in the CdS NR.[30,43] Importantly, this fitting also reveals that majority (81%) of B1 bleach shows a corresponding biphasic decay process (~490 fs, 90%; ~9 ps, 10%) on early time and the rest (19%) decays much slower. The agreement between B1 decay and B2, B3 rise in early delay time windows indicates that ~ 81% of the initially created electrons in CdS rod decay to the bulb region and ~ 19% remains on CdS rod. This electron localization efficiency is consistent with 83% rod exciton localization efficiency determined from the PLE measurement shown in Figure 9.1b. The fast (~ 490 fs) exciton localization component can be assigned to free (untrapped) excitons. Similar exciton localization time has been previously observed in CdSe/CdS quasi-type II nanorods.[30] The origin of the smaller (10%) and slower (10 ps) component is unclear, although it could be attributed to excitons in shallow traps. Similar competition of band alignment driven exciton localization and hole trapping induced exciton trapping has been reported in CdSe/CdS nanorods and tetrapods,[30,31] and has been attributed to local energetic heterogeneities and strong e-h interaction arose from dielectric contrast effect in one dimensional (1D) nanorods.[30,45,46]

### 9.2.2. Stead State $MV^{\cdot+}$ Radial Generation

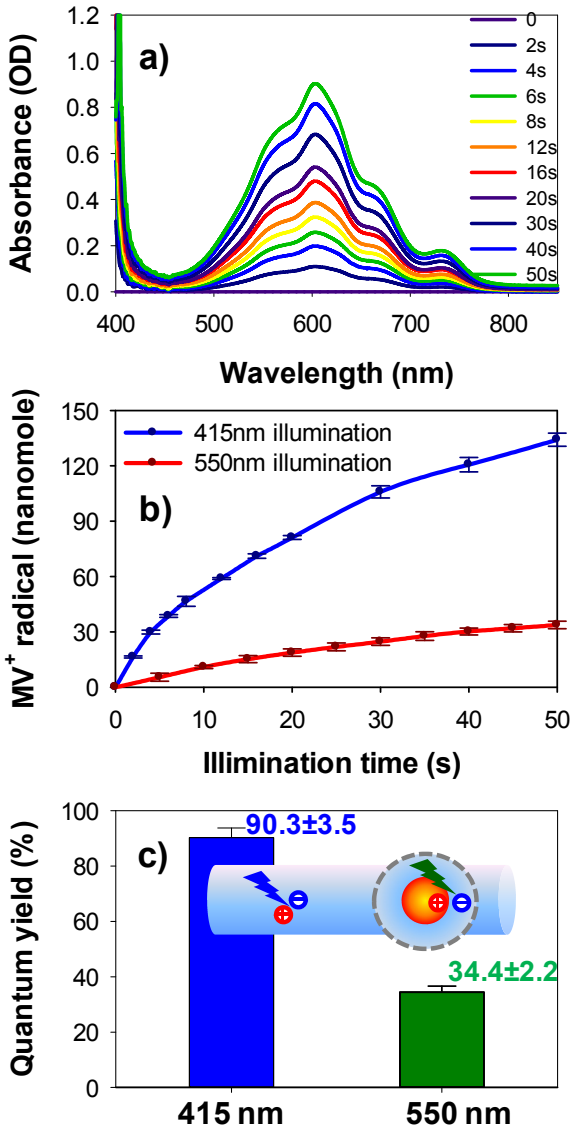


**Figure 9.3.** Steady-state photoreduction of $MV^{2+}$ using ZnSe/CdS NRs a) UV−vis difference spectra (after−before irradiation) of a solution containing ZnSe/CdS DIR, $MV^{2+}$ and 3-mercaptopropionic acid (MPA) after indicated time of 415 nm illumination, showing the generation of $MV^{+\bullet}$ radicals. Similar spectra measured at 550 nm illumination are shown in Figure A.9.1. Experimental conditions: 2mM $MV^{2+}$, 50mM pH 7.5 phosphate buffer, 50mM MPA as sacrificial electron donor, total solution volume

2mL. The concentration of MPA-capped ZnSe/CdSe nanorod for 415 nm illumination was adjusted to have an absorbance of 1.46 (OD) at 415 nm and 415 nm illumination power is 5.09 mW; the NR concentration for 550 nm illumination was three times of that for 415 nm illumination with an absorbance at 550 nm of 0.32 (OD) and the 550 nm illumination power is 5.15 mW. Under these conditions, similar photon absorption rates by the NR are maintained for 415 nm and 550 nm illumination. b) $MV^{\cdot+}$ radical generation kinetics under 415 and 550 nm excitations. c) Initial quantum yields of $MV^{+\bullet}$ radical generation under 415 nm and 550 nm excitation wavelengths.

The presence of multiple exciton species at different regions of the nanorod and their excitation wavelength dependence suggests wavelength dependent photochemistry. To investigate this effect, we studied $MV^{2+}$ photoreduction using these nanorods at two illumination wavelengths: 415 nm, at which the absorption of CdS rod dominates, and 550 nm, which is in resonance with the ZnSe to CdS charge transfer band in the bulb region. The samples contain MPA ligand exchanged ZnSe/CdS NRs, $MV^{2+}$ (2 mM) and excess MPA (50 mM) as sacrificial electron donor in anaerobic pH = 7.5 aqueous solutions. Upon 415 nm illumination, $MV^{+\bullet}$ radicals form quickly, as indicated by the growth of a distinct 605 nm band in the difference spectra shown in Figure 9.3a (see Figure A.9.1 for results under 550 nm illumination). Both MPA and $MV^{2+}$ have negligible absorption in this spectral range. In the absence of NRs or illumination, no $MV^{+\bullet}$ radicals were observed. Using reported extinction coefficient (13700 ± 300 $M^{-1}$

$cm^{-1}$ at 605 nm)[55], the amount of $MV^{+\bullet}$ radicals can be calculated to obtain the radical concentration and formation kinetics, which are shown in Figure 9.3B.

To quantify and compare the photoreduction performance under 415 and 550 nm excitations, we calculate the photon-to-$MV^{+\bullet}$ conversion quantum yields, defined as $\Phi_{MV} = \Delta(MV^{+\square}) / \Delta(h\nu)$, where $\Delta(MV^{+\square})$ is the $MV^{+\bullet}$ radical generation rate and $\Delta(h\nu)$ is the photon absorption rate. The latter can be calculated from the illumination power and absorbance at the illumination wavelength. As seen from the slope of $MV^{+\bullet}$-vs-time plots in Figure 9.3b, the $MV^{+\bullet}$ radical generation rate is largest at the beginning of the reaction and decreases slowly due to the consumption of electron/hole acceptors and the light absorption loss from generated $MV^{+\bullet}$ radical. Therefore, only the initial quantum yields, calculated from initial $MV^{+\bullet}$ radical generation rate (first three points), are compared in Figure 9.3c. Interestingly, the $MV^{2+}$ photoreduction quantum yields are ~ 34 % under 555 nm excitation and ~ 90%, at 415 nm excitation, showing a dramatic wavelength dependence.

### 9.2.3. Charge Separation and Recombination under 555 nm Excitation

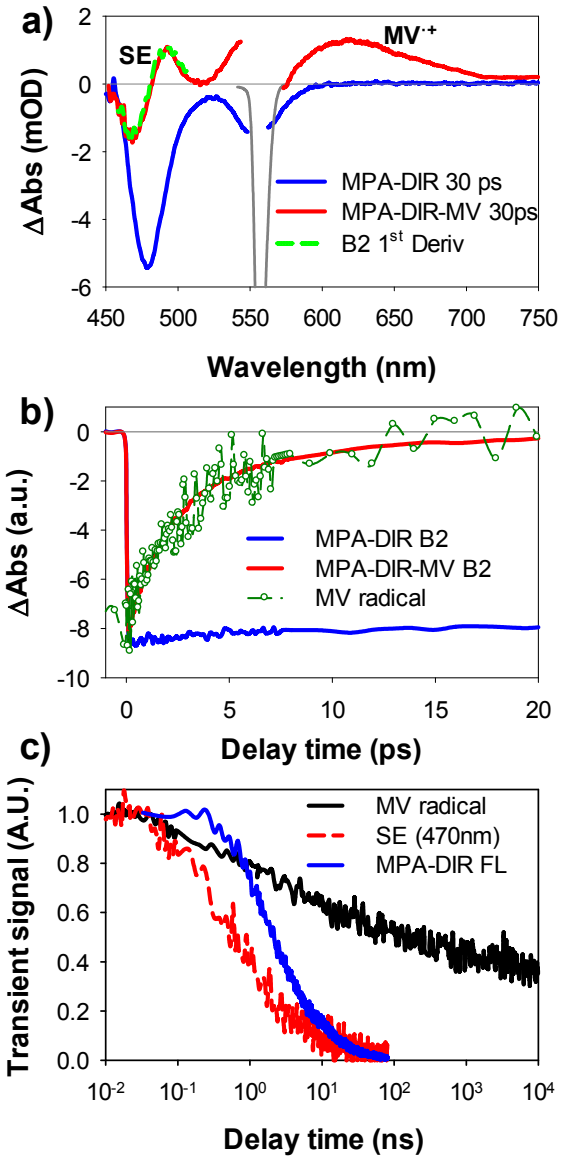


**Figure 9.4.** TA spectra and kinetics of a reaction solution under 555 nm excitation. The reaction solution is same as that for steady state $MV^{+\bullet}$ radical generation (see Figure 9.2a) except for a higher (~5 times) nanorod concentration. a) TA spectra of MPA-capped ZnSe/CdS nanorod reaction solution without (blue solid line, denoted as MPA-DIR) and with (red solid line, denoted as MPA-DIR-MV) $MV^{2+}$ at 30 ps delay time. Also shown is the spectrum of the excitation pulse (dark gray line) and the 1st derivative of B2 transition

(dashed green line). b) Comparison of B2 kinetics in ZnSe/CdS NRs with (blue solid line) and without (red solid line) $MV^{2+}$. Also shown is the $MV^{+\bullet}$ radical formation kinetics (dark green symbols), which has been scaled and displaced vertically for better comparison. c) Comparison between $MV^{+\bullet}$ radical decay kinetics (black solid line) and SE signal (470nm) (red dashed line) in MPA-DIR-MV reaction solution. Also shown in blue solid line is the fluorescence decay kinetics of MPA-DIR solution.

To investigate the origin of the wavelength dependent $MV^{2+}$ photoreduction quantum yield and identify the loss mechanisms, we conducted transient absorption measurements on the complete photoreduction systems under conditions similar to those for the steady-state $MV^{2+}$ photoreduction. The NC concentrations have been increased by ~ 5 times to allow measurement in a thinner cell (1 mm). The TA spectra of reaction solution without (denoted as MPA-DIR) and with (denoted as MPA-DIR-MV) $MV^{2+}$ at 30 ps after 555 nm excitation are compared in Figure 9.4a and corresponding kinetics of B2 bleach in the first 20 ps are compared in Figure 9.4b. These spectra were recorded under the same single exciton excitation conditions. At this excitation wavelength, the lowest energy interfacial CT exciton (B3) band in MPA capped ZnSe/CdS NRs is excited. The resulting TA spectra in MPA-DIR sample are similar to those of ZnSe/CdS NRs in toluene (Figure 9.2a), showing long-lived bleaches of B2 and B3 excicton bands. Because of more pronounced scattering of excitation light for the water soluble nanorod solution, the B3 bleach is not fully resolved and we use B2 to monitor the fate of excited electrons in nanorod since they share the same electron level. Compared with MPA-DIR,

the TA spectrum of MPA-DIR-MV at 30 ps shows much smaller bleach amplitude and a pronounced 1st order derivative feature (with a negative peak at 470 nm and a positive peak at 490 nm) at B2 exciton band, and an additional positive absorption band centered at ~610 nm. The absorption band ~610 nm can be assigned to $MV^{\cdot+}$ radical and the 1st derivative feature can be assigned to Stark effect (SE) induced exciton peak shift in charge separated state (with electron in $MV^{+\bullet}$ radical and hole in ZnSe seed), similar to other nanocrystal-$MV^{2+}$ complexes.[12,30,43,48,56,57] As shown in Figure 9.4b, compared with B2 in MPA-DIR, which shows negligible bleach recovery in the first 20 ps, the bleach of B2 in MPA-DIR-MV has almost fully recovered in the same time period, suggesting a short-lived conduction band electron in the presence of $MV^{2+}$. The B2 bleach recovery kinetics agrees well with the $MV^{+\bullet}$ radical formation kinetics in MPA-DIR-MV, indicating electron transfer to electrostatic bound $MV^{2+}$ molecules, to form $MV^{+\bullet}$ radicals with holes in ZnSe seeds (denoted as charge separated state A, shown in Figure 9.7). The $MV^{+\bullet}$ radical formation kinetics can be well fitted by a single exponential function with time constant of ~ 3.2 ps. This electron transfer rate in MPA-DIR-MV is much faster than the nanosecond intrinsic lifetime of electrons in MPA-DIR, suggesting a unity quantum yield of the initial exciton dissociation/interfacial electron transfer process.

To monitor the $MV^{+\bullet}$ radical recombination loss due to back electron transfer to the hole in the ZnSe valence band, the TA kinetics of $MV^{+\bullet}$ radical and SE signal (at 470 nm) from 10 ps to 10 μs are compared in Figure 9.4c. The maximum value of the $MV^{+\bullet}$ radical has been normalized to one to reflect the unity yield of initial electron transfer, and the normalized $MV^{+\bullet}$ radical signal amplitude represents the time dependent transient

quantum yield in the reaction solution, reflecting the extent of recombination loss. The $MV^{+\bullet}$ radical transient yield decreases gradually with time, showing a half-life time of ~170 ns. The transient quantum yield is ~ 38% at 10 μs, close to the steady state $MV^{2+}$ photoreduction quantum yield, indicating that the charge recombination loss is the main cause for low steady state quantum yield under 550 nm illumination.

Also shown in Figure 9.4c is the band edge fluorescence decay kinetics of MPA-DIR. Because transient absorption kinetics of MPA-DIR shows a long lived conduction band electron with a half-life time of ~ 10 ns, the measured PL decay can be attributed to the removal of ZnSe valence band holes by MPA.[12,17] The fluorescence decay shows a half-life time of ~ 2 ns, which is ~ 4 time longer than previously reported value in ZnSe/CdS NRs[17] and probably due to a thicker CdS shell surrounding the ZnSe seed in the ZnSe/CdS nanorod. In the absence of sacrificial electron donor, the SE signal in ZnSe/CdS-$MV^{2+}$ complex shows identical decay kinetics as $MV^{+\bullet}$ radical, reflecting the charge recombination process between hole in ZnSe seed and electron in $MV^{+\bullet}$ radical. With MPA removing hole in ZnSe seed, the SE signal decay is faster than the decay of $MV^{+\bullet}$ radicals in MPA-DIR-MV and the PL decay in MPA-DIR. It suggests that the charge separation induced SE signal is due to the presence of holes in the ZnSe seed, instead of electrons in $MV^{+\bullet}$ radical. Trapping or transfer of holes to the NR surface reduces its interaction strength with the exciton and resulting Stark effect signal amplitude. This assignment is further supported below in the kinetics obtained with 400 nm excitation, in which we show that in the absence of charge recombination of the ZnSe valence band holes with electrons in $MV^{+\bullet}$ radicals, the SE decay follows the hole

removal kinetics. Under 550 nm excitation, the SE kinetics in MPA-DIR-MV contains both ZnSe valence band hole removal process by MPA and charge recombination process with $MV^{+\bullet}$ radicals. It should be pointed out that the loss of $MV^{+\bullet}$ radical persists even after the complete removal of ZnSe valence band holes, suggesting recombination with the trapped holes or oxidized MPA molecules on hundreds of nanosecond time scale. The short spatial separation of the electron (in $MV^{+\bullet}$ radicals) and hole (in ZnSe seeds or oxidized MPA) in the charge separate state (A as shown in Figure 9.7) is the key reason for the relative low steady state quantum yield of $MV^{2+}$ photoreduction under 555 nm excitation.

### 9.2.4. Charge Separation and Recombination under 400 nm Excitation

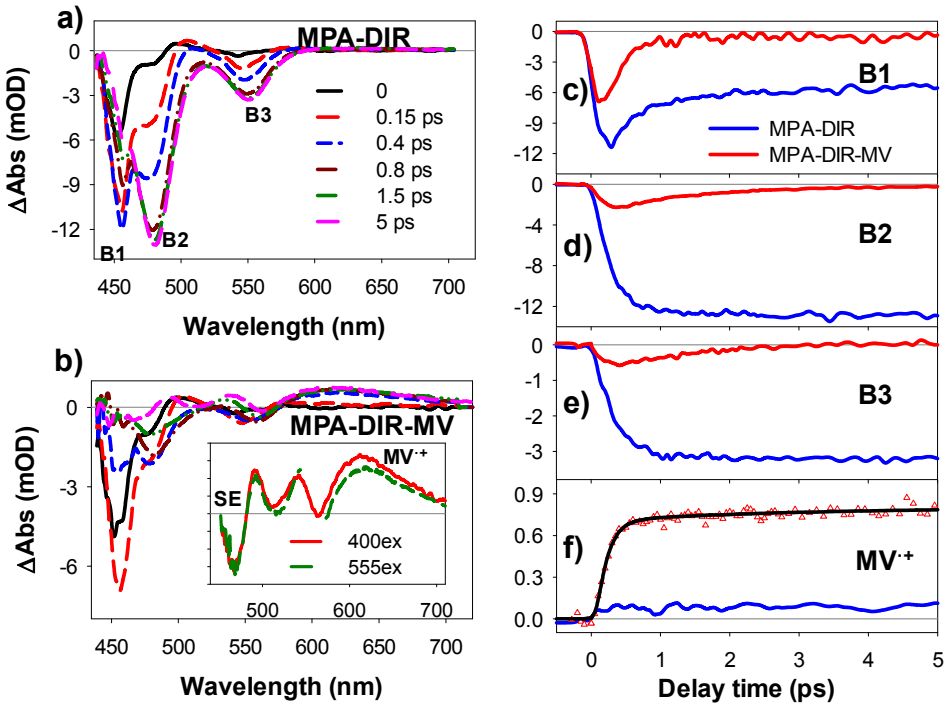


**Figure 9.5.** TA spectra and kinetics of reaction solution at 0 - 5 ps after 400 nm excitation. The reaction solution is same as that for steady state MV radical generation except for a higher (~ 5 times) NR concentration. (a, b) TA spectra of MPA-capped ZnSe/CdS DIR reaction solution without (a) and with (b) $MV^{2+}$ at indicated delay times. Inset in Figure b: comparison of TA spectra at 30 ps measured with 400 nm and 555 nm excitation. (c, d, e, f) Comparison of B1, B2, B3 and $MV^{+\cdot}$ kinetics (615nm) between MPA-DIR and MPA-DIR-MV.

Shown in Figure 9.5 are the comparison of TA spectra and kinetics in MPA-DIR and MPA-DIR-MV measured with 400 nm excitation. These spectra were recorded under same single exciton excitation conditions. It should be note that MPA-DIR in water shows similar TA spectra and B1, B2, B3 kinetics as NR in toluene in the first 100 ps.

Therefore, the early time exciton localization analysis discussed above for ZnSe/CdS NRs in toluene still applies here for MPA capped NRs in water. At later delay time, the exciton bleach decay kinetics for MPA-DIR is faster than NRs in toluene, which can be attributed to additional electron trapping pathway from ligand exchange. Compared with MPA-DIR, the B1 bleach in MPA-DIR-MV has a smaller (~ 58%) initial amplitude and nearly completely recovers in the first ~ 1 ps; the B2 (B3) bleach shows an initial amplitude of only ~ 14% and a relatively slow decay on the a few ps time scale. The decay of these exciton bleaches is accompanied by the formation of derivative-like Stark effect features at those exciton bands and a $MV^{+\bullet}$ radical absorption band at 600 nm. These spectral signatures are similar to those observed under 555nm excitation and can be also attributed to electron transfer from the NR to the $MV^{2+}$ molecules.

The $MV^{+\bullet}$ radical formation kinetics can be well fitted by a biexponential function with amplitudes and time constants of (87%, ~132 fs) and (13%, ~ 3.0 ps), respectively. The electron transfer time of fast component is ~ 4 times faster than the exciton localization time from the CdS rod to the bulb region, suggesting that 87% of the exciton generated in CdS rod undergoes ultrafast transfer to $MV^{2+}$ before exciton localization. For the slower $MV^{+\bullet}$ radical growth component, its percentage agrees with initial amplitude of B2/B3 bleach and its formation time is the same as the electron transfer time from the conduction band of B2/B3 in the bulb region, which was measured with 555 nm excitation (Figure 9.4). This indicates that in MPA-DIR-MV, only ~ 13% excitons initially generated in CdS rod localizes into bulb region and transfers electron (~ 3 ps) to $MV^{2+}$ molecule. The much faster electron transfer rate from CdS rod compared with from

the bulb region can be attributed to larger quantum confinement along radial direction (smaller diameter) in the CdS rod region.

These results suggest that excitons generated in the CdS rod region of ZnSe/CdS NRs have three charge separation pathways, as shown in Figure 9.7. 13% of the excitons localizes to the ZnSe/CdS bulb region, where they dissociate by electron transfer to $MV^{2+}$ with a time constant of 3 ps to form charge separated state A. 87% of the excitons undergoes ultrafast electron transfer (132 fs) to $MV^{2+}$ adsorbed on the CdS rod. Among them, 17 % leads to charge separated state B in which the hole is trapped on CdS rod. Here we have assumed that the adsorption of $MV^{2+}$ does not affect hole trapping on CdS rods. The remaining 70% excitons generate holes in the valence band of CdS hole, which can localize to the ZnSe seed and finally are captured by the MPA ligand. This pathway produces a charge separated state C with a much larger distance between the electron (in $MV^{+\bullet}$ radical) and the hole (in ZnSe and then thiol).

This model is further supported by the comparison of charge separated state spectra at 30 ps measured with 400 and 555 nm excitations (inset of Figure 9.5b). At this delay time, charge separation process is completed and the charge recombination and hole removal processes haven't started yet. It shows a ~ 20% smaller SE signal for the spectrum measured at 400 nm excitation. Because of the stoichiometric relationship between generated $MV^{+\bullet}$ radical and ZnSe seed localized hole (which leads to SE signal) at 555 nm excitation, the smaller SE signal at 400 nm excitation suggests 80% of the hole is localized in ZnSe seed, consistent with pathway A and C, while 20% of the hole is not localized in the ZnSe seed but trapped on CdS rod domain, corresponding to pathway B.

Because of strongly localized nature of trapped hole on CdS rod and its spatial separation from seed region in ZnSe/CdS nanorod, it has much weaker contribution on B2 Stark effect signal than the holes localized in ZnSe seed.

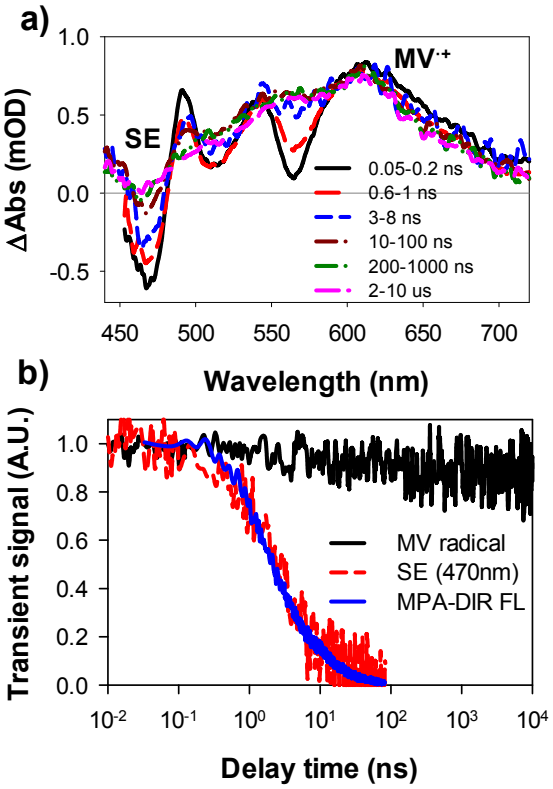


**Figure 9.6.** TA spectra and kinetics of reaction solution at 0.05 ns - 10 μs after 400 nm excitation. a) TA spectra of MPA-DIR-MV at indicated delay times b) Comparison of $MV^{+\bullet}$ radical decay kinetics (black solid line) and SE signal (470nm) (red dashed line) in MPA-DIR-MV reaction solution and fluorescence decay kinetics of MPA-DIR solution (blue solid).

The ultrafast exciton dissociation and $MV^{+\bullet}$ radical formation kinetics shown in Figure 9.5 suggest a unity initial quantum yield $MV^{+\bullet}$ radical generation at 400 nm excitation. To explain the steady state quantum yield shown in Figure 9.3, we again measure the TA spectra of MPA-DIR-MV up to 10 μs after 400 nm excitation to monitor the charge recombination loss. The TA spectra from 0.5 ns to 10 μs are shown in Figure 9.6a, which shows the pronounced SE signal and $MV^{+\bullet}$ radical absorption due to the charge separated state. The normalized comparison of the kinetics of Stark effect signal at 470 nm and $MV^{+\bullet}$ radical at 610 nm are shown in Figure 9.6b. Also compared is the band edge fluorescence decay kinetics of MPA-DIR, which monitors the removal ZnSe valence band hole by MPA molecules. SE kinetics in MPA-DIR-MV agrees with the PL decay kinetics of MPA-DIR, with a half-life time of ~ 2 ns. This agreement indicates that SE signal is caused mainly by the holes in ZnSe seed and hole removal by MPA is the dominant decay pathway. The $MV^{+\bullet}$ radical decays much more slowly compared to the kinetics measured with 555 nm excitation. The transient quantum yield at 10 μs is 88%, which is consistent with the high steady state quantum yield (Figure 9.3) and indicates efficient suppression of the charge recombination process at this excitation wavelength.

From these time-resolved studies above, the mechanisms for wavelength dependent $MV^{+\bullet}$ radical generation quantum yield under steady state illumination have been uncovered. As shown in Figure 9.7, direction excitation of the bulb region at 550 nm (or wavelength longer than B2 and), generate charge transfer excitons in bulb region with holes confined in ZnSe seed and electrons localized in the CdS shell in the bulb. These excitons dissociate by electrons transfer (~ 3 ps) to adsorbed $MV^{2+}$ molecules with

unity yield. Due to the proximity of the electrons with the holes left in ZnSe seed (or transferred thiol), the charge recombination loss is high, leading to relatively small steady $MV^{+\bullet}$ radical generation quantum yield (~35%). Illumination at B1 or shorter wavelength generates excitons in CdS nanorod domain that undergo three pathways of charge separation. In pathway A (13%), excitons are localized to the bulb region before they dissociate, which is similar to the direct excitation of the charge transfer band. In pathway B and C (87%), excitons are dissociated in the CdS rod by ultrafast (~ 130 fs) electron transfer to surface adsorbed $MV^{2+}$. In pathway B (17%) the holes localized onto the CdS surface trap states, generating a charge separate state that is similar to that observed in CdS (without the ZnSe seed). The quantum yield of this species is estimated to be ~ 66% based on previous measurement of CdS rod.[12] The remaining 70% of excitons proceed by pathway C, in which the hole is localized to the ZnSe seed, generating a charge separated state with long e-h spatial distance to effectively suppress charge recombination loss. Assuming quantum yields of $MV^{+\bullet}$ radical generation quantum yield of 35%, 66% and 100% for pathways A, B and C, respectively, we can estimate a total quantum yield of ~86% for 400 nm illumination, which is close to the measured value.

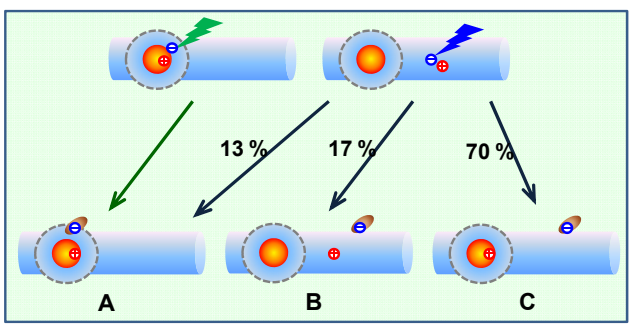

**Figure 9.7.** Schematic depiction of various charge transfer pathways in MPA-DIR-MV reaction solution under bulb region and rod region excitation conditions. A: hole in ZnSe and electron in $MV^{2+}$ on bulb region. B: hole trapped in CdS rod and electron in $MV^{2+}$ on rod region. C: hole localized to ZnSe seed and electron in $MV^{2+}$ on rod region.

Similar as ZnSe/CdS nanorods, competition of exciton trapping on CdS rod and localization to bulb region has also been observed in CdSe/CdS NRs.[30,44] On the other hand a high efficiency of $MV^{+\bullet}$ radical photogeneration was observed with a different set of CdSe/CdS nanorods, which may imply that pathway C is the dominating charge transfer process in that sample.[12] It should be noted the branching ratios among the multiple pathways likely depend sensitively on the synthetic conditions (trap density and distribution) and nanorod shape and dimensions of the nanorods (size and length of the rod, as well as the size and shell thickness of the bulb region).[30,40] Nevertheless, our results suggest that the presence of multiple exciton localization and charge transfer pathways is likely general for nanorod heterostructures. Furthermore, in the presence of catalysts, these $MV^{+\bullet}$ radical photogeneration systmes can be used for the light-driven $H_2$ evolution[12,32,33] or $CO_2$ reduction.[34,35] Therefore, wavelength dependent quantum yields of photocatalysis can be expected in systems that employ these nanorods as light harvesting components.

Because of the presence of multiple competing charge transfer pathways, further optimization of the system can be achieved by enhancing the branching ratio of pathway C and/or improve the efficiencies pathway A and B. Through selective etching of CdS

outer shell in bulb region,[16] the hole removal process by electron donor can be facilitated, which should improve the $MV^{+\bullet}$ generation efficiency for pathway A.[16] Trapping of excitons on CdS nanorod surface represent another major loss. Surface passivation (e.g. $Cd^{2+}$ layer termination) to remove the hole trapping sites could be one way to reduce the contribution of pathway B.[58] In addition, it is found that shorter nanorods and nanotetrapod heterostructures can have negligible exciton trapping in CdS nanorod domain,[44] which can also boost the efficiency of this redox mediator based solar-to-fuel conversion approach. The high efficiency of pathway C requires ultrafast electron transfer to acceptors to compete with fast localization of excitons to the seed region. To achieve efficient charge separation to acceptors with slow electron transfer rates (such as catalysts), it would be helpful to explore more sophisticated nanoheterostructures that are designed for selective hole localization to one region without accompanying electron localization closely.

## 9.3. Conclusion

In conclusion, despite the well established type II band alignment, the lowest energy charge transfer exciton in ZnSe/CdS seeded nanorod is hole in ZnSe seed and electron localized in bulb like CdS shell surrounding the seed without extending into CdS rod. Under rod excitation condition, majority of excitons localized into bulb region with rest trapped on CdS rod. Because of multiple competing pathways, the photoreduction of

$MV^{2+}$ redox mediator using ZnSe/CdS type II seeded nanorod shows dramatic wavelength dependent performance. Under lower energy excitation where excitons are created in bulb region where seed locates, the transferred electron in $MV^{+\bullet}$ radical is close to the hole left in ZnSe seed therefore the charge recombination loss is large and quantum yield is low (~ 34 %). The CdS rod excitation leads to three types of charge separated states. Majority of excitons have ultrafast electron transfer to surface bound $MV^{2+}$ before localization and hole localization into ZnSe seed, resulting in suppressed charge recombination and significantly higher quantum yield (~ 90 %). Depending on the synthetic conditions and shapes and dimensions of nanorod heterostructures, the branching ratios among the multiple pathways could vary. Nevertheless, this founding should be generally applicable to other armed nanoheterostructures (e.g. Cd or Zn based nanorod and tetrapods, dumbbells) and highlights the effect of carrier distribution and dynamics on their photocatalytic performance, thereby suggesting approaches for further nanoheterostructure design and optimization.

## References

(1) Wilker, M. B.; Schnitzenbaumer, K. J.; Dukovic, G. *Isr. J. Chem.* **2012**, *52*, 1002.

(2) Greene, B. L.; Joseph, C. A.; Maroney, M. J.; Dyer, R. B. *J. Am. Chem. Soc.* **2012**, *134*, 11108.

(3) Brown, K. A.; Wilker, M. B.; Boehm, M.; Dukovic, G.; King, P. W. *J. Am. Chem. Soc.* **2012**, *134*, 5627.

(4) Berr, M. J.; Schweinberger, F. F.; Döblinger, M.; Sanwald, K. E.; Wolff, C.; Breimeier, J.; Crampton, A. S.; Ridge, C. J.; Tschurl, M.; Heiz, U.; Jäckel, F.; Feldmann, J. *Nano Lett.* **2012**, *12*, 5903.

(5) Han, Z.; Qiu, F.; Eisenberg, R.; Holland, P. L.; Krauss, T. D. *Science* **2012**, *338*, 1321.

(6) Huang, J.; Mulfort, K. L.; Du, P.; Chen, L. X. *J. Am. Chem. Soc.* **2012**, *134*, 16472.

(7) Amirav, L.; Alivisatos, A. P. *J. Phys. Chem. Lett.* **2010**, *1*, 1051.

(8) Zhu, H.; Lian, T. *Energy Environ. Sci.* **2012**, *5*, 9406.

(9) Lo, S. S.; Mirkovic, T.; Chuang, C.-H.; Burda, C.; Scholes, G. D. *Adv. Mater.* **2011**, *23*, 180.

(10) Costi, R.; Saunders, A. E.; Banin, U. *Angew. Chem. Int. Ed.* **2010**, *49*, 4878.

(11) Donega, C. d. M. *Chem. Soc. Rev.* **2011**, *40*, 1512.

(12) Zhu, H.; Song, N.; Lv, H.; Hill, C. L.; Lian, T. *J. Am. Chem. Soc.* **2012**, *134*, 11701.

(13) Acharya, K. P.; Khnayzer, R. S.; O'Connor, T.; Diederich, G.; Kirsanova, M.; Klinkova, A.; Roth, D.; Kinder, E.; Imboden, M.; Zamkov, M. *Nano Lett.* **2011**, *11*, 2919.

(14) Tang, M. L.; Grauer, D. C.; Lassalle-Kaiser, B.; Yachandra, V. K.; Amirav, L.; Long, J. R.; Yano, J.; Alivisatos, A. P. *Angew. Chem. Int. Ed.* **2011**, *50*, 10203.

(15) Tongying, P.; Plashnitsa, V. V.; Petchsang, N.; Vietmeyer, F.; Ferraudi, G. J.; Krylova, G.; Kuno, M. *J. Phys. Chem. Lett.* **2012**, 3234.

(16) Khon, E.; Lambright, K.; Khnayzer, R. S.; Moroz, P.; Perera, D.; Butaeva, E.; Lambright, S.; Castellano, F. N.; Zamkov, M. *Nano Lett.* **2013**, *13*, 2016.

(17) O'Connor, T.; Panov, M. S.; Mereshchenko, A.; Tarnovsky, A. N.; Lorek, R.; Perera, D.; Diederich, G.; Lambright, S.; Moroz, P.; Zamkov, M. *ACS Nano* **2012**, *6*, 8156.

(18) Müller, J.; Lupton, J. M.; Lagoudakis, P. G.; Schindler, F.; Koeppe, R.; Rogach, A. L.; Feldmann, J.; Talapin, D. V.; Weller, H. *Nano Lett.* **2005**, *5*, 2044.

(19) Müller, J.; Lupton, J. M.; Rogach, A. L.; Feldmann, J.; Talapin, D. V.; Weller, H. *Phys. Rev. B* **2005**, *72*, 205339.

(20) Lupo, M. G.; Della Sala, F.; Carbone, L.; Zavelani-Rossi, M.; Fiore, A.; Lüer, L.; Polli, D.; Cingolani, R.; Manna, L.; Lanzani, G. *Nano Lett.* **2008**, *8*, 4582.

(21) She, C.; Demortière, A.; Shevchenko, E. V.; Pelton, M. *J. Phys. Chem. Lett.* **2011**, 1469.

(22) Sitt, A.; Sala, F. D.; Menagen, G.; Banin, U. *Nano Lett.* **2009**, *9*, 3470.

(23) Luo, Y.; Wang, L.-W. *ACS Nano* **2009**, *4*, 91.

(24) Kraus, R. M.; Lagoudakis, P. G.; Rogach, A. L.; Talapin, D. V.; Weller, H.; Lupton, J. M.; Feldmann, J. *Phys. Rev. Lett.* **2007**, *98*, 017401.

(25) Grazia Lupo, M.; Scotognella, F.; Zavelani-Rossi, M.; Lanzani, G.; Manna, L.; Tassone, F. *Phys. Chem. Chem. Phys.* **2012**, *14*, 7420.

(26) Steiner, D.; Dorfs, D.; Banin, U.; Della Sala, F.; Manna, L.; Millo, O. *Nano Lett.* **2008**, *8*, 2954.

(27) Rainò, G.; Stöferle, T.; Moreels, I.; Gomes, R.; Kamal, J. S.; Hens, Z.; Mahrt, R. F. *ACS Nano* **2011**, *5*, 4031.

(28) Eshet, H.; Grünwald, M.; Rabani, E. *Nano Lett.* **2013**, *13*, 5880.

(29) Kunneman, L. T.; Zanella, M.; Manna, L.; Siebbeles, L. D. A.; Schins, J. M. *J. Phys. Chem. C* **2013**, *117*, 3146.

(30) Wu, K.; Rodríguez-Córdoba, W. E.; Liu, Z.; Zhu, H.; Lian, T. *ACS Nano* **2013**, *7*, 7173.

(31) Mauser, C.; Da Como, E.; Baldauf, J.; Rogach, A. L.; Huang, J.; Talapin, D. V.; Feldmann, J. *Phys. Rev. B* **2010**, *82*, 081306.

(32) Kiwi, J.; Gratzel, M. *Nature* **1979**, *281*, 657.

(33) Okura, I.; Kim-Thuan, N.; Takeuchi, M. *Angew. Chem. Int. Ed. Engl.* **1982**, *21*, 434.

(34) Parkinson, B. A.; Weaver, P. F. *Nature* **1984**, *309*, 148.

(35) Shin, W.; Lee, S. H.; Shin, J. W.; Lee, S. P.; Kim, Y. *J. Am. Chem. Soc.* **2003**, *125*, 14688.

(36) Dorfs, D.; Salant, A.; Popov, I.; Banin, U. *Small* **2008**, *4*, 1319.

(37) Hewa-Kasakarage, N. N.; Kirsanova, M.; Nemchinov, A.; Schmall, N.; El-Khoury, P. Z.; Tarnovsky, A. N.; Zamkov, M. *J. Am. Chem. Soc.* **2009**, *131*, 1328.

(38) Ivanov, S. A.; Piryatinski, A.; Nanda, J.; Tretiak, S.; Zavadil, K. R.; Wallace, W. O.; Werder, D.; Klimov, V. I. *J. Am. Chem. Soc.* **2007**, *129*, 11708.

(39) Borys, N. J.; Walter, M. J.; Huang, J.; Talapin, D. V.; Lupton, J. M. *Science* **2010**, *330*, 1371.

(40) Kim, S.; Fisher, B.; Eisler, H. J.; Bawendi, M. *J. Am. Chem. Soc.* **2003**, *125*, 11466.

(41) Nemchinov, A.; Kirsanova, M.; Hewa-Kasakarage, N. N.; Zamkov, M. *J. Phys. Chem. C* **2008**, *112*, 9301.

(42) Zhu, H.; Song, N.; Lian, T. *J. Am. Chem. Soc.* **2011**, *133*, 8762.

(43) Wu, K.; Zhu, H.; Liu, Z.; Rodríguez-Córdoba, W.; Lian, T. *J. Am. Chem. Soc.* **2012**, *134*, 10337.

(44) Talapin, D. V.; Nelson, J. H.; Shevchenko, E. V.; Aloni, S.; Sadtler, B.; Alivisatos, A. P. *Nano Lett.* **2007**, *7*, 2951.

(45) Shabaev, A.; Efros, A. L. *Nano Lett.* **2004**, *4*, 1821.

(46) Vietmeyer, F.; McDonald, M. P.; Kuno, M. K. *J. Phys. Chem. C* **2012**, *116*, 12379.

(47) Giblin, J.; Kuno, M. *J. Phys. Chem. Lett.* **2010**, *1*, 3340.

(48) Zhu, H.; Song, N.; Rodríguez-Córdoba, W.; Lian, T. *J. Am. Chem. Soc.* **2012**, *134*, 4250.

(49) Chuang, C.-H.; Doane, T. L.; Lo, S. S.; Scholes, G. D.; Burda, C. *ACS Nano* **2011**, *5*, 6016.

(50) Scotognella, F.; Miszta, K.; Dorfs, D.; Zavelani-Rossi, M.; Brescia, R.; Marras, S.; Manna, L.; Lanzani, G.; Tassone, F. *J. Phys. Chem. C* **2011**, *115*, 9005.

(51) Hewa-Kasakarage, N. N.; El-Khoury, P. Z.; Tarnovsky, A. N.; Kirsanova, M.; Nemitz, I.; Nemchinov, A.; Zamkov, M. *ACS Nano* **2010**, *4*, 1837.

(52) She, C.; Bryant, G. W.; Demortière, A.; Shevchenko, E. V.; Pelton, M. *Phys. Rev. B* **2013**, *87*, 155427.

(53) Klimov, V. I. *J. Phys. Chem. B* **2000**, *104*, 6112.

(54) Klimov, V. I. *Annu. Rev. Phys. Chem.* **2007**, *58*, 635.

(55) Watanabe, T.; Honda, K. *J. Phys. Chem.* **1982**, *86*, 2617.

(56) Zhu, H.; Lian, T. *J. Am. Chem. Soc.* **2012**, *134*, 11289.

(57) Morris-Cohen, A. J.; Frederick, M. T.; Cass, L. C.; Weiss, E. A. *J. Am. Chem. Soc.* **2011**, *133*, 10146.

(58) Wei, H. H.-Y.; Evans, C. M.; Swartz, B. D.; Neukirch, A. J.; Young, J.; Prezhdo, O. V.; Krauss, T. D. *Nano Lett.* **2012**, *12*, 4465.

# Appendix 1.

**UV−vis difference spectra of MV radical generation under 550 nm illumination**

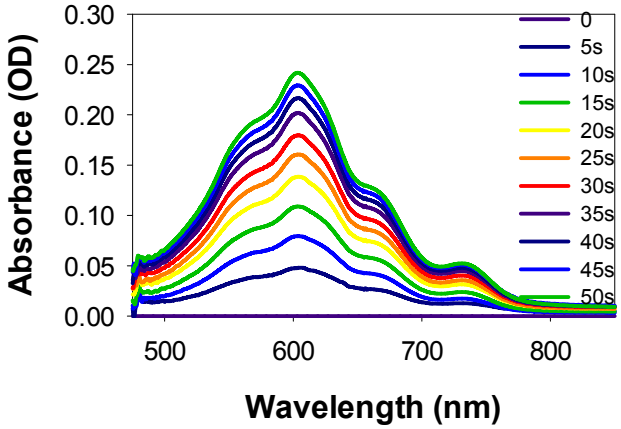


**Figure A.9.1.** UV−vis difference spectra (after−before irradiation) of a solution containing ZnSe/CdS DIR, $MV^{2+}$ and MPA after indicated time of 550 nm illumination.

# Chapter 10. Summary and Outlook

The goal of the research presented in this thesis is to understand and control the charge transfer properties from quantum confined semiconductor nanocrystals and design better nanocrystals based systems for solar-to-fuel conversion applications. We summarize these results into three parts below and also consider some of the unanswered questions and future directions.

Part I. In Chapter 3 and 4, using model QD-molecular electron acceptor systems, we aimed to understand quantitatively the rate of electron transfer from QDs under the framework of Marcus electron transfer theory and examined the effect of driving force and electronic coupling on QD charge transfer rates. Experimentally, we observed monotonic increase of electron transfer rates with driving force, showing the lack of Marcus inverted regime. Considering the electron-hole Coulomb interaction in QDs, we proposed the Auger-assisted electron transfer model assuming that the excess driving force energy can be dissipated by hole excitation through Auger electron-hole energy transfer process. This model was found to be in well agreement with experimental results and was supported by computational simulations. This study points out the fundamental difference for electron transfer process from quantum confined semiconductor nanocrystals and bulk semiconductors. This Auger-assisted ET model is believed to be generally applicable to excitonic nanomaterials as long as the Auger electron-hole energy transfer occurs. Then, using CdSe/ZnS type I core/shell QDs, we observed exponential decay of charge separation and recombination rates with ZnS shell thickness, indicating

ZnS shell acts as tunneling barrier for both electron and hole due to type I band alignment. By comparing with electron/hole surface density calculated using the effective mass model, we found the decay of charge separation and recombination rates agreed well with the electron and hole surface density decay, respectively. This agreement indicates that the relative carrier surface density provides a simple and convenient way to estimate the relative electronic coupling and the relative carrier transfer rate. This study also suggests the "wavefunction engineering" idea to independently control the charge separation and charge recombination processes. In chapter 5, we extend the study to CdTe/CdSe type II QDs with shell localized electrons and core confined holes. We compared the charge transfer properties between CdSe, CdSe/ZnSe type I and CdTe/CdSe type II QDs. Compared with CdSe QDs which show both fast charge separation and recombination rates and CdSe/ZnS type I QDs which show both reduced charge separation and recombination rates, CdTe/CdSe type II QDs simultaneously enable ultrafast charge separation and slow charge recombination. This advantageous charge transfer properties is due to the unique spatially separated electron/hole wavefunctions. This study demonstrates that the "wavefunction engineering" is an effective approach for achieving high charge separation yield and long-lived charge separated state.

Although these three chapters focus on charge transfer processes in model systems with zero dimensional QDs and molecular acceptors, the fundamental ideas presented here, e.g. Auger-assisted electron transfer and wavefunction engineering, are believed to lay down a foundation and be generally applicable to charge transfer process from other nanocrystals systems. The test and extension of these interesting ideas to other

systems including one and two dimensional nanomaterials can be explored. Compared with electron transfer study, systematic study for direct hole transfer process is absent, in part due to the very weak contribution of holes to transient absorption spectra. Compared with the well defined and discrete conduction band 1S electron level, the actual nature (both the energetics and wavefunction distribution) of excited hole is less well understood. This is further complicated by the prevalence of even less well understood hole traps. Considering the equal importance of hole transfer process for overall charge transfer loop, it would be highly desirable to deliberately control valance band hole state and systematically study the hole transfer process from nanocrystals.

Part II. In chapter 6 and 7, we investigated the annihilation and dissociation of multi-excitons in CdSe/CdS quasi-type II QDs and CdSe nanorods, where multiexciton states are generated by multiphoton absorption. Compared with CdSe QD, CdSe/CdS QD and CdSe nanorods show a 4 ~ 5 fold higher multiexciton dissociation efficiencies. The multiexciton dissociation efficiency is determined by the competition between multiexciton Auger recombination and interfacial charge separation. The unique electron/hole wavefunction distribution arising from quasi-type II band alignment (in CdSe/CdS QD) and one-dimensional shape (in CdSe nanorod) simultaneously facilitates the exciton dissociation and retards Auger recombination.

The understanding and control of multiexciton Auger recombination and the efficient conversion of multiexcitons to externally separated charges is of considerable interest for advanced nanocrystals based photovoltaic and photocatalytic devices. It would be interesting to deliver multiple electrons to a practically interesting catalyst.

Compared with the extensively studied single exciton dissociation process, the electron transfer process under the presence of multiple charge separated states remains unclear. Utilizing pump-pump-probe transient absorption to investigate that electron transfer process could lead to more insights and potentially help design systems with enhanced multiexciton dissociation efficiency. In addition to interfacial charge transfer, multiexciton extraction by energy transfer to other NCs or molecules, which produce multiple long-lived single excited states, should also be explored. Direct multiexciton generation (MEG) by one higher energy photon is a potentially promising way if nanomaterials with lower MEG energy threshold and higher MEG efficiency can be developed. Alternatively, methods to enhance light harvesting rates in advanced nanostructures, such as plasmonic enhancement or NC-antenna complexes, should also be investigated.

Part III. In last two chapters, chapter 8 and 9, we demonstrate a redox mediator based approach for solar-to-fuel conversion using semiconductor nanocrystals. We compared CdSe based nanocrystals of various compositions and shapes including CdSe/CdS core/shell QDs and CdSe/CdS seeded nanorod. Among them, CdSe/CdS nanorods show the highest $MV^{+\bullet}$ radical photogeneration and $H_2$ evolution efficiencies. Using time-resolved transient absorption and fluorescence measurements, the different photocatalytic performances was shown to be due to different charge recombination losses. CdSe/CdS nanorods show ultrafast charge separation, fast hole removal and slow charge recombination, which suppressed the charge recombination loss and led to much higher photocatalytic performance. In addition, we studied the $MV^{+\bullet}$ radical

photogeneration using ZnSe/CdS seeded nanorods. Despite the well established type II band alignment, the electron wavefunction in lowest energy charge transfer exciton was found to be localized in CdS bulb near ZnSe seed without extending through CdS rod. Under rod excitation, majority of excitons generated in the CdS rod localized rapidly to the charge transfer exciton state in the seed/bulb region and the rest remained in the CdS rod, likely caused by rapid hole trapping. This exciton localization led to dramatic wavelength dependent quantum yield for $MV^{+\bullet}$ radical photogeneration: 34% and 90% for 550 nm and 415 nm illuminations, respectively. Transient absorption spectra show larger charge recombination loss under band edge excitation due to spatial proximity of the reduced $MV^{+\bullet}$ radical and hole in ZnSe seed. Under rod excitation, the majority of excitons (70%) dissociated by ultrafast electron transfer to $MV^{2+}$, followed by rapid hole localization into the ZnSe seed to generate charge separated state with large spatial separation of $MV^{+\bullet}$ radical and holes in ZnSe seed, which suppressed the charge recombination loss.

The results demonstrate that by controlling the compositions and dimensions, quantum-confined semiconductor nanoheterostructures can be tailored to be efficient light harvesting and charge separation centers. Since exciton localization/trapping is likely a general property in semiconductor nanoheterostructures, the wavelength dependent exciton distribution and photocatalytic performance can also be expected in many other linear and branched nanoheterostructures. To achieve efficient charge separation to acceptors with slow electron transfer rates (such as catalysts), it would be helpful to explore more sophisticated nanoheterostructures that are designed with large

electron and hole spatial separation in the nanoheterostructures, such that both the intrinsic excited electron lifetime and charge separated state lifetime can be greatly prolonged. The photocatalytic systems reported previously all rely on oxidative quenching where excited electron transfer to catalyst competes with its intrinsic decay. Alternatively, similar as molecular dyes, it would be highly desirable to achieve the reductive quenching with hole removal first and create an extremely long-lived excited electron in nanocrystals. This would greatly benefit the practical photocatalytic reactions but requires sophisticated manipulation of the hole transfer process as well as the electron trapping pathways.

Ultimately, practical solar-to-fuel conversion application using nanocrystals requires the replacement of sacrificial electron donor. It would be ideal to develop fully integrated system with both water oxidation and reduction in one nanocrystal system. Alternatively, the nanocrystal based half reaction can also be integrated onto electrodes (to form photocathode/anode) with external electric circuits as the carrier source. Many fundamental and practical questions remain to be addressed, such as the choice of electrode materials and the architecture of nanocrystal based photocathode/anode. Various aspects including the mechanic stability, carrier transport, photocatalytic sites and liquid-solid junction interface have to be taken into consideration. Time resolved spectroscopy techniques as well as advanced imaging tools could be combined with photo/electro-chemical measurements to guide the photoelectrode design and optimization for efficient solar-to-fuel conversion.

In chapter 1, semiconductor nanocrystals were pictured as promising light harvesting and charge transfer centers for future solar-to-fuel conversion, because of their tunable optical, electronic and chemical properties and because of their unique excited carrier relaxation and charge transfer characteristics. After five years of research, the fundamental understanding of electron transfer from quantum confined semiconductor nanocrystals have been significantly advanced by us and other groups. The knowledge we've learned provide an important guidance of designing practical photocatalytic devices using semiconductor nanocrystals, but significant scientific and technological issues still remain. Therefore, the effort will continue, from material science, physical chemistry to device engineering, to overcome those barriers that prohibit the realization of efficient, inexpensive and robust semiconductor nanocrystal based devices for solar energy conversion.